5. ZIRCALOY OXIDES

The materials properties correlations needed for the oxides of the zircaloy fuel cladding formed at high temperatures were developed and are described in this section. The subcodes described in this section are for melting temperature (ZOPRP), specific heat capacity (ZOCP), enthalpy (ZONTHL), thermal conductivity (ZOTCON), thermal expansion (ZOTEXP), density (ZODEN), emissivity (ZOEMIS), elastic moduli (ZOEMOD, ZOPOIR), and mechanical limits and embrittlement (ZORUP).

5.1 Melting and Phase Transformation Temperatures (ZOPRP)

The subcode ZOPRP calculates the transition temperatures between the monoclinic, tetragonal, cubic, and liquid phases of zircaloy oxide. The oxygen-to-metal ratio of the oxide is the only required input to the subroutine. The monoclinic-to-tetragonal and tetragonal-to-cubic transition temperatures are constants that have been reported for ZrO_2 (1,478 and 2,558 K, respectively).[5.1-1] These temperatures are assumed to apply to zircaloy oxide, in spite of the fact that the oxide is slightly substoichiometric and may be under stress.

5.1.1 Model Development

Since atomic fraction oxygen in the zircaloy oxide compound is used as a basis to determine the solidus (appearance of the first liquid phase) and the liquidus (melting of the last solid phase) temperatures of the zircaloy oxide, the input oxygen-to-metal ratio is converted to atomic fraction using the following relationship:

$$x = \frac{YE}{(1 + YE)} \tag{5-1}$$

where

x = atomic fraction oxygen (atoms of oxygen/atoms of compound)

YE = oxygen-to-metal ratio in compound (atoms of oxygen/atoms of zirconium).

With a known atomic fraction oxygen for the zirconium oxide, the correlations developed for the PSOL and PLIQ subroutines described in Section 11.1 were used to calculate the solidus temperatures. These correlations are as follows:

For $x \leq 0.1$,

$$T_{sol} = 2{,}098 + 1{,}150 \ . \tag{5-2}$$

For $0.1 < x \leq 0.18$,

$$T_{sol} = 2{,}213 \ . \tag{5-3}$$

For $0.18 < x \leq 0.29$,

$$T_{sol} = 1{,}389.5317 + 7{,}640.0748\ x - 17{,}029.172\ x^2 \ . \tag{5-4}$$

For $0.29 < x \leq 0.63$,

$$T_{sol} = 2{,}173 \ . \tag{5-5}$$

For $0.63 < x \leq 0.667$,

$$T_{sol} = -11{,}572.454 + 21{,}818.181\ x \ . \tag{5-6}$$

For $x > 0.667$,

$$T_{sol} = -11{,}572.454 + (1.334 - x)\ 21{,}818.181 \tag{5-7}$$

where T_{sol} is the solidus temperature (K).

The liquidus temperatures are calculated using the following relationships:

For $x \leq 0.19$,

$$T_{liq} = 2{,}125 + 1{,}632.1637\ x - 5{,}321.6374\ x^2 \ . \tag{5-8}$$

For $0.19 < x \leq 0.41$,

$$T_{liq} = 2{,}111.6553 + 1{,}159.0909\ x - 2{,}462.1212\ x^2 \ . \tag{5-9}$$

For $0.41 < x \leq 0.667$,

$$T_{liq} = 895.07792 + 3{,}116.8831\ x \ . \tag{5-10}$$

For $x > 0.667$,

$$T_{liq} = 895.07792 + (1.34 - x)\, 3{,}116.8831 \qquad (5\text{-}11)$$

where T_{liq} is the liquidus temperature (K).

Figure 5-1 shows the zircaloy oxide solidus and liquidus temperatures as calculated by the subroutine for oxygen-to-metal ratios greater than 1.5.

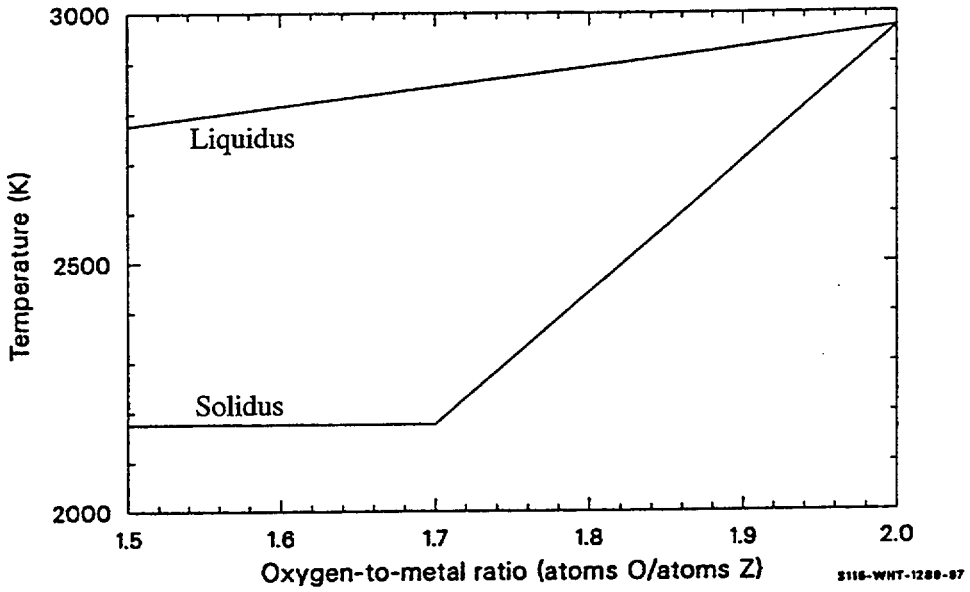

Figure 5-1. Zircaloy oxide solidus and liquidus temperatures.

5.1.2 Reference

5.1-1 R. R. Hammer, *Zircaloy-4, Uranium Dioxide and Materials Formed By Their Interaction. A Literature Review with Extrapolation of Physical Properties to High Temperatures*, IN-1093, September, 1967.

5.2 Specific Heat Capacity and Enthalpy (ZOCP, ZONTHL)

The functions ZOCP and ZONTHL return zircaloy oxide specific heat capacity and enthalpy. ZOCP requires only temperature as input, while the two enthalpy subcodes require temperature and a reference temperature for which the enthalpy will be set equal to zero.

5.2.1 Specific Heat (ZOCP)

Zircaloy oxide specific heat is modeled by the ZOCP function with the following expressions, which were taken from Reference 5.2-1.

For $300 < T < 1{,}478$ K (monoclinic ZrO_2),

$$C_p^{\circ} = 565 + 6.11 \times 10^{-2}\, T - 1.14 \times 10^{7}/T^{-2} \ . \quad (5\text{-}12)$$

For $1{,}478 \leq T \leq 2{,}000$ K (tetragonal ZrO_2),

$$C_p^{\circ} = 604.5 \ . \quad (5\text{-}13)$$

For $2{,}000 < T < 2{,}830$ K (tetragonal and cubic ZrO_2),

$$C_p^{\circ} = 171.7 + 0.2164\, T \ . \quad (5\text{-}14)$$

For $2{,}830 < T < 2{,}873$ K

$$C_p^{\circ} = 1.64e4. \quad (5\text{-}15)$$

For $T \geq 2{,}873$ K (liquid ZrO_2),

$$C_p^{\circ} = 815 \text{ J/kg•K} \quad (5\text{-}16)$$

where

C_p° = specific heat of zircaloy oxide (J/kg•K)

T = temperature (K).

The several equations correspond to the several phases of ZrO_2.

5.2.2 Enthalpy (ZONTHL)

Zircaloy oxide enthalpy is modeled in the ZONTHL function with the integrated version of Equations (5-13) through (5-16), estimates of the changes of enthalpies at the phase changes and an estimate of the heat of fusion of ZrO_2.[a]

a. Monoclinic to tetragonal transition ΔH = 48,200 J/kg; tetragonal to cubic transition ΔH = 102,000 J/kg; heat of fusion = 706,000 J/kg.

For $T \leq 300$ K,

$$H^0 = 456.6633 \times (T - 300)$$

For $300 < T < 1{,}478$ K (monoclinic ZrO_2),

$$H^0(T) - H^0(300) = 565\,T + 3.055 \times 10^{-2}\,T^2 + 1.14 \times 10^7 / T^{-1} - 2.102495 \times 10^5 \quad . \tag{5-17}$$

For $1{,}478 \leq T \leq 2{,}000$ K[a] (tetragonal ZrO_2),

$$H^0(T) - H^0(300) = 604.5\,T - 1.46 \times 10^5 \quad . \tag{5-18}$$

For $2{,}000 < T < 2{,}558$ K (tetragonal and cubic ZrO_2),

$$H^0(T) - H^0(300) = 171.7\,T + 0.1082\,T^2 + 2.868 \times 10^5 \quad . \tag{5-19}$$

For $2{,}558 \leq T < 2{,}973$ K,

$$H^0(T) - H^0(300) = 171.7\,T + 0.1082\,T^2 + 3.888 \times 10^5 \quad . \tag{5-20}$$

For $T \geq 2{,}973$ K (liquid ZrO_2),

$$H^0(T) - H^0(300) = 815\,T + 1.39 \times 10^5 \tag{5-21}$$

where

$H^0(T)$ = enthalpy of zircaloy oxide at temperature T (J/kg)

T = oxide temperature (K).

The principal contribution to the expected standard error of the enthalpy and specific heat capacity predictions for cladding oxide is not the uncertainty of the correlations for ZrO_2 because C_p measurements are typically accurate to several percent. It is the probability that the oxide film that appears on cladding differs significantly from the ZrO_2 used to produce the correlations. The oxide is substoichiometric and has enough stress from the volume expansion during oxidation to cause significant changes of the phase transition temperatures.[5.2-2] Therefore, a relatively large expected standard error of $\pm$ 0.2 times the given values is suggested for both the predicted specific heat capacity and enthalpy of zircaloy oxide.

The specific heat capacity predicted with the ZOCP function is shown in Figure 5-2. Comparison of the predicted specific heat capacity with data reported by Gilchrist,[5.2-3] which are reproduced in Table 5-1, suggests an expected standard error of ± 150 J/kg• K.Figure 5-3 is a plot of the zircaloy oxide enthalpy predicted with the ZONTHL function. The numerous steps are heats of transitions for the several phase changes of zircaloy dioxide.

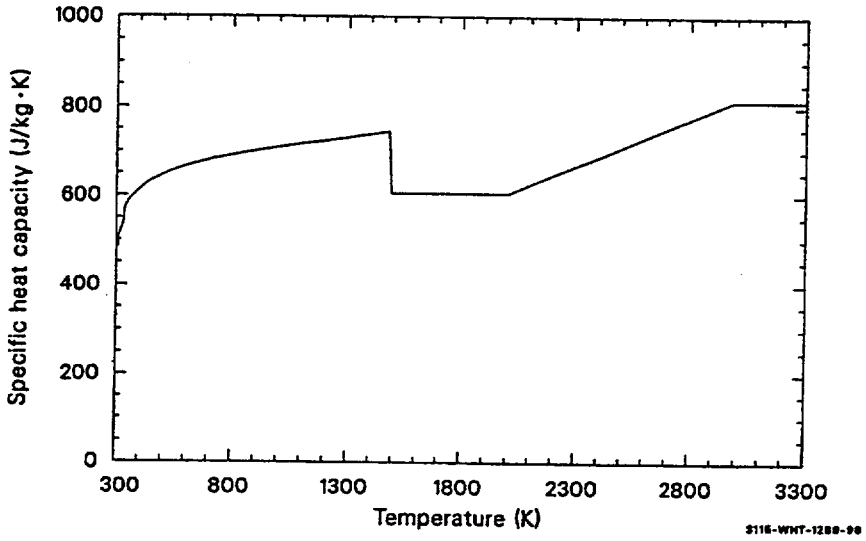

Figure 5-2. Zircaloy oxide specific heat capacity as a function of temperature.

Table 5-1. Zircaloy cladding oxide specific heat capacity data from Gilchrist.[5.2-3]

Temperature	Specific heat capacity	Comment
324	462	Measured by Gilchrist
348	481	Measured by Gilchrist
377	486	Measured by Gilchrist
422	402	Measured by Gilchrist
462	510	Measured by Gilchrist
500	523	Measured by Gilchrist
598	543	Measured by Gilchrist
698	566	Measured by Gilchrist

Table 5-1. Zircaloy cladding oxide specific heat capacity data from Gilchrist.[5.2-3] (Continued)

Temperature	Specific heat capacity	Comment
801	569	Measured by Gilchrist
899	592	Measured by Gilchrist
945	598	Measured by Gilchrist
975	601	Measured by Gilchrist
1,004	603	Measured by Gilchrist
772	563	Measured by Smithells
373	437	Measured by Washburn
774	525	Measured by Washburn
1,272	631	Measured by Washburn
325	442	Reported by Gilchrist as data from "Thermophysical Properties of Solid Material"
399	486	Reported by Gilchrist as data from "Thermophysical Properties of Solid Material"
494	510	Reported by Gilchrist as data from "Thermophysical Properties of Solid Material"
598	535	Reported by Gilchrist as data from "Thermophysical Properties of Solid Material"
692	555	Reported by Gilchrist as data from "Thermophysical Properties of Solid Material"
790	576	Reported by Gilchrist as data from "Thermophysical Properties of Solid Material"
1,198	606	Reported by Gilchrist as data from "Thermophysical Properties of Solid Material"
1,398	612	Reported by Gilchrist as data from "Thermophysical Properties of Solid Material"

5.2.3 References

5.2-1 R. R. Hammer, *Zircaloy-4, Uranium Dioxide, and Materials Formed by Their Interaction. A Literative Review with Extrapolation of Physical Properties to High Temperatures*, IN-1093, September 1967.

5.2-2 R. E. Pawel, J. V. Cathcart, J. J. Campbell, and S. H. Jury, *Zirconium Metal Water Oxidation Kinetics V. Oxidation of Zircaloy in High Pressure Steam*, ORNL/NUREG-31, December 1977.

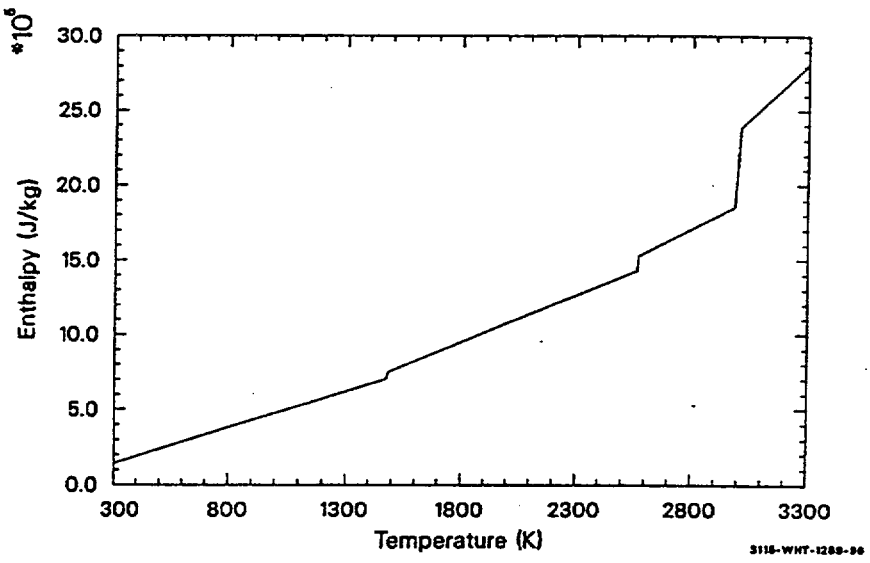

Figure 5-3. Zircaloy oxide enthalpy as a function of temperature.

5.2-3 K. E. Gilchrist, "Thermal Property Measurements on Zircaloy-2 and Associated Oxide Layers," *Journal of Nuclear Materials, 62*, 1976, pp. 257-264.

5.3 Thermal Conductivity (ZOTCON)

The function ZOTCON returns zircaloy oxide thermal conductivity. The only input information required is the temperature of the material.

5.3.1 Model Development

To obtain an accurate value of zircaloy oxide thermal conductivity, accurate calculations of the peak cladding temperature during the rapid heating of cladding due to oxidation that occurs at high temperature are important. Data from the one sample that Adams reports[5.3-4] are presented in Table 5-2. Additional sources of data are Maki,[5.3-5] Lapshov and Bashkatov,[5.3-6] and Gilchrist.[5.3-7]

Table 5-2. Stabilized zircaloy dioxide thermal conductivity data from Adams.[5.3-4]

Temperature	Thermal conductivity	Thermal conductivity corrected to 5,820 kg/m
370	1.69	1.88
460	1.69	1.88
547	1.70	1.89
641	1.78	1.98

Table 5-2. Stabilized zircaloy dioxide thermal conductivity data from Adams.[5.3-4] (Continued)

Temperature	Thermal conductivity	Thermal conductivity corrected to 5,820 kg/m
698	1.73	1.91
743	1.74	1.93
817	1.74	1.93
882	1.74	1.93
945	1.76	1.95
993	1.79	1.98
1,059	1.78	1.97
1,123	1.79	1.98
1,187	1.86	2.06
1,245	1.89	2.09
1,285	1.95	2.16
1,305	1.92	2.13
1,329	1.93	2.14
1,338	1.94	2.15
1,354	1.96	2.17
1,390	1.96	2.18
1,405	1.99	2.20
1,427	1.98	2.19
1,440	2.02	2.24
1,448	2.08	2.31
1,480	2.01	2.23
1,485	2.03	2.25
1,505	2.01	2.23
1,554	2.01	2.23
1,566	2.02	2.24
1,583	2.01	2.23

Data of Maki[5.3-5] from two samples oxidized in steam are reproduced in Table 5-3. The data cover a small temperature range and show a sharp increase in conductivity between 400 and 500 K. The principal

recommendation for the data is that they were taken with black oxide from zircaloy tubes. Two sets of data attributed to Waldman by Maki are also shown in the table.

Table 5-3. Zircaloy oxide thermal conductivity data reported by Maki.[5.3-5]

Outside temperature	Thermal conductivity	Comment
401	0.70	Sample 4
434	4.78	Sample 4
488	6.35	Sample 4
536	5.41	Sample 4
588	5.45	Sample 4
400	1.07	Sample 5
437	4.50	Sample 5
490	5.76	Sample 5
536	6.11	Sample 5
589	6.27	Sample 5
373	0.90	Data from Waldman
373	1.35	Data from Waldman

The data of Lapshov and Bashkatov[5.3-6] are presented in Table 5-4. These data are from films formed by plasma sputtering of zirconium dioxide on tungsten substrates. Since sputtered coatings are quite porous, not of the same oxygen-to-metal ratio as cladding oxide, and may not be very adherent to the substrate, these data may not be representative of zircaloy cladding oxide conductivity.

Table 5-4. Zircaloy dioxide thermal conductivity data of Lapshov and Bashkatov.[5.3-6]

Temperature (K)	Thermal conductivity
571	0.509
618	0.636
642	0.508
654	0.627
664	0.715
684	0.474
721	0.652

Table 5-4. Zircaloy dioxide thermal conductivity data of Lapshov and Bashkatov.[5.3-6] (Continued)

Temperature (K)	Thermal conductivity
739	0.448
755	0.441
771	0.558
802	0.430
817	0.512
827	0.605
855	0.456
882	0.522
929	0.477
969	0.506
984	0.509
999	0.509
1,006	0.472
1,050	0.509
1,071	0.522
1,088	0.493
1,097	0.587
1,104	0.527
1,162	0.563
1,189	0.636
1,201	0.577
1,220	0.555
1,250	0.623
1,302	0.623
1,354	0.577
1,366	0.661
1,380	0.663
1,491	0.708

Table 5-4. Zircaloy dioxide thermal conductivity data of Lapshov and Bashkatov.[5.3-6] (Continued)

Temperature (K)	Thermal conductivity
1,527	0.656
1,558	0.717
1,626	0.801
1,638	0.776
1,685	0.788
1,735	0.854

Table 5-5 presents the data of Gilchrist.[5.3-7] Two types of oxide films were employed, one nodular oxide and the other a black oxide characteristic of the kinds of layers usually reported in high temperature tests with cladding. The black oxide thermal conductivities are much lower than the nodular oxide thermal conductivities, and both kinds of oxide have conductivities that are significantly lower than the stabilized zircaloy dioxide conductivities reported by Adams. Considerable uncertainty is reported by Gilchrist because of difficulty in measuring oxide film thickness.

Table 5-5. Zircaloy oxide thermal conductivity data of Gilchrist.[5.3-7]

Temperature	Thermal conductivity	Comment
297	1.354	Black oxide
668	0.955	Black oxide
712	0.958	Black oxide
806	1.048	Black oxide
854	1.060	Black oxide
916	1.090	Black oxide
983	1.163	Black oxide
1,043	1.242	Black oxide
1,193	1.443	Black oxide
1,260	1.407	Black oxide
1,327	1.393	Black oxide
1,386	1.487	Black oxide
1,450	1.586	Black oxide
299	0.324	Nodular oxide
659	0.137	Nodular oxide

Table 5-5. Zircaloy oxide thermal conductivity data of Gilchrist.[5.3-7] (Continued)

Temperature	Thermal conductivity	Comment
733	0.160	Nodular oxide
806	0.192	Nodular oxide
867	0.219	Nodular oxide
944	0.271	Nodular oxide
1,018	0.410	Nodular oxide
1,141	0.606	Nodular oxide
1,222	0.825	Nodular oxide
1,246	0.864	Nodular oxide
1,326	0.743	Nodular oxide
1,425	0.700	Nodular oxide

Figure 5-4 is a plot of the data in Table 5-2 through Table 5-4. The plot shows that, with the exception of the anomalously high data of Maki, the principal uncertainty in thermal conductivity is caused by sample-to-sample variations. Measurement inaccuracies with any one sample are much smaller than sample-to-sample variations. It is also clear from an inspection of Figure 5-4 that the slopes of the measurements on individual samples are quite consistent. The difference between the various samples is essentially a displacement of a line with a constant slope.

The slope of the thermal conductivity of a given sample was determined with a least-squares linear fit to the data of Adams. These data were used because they extend over a large temperature range and were made with the most accurate experimental technique. The equation which results from this fit is

$$K_{ZrO_2} = 1.67 + 3.62 \times 10^{-4} T \qquad (5\text{-}22)$$

where K_{ZrO_2} is zircaloy dioxide thermal conductivity (W/m•K).

Since the black oxide data of Gilchrist are the most representative of the oxide found on cladding, Equation (5-22) is modified for zircaloy oxide by dividing the right hand side by two. The resultant expression is

$$K_o = 0.835 + 1.81 \times 10^{-4} T \qquad (5\text{-}23)$$

where K_o is zircaloy cladding oxide thermal conductivity (W/m•K).

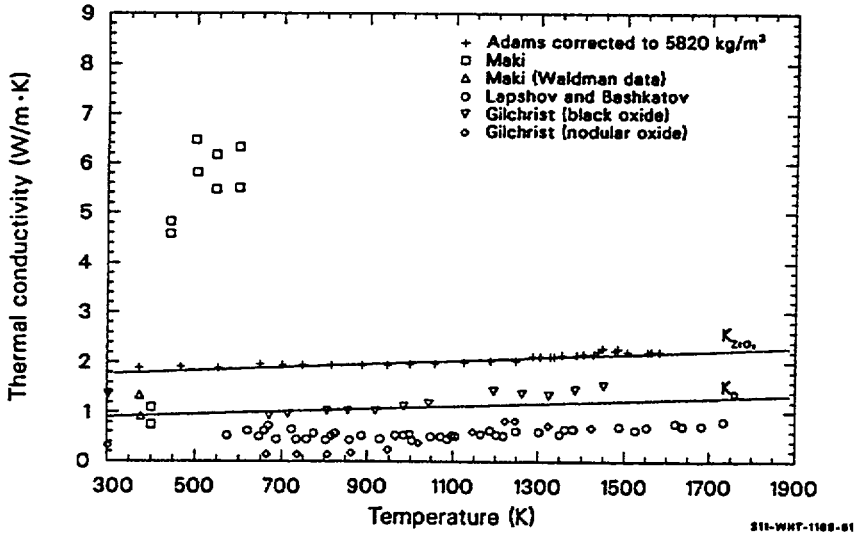

Figure 5-4. Zircaloy oxide thermal conductivity data and correlations.

Values of K_{ZrO_2} and K_o calculated with Equations (5-22) and (5-23) are shown with the data in Figure 5-4. Inspection of the figure suggests an expected standard error of + 0.75 of the measured value for K_o. For material that is known to be ZrO_2, the expected standard error is much less, approximately 10% of the value of K_{ZrO_2}.

For liquid zircaloy oxide (temperature > 2,973 K), the conductivity is assumed to be approximately the value of K_o at the melting temperature of ZrO_2:

$$K_{o(liquid)} = 1.4 \text{ W/m•K} \quad . \tag{5-24}$$

This number is a compromise between the decrease in conductivity at melt due to the loss of the phonon contribution and the increase in conductivity at melt due to the loss of porosity.

Figure 5-5 is a plot of the thermal conductivity predicted by the function ZOTCON as a function of temperature.

5.3.2 References

5.3-4 M. Adams, "Thermal Conductivity: III, Prolate Spheroidal Envelope Method," *Journal of the American Ceramic Society, 37*, 1954, pp. 74-79.

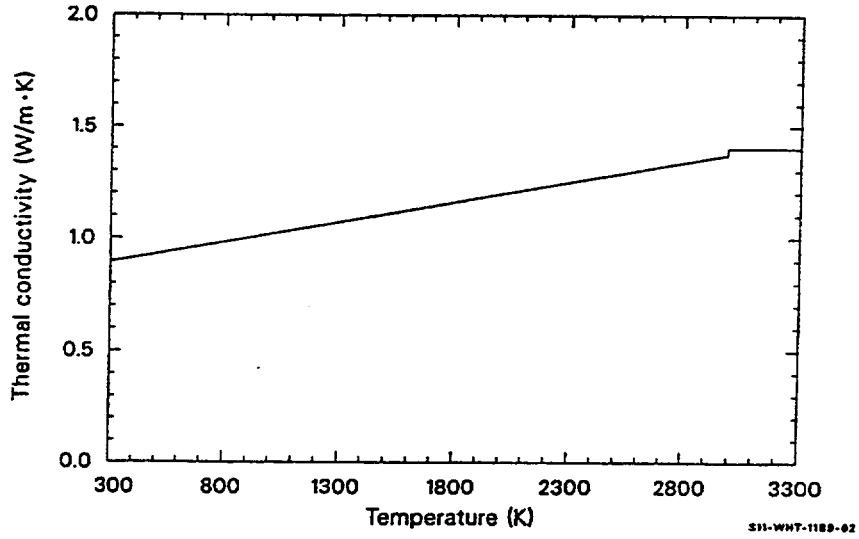

Figure 5-5. Zircaloy oxide thermal conductivity as a function of temperature.

5.3-5 H. Maki, "Heat Transfer Characteristics of Zircaloy-2 Oxide Film," *Journal of Nuclear Science and Technology, 10*, 1973, pp. 107-175.

5.3-6 V. N. Lapshov and A. V. Bashkatov, "Thermal Conductivity of Coatings of Zirconium Dioxide Applied by the Plasma Sputtering Method," *Heat Transfer, Soviet Research, 5*, 1973, pp. 19-22.

5.3-7 K. E. Gilchrist, "Thermal Property Measurements on Zircaloy-2 and Associated Oxide Layers," *Journal of Nuclear Materials, 62*, 1976, pp. 257-264.

5.4 Surface Emissivity (ZOEMIS)

One of the important modes of heat transfer to and from cladding surfaces during an abnormal transient is radiant heat transfer. Since the energy radiated is directly proportional to the emissivity of the inner and outer cladding surfaces, surface emissivity is important in descriptions of abnormal transients.

5.4.1 Summary

Surface emissivities are significantly affected by surface layers on the cladding. For cladding with thin oxide coatings, the oxide surface thickness is only a few wavelengths of near infrared radiation and is partly transparent. Oxide thickness is an important parameter for these thin coatings. Thicker oxide layers are opaque, so the oxide thickness is not as important as the nature of the outer oxide surface, which is affected by temperature and by chemical environment. The effect of temperature has been modeled, but variations in crud on the external cladding surface and chemical reaction products on the inside surface are not modeled explicitly.

The model for emissivity was constructed by considering measured emissivities reported by several investigators.[5.4-1,5.4-2,5.4-3] Expressions used to predict the emissivity of zircaloy cladding surfaces are summarized below.

When the cladding surface temperature has not exceeded 1,500 K, emissivities are modeled by Equations (5-25) and (5-26). For oxide layer thicknesses less than 3.88×10^{-6} m,

$$\varepsilon_1 = 0.325 + 0.1246 \times 10^6 \, d \ . \tag{5-25}$$

For oxide layer thicknesses of 3.88×10^{-6} m or greater,

$$\varepsilon_1 = 0.808642 - 50.0 \, d.^{a} \tag{5-26}$$

where

ε_1 = hemispherical emissivity (unitless)

d = oxide layer thickness (m).

When the maximum cladding temperature has exceeded 1,500 K, emissivity is taken to be the larger of 0.325 and

$$\varepsilon_2 = \varepsilon_1 \exp\left[\frac{1500 - T}{300}\right] \tag{5-27}$$

where

ε_1 = value for emissivity obtained from Equation (5-25)

T = maximum cladding temperature (K).

The standard error expected from the use of Equation (5-25) to predict emissivity in a reactor when cladding surface temperature has never exceeded 1,500 K is

$$\sigma_1 = \pm 0.1 \ . \tag{5-28}$$

---

a. The use of six significant figures in Equation (5-26) ensures an exact match of the values of ε_1 at $d = 3.88 \times 10^{-6}$ m.

When cladding temperature has exceeded 1,500 K, the expected standard error is estimated by σ_2 in the expression

$$\sigma_2 = \pm 0.1 \exp\left[\frac{T - 1500}{300}\right] . \quad (5\text{-}29)$$

If Equations (5-27) and (5-29) predict values of $\varepsilon_2 \pm \sigma_2$ that fall inside the range of physically possible values of emissivity (0.0-1.0), the value σ_2 is returned as the expected standard error. If the prediction $\varepsilon_2 + \sigma_2$ is greater than 1 or if $\varepsilon_2 - \sigma_2$ is less than 0, the standard error of Equation (5-29) is modified to limit $\varepsilon_2 + \sigma_2$ at 1 and/or $\varepsilon_2 - \sigma_2$ at 0.

The following subsection is a review of the available data on cladding emissivity. The approach used to formulate the model for emissivity is described in Section 5.4.3, and Section 5.4.4 is a discussion of the uncertainty of the model for cladding emissivity.

5.4.2 Literature Review

Measurements of zircaloy-2 emissivities as a function of temperature and dissolved oxygen content were reported by Lemmon.[5.4-1] The measurements utilized the hole-in-tube method and were carried out in vacuum. Data from samples with an oxide film were reported, but the nonoxidizing environment of the sample during emissivity measurements caused the emissivity to change with time. Moreover, the thicknesses of the oxide films were not reported. The Lemmon data were not used in formulating the ZOEMIS subcode because the unknown oxide thickness probably influenced the emissivity and because of complications caused by the vacuum environment.

The emissivity of zircaloy-4 was reported by Juenke and Sjodahl[5.4-2] from measurements on oxidized zircaloy in vacuum and from measurements in steam during the isothermal growth of oxide films. These authors reported a decrease in the emissivity measured in vacuum, which they attributed to the formation of a metallic phase in the oxide. This metallic phase did not form in the presence of steam. The data taken in steam were used in constructing ZOEMIS because the steam environment is similar to an abnormal reactor environment.

Figure 5-6 is a reproduction of the Juenke and Sjodahl steam data. The data suggest that emissivity decreases when oxide films become very thick (long times or high temperatures). In fact, Juenke and Sjodahl expect the total emissivity of very thick films to approach 0.3 or 0.4, which is characteristic of pure ZrO_2. However, the decrease in emissivity at temperatures greater than about 1,200 °C is greater than one would predict from oxide layer thickness alone. The correlation of this emissivity data with oxide layer thickness is discussed in Section 5.4.3.

Juenke and Sjodahl do not include very thin oxide films but do report that the total emittance rises almost instantaneously from about 0.2 to 0.7 with the introduction of steam. Data relevant to thin films are discussed below.

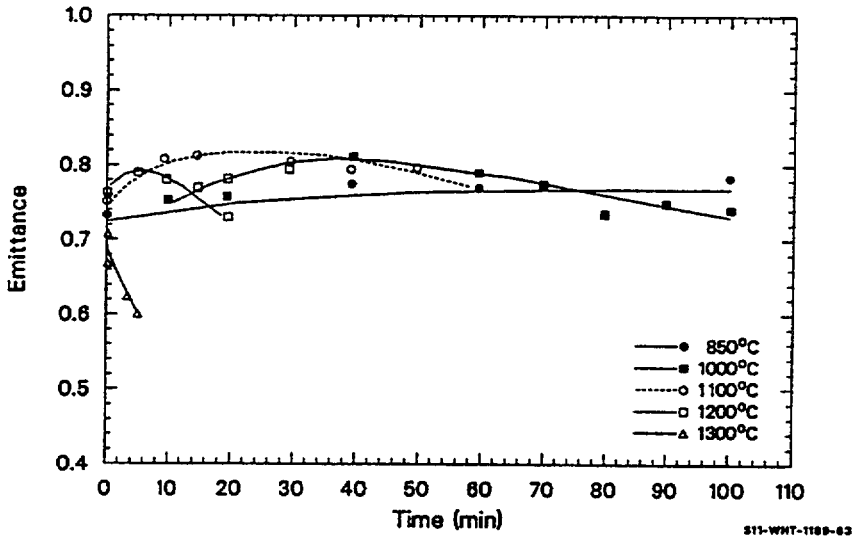

Figure 5-6. Total hemispherical emittance of zircaloy-4 versus time at temperature in steam.

The emissivity of oxide films measured in air at temperatures in the range 100 to 400 °C were reported by Murphy and Havelock[5.4-3] and are reproduced in Table 5-6. The emissivities are not strongly dependent on temperature but do increase rapidly with oxide thickness for the thin oxide layers measured. The one value of emissivity measured with an oxide thickness of 94 x 10^{-6} m is important because the oxide was approximately 30 times the thickness associated with the transition from black oxide layers to white oxide layers. The emissivity of this oxide, described as white by the authors, has a measured emissivity characteristic of surfaces which are black in the infrared region of the spectrum. Since (a) the Murphy and Havelock data were taken in an oxidizing environment and (b) the emissivity of the 94 x 10^{-6} m oxide film agrees with the emissivity of films measured in steam, all of the Murphy and Havelock data were used in the formulation of ZOEMIS.

Table 5-6. Emissivity of thin oxide films as reported by Murphy and Havelock.

		Emissivity				
Surface condition	**Oxide thickness (mm)**	**100 °C**	**150 °C**	**200 °C**	**300 °C**	**400 °C**
Pickled + 2 days in air at 400 °C	0.9	0.424	0.414	0.416	0.434	0.433
Pickled + 10 days in air at 400 °C	1.48	0.521	0.542	0.557	0.588	--

Table 5-6. Emissivity of thin oxide films as reported by Murphy and Havelock. (Continued)

		Emissivity				
Surface condition	**Oxide thickness (mm)**	**100 °C**	**150 °C**	**200 °C**	**300 °C**	**400 °C**
Pickled + 55 days in 400 °C steam under a pressure on 10.4 MPa	2.3	--	0.582	0.599	0.620	--
Pickled + 30 days in air at 400 °C + 73 days in air at 500 °C	94	--	0.748	--	--	--

Additional data were reported by Burgoyne and Garlick at the OECD-CSNI meeting on the Behavior of Water Reactor Fuel Elements under Accident Conditions in Spinad, Norway, on September 13-16, 1976. Using a hot filament calorimeter, these authors measured the emissivity of zircaloy-2 cladding surfaces coated with uniform oxide, nodular oxide, and crud. The emissivities were measured in vacuum. However, the following arguments are presented in favor of including some of these data in the data base of ZOEMIS: (a) a significant decrease in emissivity was not noticed with initial oxide thicknesses greater than 10^{-5} m until the samples were heated above approximately 800 °C (the alpha beta phase transition of zircaloy); and (b) the low temperature values of emissivity data taken with nodular and crud coated surfaces are representative of in-reactor surfaces not represented in other data. Data from Burgoyne and Garlick that did not show the sudden decrease in emissivity characteristic of the change caused by a vacuum environment were used in ZOEMIS. Table 5-7 is a summary of the measurements used.

Table 5-7. Emissivity data from Burgoyne and Garlick.

Cladding surface	**Surface layer thickness (μm)**	**Measurement temperature (K)**	**Emissivity (unitless)**
Uniform oxide	10	735	0.748
	10	805	0.770
	10	876	0.773
	10	885	0.773
	10	978	0.774
	10	986	0.767
	10	1,072	0.791
Uniform oxide	28	784	0.834
	28	884	0.818
	28	987	0.832

Table 5-7. Emissivity data from Burgoyne and Garlick. (Continued)

Cladding surface	Surface layer thickness (μm)	Measurement temperature (K)	Emissivity (unitless)
	28	1,080	0.829
Nodular oxide	130	654	0.860
	130	769	0.845
	130	775	0.857
	130	868	0.849
	130	885	0.850
	130	965	0.849
	130	975	0.837
	130	1,066	0.866
	130	1,149	0.841
Crud	35	677	0.918
	35	683	0.930
	35	769	0.890
	35	777	0.888
	35	870	0.899
	35	876	0.888
	35	966	0.913
	35	977	0.903

5.4.3 Model Development

Near infrared radiation has a wavelength of 1×10^{-6} m. Oxide films up to a few wavelengths thick should be partly transparent to infrared radiation and should therefore have emissivities strongly dependent on oxide thickness. The emissivity versus oxide thickness data of Murphy and Havelock[5.4-3] were fit with standard least-squares residual analysis to deduce Equation (5-25).

The equation for the emissivity of oxide films thicker than 4×10^{-6} m is based on the data of Burgoyne and Garlick, Juenke and Sjodahl,[5.4-2] and one measurement from Murphy and Havelock,[5.4-3] as discussed in Section 5.4.2. Oxide thicknesses were calculated from the time and temperatures reported by Juenke and Sjodahl using the correlation published by Cathcart.[5.4-4]

$$X = [2.25 \times 10^{-6} \exp(-18{,}063/T)t]^{1/2} \quad (5\text{-}30)$$

where

X = the oxide layer thickness (m)

T = temperature (K)

t = time at temperature (s).

Table 5-8 lists the emissivity, time, and temperature reported by Juenke and Sjodahl, together with the oxide thickness predicted using Equation (5-30). Values of emissivity and oxide layer thickness from Table 5-6 through Table 5-8 were used to establish Equation (5-26).

Table 5-8. Emissivity versus oxide thickness from Juenke and Sjodahl's data.

Temperature (K)	Time (s)	Calculated oxide thickness mm	Measured emissivity (unitless)
1,125	1,200	17	0.755
1,125	2,400	24	0.755
1,125	6,000	38	0.785
1,275	600	31	0.750
1,275	1,200	43	0.773
1,275	1,800	53	0.795
1,275	3,600	75	0.790
1,275	4,200	81	0.775
1,275	4,800	86	0.738
1,275	5,400	92	0.755
1,275	6,000	96	0.740
1,375	600	51	0.808
1,375	900	63	0.815
1,375	1,200	72	0.780
1,375	3,000	114	0.798
1,375	3,600	125	0.775
1,475	300	57	0.795
1,475	600	80	0.780

Table 5-8. Emissivity versus oxide thickness from Juenke and Sjodahl's data. (Continued)

Temperature (K)	Time (s)	Calculated oxide thickness mm	Measured emissivity (unitless)
1,475	900	98	0.775
1,475	1,200	113	0.722
1,575	210	70	0.620
1,575	300	83	0.600

Figure 5-7 is a comparison of the curves generated by Equations (5-25) and (5-26) with the data base used to derive these equations. Predicted values of emissivity increase rapidly until the surface oxide layer thickness is 3.88×10^{-6} m, then decrease very slowly with increasing surface layer thickness.

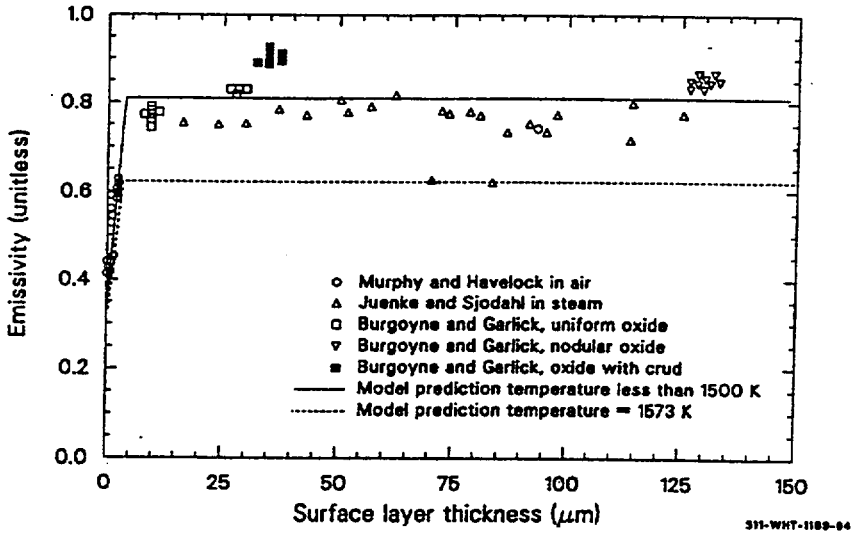

Figure 5-7. ZOEMIS calculations compared with the data base of the model.

The values of emissivity measured by Juenke and Sjodahl at 1,575 K (0.62 and 0.60) are significantly below the measured emissivities at lower temperatures. Since thicker oxide films were formed at lower temperatures, the low emissivity is not due to the thickness of the oxide film. Moreover, the low values of emissivities measured by Juenke and Sjodahl at high temperature are supported by posttest observations of cladding surfaces that have been at high temperatures.[5.4-5] Cladding surfaces that experienced film boiling, and therefore high temperatures, showed spalled oxide and somewhat whiter oxide surfaces in the region of the film boiling. The observations reported by Juenke and Sjodahl [5.4-5] and the trend toward lower values of emissivity at higher temperatures at 1,475 and 1,575 K imply that lower cladding surface emissivities are likely at temperatures above approximately 1,500 K. This trend in the

limited data has been included in ZOEMIS by (a) adding a multiplicative factor to the expression for emissivity,

$$\exp[(1500 - T)/300] \tag{5-31}$$

where T is the greater of 1,500 K and the maximum cladding temperature, and (b) limiting the minimum emissivity to 0.325, the value predicted by the model for zero oxide thickness.

5.4.4 Uncertainty

The standard errors obtained with Equations (5-25) and (5-26) and the data base used to develop these equations are listed in Table 5-9.

Table 5-9. Standard errors of ZOEMIS predictions.

Surface description	Standard error
Oxide films < 3.88×10^{-6} m	± 0.04
Pure oxide films > 3.88×10^{-6} m	± 0.05
Oxide films including samples with nodular oxides and crud	± 0.07

Standard errors shown in Table 5-9 for oxide layers without the complicating features of nodular oxides or surface crud are consistent with measurement errors of ± 3% estimated by Lemmon.[5.4-1] However, the model is intended to predict the emissivity of cladding surfaces with crud or UO_2 fission products as well as the oxide layer. The data from Burgoyne and Garlick (illustrated in Figure 5-7) suggest that crud layers introduce a systematic error of approximately ± 0.1. The value of ± 0.1 is therefore included in ZOEMIS as the best estimate for the standard error of the model prediction for emissivity during abnormal reactor operation at temperatures below 1,500 K.

The uncertainty of the prediction for emissivities above 1,500 K is difficult to estimate. Equation (5-29) was selected as a reasonable expression for the expected standard error of Equation (5-27), simply because the expression ± 0.1 exp{-(1,500 - maximum cladding temperature)/300] predicts a standard error approximately equal to the change in emissivity caused by the empirical multiplicative factor of Equation (5-31).

In Figure 5-8, the data base and model predictions shown in Figure 5-7 are repeated. The standard error expected with ZOEMIS for temperatures below 1,500 K is shown by the cross-hatched area centered on the solid line. The cross-hatched area centered on the dashed line shows the standard error estimated for temperatures of 1,573 K.

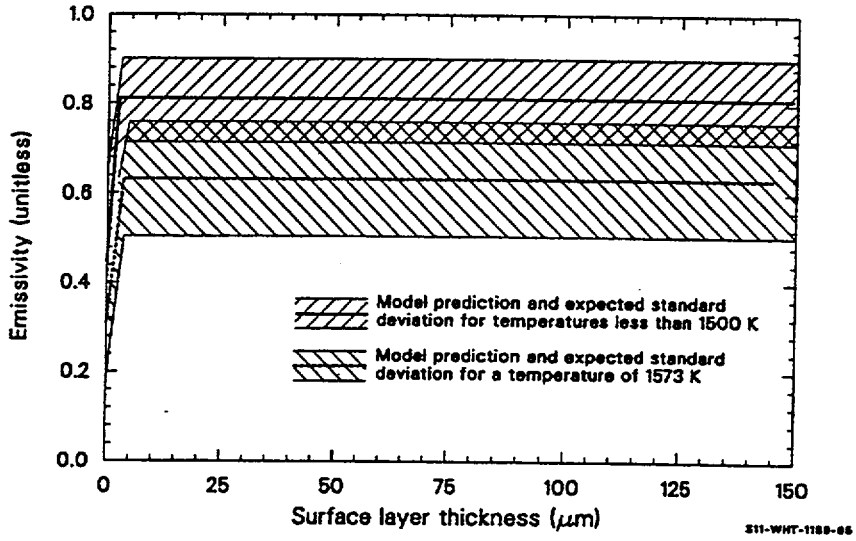

Figure 5-8. Expected standard errors of emissivity for temperatures below 1,500 K and at 1,573 K.

5.4.5 References

5.4-1 A. W. Lemmon, Jr., *Studies Relating to the Reaction Between Zirconium and Water at High Temperatures*, BMI-1154, January 1957.

5.4-2 E. F. Juenke and L. H. Sjodahl, "Physical and Mechanical Properties: Emittance Measurements," *AEC Fuels and Materials Development Program*, GEMP-1008, 1968, pp. 239-242.

5.4-3 E. V. Murphy and F. Havelock, "Emissivity of Zirconium Alloys in Air in the Temperature Range 100 - 400 °C," *Journal of Nuclear Materials, 60*, 1976, pp. 167-176.

5.4-4 J. V. Cathcart, *Quarterly Progress Report on the Zirconium Metal Water Oxidation Kinetics Program Sponsored by the NRC Division of Reactor Safety Research for April-June 1976*, ORNL/NUREG-TM-41, August 1976.

5.4-5 *Quarterly Technical Progress Report on Water Reactor Safety Programs Sponsored by the Nuclear Regulatory Commission's Division of Reactor Safety Research. October-December 1975*, ANCR-NUREG-1301, May 1976, p. 67.

5.5 Thermal Expansion and Density (ZOTEXP, ZODEN)

The subroutine ZOTEXP calculates the zircaloy oxide thermal strain from a reference temperature of 300K and the current zircaloy oxide temperature. The thermal strain for zircaloy oxide is zero at 300K.

5.5.1 Thermal Expansion (ZOTEXP)

Expressions used in ZOTEXP to calculate the thermal strains of solid zirconium oxide are taken from Hammer:[5.5-1]

For $300 < T < 1{,}478$ K (monoclinic ZrO_2),

$$\varepsilon_0 = 7.8 \times 10^{-6} T - 2.34 \times 10^{-3} \quad . \tag{5-32}$$

For $1{,}478 \leq T < 2{,}973$ K (tetragonal and cubic ZrO_2),

$$\varepsilon_0 = 1.302 \times 10^{-5} T - 3.338 \times 10^{-2} \tag{5-33}$$

where ε_0 is the linear thermal strain of zircaloy oxide(m/m). These expressions show a 7.7% decrease in volume at the monoclinic tetragonal phase change (1,478 K).

For liquid zirconium oxide, a 5% reduction in volume is assumed when the oxide melts. This assumption corresponds to the assumption that the 5% porosity of the oxide is removed when it melts. The resultant expression is

$$\varepsilon_0 = -1.1 \times 10^{-2}, \tag{5-34}$$

for $T \geq 2{,}973$ K.

5.5.2 Density (ZODEN)

Thermal expansion Equations (5-32) through (5-34) are used in ZODEN to calculate the density of zircaloy oxide. The relation employed is

$$\rho_x = \rho_{xo} (1 - 3\varepsilon_0) \tag{5-35}$$

where

ρ_x = zirconium oxide density at the given temperature (kg/m^3)

ρ_{xo} = zirconium oxide density at 300 K (kg/m^3).

The value of ρ_{xo} used is the density of black oxide reported by Gilchrist,[5.5-2] 5,800 kg/m^3.

The expected standard error of Equations (5-32) and (5-33) is large, the greater of half the predicted value or $\pm$ 5 x 10^{-3}, because the equations are based on zircaloy dioxide data. The cladding oxide is not only substoichiometric but is formed under large stress because of the different densities of the oxide and the zircaloy on which it is formed.

The zircaloy dioxide thermal strains predicted by ZOTEXP are shown in Figure 5-9, and the density of the oxide predicted by ZODEN is illustrated in Figure 5-10. ZrO_2 thermal expansion data by Fulkerson[5.5-3] and from pages 17 and 70 of Brassfield et al.[5.5-4] are listed in Table 5-10 and Table 5-11 and included in Figure 5-11 so that they may be compared with code predictions.

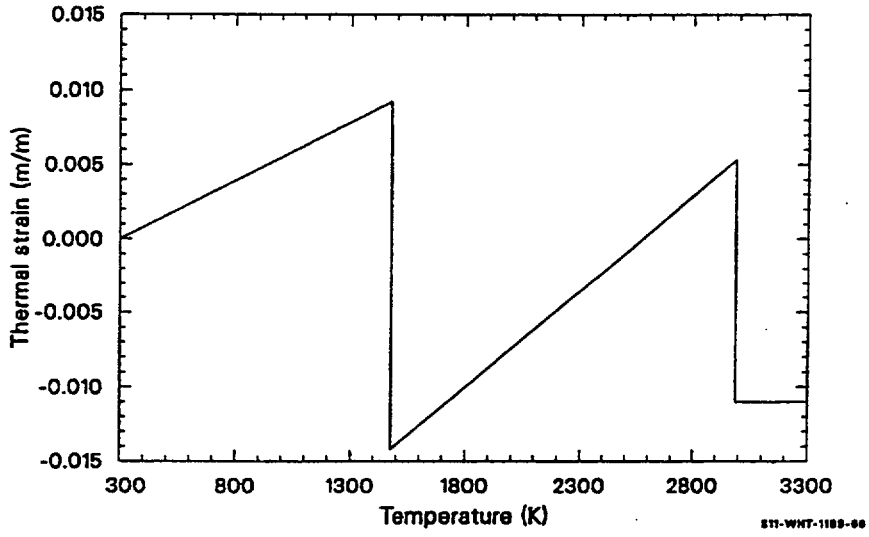

Figure 5-9. Zircaloy oxide thermal strain.

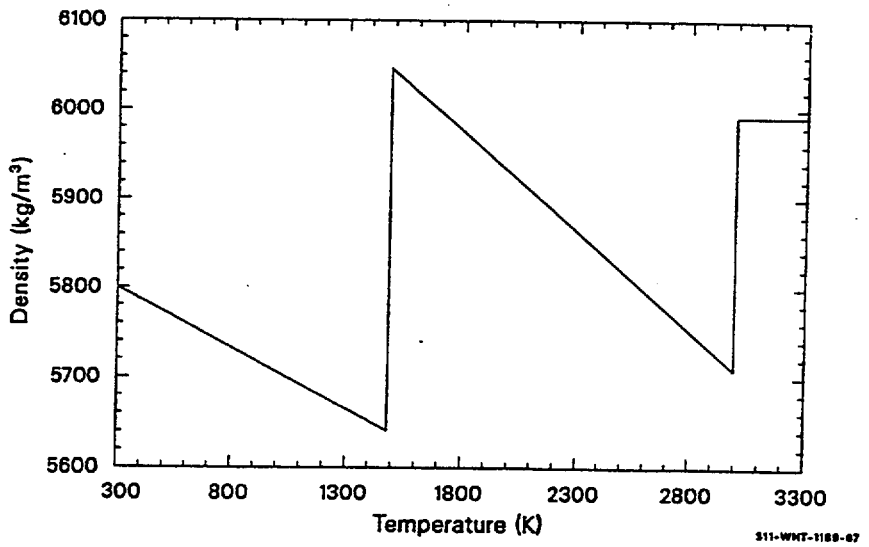

Figure 5-10. Zircaloy oxide density as a function of temperature

Table 5-10. Zircaloy dioxide thermal expansion data by Fulkerson.[5.5-3]

Temperature (K)	Thermal strain (10^{-3}m/m)
289	0
473	1.34
571	2.05
673	2.82
773	3.64
818	4.02
922	4.78
1,019	5.61
1,119	6.63
1,222	7.51
1,308	8.06
1,330	8.25
1,349	8.33
1,369	8.38
1,390	8.34
1,430	7.63
1,450	6.10
1,466	3.27
1,487	1.16
1,508	0.17
1,529	-0.38
1,550	-0.82
1,571	-1.05

Table 5-11. Zircaloy dioxide thermal expansion data from Brassfield et al.[5.5-4]

Temperature (K)	Thermal strain (10^{-3}m/m)
300	0
537	2.1
778	3.7
1,031	5.05
1,238	7.35
1,383	9.10
1,488	-1.8

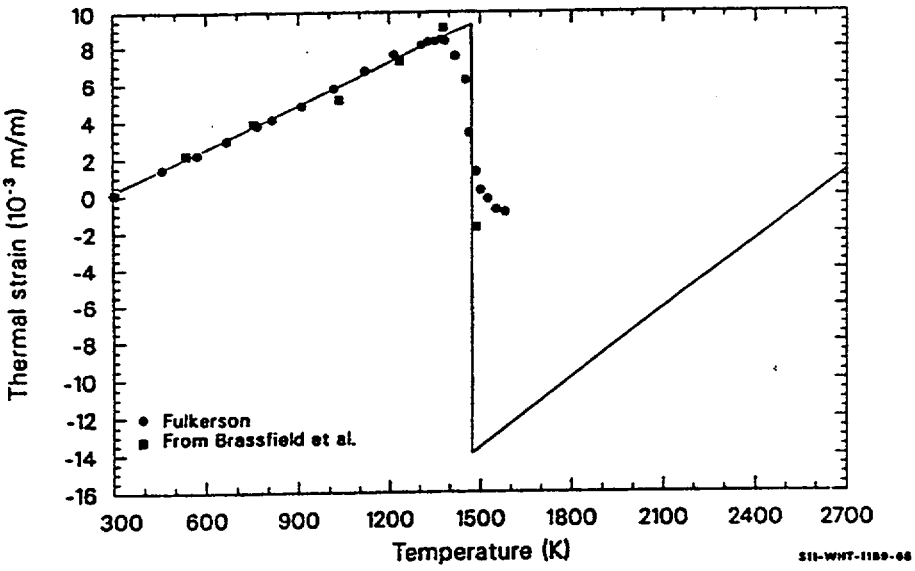

Figure 5-11. Zircaloy oxide thermal strain data compared to code prediction.

5.5.3 References

5.5-1 R. R. Hammer, *Zircaloy-4, Uranium Dioxide and Materials formed by their Interaction. A Literature Review with Extrapolation of Physical Properties to High Temperatures*, IN-1093, September 1967.

5.5-2 K. E. Gilchrist, "Thermal Property Measurements on Zircaloy-2 and Associated Oxide Layers," *Journal of Nuclear Materials, 62*, 1976, pp. 257-264.

5.5-3 S. D. Fulkerson, *Apparatus for Determining Linear Thermal Expansions of Materials in Vacuum or Controlled Atmosphere*, ORNL-2856, 1960, p. 20.

5.5-4 H. C. Brassfield, J. F. White, L. Sjodahl, and J. T. Bittel, *Recommended Property and Reaction Kinetics Data for Use in Evaluating a Light Water Cooled Reactor Loss-of-Coolant Incident Involving Zircaloy-4 or 304-SS Clad UO_2*, GEMP 482, 1968.

5.6 Elastic Moduli (ZOEMOD, ZOPOIR)

The function ZOEMOD calculates Young's modulus for zircaloy oxide from the zircaloy oxide temperature and oxygen-to-metal ratio. The function ZOPOIR calculates the Poisson's ratio for liquid and solid zircaloy oxide.

5.6.1 Young's Modulus (ZOEMOD)

Young's modulus for zircaloy oxide is returned by the ZOEMOD function. Oxide temperature and oxide oxygen-to-metal ratio are the only required inputs. The function uses the following correlation to calculate the modulus for $300 < T < 1{,}478$ K (monoclinic phase):

$$Y_0 = -3.77 \times 10^7 T + 1.637 \times 10^{11} \quad . \tag{5-36}$$

For $1{,}478 \leq T < T_{SOL}$ (tetragonal and cubic phase),

$$Y_0 = -8.024 \times 10^7 T + 2.255 \times 10^{11} \quad . \tag{5-37}$$

For $T \geq T_{SOL}$,

$$Y_0 = 1 \tag{5-38}$$

where

Y_o = zircaloy oxide Young's modulus (Pa)

T = oxide temperature (K)

T_{SOL} = zircaloy oxide solidus temperature (K) (obtained from the ZOPRP subroutine).

The equations are least squares fits to data from Brassfield et al.[5.6-1] Table 5-12 reproduces the data, and Figure 5-12 shows the data and values of Y_o calculated with the ZOEMOD function. The function sets $Y_o = 1$ Pa for temperatures above 2,810 K where Equation (5-37) would predict a negative modulus. Since

so few data are available, a large expected standard error of ± 0.2 times the predicted value is recommended.

Table 5-12. Zircaloy dioxide modulus of elasticity data from Brassfield et al.[5.6-1]

Temperature (K)	Elastic modulus (10^{10} Pa)	Comment
1,323	11.38	Monoclinic phase
1,453	10.89	Monoclinic phase
1,498	10.48	Tetragonal phase
1,563	10.10	Tetragonal phase
1,633	9.41	Tetragonal phase

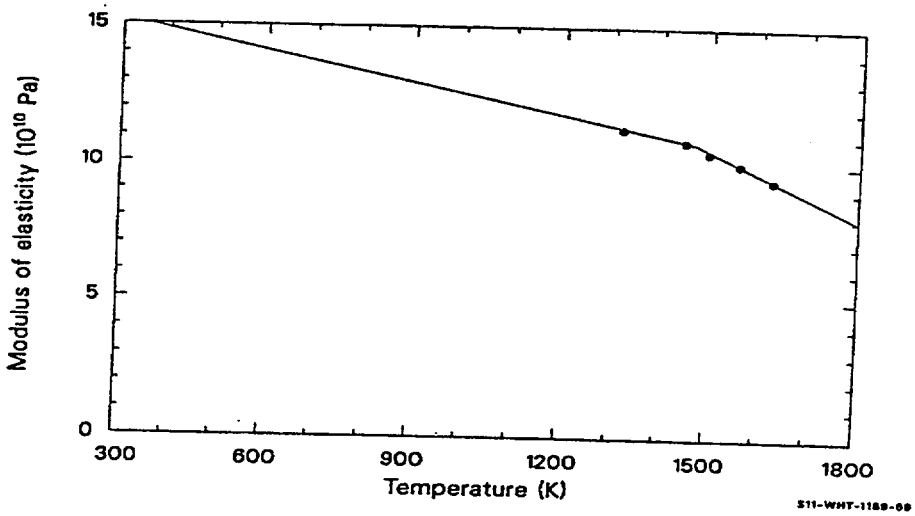

Figure 5-12. Data and calculated values of Young's modulus for zircaloy oxide.

5.6.2 Poisson's Ratio (ZOPOIR)

ZOPOIR returns constant values of 0.3 and 0.5 for the Poisson's ratios of solid and liquid zircaloy oxide, respectively. No data for these ratios have been found. The number 0.3 is merely typical of many solid materials, and 0.5 is the constant volume, isotropic material value of Poisson's ratio. The expected standard error is therefore large, ± 0.2

5.6.3 Reference

5.6-1 H. C. Brassfield, J. F. White, L. Sjodahl, and J. T. Bittel, *Recommended Property and Reaction Kinetics Data for Use in Evaluating a Light Water Cooled Reactor Loss-of-Coolant Incident Involving Zircaloy-4 or 304-SS Clad UO_2*, GEMP 482, 1968, p. 89.

5.7 Mechanical Limits and Embrittlement (ZORUP)

The function ZORUP returns zircaloy oxide failure stress as a function of temperature. The correlations used in the function ZORUP to calculate the oxide failure stress are listed below.

5.7.1 Model Development

For $300 \leq T < 1{,}478$ K (monoclinic phase of ZrO_2),

$$S_B = -5.06 \times 10^4 T + 1.57 \times 10^8 \ . \quad (5\text{-}39)$$

For $1{,}478 \leq T < 1{,}869.4$ K (tetragonal and cubic phases of ZrO_2),

$$S_B = -2.075 \times 10^5 T + 3.889 \times 10^8 \ . \quad (5\text{-}40)$$

For $1{,}869.4 \leq T \leq T_{SOL}$,

$$S_B = 10^6 \ . \quad (5\text{-}41)$$

For $T > T_{SOL}$,

$$S_B = 0 \quad (5\text{-}42)$$

where

S_B = circumferential or axial stress on the oxide at failure (Pa)

T = oxide temperature (K)

T_{SOL} = zircaloy oxide solidus temperature (K) (obtained from the ZOPRP subroutine).

These correlations are fits to the three ZrO_2 tensile strength data sets reported by Brassfield et al.[5.7-1] The data are shown in Table 5-13 and are compared with the correlation values in Figure 5-13.

Table 5-13. Zircaloy dioxide tensile strength data from Brassfield et al.[5.7-1]

Temperature (K)	Tensile strength (MPa)
1,303	91.2
1,473	82.6
1,813	12.7

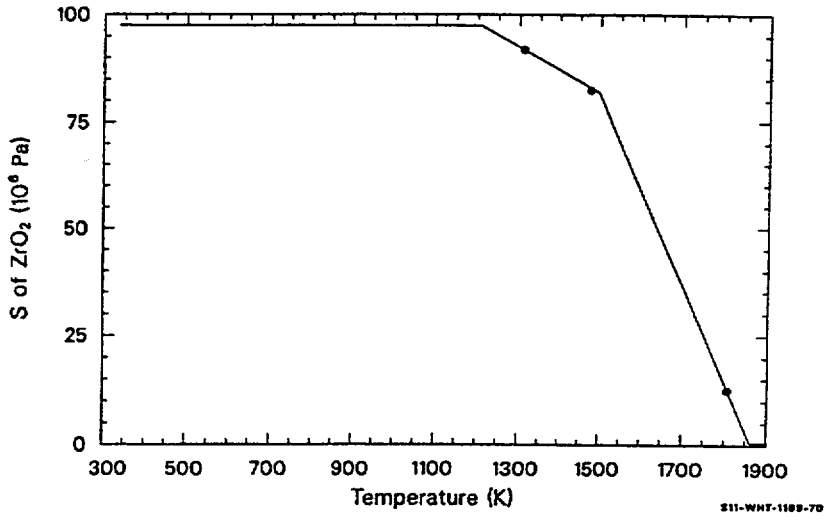

Figure 5-13. Zircaloy oxide failure stress data and correlations versus temperature.

The values and shape of the curve are similar to the values and shape of the more extensive data for UO_2 failure. In the temperature range of the data, the oxide failure stress is about three times the failure stress of zircaloy. In spite of these similarities, the very limited data used to construct the expressions for oxide failure stress suggest a large expected standard error for the correlation, $\pm$ 0.7 times the predicted value.

Figure 5-14 is a plot of the failure stresses returned by the function.

5.7.2 Reference

5.7-1 H. C. Brassfield, J. F. White, L. Sjodahl, and J. L. Bittel, *Recommended Property and Reaction Kinetics Data for Use in Evaluating a Light Water Cooled Reactor Loss-of-Coolant Incident Involving Zircaloy-4 or 304-SS Clad UO_2,* GEMP 482, 1968, p. 89.

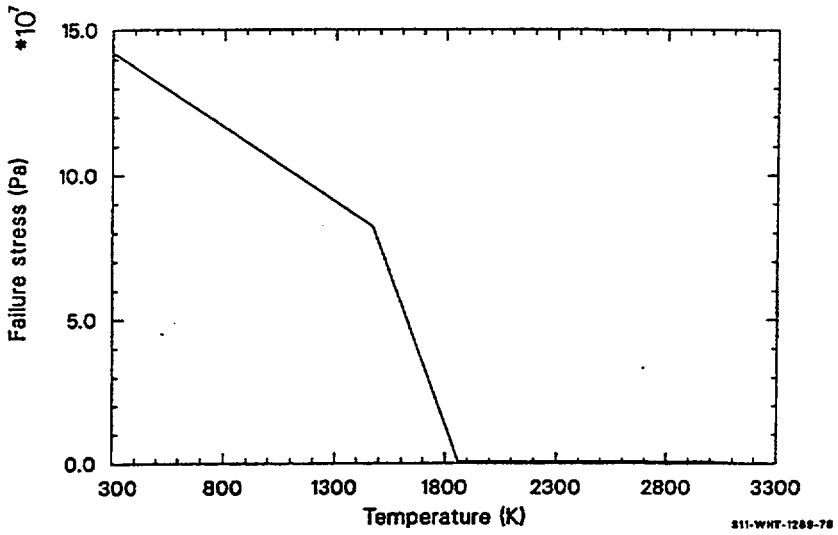

Figure 5-14. Zircaloy oxide failure stress calculated with the ZORUP function.

6. CONTROL ROD CLADDING

A collection of properties of 304 stainless steel has been prepared to allow modeling of temperature dependent phenomena and possible failure by melting or oxidation of stainless steel control rod cladding. Properties included are melting temperatures (SHYPRP), specific heat capacity (SCP), enthalpy (SENTHL), thermal conductivity (STHCON), thermal expansion (STHEXP), and density (SDEN).

6.1 Melting Temperatures (SHYPRP)

The subroutine SHYPRP provides 304 stainless steel melting temperatures. There is no required input.

6.1.1 Model Development

For this alloy, page 19-3 of Reference 6.1-1 reports a melting range of 1,671 to 1,727 K. These numbers are used for the solidus (first liquid phase appears) and liquidus (last solid phase melts) temperatures of control rod cladding.

6.1.2 Reference

6.1-1 D. Peckner and I. M. Bernstein (eds.), *Handbook of Stainless Steel*, New York: McGraw-Hill Book Company, 1977.

6.2 Specific Heat Capacity and Enthalpy (SCP, SENTHL)

The function SCP returns the specific heat capacity of 304 stainless steel as a function of temperature. The function SENTHL uses the specific heat capacity to calculate the enthalpy change of the control rod cladding as a function of (1) material temperature, and (2) a reference temperature (for which the enthalpy change is zero). The reference temperature used is 300 K.

6.2.1 Model Development

Depending on the temperature range, two expressions are used for specific heat capacity. The first [Equation (6-1)] is a curve-fit to three sets of heat capacity data compiled by Touloukian and Buyco.[6.2-1] These Touloukian and Buyco data (labeled as curves 1, 3, and 4 in Reference 6.2-1) are for steels with composition of 17 - 20% Cr and 8 - 11% Ni (similar to 304 stainless steel). Although there is no data in the Touloukian and Buyco reference for temperatures above 1,523 K, Equation (6-1) is extrapolated to the 304 stainless steel solidus temperature of 1,671 K. For higher temperatures, the second expression [Equation (6-2)] uses a constant specific heat capacity calculated from Equation (6-1) for a temperature of 1,671 K.

For $300 \leq T < 1{,}671$ K,

$$C_{ps} = 326 - 0.242\,T + 3.71\,T^{0.719} \quad . \tag{6-1}$$

For $T \geq 1{,}671$ K,

$$C_{ps} = 691.98 \quad (6\text{-}2)$$

where

C_{ps} = control rod cladding specific heat capacity (J/kg• K)

T = control rod cladding temperature (K).

The function SENTHL returns the enthalpy change of 304 stainless steel between a reference temperature and a material temperature For material temperatures below 1,671 K, (304 stainless steel solidus temperature), the integral of Equation (6-1) with respect to temperature is used for the absolute enthalpy [Equation (6-3)]. Above 1,671 K, the integral of Equation (6-2) with respect to temperature is used [Equations (6-4) and (6-5)]. Equation (6-4) includes a heat of fusion of 2.8×10^5 J/kg that is added linearly over the 304 stainless steel melting range between 1,671 and 1,727 K. This alloy heat of fusion was calculated as a weighted average from the individual heat of fusion for iron, chromium, and nickel given by Brassfield et al.[6.2-2] and the composition of 304 stainless steel given by Murfin et al.[6.2-3]

For $300 < T \leq 1{,}671$ K,

$$h_s = 326\,T - 0.121\,T^2 + 2.15823\,T^{1.719} \quad . \quad (6\text{-}3)$$

For the melting range of $1{,}671 \leq T < 1{,}727$ K,

$$h_s = -85.55565 \times 10^5 + 5691.98\,T \quad . \quad (6\text{-}4)$$

For $T \geq 1{,}727$ K,

$$h_s = 0.79435 \times 10^5 + 691.98\,T \quad . \quad (6\text{-}5)$$

where

h_s = control rod cladding enthalpy (J/kg)

T = control rod cladding temperature (K).

The estimated standard error of Equation (6-1) as determined by a statistical analysis of the Touloukian and Buyco[6.2-1] is ± 19 J/kg•K of the calculated values. Figure 6-1 illustrates the predicted values of specific heat capacity versus temperature [calculated from Equations (6-1) and (6-2)] along with the data points from which the correlation was derived.

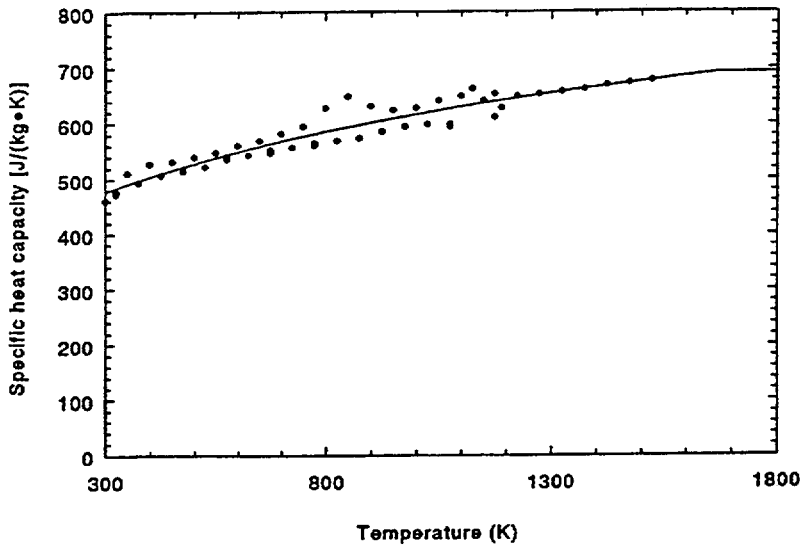

Figure 6-1. Stainless steel specific heat capacity at constant pressure.

6.2.2 References

6.2-1 Y. S. Touloukian and E. H Buyco, *Thermophysical Properties of Matter Volume 4: Specific Heat - Metallic Elements and Alloys,* New York: IFI/Plenum Data Corp., 1970, pp. 708-710.

6.2-2 H. C. Brassfield, J. F. White, L. Sjodahl, and J. T. Bittel, *Recommended Property and Reaction Kinetics Data for Use in Evaluating a Light Water Cooled Reactor Loss-of-Coolant Incident Involving Zircaloy-4 of 304-SS Clad UO_2,* GEMP482, 1968, p. 89.

6.2-3 W. B. Murfin et al., *Core Meltdown Experimental Review,* SAND74-0382, NUREG-0205, 1977, p. 4-8.

6.3 Thermal Conductivity (STHCON)

6.3.1 Model Development

The thermal conductivity of 304 stainless steel as a function of temperature is calculated by the STHCON function. Equation (6-6) is a fit to the values of 14.65 W/m•K at 374 K and 25.83 W/m•K at 965 K obtained from page 19-18 of Reference 6.3-1. Equation (6-8) is an approximation of the thermal conductivity at the lowest temperature for which the steel is completely melted. To obtain this approximation, Equation (6-6) was evaluated at 1,727 K and then reduced by 50%, noting that the thermal conductivity of a metal with a face-centered cubic structure like 304 stainless steel is reduced by half when melted.[6.3-2] Equation (6-7) interpolates between the result of Equation (6-8) predicted at 1,671 K and the value predicted by Equation (6-8) at and above 1,727 K.

For $300 \leq T < 1{,}671$ K,

$$K_s = 7.58 + 0.0189\,T \quad . \tag{6-6}$$

For $1{,}671 \leq T < 1{,}727$ K,

$$K_s = 610.9393 - 0.3421767\,T \quad . \tag{6-7}$$

For $T \geq 1{,}727$ K,

$$K_s = 20 \tag{6-8}$$

where

K_s = control rod cladding thermal conductivity (W/m•K)

T = control rod cladding temperature (K).

The expected standard error of the predicted conductivities is $\pm$ 0.02 of the predicted conductivity. The predicted thermal conductivity as a function of temperature is shown in Figure 6-2.

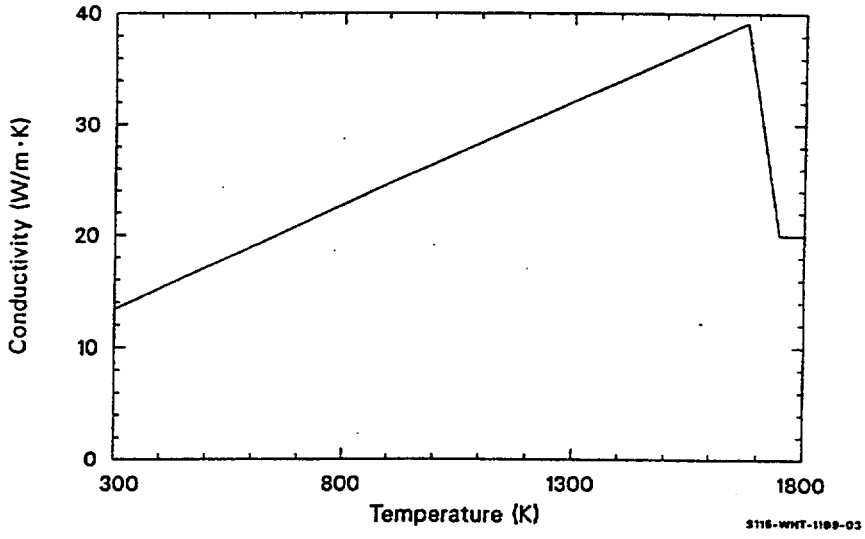

Figure 6-2. Stainless steel thermal conductivity.

6.3.2 References

6.3-1 D. Peckner and I. M. Bernstein (eds.), *Handbook of Stainless Steel*, New York: McGraw-Hill Book Company, 1977.

6.3-2 S. Nazare, G. Ondracek, and B. Schulz, "Properties of Light Water Reactor Core Melts," *Nuclear Technology, 32*, 1977, pp. 239-246.

6.4 Thermal Expansion and Density (STHEXP, SDEN)

The function STHEXP calculates 304 stainless steel thermal expansion strain, and SDEN computes the density of this material. STHEXP requires the control rod cladding temperature and a reference temperature of 300 K (for which thermal strain will be zero), while SDEN requires only the temperature.

6.4.1 Model Development

The expressions used to calculate thermal expansion strains are

For $300 \leq T < 1{,}671$ K,

$$\varepsilon_s = 1.57 \times 10^{-5} \times T + 1.69 \times 10^{-9} \times T^2 \ . \quad (6\text{-}9)$$

For $1{,}671 \leq T < 1{,}727$ K,

$$\varepsilon_s = -2.986634 \times 10^{-1} + 1.972573 \times 10^{-4} \times T \ . \quad (6\text{-}10)$$

For $T \geq 1{,}727$ K,

$$\varepsilon_s = 4.2 \times 10^{-2} \quad (6\text{-}11)$$

where

ε_s = control rod cladding thermal strain (m/m)

T = control rod cladding temperature (K).

Equation (6-9) is derived from thermal expansion rates of 17.2×10^{-6} and 18.9×10^{-6} m/m•K at 455 and 959 K. These values were taken from a curve on page 197 of Reference 6.4-1. A linear fit to the thermal expansion rates yields an expression which can be integrated to produce Equation (6-9). The constant of integration is ignored because the quantity returned by STHEXP is the strain predicted by Equations (6-9) through (6-11) at the given temperature minus the strain predicted at the reference temperature. Equation (6-11) is the strain predicted by Equation (6-9) at the lowest temperature for which the steel is completely melted, 1,727 K, plus an assumed additional expansion of 1% (3%volume increase) because of the melting. Equation (6-10) is a linear interpolation of the values predicted by Equation (6-9)

at 1,671 K and Equation (6-11) at 1,727 K. The expected standard error of these expressions is about 0.10 of the predicted value.

The function SDEN uses the general relation between density and thermal strain, together with a reference density of 7.8 x 10^3 kg/m^3 at 300 K obtained from page 87 of Reference 6.4-2. The expected standard error of this density is the uncertainty of reference density, ± 50 kg/m^3.

The thermal expansion strain returned by STHEXP for a reference temperature of 300 K is illustrated in Figure 6-3, and the density calculated with the SDEN function is shown in Figure 6-4.

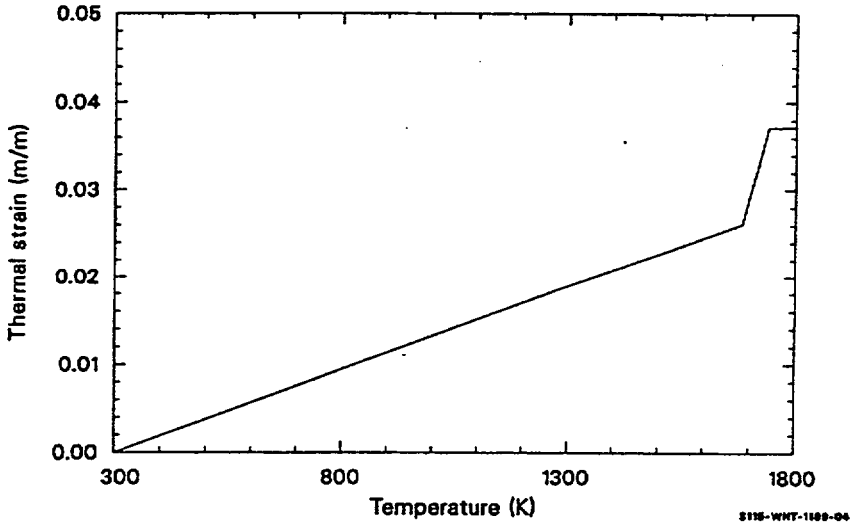

Figure 6-3. Stainless steel thermal expansion strain.

6.4.2 References

6.4-1 D. Peckner and I. M. Bernstein (eds.), *Handbook of Stainless Steel*, New York: McGraw-Hill Book Company, 1977.

6.4-2 H. C. Brassfield, J. F. White, L. Sjodahl, and J. T. Bittel, *Recommended Property and Reaction Kinetics Data for Use in Evaluating a Light Water Cooled Reactor Loss-of-Coolant Incident Involving Zircaloy-4 of 304-SS Clad UO_2*, GEMP 482, 1968.

6.5 Stainless Steel Oxidation in Steam (SOXIDE, SOXWGN, SOXTHK)

Three subcodes are employed to describe the oxygen uptake of 304 stainless steel. The SOXIDE subroutine returns the linear power generated by the oxidation of stainless steel, the oxidation weight gain at the end of a time step, and an estimate of the oxide layer thickness at the end of a time step. Required input information is the cladding temperature, the time step duration, the outside diameter of the as fabricated cladding, the initial weight gain, and the initial oxide layer thickness. SOXWGN is a function that returns the parabolic rate constant for the oxidation weight gain of stainless steel as a function of

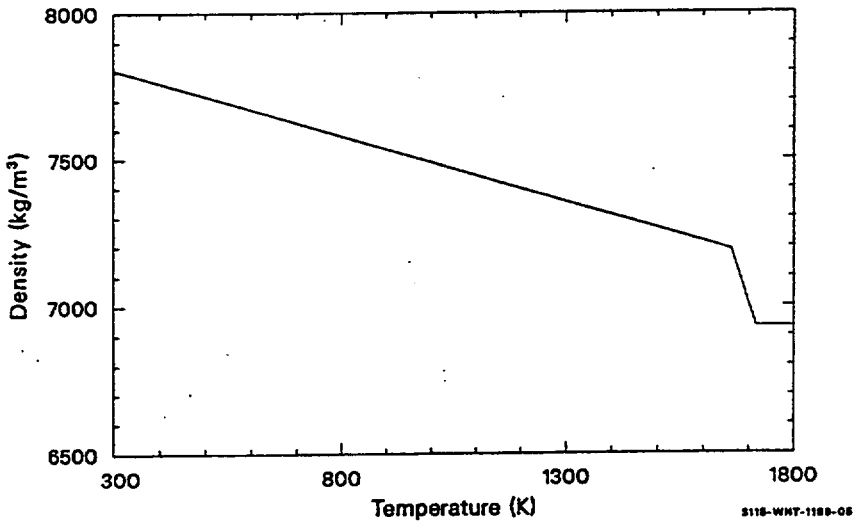

Figure 6-4. Stainless steel density.

temperature. The parabolic rate constant for the oxide layer thickness is calculated by SOXTHK as a function of temperature.

6.5.1 Model Development

The equation used to model the oxidation parameters is of the form

$$Z_f = \left[Z_i^2 + 2A\exp\left(-\frac{B}{T}\right)\Delta t\right]^{1/2} \tag{6-12}$$

where

Z_f = value of the oxidation parameter (oxide layer thickness or cladding weight gain per unit surface area due to oxidation) at the end of a time span of Δt

Z_i = value of the oxidation parameter at the start of the time span

T = temperature of the oxide layer (K)

Δt = time span (s)

A,B = rate constants.

There is some question as to the exact value of the A coefficient for the oxide thickness version of Equation (6-12). The values currently considered are 300 m^2/s and 30,000 m^2/s. The former is currently used in the code.

Table 6-1 lists the rate constants used with Equation (6-12) to model weight gain or oxide layer thickness. The parabolic rate constants calculated by SOXWGN and SOXTHK are the quantities

Table 6-1. Rate constants for use with Equation (6-12) to predict oxidation.

Oxidation parameter	A	B
Cladding weight gain (kg/m^2 surface)	1.2×10^8 $kg^2/m^4 \cdot s$	42,428 K
Oxide thickness	300 m^2/s	42,428 K

$$R = 2A \exp(-B/T) \tag{6-13}$$

where R is the parabolic rate constant for oxidation parameter described by rate constants A and B.

The expression used to model the linear power generated by the oxidation of stainless steel is

$$P = 4.85\times10^6 D_0 \frac{(M_f - M_i)}{\Delta t} \tag{6-14}$$

where

P = rate of heat generation per unit length of 304 stainless steel cladding (W/m)

D_o = cladding outside diameter without oxidation (m)

M_f = mass gain per unit surface area due to oxidation at end of time step (kg/m^2)

M_i = mass gain per unit surface area due to oxidation at start of time step (kg/m^2).

The power represented by this equation is about one-tenth the power represented by the corresponding equation for zircaloy oxidation when the mass gains are similar

Equation (6-12), with oxidation rate constants for weight gain, was taken from page 50 of Reference 6.5-1. If the composition and density of the oxide are known, the rate constant for the oxide layer thickness can be determined from the rate constant for oxidation weight gain:

$$A = \frac{B}{WFOX^2(\rho)^2} \tag{6-15}$$

where

A = rate constant for oxide layer thickness (m^2/s)

B = rate constant for oxidation weight gain ($kg^2/m^4 \bullet s$)

WFOX = mass fraction oxygen in the oxide (kg oxygen/kg oxide)

ρ = density of the oxide film (kg/m^3).

However, determination of a rate constant for the oxide layer thickness is complicated by uncertainty about the oxide density because of considerable foaming of the stainless steel during oxidation.[6.5-1,6.5-2] Moreover, page 53 of Reference 6.5-1 reports very complex oxide structures. The oxide is expected to contain some FeO, Fe_3O_4, Fe_2O_3, CrO_3, Cr_2O_3, NiO, and mixed spinels. The rate constant in Table 6-1 was calculated by assuming the composition of FeO and a density of 3,000 kg/m^3 (about half the density of nonporous FeO).

Equation (6-14) for the linear power generated by oxidation is derived by subtracting the heat required to dissociate H_2O, 2.4182×10^5 J/mole,[6.5-3] from the heat of reaction of iron and oxygen to form FeO, 2.67×10^5 J/mole.[6.5-4] The resultant heat of formation for one mole of FeO from one mole of H_2O is multiplied by the rate of oxygen uptake in moles and the circumference of the cladding to obtain Equation (6-14).

The expected standard deviation of the oxide layer thickness is $\pm$ 50% of the predicted thickness. The expected standard deviation of the oxidation weight gain and oxidation power is somewhat less, $\pm$ 25% of the predicted value, because the oxide composition and density do not affect the prediction of these quantities.

Figure 6-5 and Figure 6-6 illustrate the parabolic constants calculated with the SOXWGN and SOXTHK functions. The time step averaged power per meter of rod calculated with SOXIDE for a 1.25×10^{-2}m diameter rod with no initial oxide layer and a 1 second time step is shown in Figure 6-7. Figure 6-8 and Figure 6-9 illustrate oxygen uptake and the oxide layer thickness expected after a 1 second time step with no initial oxidation.

6.5.2 References

6.5-1 H. C. Brassfield, J. F. White, L. Sjodahl, and J. T. Bittel, *Recommended Property and Reaction Kinetics Data for Use in Evaluating a Light Water Cooled Reactor Loss-of-Coolant Incident Involving Zircaloy-4 of 304SS Clad UO_2*, GEMP 482, 1968.

6.5-2 J. C. Hesson et al., *Laboratory Simulations of Cladding--Steam Reactions Following Loss of Coolant Accidents in Water Cooled Power Reactors*, ANL-7609, 1970, pp. 12-18.

6.5-3 J. A. Dean (ed.), *Lange's Handbook of Chemistry*, 12th Edition, New York: McGraw-Hill Book Company, 1979.

6.5-4 F. D. Rossini et al., *Selected Values of Chemical Thermodynamic Properties, Circular of the National Bureau of Standards 500*, Washington, D. C.: United States Government Printing Office, 1952.

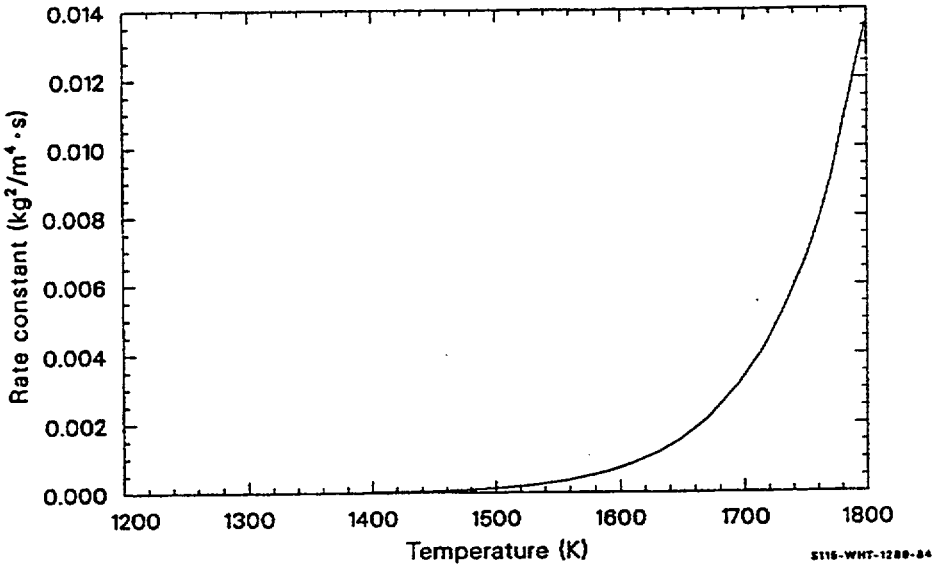

Figure 6-5. Parabolic constant for oxygen weight gain.

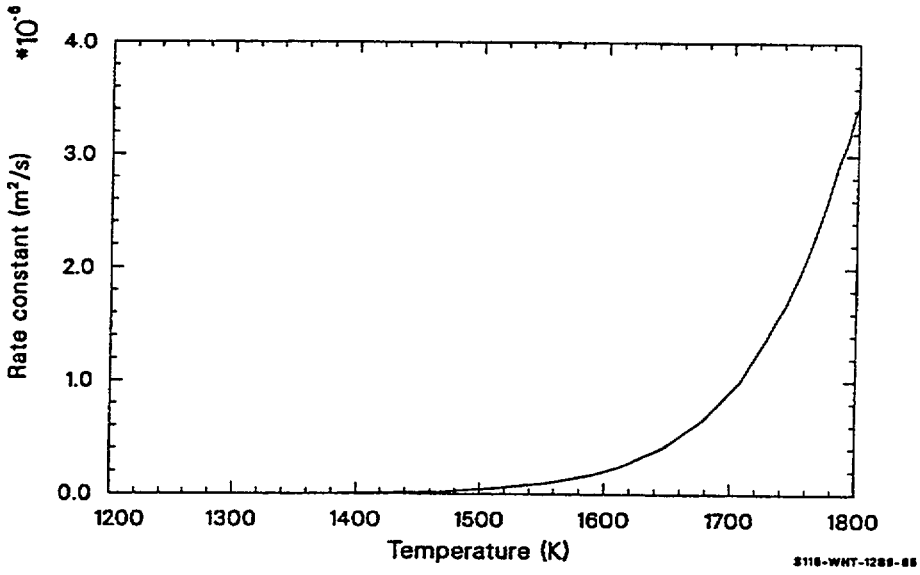

Figure 6-6. Parabolic constant for oxide layer thickness.

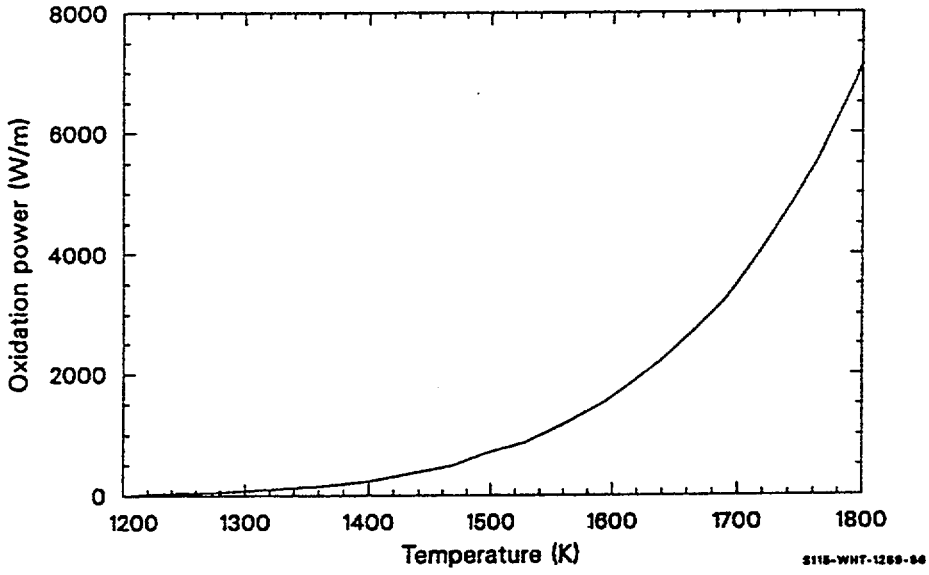

Figure 6-7. Average power per meter during 1 second for a 1.25 x 10^{-2} m stainless steel rod with no initial oxide layer.

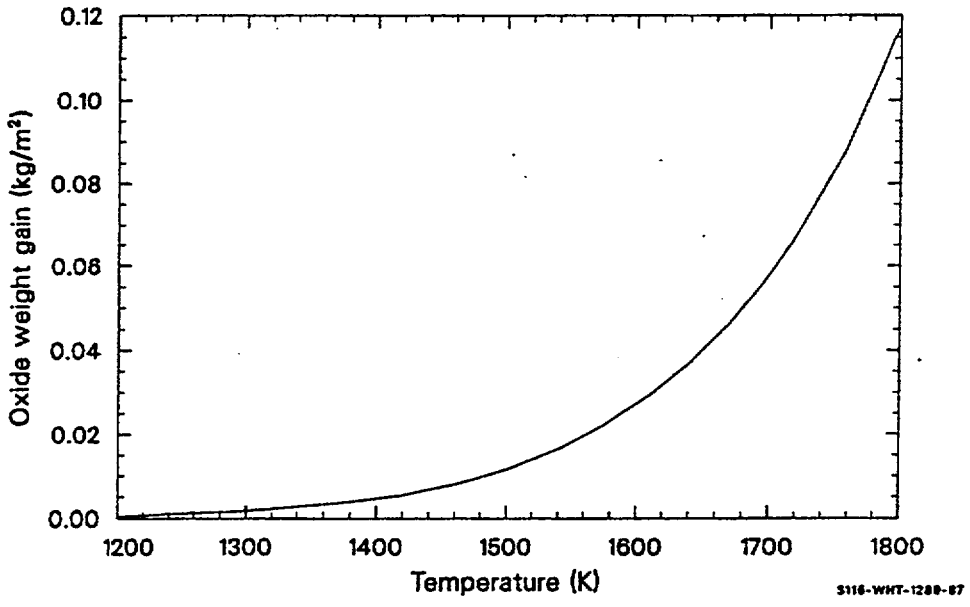

Figure 6-8. Oxygen uptake after 1 second with no initial oxidation.

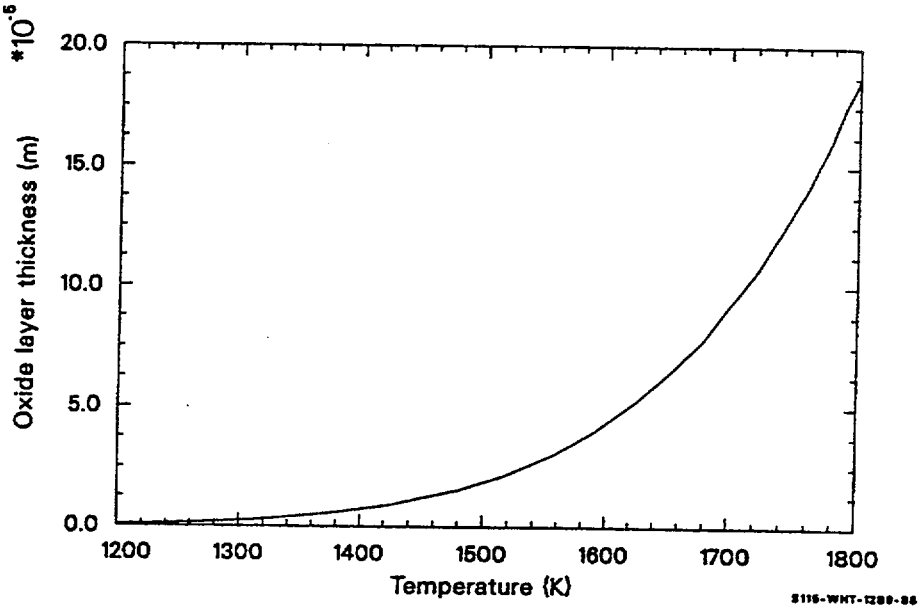

Figure 6-9. Oxide layer thickness after 1 second with no initial oxidation.

7. STAINLESS STEEL OXIDES

With the expansion of severe accident analysis computer codes to include boiling water reactors (BWR) using stainless steel control blades, it became apparent that materials properties information was needed for the stainless steel oxides formed at high temperatures. Correlations were developed to calculate specific heat capacity (SOCP), enthalpy (SONTHL), thermal conductivity (SOTCON), thermal expansion (SOTEXP), and density (SODEN).

7.1 Specific Heat Capacity and Enthalpy (SOCP, SONTHL)

The function SOCP calculates the specific heat capacity for stainless steel oxide at constant pressure as a function of temperature. The function SONTHL calculates the enthalpy change for stainless steel oxide at constant pressure as a function of temperature and a reference temperature of 300 K, for which the enthalpy change will be zero.

7.1.1 Specific Heat Capacity (SOCP)

The function SOCP returns the specific heat capacity at constant pressure for a mixture of the iron oxides, FeO, Fe_2O_3, and Fe_3O_4, as a function of temperature. These iron oxides are presumed to be the major components of stainless steel oxide. The expressions used to calculate specific heat capacity are:

FeO:

For $300 < T \leq 1{,}642$ K (solid phase),

$$C_p = 676.2 + 0.1432\,T \quad . \tag{7-1}$$

For $T > 1{,}642$ K (liquid phase),

$$C_p = 989 \quad . \tag{7-2}$$

Fe_2O_3:

For $300 < T \leq 950$ K (alpha phase),

$$C_p = 337.6 + T(1.099 - 2.372 \times 10^{-5}\,T) \quad . \tag{7-3}$$

For $950 < T \leq 1{,}050$ K (beta phase),

$$C_p = 1248 \quad . \tag{7-4}$$

For $1{,}050 < T \leq 1{,}838$ K (gamma phase),

$$C_p = 829.9 + 4.26 \times 10^{-2} T \ . \quad (7\text{-}5)$$

For T > 1,838 K (liquid phase),

$$C_p = 829.9 + 4.26 \times 10^{-2} T \ . \quad (7\text{-}6)$$

Fe_3O_4:

For 300 < T ≤ 1,000 K (alpha phase),

$$C_p = 394.9 + T(0.8705 - 4.976 \times 10^{-7} T) \ . \quad (7\text{-}7)$$

For 1,000 < T ≤ 1,864 K (beta phase),

$$C_p = 866.5 \ . \quad (7\text{-}8)$$

For T > 1,864 K (liquid phase),

$$C_p = 866.5 \ . \quad (7\text{-}9)$$

Since no data were found for the liquid phase specific heat capacity, the specific heat capacity at the melting point of each oxide was used as an estimate. The final specific heat capacity for stainless steel oxide calculated by the SOCP subroutine is a simple average of the calculated specific heat capacities of each oxide of iron.

$$SOCP_F = \frac{[SOCP_{(FeO)} + SOCP_{(Fe\ O_3)} + SOCP_{(Fe\ O_4)}]}{3} \ . \quad (7\text{-}10)$$

Figure 7-1 shows the calculated specific heat capacity for stainless steel oxide as a function of temperature. Table 7-1 to Table 7-3 contain the specific data from Touloukian[7.1-1] that were used to derive the equations used in the calculation.

Table 7-1. FeO specific heat capacity data.

	Temperature (K)	Specific heat capacity (cal/gK)
Solid phase:		
	300	0.1672
	400	0.1747
	500	0.1789
	600	0.184
	700	0.1876
	800	0.191
	900	0.1942
	1,000	0.1973
	1,100	0.2004
	1,200	0.2034
	1,300	0.2064
	1,400	0.2094
	1,500	0.2123
	1,600	0.2153
	1,650	0.2168
Liquid phase:		
	1,650	0.2366
	1,700	0.2366
	1,800	0.2366

Table 7-2. Fe_2O_3 specific heat capacity data.

	Temperature (K)	Specific heat capacity (cal/gK)
Alpha phase:		
	391.0	0.182
	393.5	0.184
	414.0	0.186
	450.5	0.197
	490.5	0.204
	493.0	0.207
	508.0	0.207
	533.0	0.217
	419.2	0.187
	435.0	0.189
	463.0	0.211
	479.5	0.217
	483.7	0.206
	505.5	0.214
	535.0	0.222
	567.0	0.22
	592.5	0.223
	626.5	0.238
	654.5	0.264
	682.0	0.272
	685.5	0.273
	701.5	0.27
	715.5	0.287
	737.5	0.271
	763.0	0.288
	799.0	0.291

Table 7-2. Fe_2O_3 specific heat capacity data. (Continued)

	Temperature (K)	Specific heat capacity (cal/gK)
	823.0	0.298
	840.0	0.314
	880.0	0.335
	904.0	0.342
	864.0	0.326
	870.5	0.32
	889.0	0.322
	936.0	0.328
	941.0	0.358
	301.23	0.1563
	310.2	0.1592
	319.04	0.1616
	327.77	0.164
	336.53	0.1664
	345.42	0.1687
	300.0	0.1796
	400.0	0.1922
	500.0	0.2044
	600.0	0.2163
	700.0	0.2281
	800.0	0.2399
	900.0	0.2516
	950.0	0.2575
Beta phase:		
	973.0	0.367
	991.5	0.376
	950.0	0.2254

Table 7-2. Fe_2O_3 specific heat capacity data. (Continued)

	Temperature (K)	Specific heat capacity (cal/gK)
	1,000.0	0.2254
	1,050.0	0.2254
Gamma phase:		
	1,050.0	0.2101
	1,100.0	0.2106
	1,200.0	0.2118
	1,300.0	0.2128
	1,400.0	0.214
	1,500.0	0.2154
	1,600.0	0.2162
	1,700.0	0.2172
	1,750.0	0.2178

Table 7-3. Fe_3O_4 specific heat capacity data.

	Temperature (K)	Specific heat capacity (cal/gK)
Alpha phase:		
	300.0	0.1569
	400.0	0.1778
	500.0	0.1986
	600.0	0.2193
	700.0	0.2402
	800.0	0.261
	900.0	0.2818
Beta phase:		
	1,100.0	0.2073
	1,200.0	0.2073

Table 7-3. Fe_3O_4 specific heat capacity data.

Temperature (K)	Specific heat capacity (cal/gK)
1,300.0	0.2073
1,400.0	0.2073
1,500.0	0.2073
1,600.0	0.2073
1,700.0	0.2073
1,800.0	0.2073

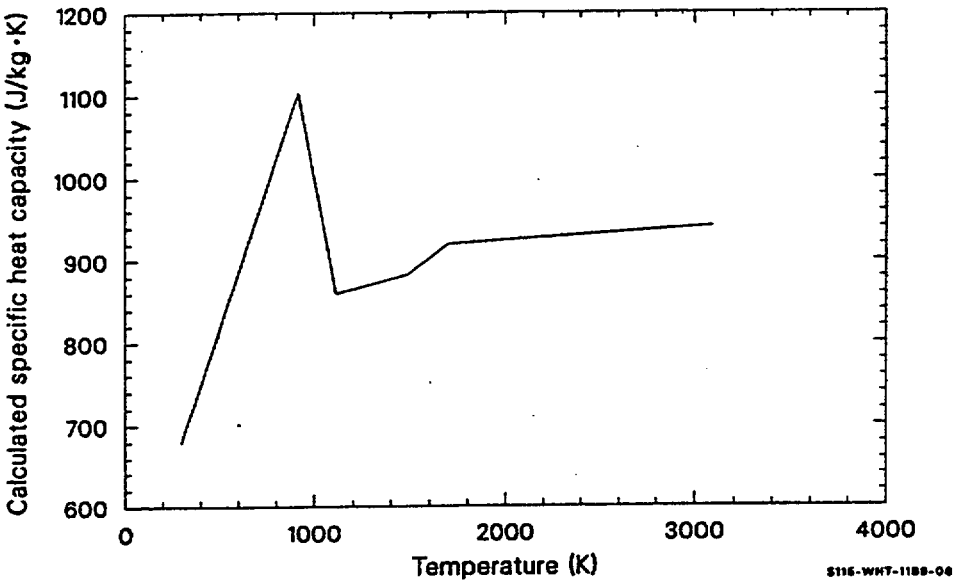

Figure 7-1. Specific heat capacity for stainless steel oxide calculated by SOCP.

7.1.2 Enthalpy (SONTHL)

The function SONTHL calculates the enthalpy change for stainless steel oxide as a function of temperature and a reference temperature of 300 K. At 300 K, the enthalpy change is zero. The expressions used to calculated the enthalpy of stainless steel oxide are:

For $300 < T < 950$ K,

$$h_s = -1.7264166 \times 10^5 + T[469.6 + T(0.3521 - 2.691 \times 10^{-6} T)] \quad . \tag{7-11}$$

For $950 \leq T < 1{,}000$ K,

$$h_s = -2.9379084 \times 10^5 + T[773.0 + T(0.1690 - 5.53 \times 10^{-7} T)] \quad . \tag{7-12}$$

For $1000 \leq T < 1{,}050$ K,

$$h_s = -3.530784 \times 10^5 + T(930.2 + 2.387 \times 10^{-2} T) \quad . \tag{7-13}$$

For $1{,}050 \leq T \leq 1{,}642$ K,

$$h_s = -1.6657291 \times 10^5 + T(790.0 + 3.07 \times 10^{-02} T) \quad . \tag{7-14}$$

For $T > 1{,}642$ K,

$$h_s = -2.7403984 \times 10^5 + T(895.1 + 7.1 \times 10^{-03} T) \tag{7-15}$$

where

h_s = the enthalpy change for stainless steel oxide (J/kg)

T = the stainless steel oxide temperature (K).

The above enthalpy expressions were obtained by averaging at each temperature range the enthalpies of FeO, Fe_2O_3, and Fe_3O_4, the main components presumed to be present in the oxide of stainless steel. For each iron oxide, the enthalpies that were averaged were obtained by integrating the polynomials obtained from fitting the specific heat capacity data from Touloukian et al.[7.1-1] The specific heat capacity data used to obtain the polynomials are presented in Table 7-1 through Table 7-3.

Figure 7-2 is a plot of the enthalpy change for stainless steel oxide calculated by the subroutine SONTHL.

7.1.3 Reference

7.1-1 Y. S. Touloukian and E. H. Buyco, *Thermal Physical Properties of Matter, V5, Specific Heat - Nonmetallic Solids*, New York: IFI/Plenum, 1970, pp. 107-117.

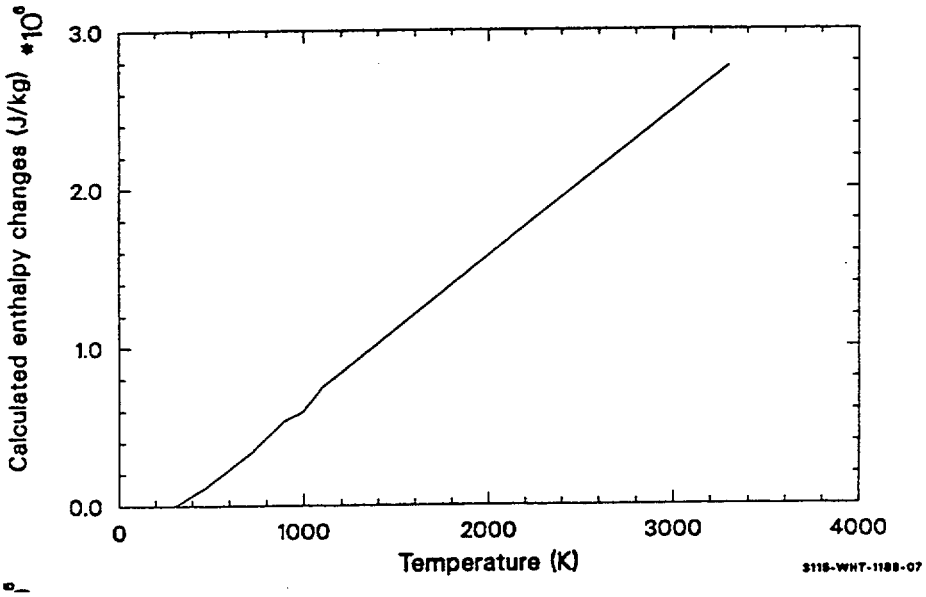

Figure 7-2. Enthalpy change for stainless steel oxide calculated by SONTL.

7.2 Thermal Conductivity (SOTCON)

The thermal conductivity of stainless steel oxide as a function of temperature is calculated by the function SOTCON. The only input required is the temperature of the stainless steel oxide (SOTEMP).

7.2.1 Model Development

The correlation used to calculate the thermal conductivity is derived from a polynomial fit of data (Table 7-4) from Reference 7.2-1. Due to lack of available data, the calculation was truncated at a temperature of 800 K. The equation used to calculate the thermal conductivity is:

Table 7-4. Stainless steel oxide thermal conductivity from Touloukian.

Temperature	Thermal conductivity
317.1	0.0444
335.7	0.0435
353.9	0.0435
385.6	0.0431
453.2	0.0414

$$K_s = 4.6851 + 100\,T(-3.3292 \times 10^{-7} - 2.5618 \times 10^{-8}\,T) \quad (7\text{-}16)$$

where

K_s = the stainless steel oxide thermal conductivity (W/m•K)

T = the stainless steel oxide temperature (K).

The expected standard error of the predicted conductivities is $\pm$ 0.2 times the calculated conductivity for temperatures in the range from 300 to 800 K. For temperatures greater than 800 K, the uncertainty of the calculation increases. A plot of the thermal conductivities calculated by the function SOTCON is shown in Figure 7-3.

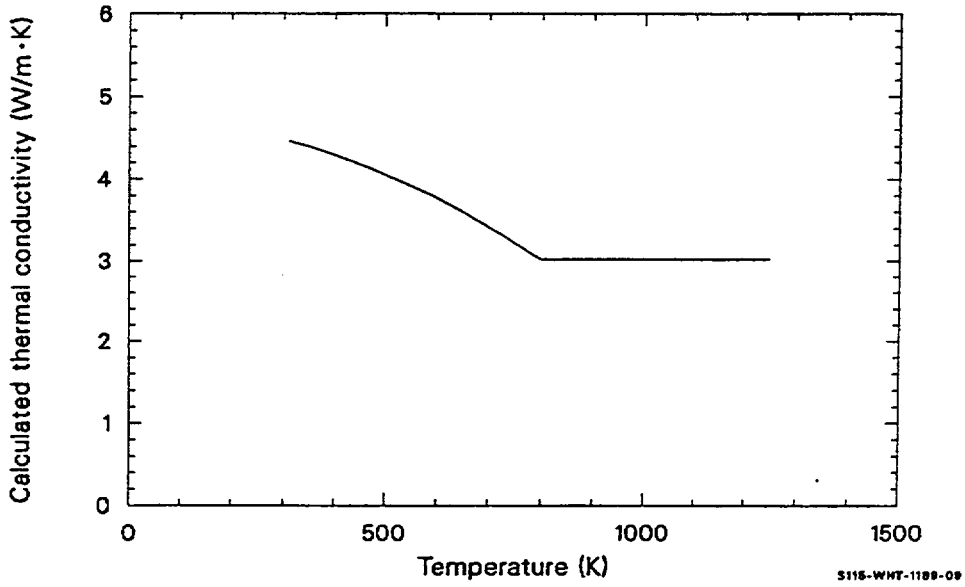

Figure 7-3. Thermal conductivities for stainless steel oxide calculated by SOTCON.

7.2.2 Reference

7.2-1 S. Touloukian, R. W. Powell, C. Y. Ho, and P. G. Klemens, *Thermal Physical Properties of Matter, V2, Thermal Conductivity - Non-Metallic Solids*, New York: IFI/Plenum, 1970, pp. 154-156

7.3 Thermal Expansion and Density (SOTHEX, SODEN)

The subcode SOTHEX calculates the stainless steel oxide thermal expansion strain, and the subcode SODEN computes the density from room temperature to the oxide melting point. SOTHEX requires the temperature of the stainless steel oxide and a reference temperature (for which the thermal strain will be zero), while SODEN requires only the temperature of the stainless steel oxide.

7.3.1 Thermal Expansion (SOTHEX)

The thermal expansion value calculated for stainless steel oxide was obtained by taking an average of the calculated thermal expansion of FeO, Fe_2O_3, and Fe_3O_4. The equations used were obtained from Reference 7.3-1 and are as follows:

$$\varepsilon_{s(FeO)} = -0.409 + 1.602 \times 10^{-3} T - 7.913 \times 10^{-7} T^2 + 5.348 \times 10^{-10} T^3 \ . \quad (7\text{-}17)$$

$$\varepsilon_{s(Fe_2O_3)} = -2.537 + 7.30 \times 10^{-4} T + 4.964 \times 10^{-7} T^2 - 1.140 \times 10^{-10} T^3 \ . \quad (7\text{-}18)$$

$$\varepsilon_{s(Fe_3O_4)} = -0.214 + 6.929 \times 10^{-4} T - 1.107 \times 10^{-7} T^2 + 8.078 \times 10^{-10} T^3 \ . \quad (7\text{-}19)$$

$$es\varepsilon_{s(average)} = \frac{\varepsilon_{s(FeO)} + \varepsilon_{s(Fe_2O_3)} + \varepsilon_{s(Fe_3O_4)}}{3} \quad (7\text{-}20)$$

where

$\varepsilon_{s(FeO)}$ = the thermal expansion strain for FeO (m/m)

$\varepsilon_{s(Fe_2O_3)}$ = the thermal expansion strain for Fe_2O_3 (m/m)

$\varepsilon_{s(Fe_3O_4)}$ = the thermal expansion strain for Fe_3O_4 (m/m)

$\varepsilon_{s(average)}$ = the thermal expansion strain taken as the average of the calculated strains for the three oxides (m/m)

T = the temperature of the stainless steel oxide (K).

The calculated thermal expansion strain for stainless steel oxide was obtained by averaging the thermal expansion strains calculated for each oxide of iron. This average strain value was used as an approximation for the thermal expansion strain of stainless steel oxide because no data for the thermal expansion strain of the oxide mixture found on oxidized stainless steel surfaces are available.

The thermal expansion strains computed by the function SOTHEX for stainless steel oxide using a reference temperature of 300 K is illustrated in Figure 7-4.

7.3.2 Density (SODEN)

The function SODEN uses the general relation between density and thermal expansion strain to calculate the density of stainless steel oxide. A density of $8.0e^3$ kg/m^3 at 300 K[7.3-2] is used as a reference density. The expected standard error of $\pm$ 0.5 kg/m^3 for the density of stainless steel oxide is due to the

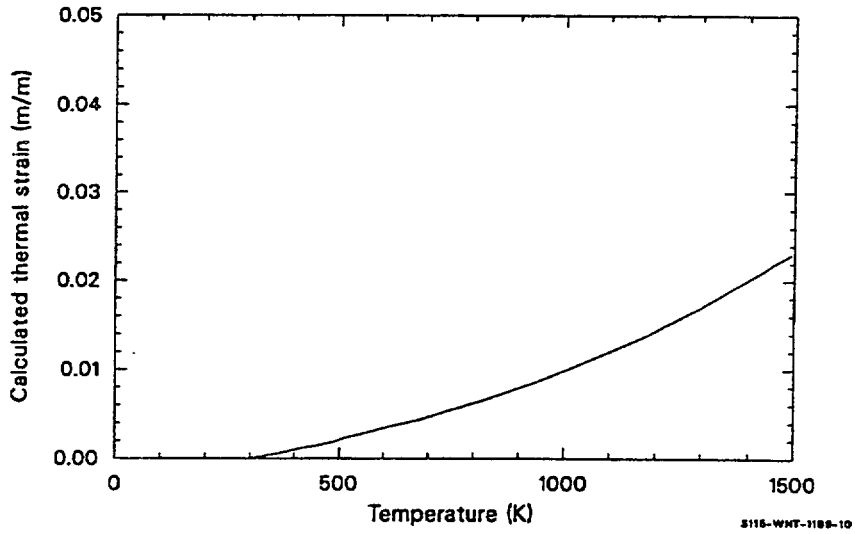

Figure 7-4. Thermal expansion strain as a function of temperature calculated by SOTHEX.

uncertainty of the reference density. Figure 7-5 shows the density of stainless steel oxide calculated by the function SODEN using the thermal expansion strains calculated in SOTHEX.

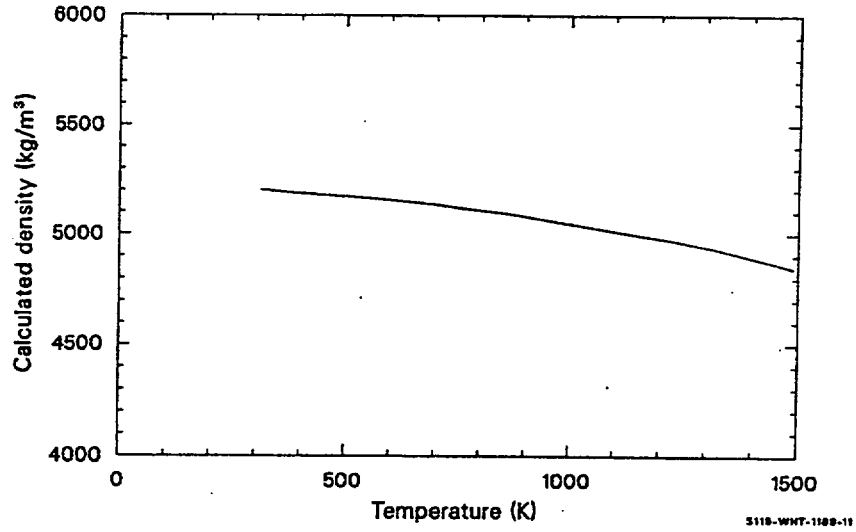

Figure 7-5. Density calculated by SODEN using the thermal strain calculated by SOTHEX.

7.3.3 References

7.3-1 Y. S. Touloukian, R. K. Kirby, R. E. Taylor, and P. D. Desai, *Thermal Physical Properties of Matter, V12, Thermal Expansion - Metallic Elements and Alloys*, New York: IFI/Plenum, 1970, pp. 366-372.

7.3-2 *Handbook of Chemistry and Physics*, The Chemical Rubber Company, 50th Edition, 1969-1970.

8. NEUTRON ABSORBERS (SILVER-INDIUM-CADMIUM CONTROL RODS AND BORON CARBIDE CONTROL BLADES)

A set of control rod neutron absorber properties for silver-indium-cadmium (Ag-In-Cd) alloys (80% Ag, 15% In, 5% Cd by weight) and boron carbide (B_4C) has been prepared to allow modeling of the possible flow and freezing of these materials during a severe core disruption. Properties for both substances have been included in each subcode. An input argument, ICTYPE, is used to determine which substance properties are returned. (ICTYPE = 1 for the Ag-In-Cd control rod properties, and ICTYPE = 2 for the BWR B_4C control rod properties.)

No models have been provided for mixtures of neutron absorbers and their stainless steel cladding because it has been reported[8.0-1] that Ag-In-Cd alloy is insoluble in stainless steel and because the very different melting temperatures of stainless steel (1,700 K) and B_4C (2,700 K)[8.0-2] make it likely that the stainless steel will oxidize or melt and run away from hot regions before B_4C and stainless steel mix.

8.0.1 References

8.0-1 W. B. Murfin et al., *Core Meltdown Experimental Review*, SAND74-0382, NUREG-0205, 1977, p. 4-38.

8.0-2 Chase et al., *JANAF Thermochemical Tables*, 1986, pp. 541-543.

8.1 Melting Temperature (AHYPRP)

The subroutine AHYPRP provides absorber solidus (appearance of the first liquid phase) and liquidus (melting of the last solid phase) temperatures. There is no required input other than a parameter to identify which absorber material is used.

8.1.1 Model Development

For the typical Ag-In-Cd alloy, Reference 8.1-1 reports an approximate melting range of 1,073 to 1,123 K. These numbers are thus used for the solidus and liquidus temperatures of the alloy.

The melting temperature of 2,700 K reported on page 541 of Reference 8.1-2 is used for the solidus and liquidus temperature of B_4C.

8.1.2 References

8.1-1 D. A. Petti, *Silver-Indium-Cadmium Control Rod Behavior and Aerosol Formation in Severe Reactor Accidents*, NUREG/CR-4876, EGG-2501, April 1987.

8.1-2 Chase et al., *JANAF Thermochemical Tables*, 1986, pp. 541-543.

8.2 Specific Heat Capacity and Enthalpy (ACP, AENTHL)

The function ACP provides absorber specific heat capacities as a function of temperature. AENTHL returns the absorber enthalpies as a function of temperature and a reference temperature for which the enthalpy will be zero.

8.2.1 Specific Heat Capacity of Ag-In-Cd (ACP)

The expressions used for the specific heat capacity of Ag-In-Cd are atomic fraction weighted averages of the specific heat capacities of silver, indium, and cadmium

$$C_p = \frac{0.808C_{pm_{Ag}} + 0.143C_{pm} + 0.049C_{pm_{Cd}}}{0.109\frac{kg}{mole}\text{Alloy}} \quad (8\text{-}1)$$

where

C_p = alloy specific heat capacity (J/kg• K)

$C_{pm_{Ag}}$ = molar heat capacity of silver (J/mole•K)

$C_{pm_{In}}$ = molar heat capacity of indium (J/mole• K)

$C_{pm_{Cd}}$ = molar heat capacity of cadmium (J/mole• K).

Expressions for the silver, indium, and cadmium molar heat capacities up to the beginning of melting, 1,073 K, were taken from Table 2-24 of Reference 8.2-1. All are correlations of the form

$$C_{pm} = a + b \times 10^{-3}\, T + d \times 10^{5}/\, T^{-2} \quad (8\text{-}2)$$

where

C_{pm} = molar heat capacity (J/mole•K)

T = temperature (K)

and the constants a, b, and d are listed in Table 8-1. For temperatures above 1,073 K, C_p is assumed to be equal to its value at 1,050 K. Figure 8-1 shows the heat capacity of Ag-In-Cd calculated by ACP. A standard error of 10% of the calculated value is predicted.

Table 8-1. Molar heat capacity constants for Equation (8-1) from Reference 8.2-1.

Metal	a (J/mole• K)	b (J/mole• K)	d (J• K/mole)
Silver	21.3	4.27	1.51
Indium	24.3	10.5	0
Cadmium	22.2	12.3	0

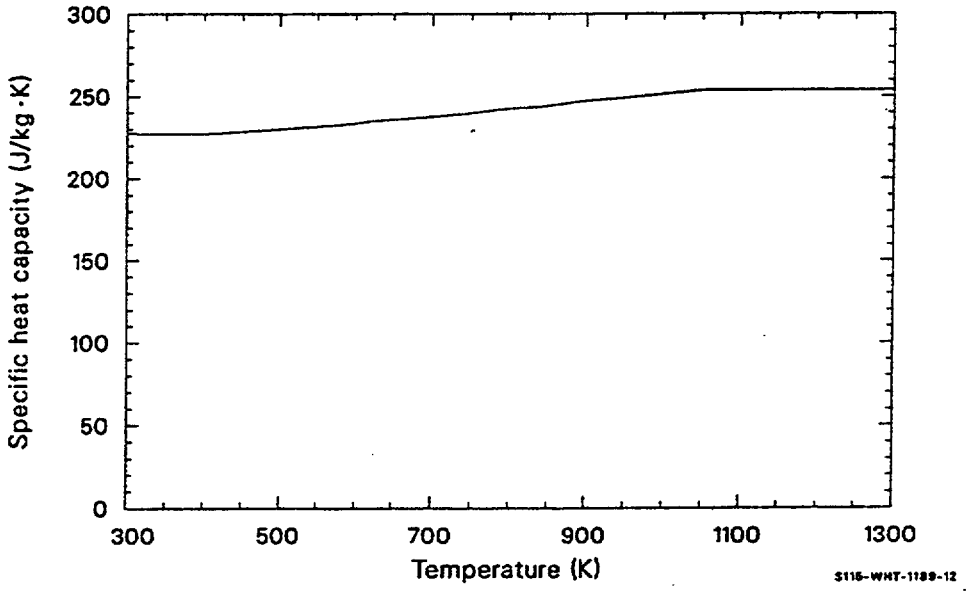

Figure 8-1. Silver-indium-cadmium absorber heat capacity.

8.2.2 Specific Heat Capacity for Boron Carbide(ACP)

The expressions used for the specific heat capacity of B_4C are listed below:

For $T < 2{,}700$ K,

$$C_p = 563 + T\,(1.54 - T\,2.94 \times 10^{-4}) \ . \tag{8-3}$$

For $T \geq 2{,}700$ K,

$$C_p = 2{,}577.740 \ . \tag{8-4}$$

Equations (8-3) and (8-4) were developed from a curve given on page 588 of Reference 8.2-2. Figure 8-2 shows the heat capacity of boron carbide as calculated by the function ACP. The prediction has a standard error near 0.10 of its value.

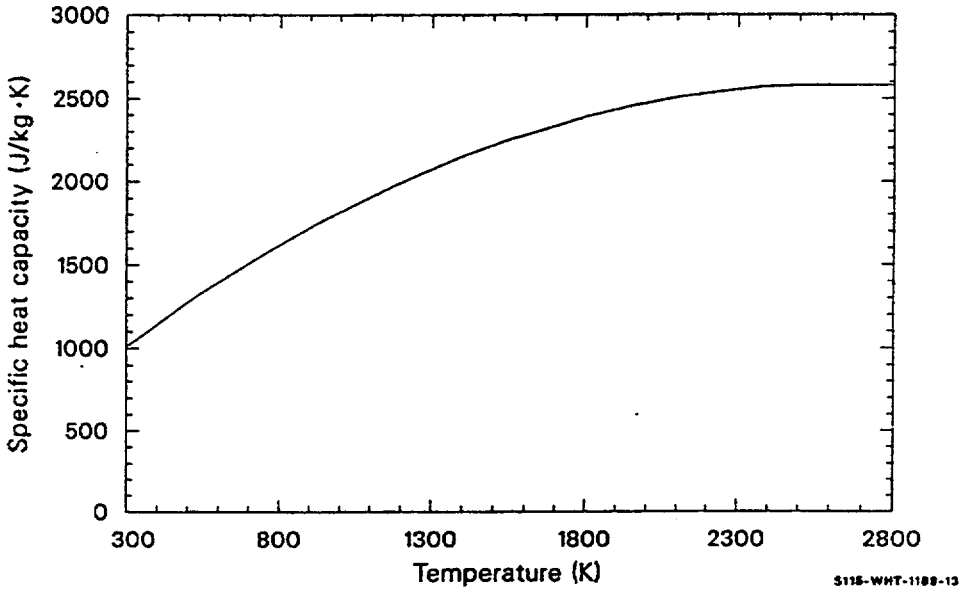

Figure 8-2. Boron carbide absorber heat capacity.

8.2.3 Enthalpy of Ag-In-Cd (AENTHL)

Integrals of Equations (8-2), (8-3), or (8-4) are used to compute enthalpy changes in the AENTHL function for the Ag-In-Cd absorber (ICTYPE = 1). The heat of fusion which is included in the AENTHL function is an estimate. The Ag-In-Cd heat of fusion, 9.5610^4 J/kg, was estimated by multiplying the molar heats of fusion of silver, indium, and cadmium by the atomic fraction of each element in the alloy; summing the calculated fractional heats of fusion; and dividing the sum by 0.109, the weight of a g-mole of the alloy in kilograms. The elemental heats of fusion were obtained from Tables 2 through 24 of Reference 8.2-1. Figure 8-3 shows the enthalpy changes calculated for Ag-In-Cd by AENTHL. The prediction has a standard error near 0.10 of its value.

8.2.4 Enthalpy of Boron Carbide (AENTHL)

An integral of Equation (8-3) is used to compute enthalpy changes in the AENTHL function for the B_4C absorber (ICTYPE = 2). The estimated heat of fusion for B_4C was taken to be that of UO_2, 2.74×10^5 J/kg. Figure 8-4 shows the enthalpy changes calculated for B_4C by AENTHL. The prediction has a standard error near 0.10 of its value.

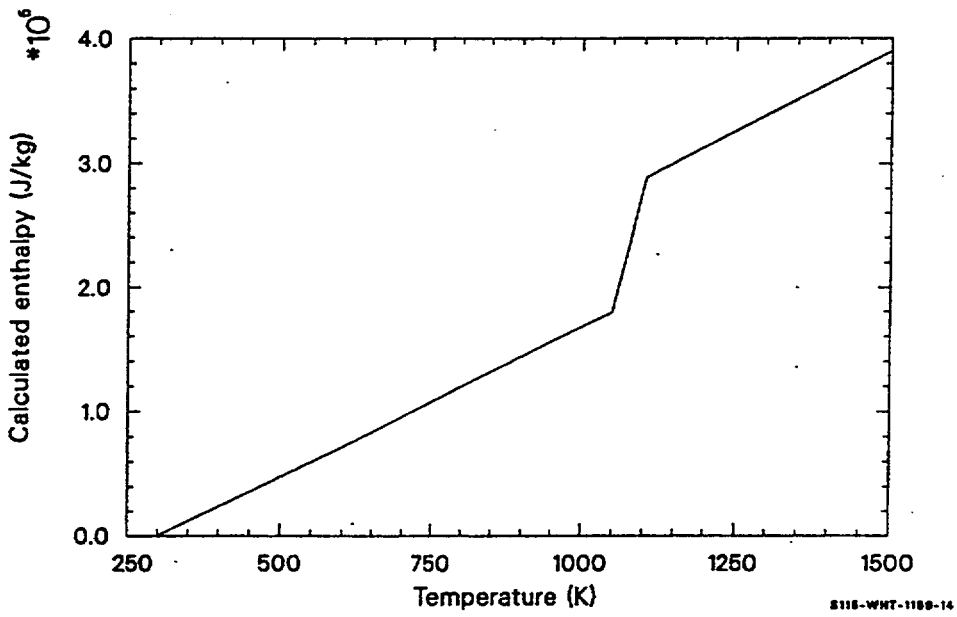

Figure 8-3. Silver-indium-cadmium absorber enthalpy.

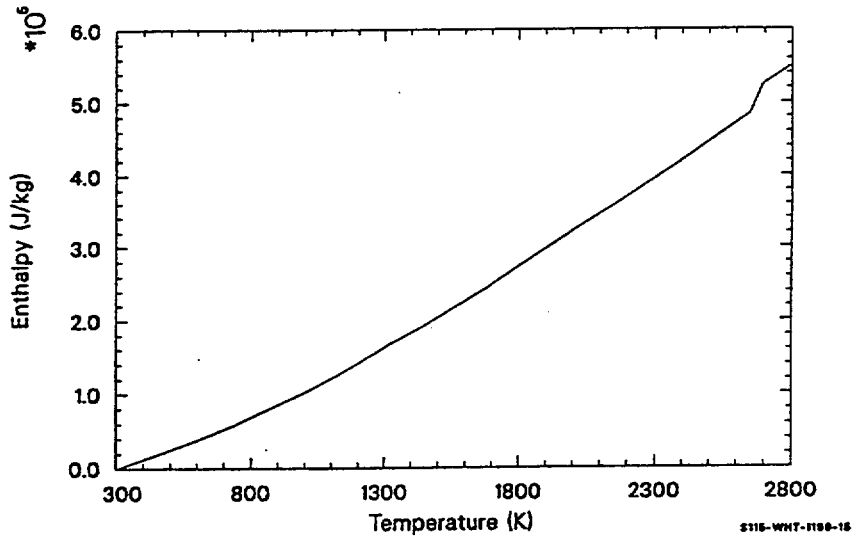

Figure 8-4. Boron carbide absorber enthalpy.

8.2.5 References

8.2-1 C. T. Lynch (ed.), *Handbook of Materials Science, II: Metals, Composites and Refractory Materials*, Cleveland: CRC Press, Inc., 1975.

8.2-2 Aerojet Nuclear Company, *Materials Properties Data Book*, AGC2275, 1970.

8.3 Thermal Conductivity (ATHCON)

The only input required by ATHCON to calculate the thermal conductivity of Ag-In-Cd or B_4C is the absorber temperature.

8.3.1 Thermal Conductivity of Ag-In-Cd (ATHCON)

The expressions used for Ag-In-Cd are listed below:

For $300 \leq T < 1{,}050$ K,

$$K_a = 2.805 \times 10^1 + T\,(1.101 \times 10^{-1} - 4.436 \times 10^{-5}\,T)\ . \tag{8-5}$$

For $1{,}050 \leq T < 1{,}100$ K,

$$K_a = 1.076458 \times 10^3 - 0.934962\,T\ . \tag{8-6}$$

For $T \geq 1{,}100$ K,

$$K_a = 48 \tag{8-7}$$

where

K_a = absorber thermal conductivity (W/m•K)

T = absorber temperature (K).

The correlation, Equation (8-5) was derived by fitting a second degree polynomial to the first, fourth, and seventh entries of a table of properties provided by Reference 8.3-1. The table is reproduced as Table 8-2. Equation (8-7) was derived by dividing the conductivity predicted by Equation (8-5) for 1,098 K (the middle of the melting range) by two to estimate the conductivity when this face centered cubic solid[8.3-1] melts. The method for estimating liquid conductivities follows recommendations by Nazare et al.[8.3-2] Equation (8-6) is simply a linear interpolation between the conductivity predicted by Equation (8-5) at the beginning of melting (1,073 K) and Equation (8-7) when melting is complete. Figure 8-5 is a comparison of the predictions of Equations (8-5) through (8-7) with the recommended values of Table 8-2. Figure 8-6

shows the thermal conductivity of the Ag-In-Cd absorber calculated by ATHCON. An expected standard error of 0.20 is recommended.

Table 8-2. Thermal conductivity values for Ag-In-Cd recommended by Cohen et al.[8.3-1]

Temperature (K)	Thermal Conductivity (W/m•K)
323	59.0
373	62.8
473	70.3
573	76.6
673	82.0
773	86.6
873	90.4

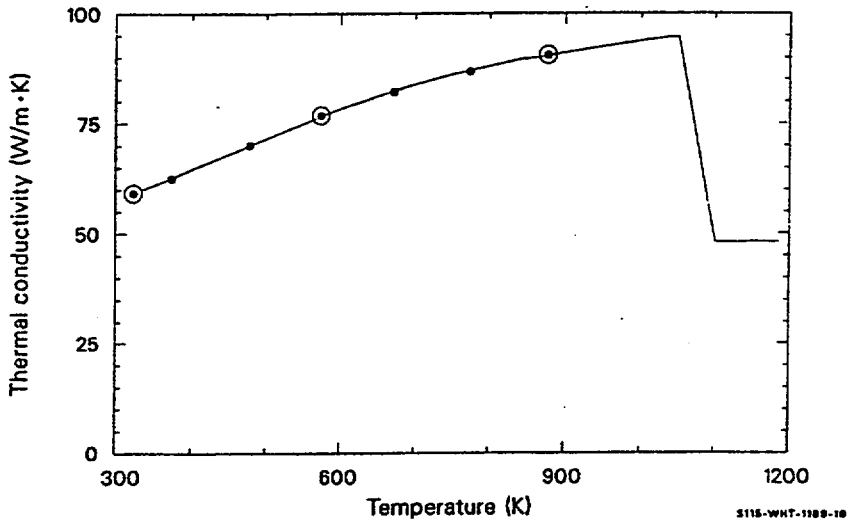

Figure 8-5. Thermal conductivity of silver-indium-cadmium alloy.

8.3.2 Thermal Conductivity of Boron Carbide (ATHCON)

The expression for B_4C, thermal conductivity, [Equation (8-8)] is a curve-fit to two sets of data compiled by Touloukian et al.[8.3-3] These data sets (labeled as curves 3 and 7 in Reference 8.3-3) are for B_4C powder with a density of ~ 1,900 kg/m^3 (~ 76% theoretical) and cover a temperature range from 333 K through 1,103 K. The Equation (8-8) correlation is extrapolated above 1,100 K based upon the trend

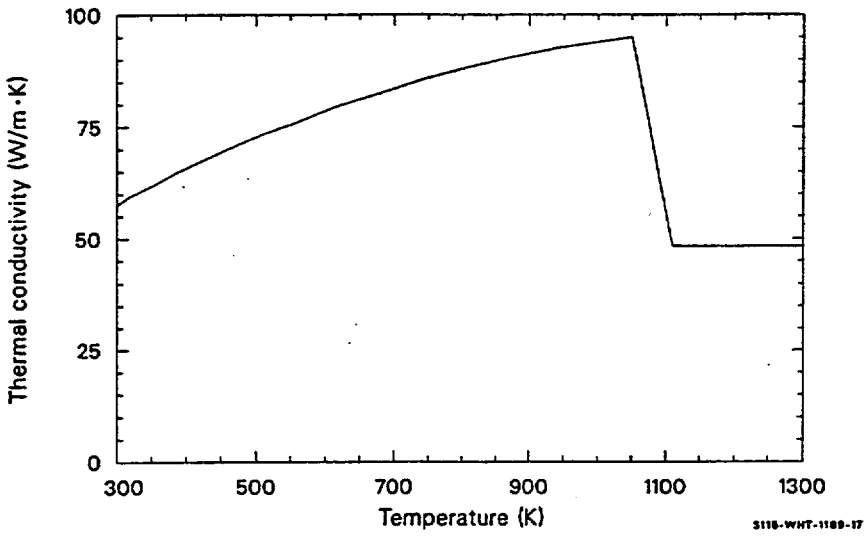

Figure 8-6. Thermal conductivity of silver-indium-cadmium absorber.

established by four other Touloukian et al., data sets (labeled as curves 1, 4, 9, and 10 in Reference 8.3-3) for B_4C with a density of ~ 2,500 kg/m^3 (~ 100% theoretical).

For $T \geq 300$ K,

$$K_a = 4.60 + 0.00205\ T + 2.65\ e^{(-T/448)} \qquad (8\text{-}8)$$

where

K_a = absorber thermal conductivity (W/m•K)

T = absorber temperature (K).

The estimated standard error of Equation (8-8) as determined by a statistical analysis of the Touloukian et al., data[8.3-3] is ± 15% of the calculated values. Figure 8-7 shows the predicted values of B_4C thermal conductivity versus temperature [calculated from Equation (8-8)] along with the data points from which the correlation was derived. As indicated, the correlation is intended to apply to B_4C powder with a density of ~ 76% of the theoretical value.

8.3.3 References

8.3-1 I. Cohen, E. F. Losco, and J. D. Eichenberg, "Metallurgical Design and Properties of Silver-Indium-Cadmium Alloys for PWR Control Rods," *Bettis Technical Review*, 1958.

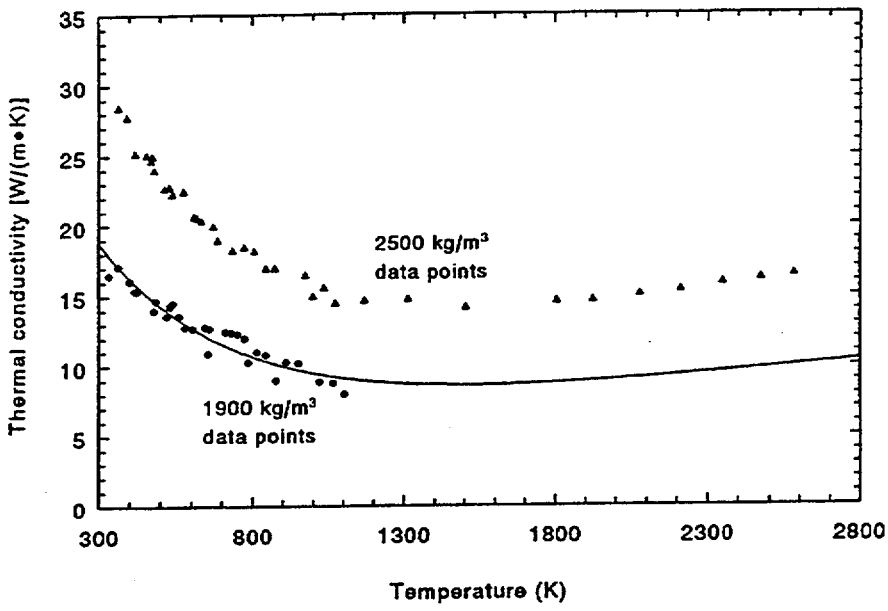

Figure 8-7. Thermal conductivity of boron carbide absorber.

8.3-2 S. Nazare, G. Ondracek, and B. Schulz, "Properties of Light Water Reactor Core Melts," *Nuclear Technology, 32*, 1977, pp. 239-246.

8.3-3 Y. S. Touloukian et al., *Thermophysical Properties of Matter Volume 2: Thermal Conductivity - Nonmetallic Solids,* New York: IFI/Plenum Data Corp., 1970, pp. 572-574.

8.4 Thermal Expansion and Density (ATHEXP, ADEN)

The function ATHEXP calculates absorber thermal expansion strain, while ADEN is designed to use this information to calculate absorber densities. ATHEXP requires input values of the materials temperature and a reference temperature (for which strain will be taken as zero). ADEN requires only temperature.

8.4.1 Thermal Expansion Strain of Ag-In-Cd

The expressions used for the thermal expansion strain of Ag-In-Cd absorbers are listed below:

For $300 \leq T < 1{,}050$ K,

$$\varepsilon_a = 2.25 \times 10^{-5} (T - 300) \ . \qquad (8\text{-}9)$$

For $1{,}050 \leq T < 1{,}100$ K,

$$\varepsilon_a = -0.25875 + 2.625 \times 10^{-4} \times T \ . \qquad (8\text{-}10)$$

For $T \geq 1{,}100$ K,

$$\varepsilon_a = 3.0 \times 10^{-2} \qquad (8\text{-}11)$$

where

ε_a = absorber thermal expansion strain (m/m)

T = absorber temperature (K).

Equation (8-9) is taken from Table V of Reference 8.4-1. Equation (8-11) was obtained by modifying the prediction of Equation (8-9) to allow for an increase of 0.038 in volume (0.013 in length) at the center of the melting range of 1,073 to 1,123 K because page 186 of Reference 8.4-2 reports this value for the change in volume of silver, the major component of the alloy, during melting. Equation (8-10) is a linear interpolation between the predictions of Equations (8-9) and (8-11) for the beginning and end of the melting range. The expected standard error of Equations (8-9) through (8-11), ± 0.10 of the predicted strain, is small because the data cover most of the range of the correlations. Figure 8-8 shows the predicted thermal expansion strain for Ag-In-Cd.

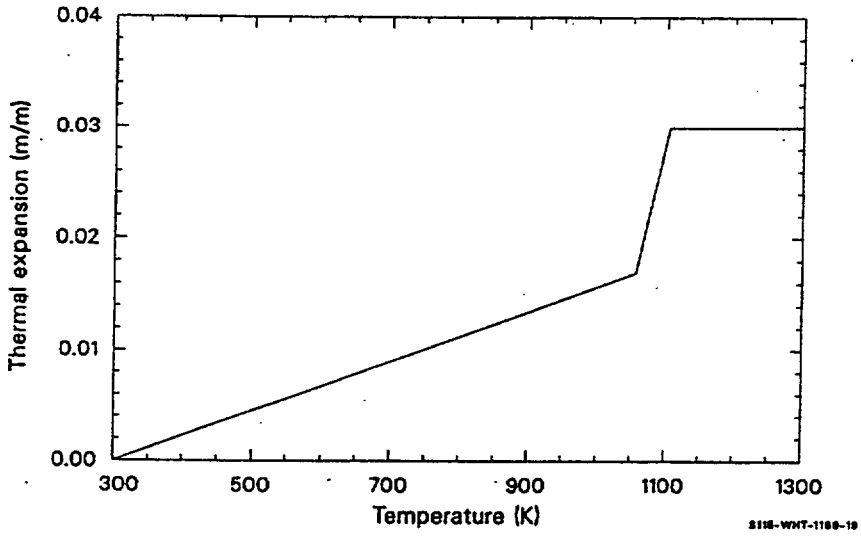

Figure 8-8. Thermal expansion strain of silver-indium-cadmium absorber

8.4.2 Thermal Expansion Strain of Boron Carbide

The expression used to calculate thermal expansion strains of B_4C is

$$\varepsilon_a = -1.10 \times 10^{-3} + T\,(3.09 \times 10^{-6} + 1.88 \times 10^{-9}\,T)\ . \qquad (8\text{-}12)$$

This correlation is a fit to values of 0, 2.58×10^{-3}, and 5.32×10^{-3} at 300, 800 and 1,200 K, respectively, obtained from a curve presented on page 949 of Reference 8.4-3. The expected standard error is $\pm$ 0.2 of the predicted strain. Figure 8-9 shows the predicted thermal expansion strain for B_4C.

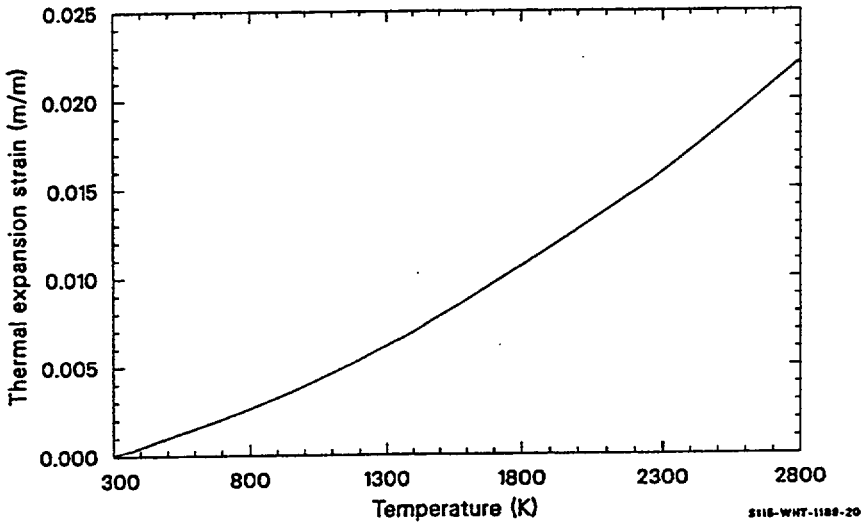

Figure 8-9. Thermal expansion strain of boron carbide absorber.

8.4.3 Density Calculations for Ag-In-Cd and Boron Carbide

The function ADEN uses the general relation between density and thermal strain, together with reference densities of 10.17×10^3 kg/m^3 at 300 K for Ag-In-Cd (Reference 8.4-1, Table V) and 2.5×10^3 kg/m^3 at 300 K for B_4C (page 943 of Reference 8.4-3). For Ag-In-Cd, the expected standard error is only 0.02 of the predicted density; but for B_4C, it is $\pm$ 0.30 of the predicted density.

The prediction for Ag-In-Cd and B_4C versus temperature given by the function are shown in Figure 8-10 and Figure 8-11.

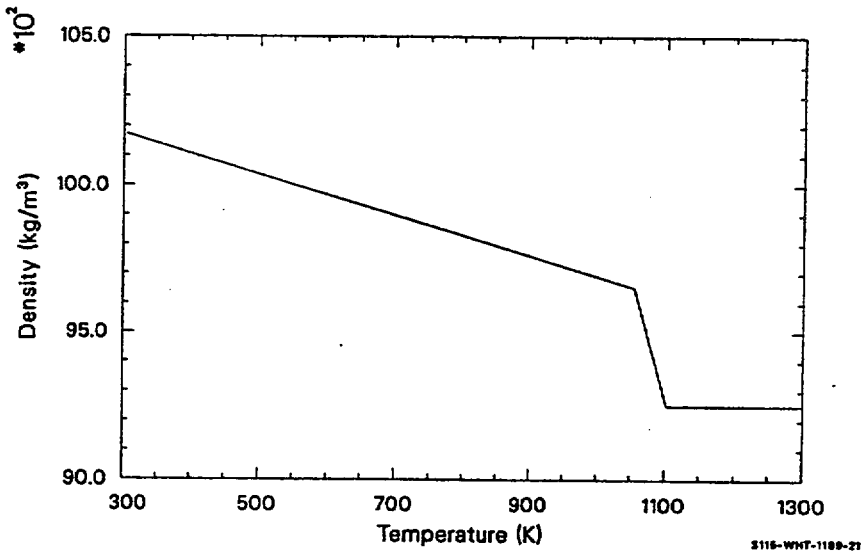

Figure 8-10. Density of silver-indium-cadmium absorber.

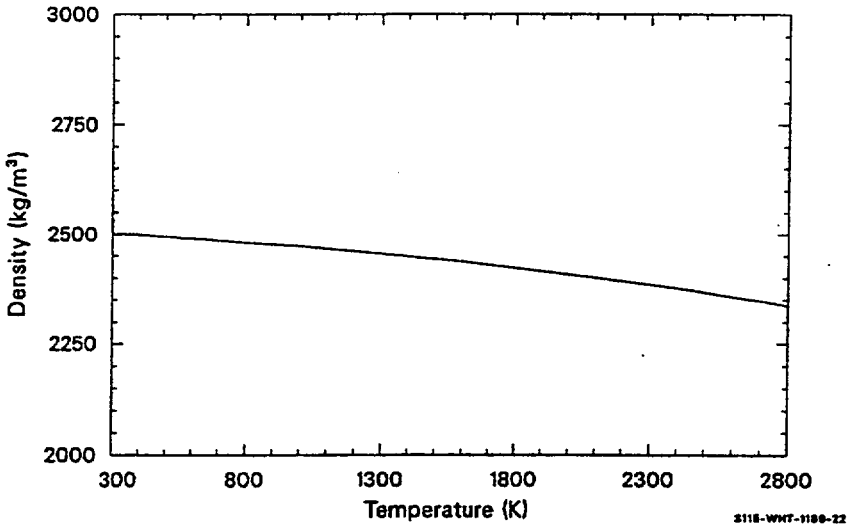

Figure 8-11. Density of boron carbide absorber.

8.4.4 References

8.4-1 I. Cohen, E. F. Losco and J. D. Eichenberg, "Metallurgical Design and Properties of Silver-Indium-Cadmium Alloys for PWR Control Rods," *Bettis Technical Review*, 1958.

8.4-2 C. J. Smithells and E. A. Brandes (eds.), *Metals Reference Book*, London and Boston: Butterworths, 1956.

8.4-3 A. Goldsmith, T. E. Waterman, and H. J. Hirschhorn, *Handbook of Thermophysical Properties of Solid Materials. Revised Edition Volume III: Ceramics*, New York: The MacMillan Company, 1961.

8.5 Surface Tension (ASTEN)

8.5.1 Model Development

The function ASTEN returns the interfacial surface tension of absorber material on stainless steel cladding. The value used for both the Ag-In-Cd and B_4C absorbers is

$$ST = 0.3 \tag{8-13}$$

where ST is the interfacial surface tension (N/m).

The number used is an engineering estimate based on the relative magnitudes of zirconium and silver liquid surface tensions given by Allen[8.5-1] and the interfacial surface tension for zircaloy and zirconium-uranium-oxygen compounds given in the ZUSTEN function of Section 11.6. The expected error of this number is + 2.0,-0.2.

8.5.2 Reference

8.5-1 B. C. Allen, "The Surface Tension of Liquid Transition Metals at Their Melting Points," *Transactions of the Metallurgical Society of AIM, 227*, 1963, pp. 1175-1183.

8.6 Viscosity (AVISC)

The function AVISC returns an estimate of the viscosity of Ag-In-Cd or B_4C neutron absorbers as a function of temperature.

8.6.1 Viscosity of Ag-In-Cd

For Ag-In-Cd, a viscosity of 10^{10} Pa• s is returned for temperatures below 1,050 K. When the temperature is above 1,100 K, a mole fraction weighted average of the alloy component viscosities is used.

$$\eta_l \left(f_{Ag}\,\eta_{Ag} + f_{In}\,\eta_{In} + f_{Cd}\,\eta_{Cd}\right) \tag{8-14}$$

where

η_l = viscosity of liquid absorber (Pa•s)

f_{Ag} = mole fraction of silver in the alloy, 0.808

η_{Ag} = viscosity of silver (Pa•s)

f_{In} = mole fraction of indium in the alloy, 0.143

η_{In} = viscosity of indium (Pa•s)

f_{cd} = mole fraction of cadmium in the alloy, 0.049

η_{Cd} = viscosity of cadmium (Pa• s).

The component viscosities are calculated with expressions obtained from procedures recommended by Nazare, Ondracek, and Schulz.[8.6-1]

$$\eta_{Ag} = 2.95\times10^{-4}\exp\left(\frac{3187}{T}\right) \tag{8-15}$$

$$\eta_{In} = 3.18\times10^{-4}\exp\left(\frac{768}{T}\right) \tag{8-16}$$

$$\eta_{Cd} = 3.91\times10^{-4}\exp\left(\frac{1119}{T}\right) \tag{8-17}$$

where T is the absorber temperature (K).

When the temperature is between 1,050 and 1,100 K, an interpolation scheme is used

$$\eta = \frac{\eta_l(T-1050) + 10^{10}(1100-T)}{50} \tag{8-18}$$

where η is the viscosity of the absorber in the two-phase temperature range, 1,050 to 1,100 K (Pa• s). Figure 8-12 is a plot showing the calculated liquid phase viscosity of Ag-In-Cd. The expected standard error is $\pm$ 0.8 of the predicted value because there are no data to support the model.

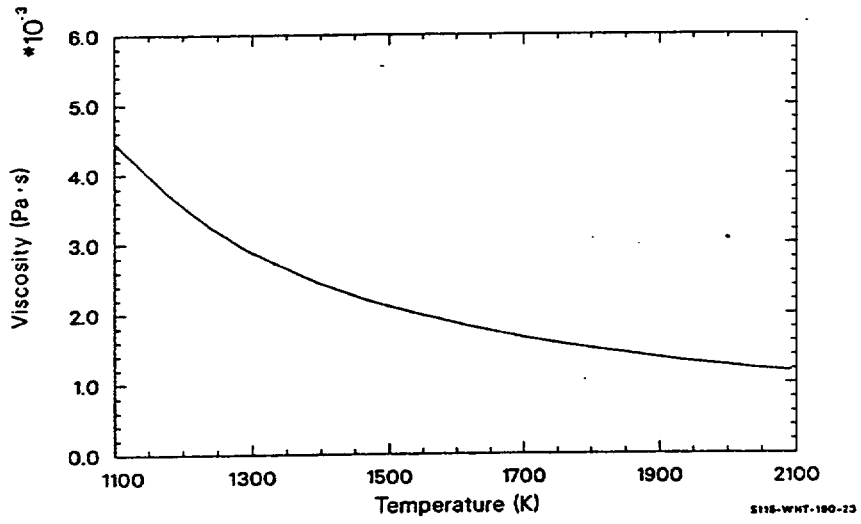

Figure 8-12. Viscosity of silver-indium-cadmium absorber.

8.6.2 Viscosity of Boron Carbide

For B_4C absorbers, a viscosity of 10^{10} Pa•s is returned for temperatures less than 2,700 K. When the temperature is at or above 2,700 K, the expression used is

$$\eta_{B_4C} = 1.21\times10^{-4}\exp\left(\frac{9158}{T}\right) \tag{8-19}$$

where ηB_4C is the viscosity of liquid B_4C absorber (Pa• s).

Figure 8-13 is a plot showing the calculated liquid phase viscosity of B_4C. The expected error of the B_4C viscosity models is $\pm$ 0.8 of the predicted value because there are no data in support of the model.

8.6.3 Reference

8.6-1 S. Nazare, G. Ondracek, and B. Schulz, "Properties of Light Water Reactor Core Melts," *Nuclear Technology, 32*, 1977, pp. 239-246.

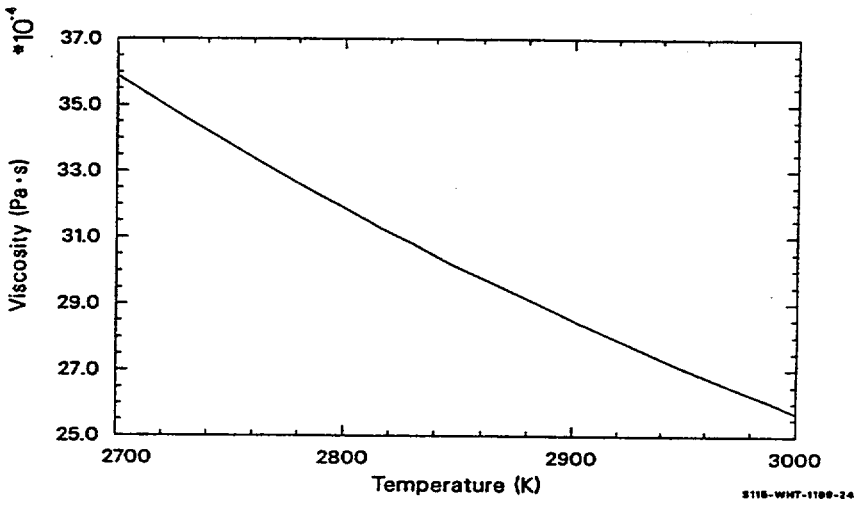

Figure 8-13. Viscosity of boron carbide absorber.

9. CADMIUM

9.1 Specific Heat (CDCP)

The specific heat is calculated by subroutine **CDCP** as a function of temperature. The temperature dependent specific heat[9.1-1] values are shown in Table 9-1. Linear interpolation is provided for temperature calls which fall between tabular values. Regardless of the input temperature, a specific heat value is always returned. Calls to **CDCP** that are outside the table range will be returned with either the first or last table value. **CDCP** also returns the flag **IERR** that is normally 0, but will be set to 1 if the input temperature lies outside the range 300 K to 4,000 K.

Table 9-1. Cadmium specific heat as a function of temperature.

Temperature (K)	Specific heat [J/(Kg•K)]
298.15	231.3
400.0	241.8
500.0	252.6
594.0	263.7
594.001[a]	264.4

a. liquid phase.

9.1.1 Reference

9.1-1 A. Cronenberg, *Handbook of Material Melt Properties for Savannah River Plant Accident Analysis Studies*, ESA-SCDAP-101, April 1989.

9.2 Thermal Conductivity (CDTCON)

Thermal conductivity is calculated by subroutine **CDTCON** as a function of temperature. The temperature dependent thermal conductivity[9.2-1] values are shown in Table 9-2. Linear interpolation is provided for temperature calls that fall between tabular values. Regardless of the input temperature, a thermal conductivity value is always returned. Calls to **CDTCON** that are outside the table range will be returned with either the first or last table value. **CDTCON** also returns the flag **IERR** that is normally 0, but will be set to 1 if the input temperature lies outside the range 300 K to 4,000 K.

Table 9-2. Cadmium thermal conductivity as a function of temperature.

Temperature (K)	Thermal conductivity [W/(m•K)]
273.15	97.5
293.15	97.0

Table 9-2. Cadmium thermal conductivity as a function of temperature. (Continued)

Temperature (K)	Thermal conductivity [W/(m•K)]
303.15	96.8
333.15	96.2
373.15	95.3
403.15	94.7
433.15	94.2
473.15	92.9
503.15	91.9
533.15	90.8
573.15	88.9
594.0	87.9
594.001[a]	41.6
600.0	42.0
700.0	49.0
800.0	55.9
1,040.0	72.5

a. liquid phase.

9.2.1 Reference

9.2-1 A. Cronenberg, *Handbook of Material Melt Properties for Savannah River Plant Accident Analysis Studies*, ESA-SCDAP-101, April 1989.

9.3 Density (CDDEN)

Density is calculated by subroutine **CDDEN** as a function of temperature. The temperature dependent density[9.3-1] values are shown in Table 9-3. Linear interpolation is provided for temperature calls which fall between tabular values. Regardless of the input temperature, a density value is always returned. Calls to **CDDEN** that are outside the table range will be returned with either the first or last table value. **CDDEN** also returns the flag **IERR** that is normally 0, but will be set to 1 if the input temperature lies outside the range 300 K to 4,000 K.

Table 9-3. Cadmium density as a function of temperature.

Temperature (K)	Density (kg/m^3)
273.15	8,670
303.15	8,640
333.15	8,610
363.15	8,580
403.15	8,541
433.15	8,511
473.15	8,470
503.15	8,439
533.15	8,406
573.15	8,360
594.00	8,336
594.01[a]	8,020
602.0	8,010
623.0	7,990
773.0	7,820
873.0	7,720

a. liquid phase.

9.3.1 Reference

9.3-1 A. Cronenberg, *Handbook of Material Melt Properties for Savannah River Plant Accident Analysis Studies*, ESA-SCDAP-101, April 1989.

9.4 Enthalpy (CDENTH)

The enthalpy of cadmium is calculated by subroutine CDENTH as a function of temperature. The temperature dependent enthalpy[9.4-1] values are shown in Table 9-4. CDENTH also returns the flag IERR that is normally 0 but will be set to 1 if the input temperature (T) lies outside the range 300 k to 4,000 K. Regardless of the input temperature, an enthalpy is always returned. If the temperature is outside the table range, either the first or last tabular value of enthalpy will be returned. Included in the input call to CDENTH is the call variable and TREF. TREF is the reference temperature at which the enthalpy is calculated. This is normally 298 K. Note that if $T \leq 298.0$ or if $T \leq$ TREF, then the returned enthalpy value is zero.

Table 9-4. Cadmium enthalpy as a function of temperature.

Temperature (K)	Enthalpy (J/kg)
298.0	0.0
400.0	24,050.0
500.0	48,770.0
594.0	72,960.0
594.001[a]	128,050.0
600.0	129,650.0
800.0	182,510.0
1,000.0	235,370.0

a. liquid phase.

9.4.1 Reference

9.4-1 A. Cronenberg, *Handbook of Material Melt Properties for Savannah River Plant Accident Analysis Studies*, ESA-SCDAP-101, April 1989.

10. GRID SPACER MATERIAL (INCONEL)

Material properties for Inconel, which include melting temperature, enthalpy, thermal conductivity and density, are available in the MATPRO library. This information is discussed below.

10.1 Melting Temperatures (HPROP)

The subroutine HPROP provides Inconel 718 melting temperatures. No input information is required.

For Inconel 718, page 267 of Reference 10.4-1 reports a melting range of 1,533 through 1,609 K. These numbers are used for the solidus and liquidus temperatures of Inconel grid spacers.

10.2 Enthalpy Correlations (USERP)

Enthalpy is calculated by subroutine USERP as a function of temperature. The temperature dependent enthalpy values are shown in Table 10-1.[10.4-1] Linear interpolation is provided for temperature calls which fall between tabular values. Calls to USERP that are outside the table range will be returned with either the first or last table value. The reference temperature for enthalpy is 0 K.

Table 10-1. Enthalpy of Inconel as a function of temperature.

Temperature (K)	Enthalpy (J/kg)
298	127,420
373	160,100
473	205,550
573	253,170
673	302,950
773	354,910
873	409,030
973	465,320
1,073	523,770
1,533	791,700
1,663	869,100
1,664	117,190
1,800	125,290
2,000	137,200
2,200	149,100

Table 10-1. Enthalpy of Inconel as a function of temperature. (Continued)

Temperature (K)	Enthalpy (J/kg)
2,400	161,010
2,600	172,920
6,000	375,360

10.3 Thermal Conductivity (USERP)

Thermal conductivity is calculated by subroutine USERP as a function of temperature. The temperature dependent thermal conductivity values are shown in Table 10-2.[10.4-2] Linear interpolation is provided for temperature calls which fall between tabular values. Calls to USERP that are outside the table range will be returned with either the first or last table value.

Table 10-2. Thermal conductivity of Inconel as a function of temperature.

Temperature (K)	Thermal conductivity [W/(m·K)]
298	11.45
373	12.68
473	14.27
573	15.85
673	17.44
773	19.03
873	20.62
973	22.21
1,073	23.80
6,000	23.80

10.4 Density (USERP)

Density is treated by subroutine USERP as a constant value. The constant density value returned by USERP is 8,000 kg/m^3.[10.4-2]

10.4.1 References

10.4-1 C. T. Lynch (ed.), *Handbook of Materials Science, Volume II: Metals, Composites, and Refractory Materials*, Cleveland, OH: CRC Press, Inc., 1975.

10.4-2 S. Touloukian et al., *Thermophysical Properties of Matter*, The TPRC Data Series, New York, Plenum Publishing Corp., February 1978.

11. ZIRCONIUM-URANIUM COMPOUNDS

Extension of the MATPRO materials properties package to high temperatures requires consideration of mixtures and compounds that are not formed until zircaloy cladding melts. One approach to providing the properties of molten mixtures of core material has been to define standard compounds of core materials--Corium A, Corium E, Corium AX1, Corium EX1, Corium EX2, Corium EX3, etc.[11.0-1] This approach has been avoided here because deciding when to switch from properties of one kind of melt to another would needlessly complicate serious efforts to model severe core damage. The six different types of corium listed above are replaced with a single class of material whose properties vary with zirconium, uranium, and oxygen concentration in the subroutines originally supplied with MATPRO and with zirconium, uranium, stainless steel, oxygen, Ag-In-Cd, and/or B_4C in newer versions of the subcodes described in this section.

In the older versions of the subcodes, concentrations of iron, chrome, nickel, silver, indium, cadmium, and other low melting components have been ignored because compounds rich in these components will probably migrate to cooler regions of the core before the melting temperature of zircaloy is attained. In the newer versions of the subcodes, only the concentrations of chrome, nickel, and a few other low melting components have been ignored. Since both versions are supplied, a discussion of each subcode version will be included in this section.

Data for all the properties modeled in this section are very scarce, so most of the subcodes use interpolations of materials properties that are available--the properties of UO_2, ZrO_2, and zircaloy in the original version and these core component elements plus FeO, Fe_2O_3, Fe_3O_4, silver, and B_4C in the newer version. These materials are used as a basis for interpolation rather than the properties of elemental uranium, zirconium, and oxygen because UO_2, ZrO_2 and zircaloy more closely approximate the compositions of interest.

For Zr-U-O compounds, a Gibbs triangle plot[11.0-2] of the compositions of Zr-U-O compounds (as shown in Figure 11-1) illustrates this point. It can be shown that the composition of a mixture of any two ternary Zr-U-O alloys will lie on a straight line joining the points representing the original compositions on a Gibbs plot. Severe core damage will melt zircaloy (represented here as mostly zirconium) that has been previously oxidized to some state between oxygen stabilized zircaloy, Zr(O), and ZrO_2. This melt will dissolve and mix with UO_2. The gross compositions of interest are thus most likely to lie in the shaded region of the plot. (Some uranium rich phases, which could melt and flow out of the hot region, are the only known exceptions to this general observation.)

When interpolated properties are used, the atomic fraction of each core material in the corium compound is input and is converted to a mole fraction using the following relation:

$$mfc_i = \frac{af_i}{\sum_{i=1}^{n} af_i} \qquad (11\text{-}1)$$

where

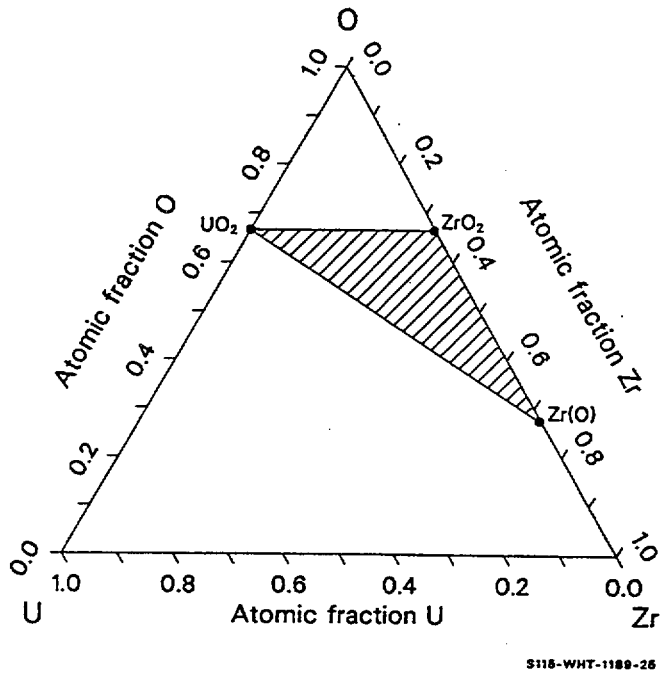

Figure 11-1. Compositions of Zr-U-O compounds on a Gibbs triangle plot.

mfc_i = mole fraction of the i-th core component in the compound

af_i = atomic fraction of the i-th core component in the compound

n = number of core components in the compound.

An inspection of Equation (11-1) reveals several limitations. First,

$$1 = \sum_{i=1}^{n} af_i \tag{11-2}$$

and thus all but one of the three atomic fractions must be input. Also, the atomic fraction of oxygen must lie in the range

$$af_u \le \frac{\sum_{i=1}^{n} af_i - \sum_{j=1}^{m} afo_j}{2} \le \sum_{j=1}^{m} afo_j \tag{11-3}$$

where

af_i = atomic fraction of the i-th component in the compound

afo_j = atomic fraction of the j-th component that reacts with oxygen in the compound

af_u = atomic fraction of uranium in the compound

n = number of core components in the compound

m = number of core components that react with oxygen in the compound.

If Equation (11-1) is to return physically meaningful positive fractions. The right-hand inequality means that the compound must not be oxidized beyond a metal dioxide, and the left-hand inequality requires that at least enough oxygen must be present to oxidize the uranium to UO_2. With uranium and zirconium as the only components in the core compound that react with oxygen, Figure 11-1 shows that the right-hand inequality requires the compound to lie below the line drawn between the points labeled UO_2 and ZrO_2. The left-hand inequality requires that the compound lie above a line from the point labeled UO_2 to the point labeled Zr. In this case, all of the shaded triangle lies within this region; so all compounds formed out of UO_2 and zircaloy oxidized as far as ZrO_2 will be in the acceptable range.

All subcodes which use Equation (11-1) check for acceptable ranges of oxygen concentration and raise or lower the presumed oxygen content to force it to fall within the range given by Equation (11-3). An error message is printed when the range is exceeded.

In the older, more limited versions of the MATPRO core materials properties subroutines, for input values of af_u and af_{Zr} that imply that $(1 - af_u - af_{Zr})/2$ is greater than $af_u + af_{Zr}$, the input values of af_u and af_{Zr} are replaced by

$$af_{u1} = \frac{af_u}{3(af_u + af_{Zr})} \tag{11-4}$$

$$af_{Zr1} = \frac{af_{Zr}}{3(af_u + af_{Zr})} \tag{11-5}$$

where

af_u = atomic fraction of uranium in the compound

af_{Zr} = atomic fraction zirconium in the compound

af_{u1} = revised atomic fraction of uranium in the compound

af_{Zr1} = revised atomic fraction of zirconium in the compound.

Inspection of Equations (11-2), (11-4), and (11-5) shows that the transformation preserves the uranium-to-zircaloy ratio but decreases $(1 - af_{u1} - af_{Zr1})/2$ to $af_{u1} + af_{Zr1}$.

For input values of af_u and af_{Zr} that imply that $(1 - af_u - af_{Zr})/2$ is less than af_u, input values of af_u and af_{Zr} are replaced by

$$af_{u1} = \frac{af_u}{3(af_u + af_{Zr})} \tag{11-6}$$

$$af_{Zr1} = \frac{af_{Zr}}{3(af_u + af_{Zr})} \ . \tag{11-7}$$

Inspection of Equations (11-2), (11-6), and (11-7) shows that this transformation preserves the uranium-to-zircaloy ratio but increases $(1 - af_{u1} - af_{Zr1})/2$ to af_{u1}.

The above described transformations are not used in the later version of the core materials properties subroutines. However, since the older versions of these subroutines are contained in the MATPRO package along with the newer versions, where applicable, descriptions of both routines are included in this document.

11.0.1 References

11.0-1. S. Nazare, G. Ondracek, and B. Schulz, "Properties of Light Water Reactor Core Melts," *Nuclear Technology, 32*, 1977, pp. 239-246.

11.0-2. F. Rhines, *Phase Diagrams in Metallurgy and Their Development and Application*, New York: McGraw-Hill Book Company, 1956, pp. 110-113.

11.1 Zirconium Uranium Oxygen Compound Melting, Solution, and Precipitation (PSOL, PLIQ, ZUSOLV, COEF)

11.1.1 Introduction

Mechanistic modeling of severe core damage processes in LWRs requires models to describe the melting of core materials and the solution of UO_2 fuel by liquid zircaloy. In particular, the temperature at which a liquid phase first appears during the heating of a Zr-U-O compound, the solidus temperature, is required to model the structural failure of reactor core material. The temperature at which the last solid phase disappears during heating, the liquidus temperature, is required to determine the amount of solid core material that can be dissolved by molten zircaloy.

Three subcodes were developed to model the melting and solution properties of Zr-U-O compounds. The solidus temperature as a function of the atomic fraction zircaloy and the atomic fraction oxygen is modeled in the PSOL subcode. The PLIQ subcode returns the liquidus temperature using the same fractions required by PSOL.

The ZUSOLV subcode models solution behavior. Given the temperature, solvent composition, and solute composition, it determines whether the solvent, usually zircaloy with some oxygen, is supersaturated. If the solvent is supersaturated, the fraction that will freeze and the equilibrium composition of the solid and liquid phases is calculated. If the solvent is not supersaturated at the given temperature, the saturation composition of the liquid phase and the atomic fraction of the solute, usually uranium dioxide, is calculated.

The subcode COEF in SCDAP calculates the coefficients a and b of the equation ax + b, the equation of a line, and the intersection coordinates of two lines. The coordinates of two points on a line are input into the subcode if the equation of the line is to be calculated, and the constant and dependent variable for each line is input if the intersection of two lines is to be calculated. This subcode is used exclusively with ZUSOLV to calculate positions on isopleths in determining the composition of Zr-U-O mixtures.

The three subcodes, PSOL, PLIQ, and ZUSOLV are based on analytical expressions for the liquidus and solidus phase boundary compositions in the ternary Zr-U-O system. These expressions, which are given in the model development section, were produced by interpolating the liquidus and solidus compositions determined as a function of temperature for the several available binary systems or isopleths for which liquidus and/or solidus temperatures as a function of composition are known. The analytical expressions are used with standard metallurgical techniques, the lever rule and the mixing rule, to calculate the solution parameters given by ZUSOLV. PSOL and PLIQ employ a matrix that provides an approximate inversion of the analytical expressions for composition as a function of temperature. The matrix uses a grid of 100 positions to represent the range of possible compositions and assigns a fixed temperature to each grid position.

11.1.2 Data for the Zr-U-O System

The equations for the solidus and liquidus surfaces were obtained from numerous temperature composition phase diagrams, which are available in the literature. In this section, all of these diagrams have been redrawn to a common scale and units of atomic fraction so that they might be easily compared and checked for consistency.

11.1.2.1 Binary Systems. Solidus and liquidus temperatures of zirconium-oxygen mixtures have been published by Domagala and McPherson[11.1-1] and modified by Ruh and Garrett.[11.1-2] Figure 11-2 shows a phase diagram drawn from these references. The diagram of Domagala and McPherson was converted from weight fraction to atomic fraction using the expression

$$f_0 = \frac{f_0^{mass}/16}{f_0^{mass}/16 + (1 - f_0^{mass})/91.22} \qquad (11\text{-}8)$$

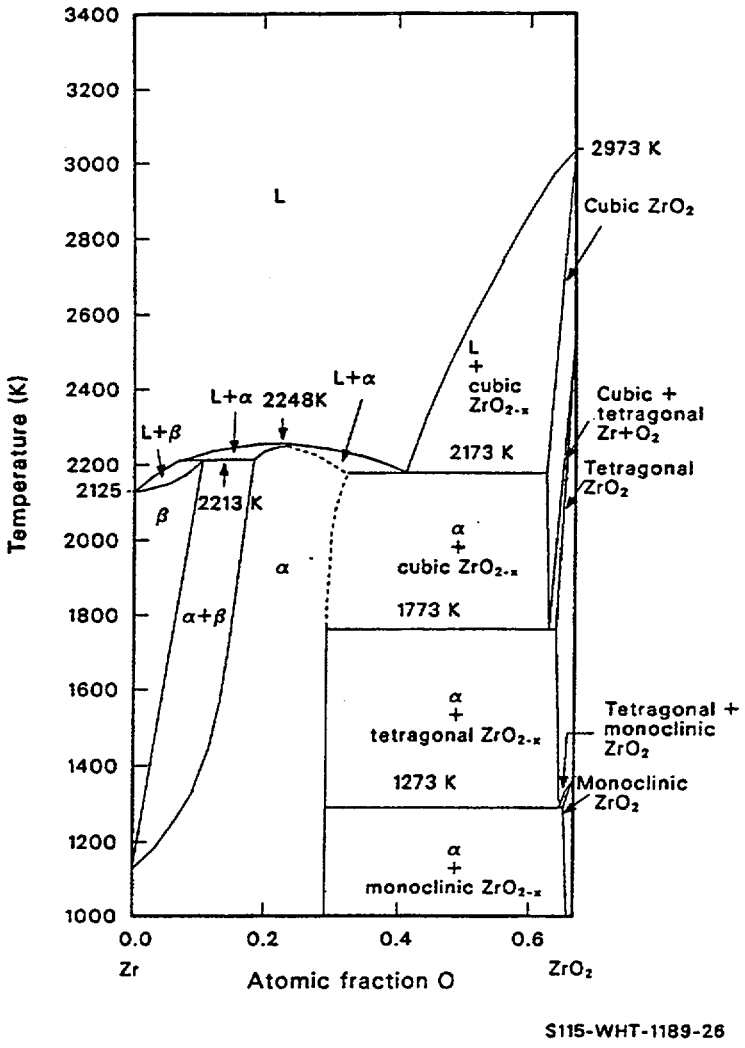

Figure 11-2. Zirconium-zirconium dioxide phase diagram.

where

f_o = atomic fraction of oxygen in a Zr-O compound

f_0^{mass} = mass fraction of oxygen in a Zr-O compound.

The solidus curve is made up of several segments, one above the beta phase, one above the alpha phase, and one above the cubic ZrO_2 phase. The liquidus is composed of the two segments under the liquid region.

Figure 11-3 is a temperature composition plot for the U-O binary system, taken from Roth et al.[11.1-3] Their diagram was converted to atomic fraction oxygen using the relation

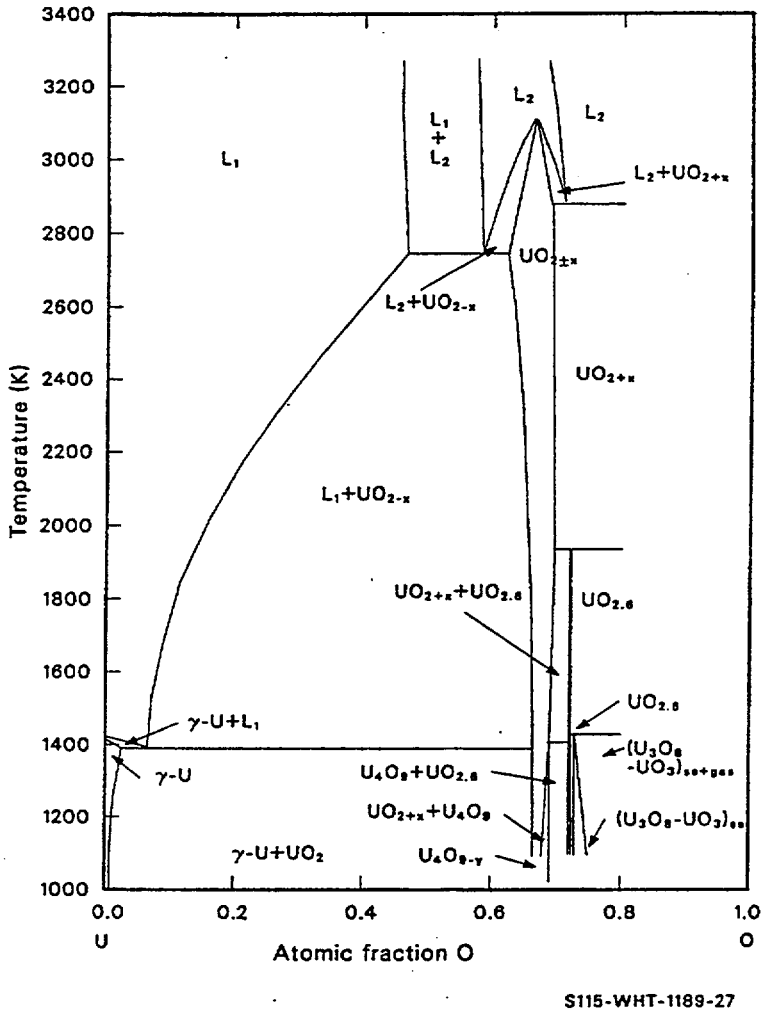

Figure 11-3. Uranium oxygen phase diagram.

$$f_0 = \frac{R}{1+R} \tag{11-9}$$

where R is the oxygen-to-metal ratio (atoms oxygen/atoms uranium).

The figure shows four solidus segments enclosing the UO_2 region, two liquidus segments under the L_1 phase, and another two liquidus segments under the L_2 phase. Latta and Fryxell[11.1-4] have published detailed solidus and liquidus temperature data for the curves above 2,700 K in Figure 11-3. Their data are shown in Figure 11-4 and reproduced in Table 11-1.

Table 11-1. Solidus and liquidus temperatures of UO_{2+x} from Latta and Fryxell.

Sample no.	Pretest O/U	Post-Test O/U	Solidus (K)	Liquidus (K)
221	2.23	-	2,837	3,031
217	2.23	-	2,851	3,013
188	2.184	2.169	2,878	3,045
201	2.13	2.109	2,940	3,078
192	2.12	2.103	2,907	3,071
303	2.095	2.092	3,003	3,088
208	2.095	2.050	3,001	3,090
172	2.058	2.058	3,067	3,109
204	-	2.022	3,085	3,136
193	2.019	2.009	3,109	3,125
212	1.998	1.998	3,118	3,138
190	1.997	2.008	3,118	2,138
194	1.997	2.000	3,120	3,135
209	1.993	1.995	3,107	3,133
189	1.980	1.990	3,105	3,133
146	1.980	1.985	3,106	3,133
153	1.956	1.955	3,076	3,130
138	1.943	1.943	3,069	3,118
184	1.920	1.930	3,043	3,113
150	1.890	1.929	3,002	3,105
154	1.856	1.861	2,970	3,083
177	1.809	1.795	2,888	3,033
156	1.803	1.849	2,893	3,033
159	1.793	1.809	2,874	3,031
129	1.75	1.803	2,818	2,983
104	1.790	1.759	2,863	3,013
164	1.736	1.736	2,786	2,968

Table 11-1. Solidus and liquidus temperatures of UO_{2+x} from Latta and Fryxell. (Continued)

Sample no.	Pretest O/U	Post-Test O/U	Solidus (K)	Liquidus (K)
166	1.662	1.689	2,686	2,923
222	1.60	-	2,696	2,857
168	1.556	-	2,708	2,783
207	1.50	1.593	2,701	2,771

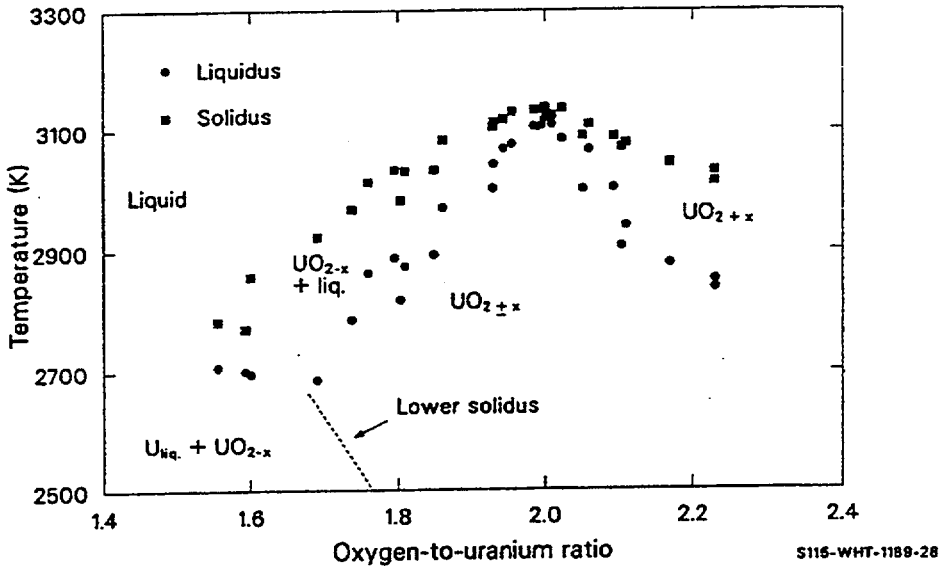

Figure 11-4. Solidus and liquidus temperatures of uranium oxides according to Latta and Fryxell.

Figure 11-5 shows an isopleth extending from $Zr_{0.7}O_{0.3}$ (approximately the composition of alpha phase zirconium saturated with oxygen) to $U_{0.33}O_{0.67}$ (the composition of uranium dioxide written in atomic fraction units). The isopleth was presented as a quasi-binary section by Skokan.[11.1-5] This presentation is in conflict with the phase diagram reproduced as Figure 11-2, which shows noncongruent melting of the alpha phase (the liquid-plus-alpha region between the alpha phase and liquid regions near 0.3 atomic fraction oxygen in Figure 11-2).

The UO_2-ZrO_2 quasi-binary system according to Romberger et al.[11.1-6] is shown in Figure 11-6. The liquidus and solidus exhibit a minimum at a 0.5-0.5 mix of the two components, and the liquidus dips sharply to touch the solidus at this minimum. Recent data presented by Hofmann[11.1-7] suggest that the $U_{0.33}O_{0.67}$ rich solidus does not rise as fast as shown in Figure 11-6. Hofmann finds a solidus temperature in the range 2,793 to 2,893 K for 0.1 mole fraction ZrO_2 (0.1 atomic fraction $Zr_{0.33}O_{0.67}$) and in the range 2,796 to 2,842 K for 0.25 mole fraction ZrO_2.

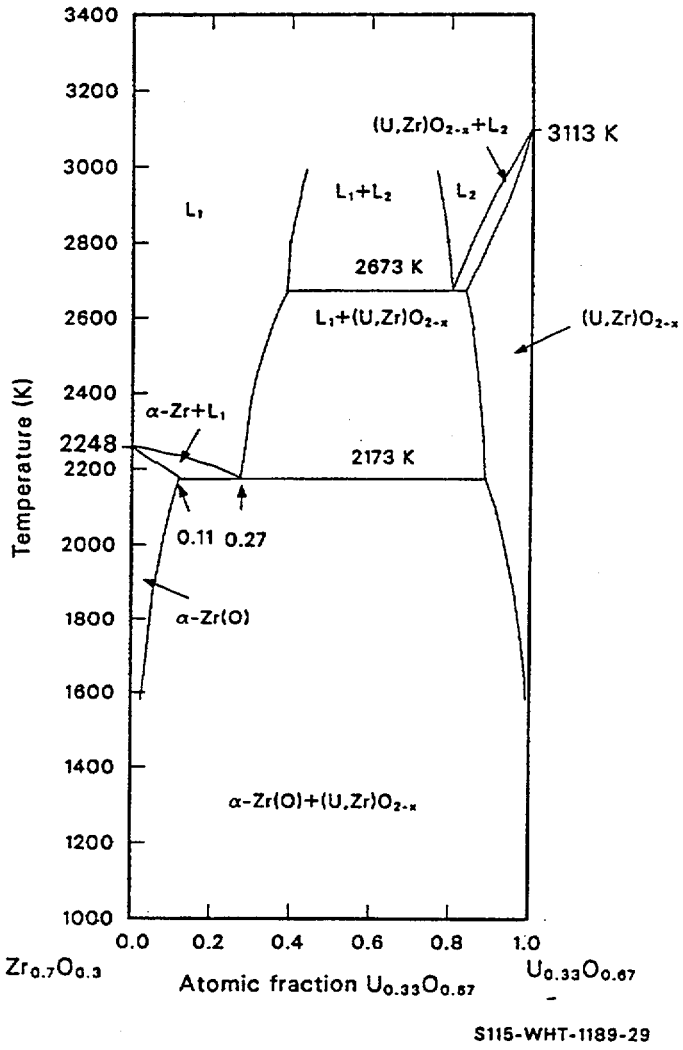

Figure 11-5. Oxygen saturated, alpha phase zirconium uranium dioxide isopleth.

Figure 11-7 is a reproduction of the liquidus and solidus curves of the U-Zr binary system.[a] The components are mutually soluble for temperatures above 1,136 K, so the solidus and liquidus form the classic lens shaped, two-phase region for such systems.

11.1.2.2 Ternary System Data. The only Zr-U-O system data in the temperature range from 1,400 to 3,100 K are the temperature composition plots published by Hofmann and Politis[11.1-8] and extended by Skokan.[11.1-5] Ternary temperature composition plot sections from these authors are reproduced as Figure 11-8 through Figure 11-14. The figures are all plotted on a Gibbs coordinate system, which is an equilateral triangle with each vertex representing one of the three components. The fraction of each component is proportional to the distance from the side opposite the component's vertex. The system

a. P. Hoffman, private communication, EG&G Idaho, Inc., 1985.

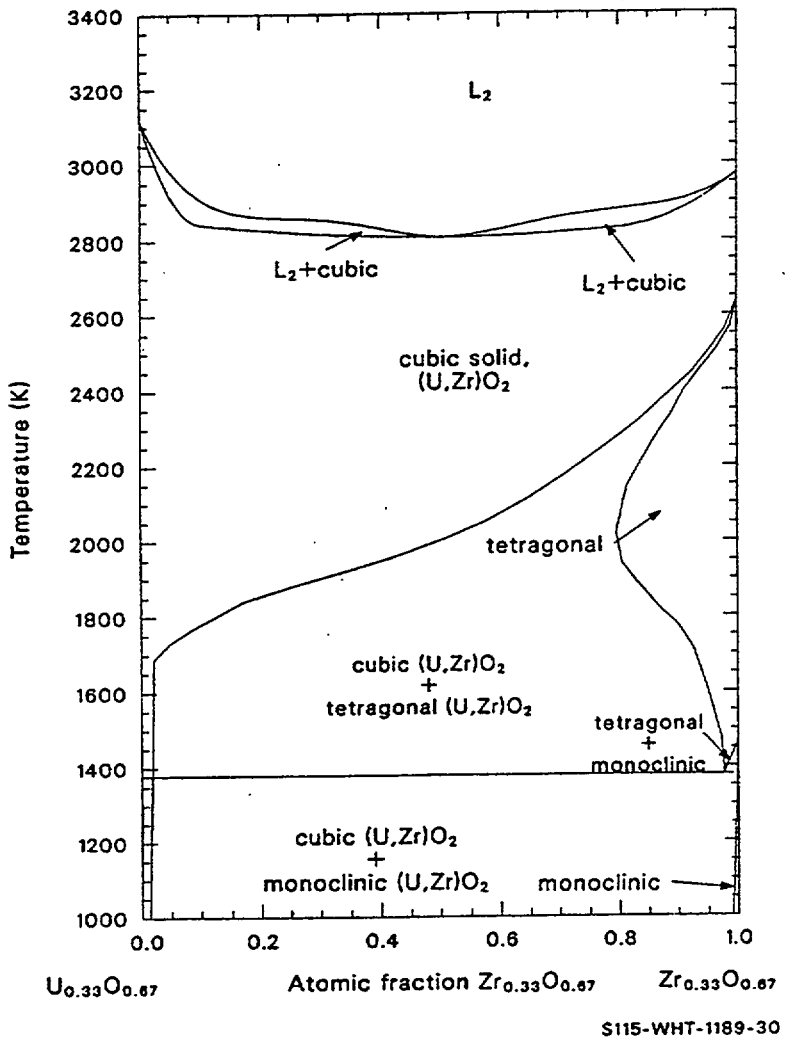

Figure 11-6. Uranium dioxide zirconium dioxide quasi-binary phase diagram.

is used because it ensures that the sum of the fraction of each component is one for any gross composition plotted.

Figure 11-8, the phase diagram at 1,273 K,[11.1-8] shows no liquid phase and very limited single-phase regions along the U-O, Zr-O, and U-Zr sides. A large, three-phase region connecting α-Zr(O), (γ-U, β-Zr) with about 0.8 U, and UO_2 dominates the diagram.

The 1,773 K system[11.1-8] (Figure 11-9) shows a liquid phase in the lower left-hand side of the diagram, the U-rich and O-poor region. The phase is in equilibrium with UO_2 via tie lines in the UO_2 + L region, with α-Zr(O) via tie lines in the narrow L + α - Zr(O) region, and with UO_2 and α-Zr(O) via the large, three-phase triangle that dominates the center of the phase diagram. The locations of the tie lines are not known, so the tie lines are not shown. Although most authors show the top of the UO_2 + L region as a point, it is drawn in Figure 11-9 as a short segment because the several liquid compositions at the bottom of the UO_2+ L region must connect to more than one composition at the edge of the one phase region near the UO_2 composition. The presence of the large, three phase region in the center, UO_2 + L + α - Zr(O),

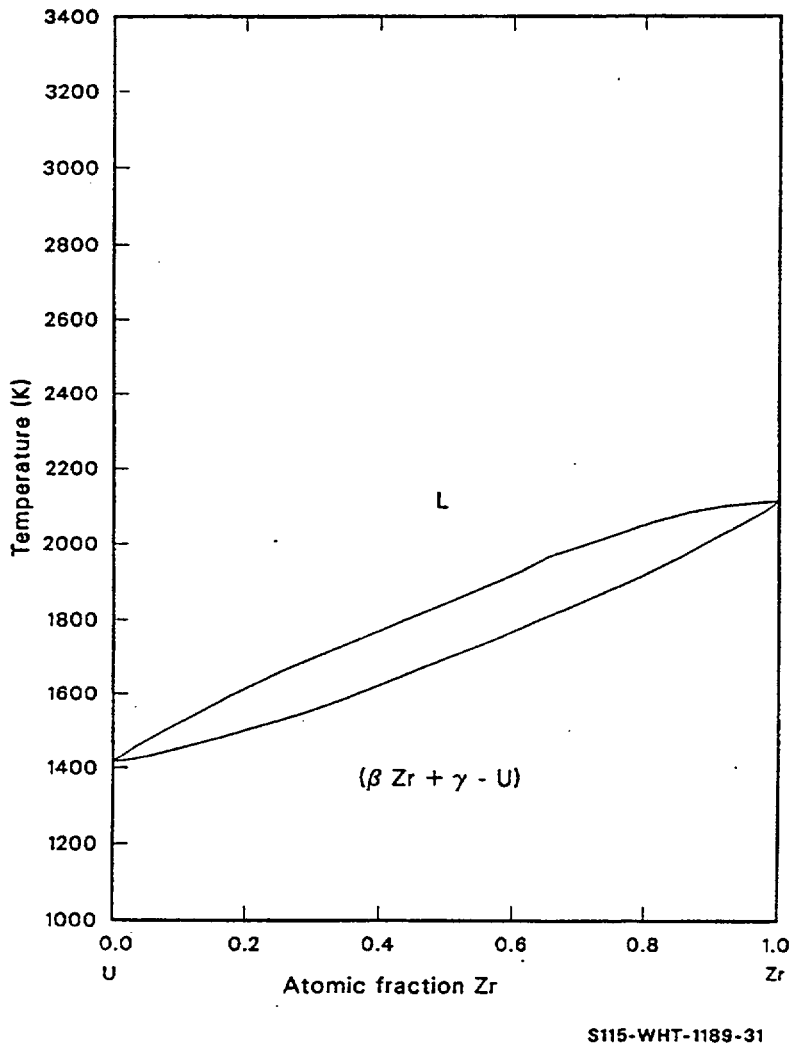

Figure 11-7. Uranium zirconium system liquidus and solidus.

suggests that compositions enclosed in the triangle will experience some melting when the liquid phase passes the lowest vertex of the three-phase triangle, i.e., near 1,600 K.

Figure 11-10 shows the phase diagram at 1,873 K.[11.1-5] The right-hand vertex of the L region has moved toward the Zr vertex of the Gibbs coordinates, in excellent agreement with the liquidus temperature shown in Figure 11-7. The right vertex of the (γ-U, β-Zr) phase is in excellent agreement with the U-Zr binary system solidus, too. A similar agreement is evident between the right-hand side of Figure 11-10 and the Zr-ZrO_2 binary system shown in Figure 11-2. However, the left-hand side of Figure 11-10 disagrees with the liquidus shown for the U-O binary in Figure 11-3. According to Figure 11-3, the liquidus should be above 0.1 atomic fraction O at 1,773 K. It is shown at about 0.02 fraction O in Figure 11-10. The two phase α - Zr(O) + L region was added to Skokan's figure to avoid showing a common boundary between three phase regions.[11.1-8]

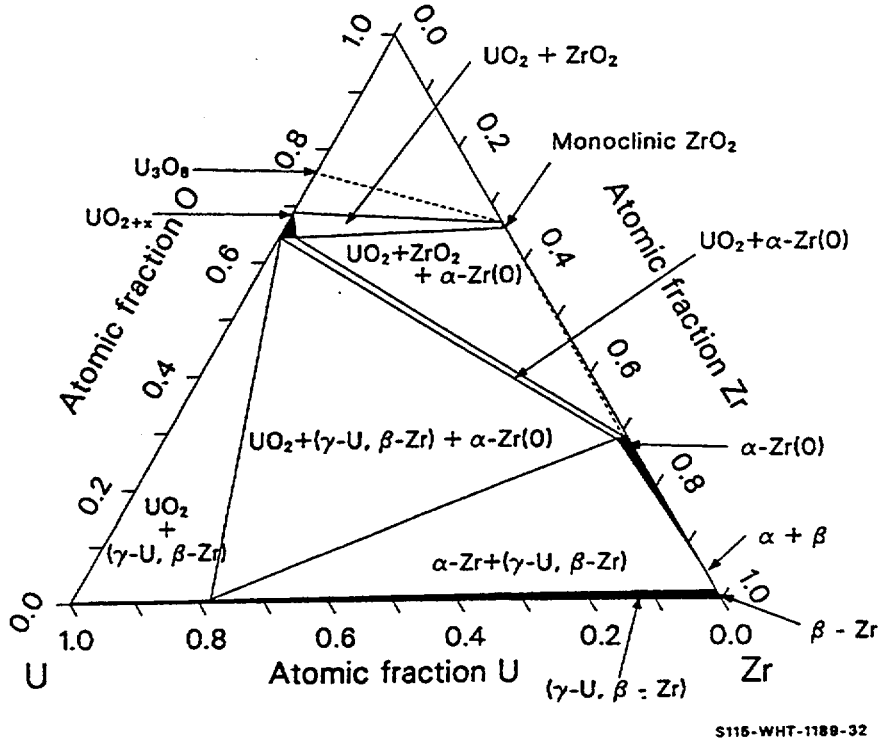

Figure 11-8. Phases of the Zr-U-O system at 1,273 K.

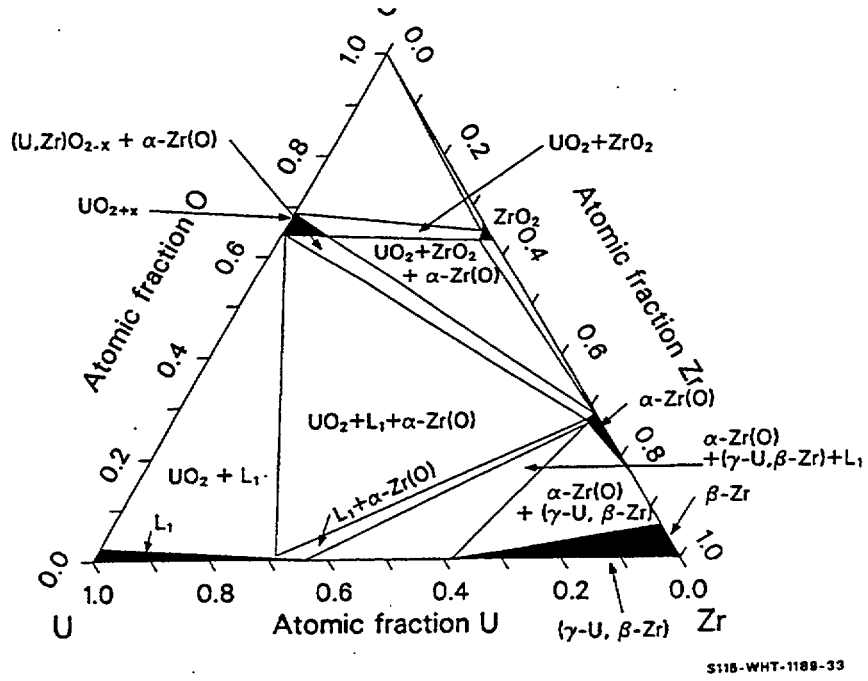

Figure 11-9. Phases of the Zr-U-O system at 1,773 K.

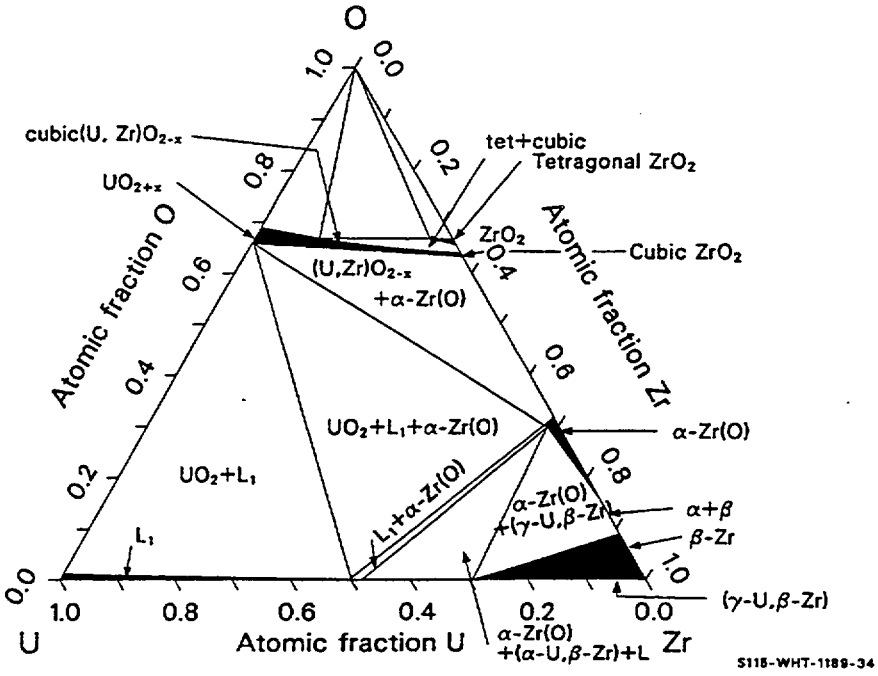

Figure 11-10. Phases of the Zr-U-O system at 1,873 K.

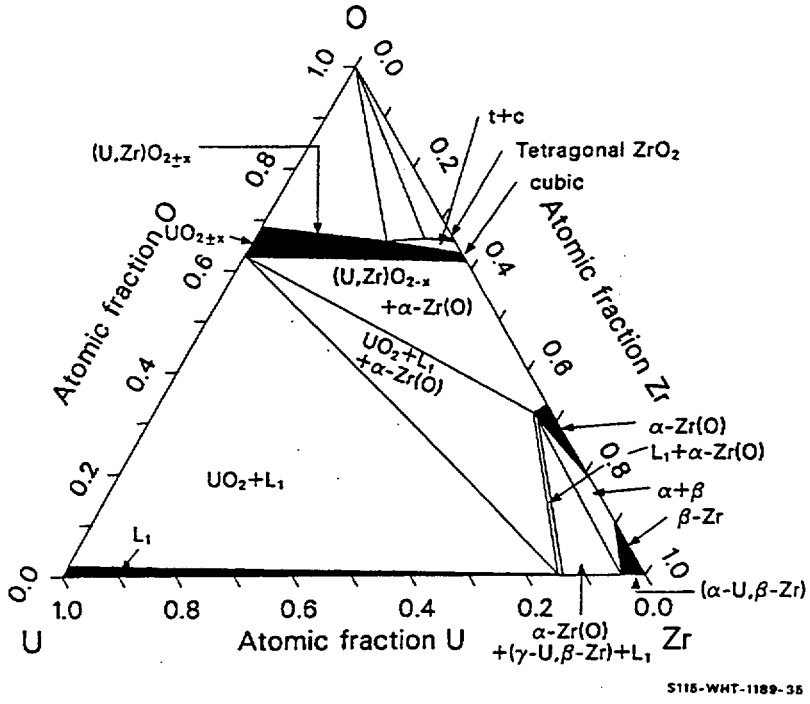

Figure 11-11. Phases of the Zr-U-O system at 2,073 K.

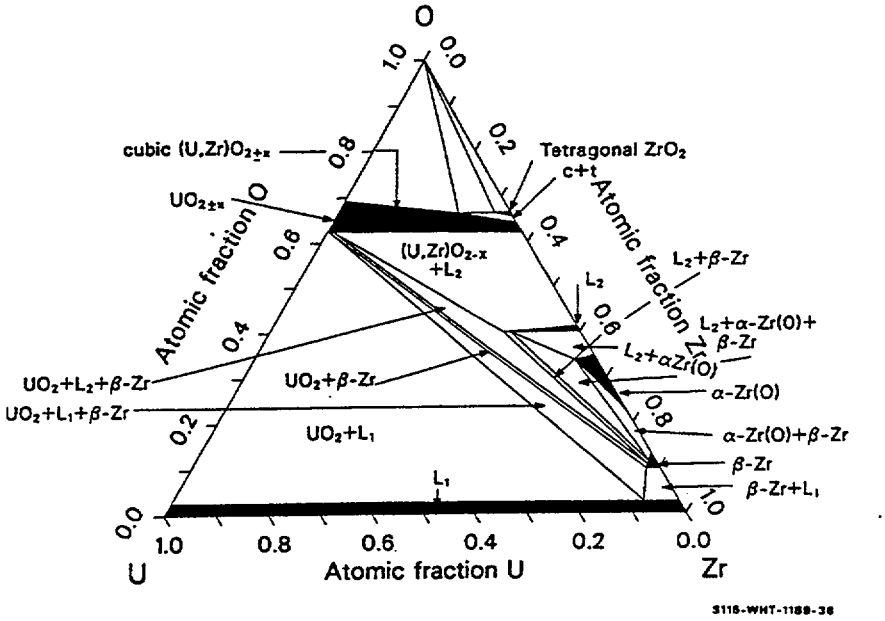

Figure 11-12. Phases of the Zr-U-O system at 2,178 K.

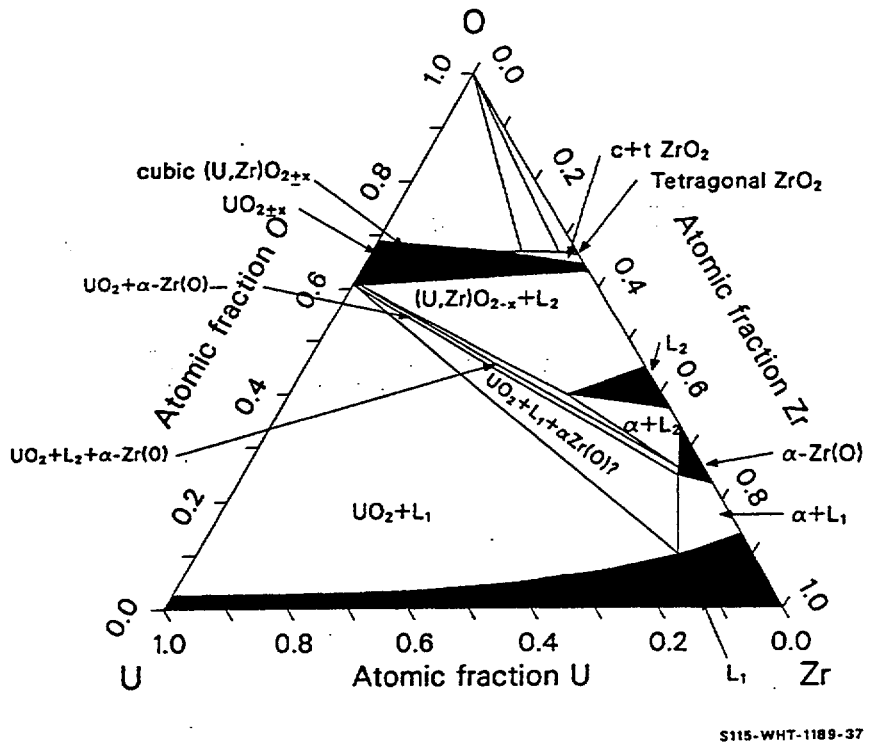

Figure 11-13. Phases of the Zr-U-O system at 2,223 K.

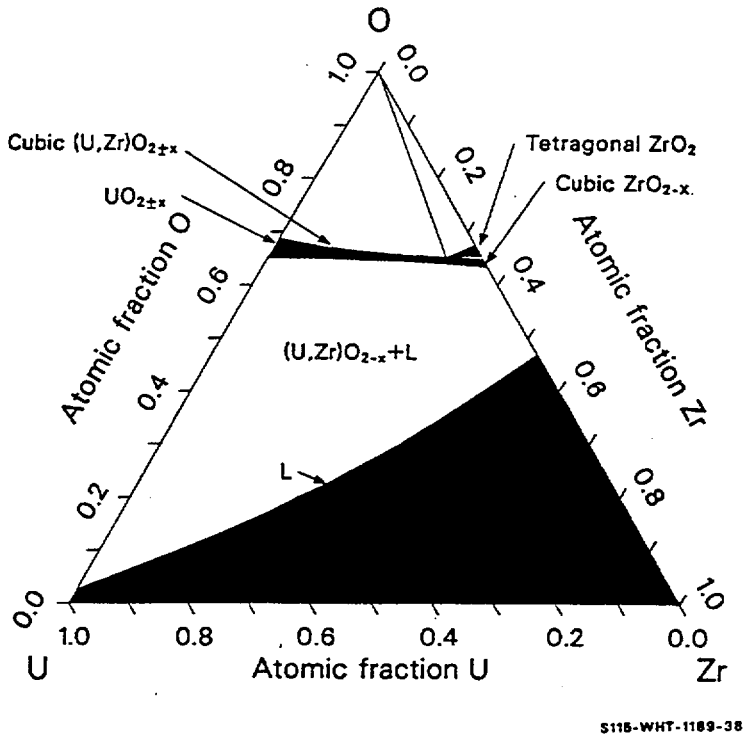

Figure 11-14. Phases of the Zr-U-O system at 2,273 K

Figure 11-11, the phase diagram at 2,073 K,[11.1-5] shows behavior similar to Figure 11-10. The U-Zr and Zr-ZrO_2 binaries are in excellent agreement with the figure, but the U-O binary would place the top left vertex of the L region considerably higher than it is shown on the ternary diagram. One should note that Figure 11-11 is an important addition to the binary systems data because it provides points like the left hand extreme of the α-Zr(O) region that are not available on any binary isopleth. The two phase α-Zr(0)+L region was added to Skokan's figure for 2,073 K for the same reason the region was added to Figure 11-10.[11.1-8]

Figure 11-11, Figure 11-12, and Figure 11-13[11.1-5] show the complex behavior caused by the appearance of the oxygen rich liquid phase, L_1', that corresponds to the liquidus minimum at about 0.4 atomic fraction oxygen in Figure 11-12. The tentative diagrams presented by Skokan for 2,178 and 2,223 K were modified to include narrow two-phase regions between the $UO_2 + L_1' + \beta$-Zr and $UO_2 + L_1 + \beta$-Zr three-phase regions proposed by Skokan.

Figure 11-14, the relatively simple phase diagram at 2,273 K,[11.1-9] shows that the L_1' phase region no longer exists as a separate liquid when temperature increases 50 K above the temperature of Figure 11-13. The fairly simple system shown in Figure 11-14 is probably characteristic of the Zr-U-O system until temperatures near 2,673 K, when another oxygen rich phase, L_2 in Figure 11-13, Figure 11-15, and Figure 11-16, appears.

Unfortunately, no ternary system phase diagrams have been published for temperatures above 2,273 K. Data for these temperatures must be interpolated from binary phase diagrams.

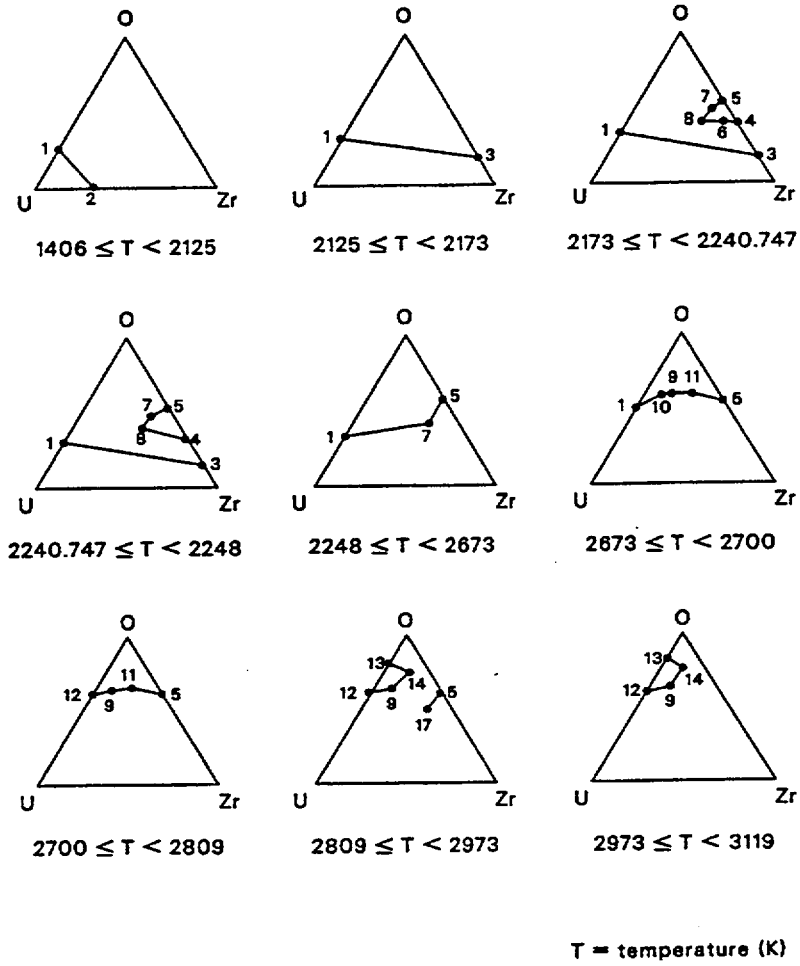

Figure 11-15. Points that are connected to form the ternary Zr-O-U system liquidus lines.

11.1.3 Model Development

The expressions used in the PSOL, PLIQ, and ZUSOLV codes were developed by constructing polynomial expressions for the solidus and liquidus temperatures as a function of composition of the various binary systems, inverting these expressions to produce correlations for composition as a function of temperature, and connecting the resulting liquidus and solidus compositions with straight-line segments on the ternary phase diagram. Where additional correlations could be obtained from the ternary systems published, they were also employed.

Figure 11-15 shows the points that are connected to form the ternary liquidus, and Table 11-2 provides the analytical expressions for the compositions represented by the points. Figure 11-16 shows the points that are connected to form the ternary solidus, and Table 11-3 provides the analytical expressions for the compositions represented by the points. Dashed lines in Figure 11-16 represent tie lines across multiple-phase regions and are therefore not a section through a solidus surface in the three-dimensional, temperature composition phase diagram.

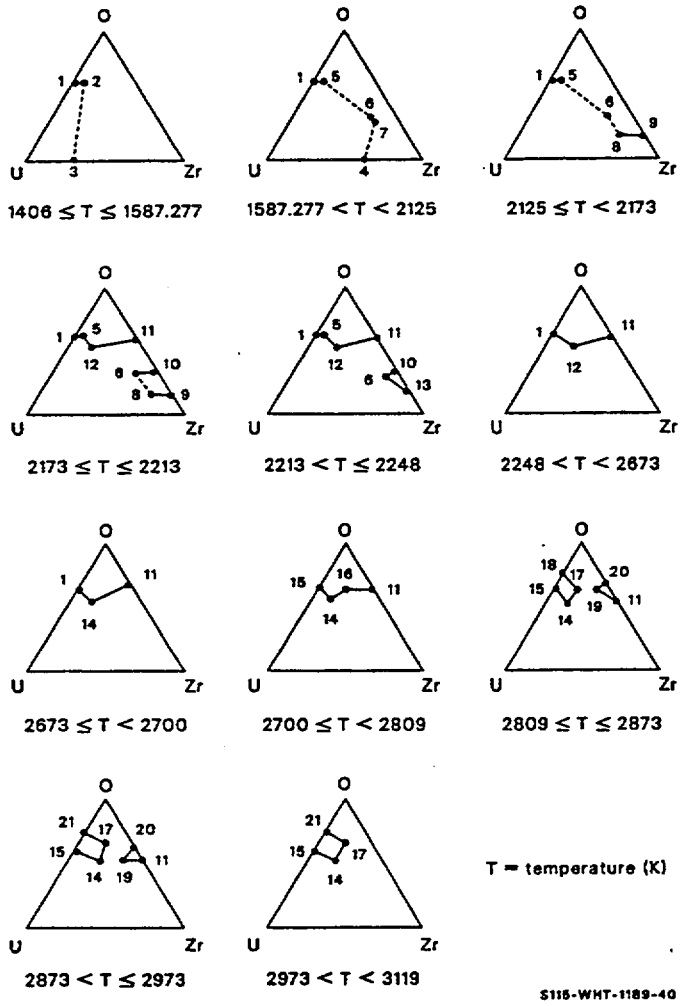

Figure 11-16. Points that are connected to form the ternary Zr-O-U system solidus lines.

Table 11-2. Correlations for liquidus compositions.

1. L_1 boundary U-O binary system	$f_0 = \frac{2940.587 - \sqrt{2940.587^2 + 4833.744(1026.259 - T)}}{4833.744}$
2. L_1 boundary U-Zr binary system	$f_{Zr} = \frac{478.5 - \sqrt{478.5^2 + 238(1406 - T)}}{238}$
3. Zr-rich L_1 boundary, Zr-ZrO_2 binary system for $2{,}125 \le T \le 2{,}213$ K	$f_0 = \frac{1114.952 - \sqrt{1114.952^2 + 13704.72(2125 - T)}}{13704.72}$
For $2{,}213 < T \le 2{,}248$ K	$f_o = \frac{263.9718 - \sqrt{263.9718^2 + 1060.128(2182.271 - T)}}{1060.128}$

Table 11-2. Correlations for liquidus compositions. (Continued)

4. Zr-rich L_1' boundary, Zr-ZrO_2 binary system	$f_O = \frac{694.3412 - \sqrt{694.3412^2 + 2788.519(2075.109 - T)}}{2788.519}$
5. O-rich L_1 and L_1' boundary, Zr-ZrO_2 binary system	$f_O = \frac{1785.754 - \sqrt{1785.754^2 + 390.6488(764.6003 - T)}}{390.6488}$
6. Zr-rich L_1 boundary $Zr_{0.7}O_{0.3}$-$U_{0.33}O_{0.67}$ isopleth	$f_{U_{0.33}O_{067}} = \frac{-13.40961 + \sqrt{13.40961^2 + 829.9846(2240.747 - T)}}{829.9846}$
7. O-rich L_1 boundary $Zr_{0.7}O_{0.3}$-$U_{0.33}O_{0.67}$ isopleth	$f_{U_{0.33}O_{067}} = \frac{11234.85 - \sqrt{11234.85^2 - 27575.76(1883.545 + T)}}{27575.76}$
8. Forced to lie on the line from solidus point 11 to solidus point 5	interpolation
9. O-rich L_2 boundary $Zr_{0.7}O_{0.3}$-$U_{0.33}O_{0.67}$ isopleth	$f_{U_{0.33}O_{067}} = \frac{4930 - \sqrt{4930^2 - 6000(311 + T)}}{3000}$
10. Linear interpolation between point 9's location at the given temperature and point 12 at 2,700 K	location of 10 = [location of 12 at 2,700 K (T-2,673) + location of 9 at T (2,700-T)] /27
11. Linear interpolation between point 9's location at the given temperature and point 14 at 2,809 K	location of 11 = [location of 14 at 2,809 K (T-2,673) + location of 9 at T (2,809-T)] /136
12. O-rich substoichiometric boundary of L_2 U-O binary system	$f_O = \frac{2 - \frac{\sqrt{3119 - T}}{1610}}{3 - \frac{\sqrt{3119 - T}}{1610}}$
13. U-rich hyperstoichiometric boundary of L_2, U-O binary system	$f_O = \frac{2 + \frac{\sqrt{3119 - T}}{1610}}{3 + \frac{\sqrt{3119 - T}}{1610}}$
14. $U_{0.33}O_{0.67}$-rich L boundary, $U_{0.33}O_{0.67}$-O system for $3{,}119 \geq T \geq 2{,}989$	$f_{Zr_{0.33}O_{0.67}} = \frac{3119 - T}{433.3333}$

Table 11-2. Correlations for liquidus compositions. (Continued)

for $2{,}989 \geq T \geq 2{,}832$	$f_{Zr_{0.33}O_{0.67}} = \dfrac{443.0286 + \sqrt{443.0286^2 + 2194.367(2920.676 - T)}}{2194.367}$
for $2{,}832 \geq T \geq 2{,}809$	$f_{Zr_{0.33}O_{0.67}} = 0.5 - \sqrt{0.25 - \dfrac{35809.46 - T}{132001.8}}$
15. $Zr_{0.33}O_{0.67}$-rich L_2 boundary $U_{0.33}O_{0.67}$-$Zr_{0.33}O_{0.67}$ binary system for $2{,}809 < T \leq 2{,}821$	$f_{Zr_{0.33}O_{0.67}} = 0.5 + \sqrt{0.25 - \dfrac{5794.401 - T}{11941.6}}$
for $2{,}821 < T \leq 2{,}851.341$	$f_{Zr_{0.33}O_{0.67}} = \dfrac{4162.934 - \sqrt{4162.934^2 + 6838.223(327.3354 - T)}}{6838.223}$
for $2{,}851.341 < T \leq 2{,}862$	$f_{Zr_{0.33}O_{0.67}} = \dfrac{T - 2817.588}{59.2158}$
for $2{,}862 < T \leq 2{,}973$	$f_{Zr_{0.33}O_{0.67}} = \dfrac{793 + \sqrt{793^2 - 1160(3399 - T)}}{1160}$
16.	Point 15 with y coordinate increased 0.01
17. Intersection of lines from 0.7 Zr, 0.3 O to point 15 and point 5 to the $L_1/L_1 + L_2$ boundary location is given by	$f_{U_{0.33}O_{0.67}} = \dfrac{41641.97 - \sqrt{41641.97^2 - 94995.94(15257.48 - T)}}{94995.94}$

Table 11-3. Correlations for solidus compositions.

1. U-rich solid UO_{2-x} boundary for $T < 2{,}700$ K, U-O binary system	$f_o = \dfrac{473984.9 + \sqrt{473984.9^2 - 763564.9(291499.1 + T)}}{763564.9}$
2.	Point 1 with x-coordinate increased 0.01times the ratio of the Zr content of the U-Zr binary system liquidus/0.1993
3. The U-Zr binary system liquidus	point 2 of Table 11-1
4. β-Zr, γ-U phase boundary, U-Zr binary system	$\dfrac{-208.5 + \sqrt{208.5^2 - 302(1406 - T)}}{302}$
5.	Point 1 with x coordinate increased 0.01

Table 11-3. Correlations for solidus compositions. (Continued)

6. U-rich, O-rich extriem of the alpha zircaloy phase region.	
For $1{,}587.277 \le T < 2{,}223$	$x = 0.6248868 + T[2.938827\times10^{-4} + T(-9.967758\times10^{-8})]$
For $2{,}223 \le T \le 2{,}248$	$x = -7.207558 + T3.595666\times10^{-3}$
For $1{,}587.277 \le T\ 2{,}178$	$y = 0.5935931 + T(-4.90869\times10^{-4} + T1.629741\times10^{-7})$
For $2{,}178 \le T \le 2{,}248$	$y = 2.848266 - T1.71115\times10^{-3}$
7.	Point 6 displaced 0.01 parallel to the O-Zr side of the Gibbs triangle
8. U-rich, O-poor extriem of the beta phase zircaloy region	$x = 32.99604 + T(-2.99394\times10^{-2} + T6.984916\times10^{-6})$
	$y = -27.11131 + T[2.472659\times10^{-2} + T(-5.619063\times10^{-6})]$
9. Zr-rich boundary of the beta phase, Zr-ZrO_2 binary system	$f_o = \dfrac{-131.723 + \sqrt{131.723^2 - 5602.96(2125 - T)}}{5602.96}$
10. O-rich part of the alpha phase boundary, which is in equilibrium with liquid L_1', Zr-ZrO_2 binary system	$f_o = \dfrac{10100.05 + \sqrt{10100.05^2 - 40562.47(266.9135 + T)}}{40562.47}$
11. Zr-rich boundary of the cubic ZrO_2 phase, which is in equilibrium with liquid, Zr-ZrO_2 binary system	$f_o = \dfrac{52252.48 + \sqrt{52252.48^2 - 9551941(30182.27 - T)}}{95519.41}$
12. $Zr_{0.7}O_{0.3}$-rich boundary of cubic $(U,Zr)O_{2-x}$ phase for $2{,}173 \le T \le 2{,}673$, $Zr_{0.7}O_{0.3}$-$U_{0.33}O_{0.67}$ isopleth	$f_{U_{0.33}O_{0.67}} = \dfrac{105794.3 + \sqrt{105794.3^2 - 128402.4(84438.99 + T)}}{128462.5}$
13. Zr-rich part of the alpha phase boundary, which is in equilibrium with liquid L_1, Zr-ZrO_2 binary system	$f_o = \dfrac{1941.412 - \sqrt{1941.412^2 + 7796.837(1764.588 - T)}}{7796.837}$
14. $Zr_{0.7}O_{0.3}$-rich boundary of cubic $(U,Zr)O_{2-x}$ phase for $2{,}673 \le T \le 3{,}119$ K, $Zr_{0.7}O_{0.3}$-$U_{0.33}O_{0.67}$ isopleth	$f_{U_{0.33}O_{0.67}} = \dfrac{2489.661 + \sqrt{2489.661^2 - 4179.972(3918 - T)}}{4179.972}$

Table 11-3. Correlations for solidus compositions. (Continued)

15. U-rich solid UO_{2-x} boundary for $2{,}700 \le T \le 3{,}119$, U-O binary system	$f_o = \dfrac{2 - \dfrac{\sqrt{418.85^2 + 1469(3119 - T)} - 418.85}{1469}}{3 - \dfrac{\sqrt{418.85^2 + 1469(3119 - T)} - 418.85}{1469}}$
16. Linear interpolation between point 14's location at the given temperature and point 17 at 2,809 K	location of 16 = [location of 17 at 2,809 (T - 2,673) + location of 14 at T(2809-T)]/136,
17. $U_{0.33}O_{0.67}$-rich cubic phase boundary, $U_{0.33}O_{0.67}$-$Zr_{0.33}O_{0.67}$ binary system	
For $3{,}119 \ge T \ge 2{,}843$	$f_{Zr_{0.33}O_{0.67}} = \dfrac{107 - \sqrt{107^2 - 41.44(3119 - T)}}{1036}$
For $2{,}843 > T$	$f_{Zr_{0.33}O_{0.67}} = 0.5 - \sqrt{0.25 - \dfrac{(2862.125 - T)}{212.5}}$
18. O-rich solid UO_{2+x} boundary for $2{,}809 \le T \le 2{,}873$, U-O binary	$f_o = \dfrac{478156.7 - \sqrt{478156.7^2 - 67587(3383979 - T)}}{675870}$
19. $Zr_{0.33}O_{0.67}$-rich cubic phase boundary, $U_{0.33}O_{0.67}$-$Zr_{0.33}O_{0.67}$ binary system	
For $2{,}809 \le T \le 2{,}832$	$f_{Zr_{0.33}O_{0.67}} = 0.5 + \sqrt{\dfrac{0.25 - (2872.889 - T)}{255.5556}}$
For $2{,}832 < T \le 2{,}973$	$f_{Zr_{0.33}O_{0.67}} = \dfrac{2212.5 + \sqrt{2212.5^2 - 2850(4548 - T)}}{2850}$
20. $Zr_{0.33}O_{0.67}$ coordinates	x = 2/3 and y = 0.5873503
21.O-rich solid UO_{2+x} boundary for $2{,}873 \le T \le 3119$, U-O binary system	$f_o = \dfrac{37574.67 - \sqrt{37574.67^2 - 48052.59(31862.23 - T)}}{48052.59}$

Table 11-4 lists the liquidus equation number as identified in Table 11-2, the data that were used to construct the equation, and any appropriate comments about the derivation of the equation. The rather complex definition of point 17 given in Table 11-2 is caused by the fact that points 15 of the liquidus lines and point 19 of the solidus lines form a three phase region connecting L_1, L_2, and the ZrO_2 cubic phase.

Point 17 is the L_1 vertex of the three phase region and was located as described to allow tie lines betweenZrO_2 and L_1 on the right side of point 17.

Table 11-4. Data used to produce liquidus correlations.

Number	Coordinations	Comments
1.	(0.0655 atomic fraction O, 1,391 K) (0.347 atomic fraction O, 2,485 K) (0.454 atomic fraction O, 2,700 K)	L_1 boundary, U-O binary system, Figure 11-3
2.	(0 atomic fraction Zr, 1,406 K) (0.5 atomic fraction Zr, 1,825 K) (1 atomic fraction Zr, 2,125 K)	Figure 11-7
3.	a. $2{,}213 < T \leq 2{,}248$ K (0.0673 atomic fraction O, 2,213 K) (0.249 atomic fraction O, 2,248 K)	The point at 2,248 K was required to be a minimum, Figure 11-2
	b. $2{,}125 \leq T \leq 2{,}213$K (0 atomic fraction O, 2,125 K) (0.0673 atomic fraction O, 2,213 K)	The slope at 2,213 K was required to equal the slope of the correlation of 3a, Figure 11-2
4.	(0.249 atomic fraction O, 2,248 K) (0.413 atomic fraction O, 2,173 K)	The point at 2,248 K was required to be a maximum, Figure 11-2
5.	(0.413 atomic fraction O, 2,173 K) (0.538 atomic fraction O, 2,573 K) (0.667 atomic fraction O, 2,973 K)	O-rich L_1 and L_1 boundary, Zr-ZrO_2, Figure 11-2
6.	(0 atomic fr. $U_{0.33}O_{0.67}$, 2,240.747 K) (0.135 atomic fr. U0.33O0.67, 2,222 K) (0.27 atomic fr. U0.33O0.67, 2,173 K)	Zr-rich L_1 boundary, Figure 11-5
7.	(0.27 atomic fr. $U_{0.33}O_{0.67}$, 2,173 K) (0.32 atomic fr. U0.33O0.67, 2,222 K) (0.38 atomic fr. U0.33O0.67, 2,673 K)	O-rich L_1 boundary, Figure 11-5
9.	(0.8 atomic fr. $U_{0.33}O_{0.67}$, 2,673 K) (0.9 atomic fr. U0.33O0.67, 2,911 K) (1 atomic fr. U0.33O0.67, 3,119 K)	O-rich L_2 boundary, Figure 11-5
12.	See Table 11-3	Least squared deviation fit to the data of Latta and Fryxell
13.	See comments	Assumed symmetry about the UO_2 composition in Figure 11-3

Table 11-4. Data used to produce liquidus correlations. (Continued)

Number	Coordinations	Comments
14.	a. 3,119 > T ≥ 2,989 K (0 atomic fr. $Zr_{0.33}O_{0.67}$, 3,119 K) (0.3 atomic fr. $Zr_{0.33}O_{0.67}$, 2,989 K)	$U_{0.33}O_{0.67}$-rich L2 boundary, Figure 11-6
	b. 2,989 > T ≥ 2,832 K (0.3 atomic fr. $Zr_{0.33}O_{0.67}$, 2,989 K) (0.4 atomic fr. $Zr_{0.33}O_{0.67}$, 2,924K) (0.4868 at. fr. $Zr_{0.33}O_{0.67}$, 2,832 K)	
	c. 2,832 > T ≥ 2,809 K (0.4868 at. fr. $Zr_{0.33}O_{0.67}$, 2,832 K) (0.5 atomic fr. $Zr_{0.33}O_{0.67}$, 2,809 K)	The point at 2,809 K was required to be a minimum
15.	a. 2,809 ≥ T ≥ 2,821 K (0.5 atomic fr. $Zr_{0.33}O_{0.67}$, 2,809 K) (0.5317 at. fr. $Zr_{0.33}O_{0.67}$, 2,821 K)	$Zr_{0.33}0_{0.67}$-rich boundary, Figure 11-6. The point at 2809 K was required to be a minimum. Section b's range was reduced because it contained a local maximum that is not physically possible. The offending section was replaced with a linear fit, Section c
	b. 2,821 > T ≥ 2,851.341 K (0.5317 at. fr. $Zr_{0.33}O_{0.67}$, 2,821 K) (0.55 at. fr. $Zr_{0.33}O_{0.67}$, 2,838 K) (0.65 at. fr. $Zr_{0.33}O_{0.67}$, 2,850 K)	
	c. 2,851.341 > T ≥ 2,862 K (0.57 at. fr. $Zr_{0.33}O_{0.67}$, 2,851.341156 K) (0.75 at. fr. $Zr_{0.33}O_{0.67}$, 2,862 K)	
	d. 2,862 > T ≥ 2,973 K (0.75 at. fr. $Zr_{0.33}O_{0.67}$, 2,862 K) (0.85 at. fr. $Zr_{0.33}O_{0.67}$, 2,889 K) (1.00 at. fr. $Zr_{0.33}O_{0.67}$, 2,973 K)	
17.	(0.38 at. fr. $Zr_{0.33}O_{0.67}$, 2,673 K) (0.4023 at. fr. $Zr_{0.33}O_{0.67}$, 2,873 K) (0.65 at fr. $Zr_{0.33}O_{0.67}$,2,821 K)	The coordinates given are for the $L_1/L_1 + L_2$ boundary, Figure 11-8

Table 11-5 lists the solidus equation number as identified in Table 11-3, the data that were used to construct the equation, and any appropriate comments about the derivation of the equation.

Table 11-5. Data used to produce solidus correlations.

Number	Coordinations	Comments
1.	(0.6626 atomic fraction O, 1,391 K) (0.6375 atomic fraction O, 2,514 K) (0.626825706 at. fr. O, 2,700 K)	U-rich solid UO_{2-x} boundary for T > 2,700 K, Figure 11-3
4.	(0 atomic fraction Zr, 1,406 K) (0.5 atomic fraction Zr, 1,690 K) (1 atomic fraction Zr, 2,125 K)	Figure 11-7
6.	a. For 1,587.277 ≥ T > 2,223 K, x coordinate (1,273 K, 0.8374) (1,773 K, 0.8364) (1,873 K, 0.8113) (2,073 K, 0.8113) (2,178 K, 0.7896)	Ternary phase diagrams were used to provide a correlation for the x- and y-coordinates. The point does not appear on any available binary system
	b. For 2,223K ≥ T > 2,223 K, x coordinate (2,223 K, 0.785608339) (2,248 K, 0.8755)	The first point of the set for b was generated by requiring continuity with a
	c. For 1,587.227 ≥ T ≥ 2,178 K, y coordinate (1,273 K, 0.2339) (1,773 K, 0.2213) (1,873 K, 0.2616) (2,073 K, 0.2767) (2,178 K, 0.2948)	
	d. For 2,178 ≥ T ≥ 2,248 (2,178 K, 0.297578048) (2,248 K, 0.2156)	
8.	a. For the x coordinate (2,073 K, 0.948278264) (2,178 K, 0.9224) (2,213 K, 0.948)	Ternary phase diagrams were used. The point 2,073 K was calculated to fit the binary correlation.
	b. For the y coordinate (2,073 K, 0) (2,178 K, 0.0882) (2,213 K, 0.090066642)	

Table 11-5. Data used to produce solidus correlations. (Continued)

Number	Coordinations	Comments
9.	(0 atomic fraction O, 2,125 K) (0.0545 atomic fraction O, 2,156 K) (0.104 atomic fraction O, 2,213 K)	Zr-rich boundary of the beta phase, Zr-ZrO_2 system, Figure 11-17. The data of Domagala and were converted from weight fractions.
10.	(0.249 atomic fraction O, 2,248 K) (0.292 atomic fraction O, 2,173 K)	O-rich part of the alpha phase boundary which is in equilibrium with liquid L_1', Zr-ZrO_2 binary phase system, Figure 11-1. The point at 2,248 K was required to be a max.
11.	(0.6246 atomic fraction O, 2,173 K) (0.65 atomic fraction O, 2,611 K) (0.667 atomic fraction O, 2,973 K)	Zr-rich boundary of the cubic ZrO_2 phase which is in equilibrium with liquid, Zr-ZrO_2 binary phase system, Figure 11-2.
12.	(0.834 at. fr. $U_{0.33}O_{0.67}$, 2,673 K) (0.8681 at. fr. $U_{0.33}O_{0.67}$, 2,432 K) (0.8868 at. fr. $U_{0.33}O_{0.67}$, 2,173 K)	$Zr_{0.7}O_{0.3}$- rich boundary of cubic $(U,Zr)O_{2-x}$ phase for $2173 \geq T \geq 2673$ K, $Zr_{0.7}O_{0.3}U_{0.33}O_{0.67}$ isopleth, Figure 11-8.
13.	(0.249 atomic fraction O, 2,248 K) (0.182 atomic fraction O, 2,213 K)	Zr-rich part of the alpha phase boundary which is in equilibrium with liquid L_1, Zr-ZrO_2 binary system, Figure 11-1. The point at 2,248 K was required to be a maximum.
14.	(0.834 at. fr. $U_{0.33}O_{0.67}$, 2,673 K) (0.91915 at. fr. $U_{0.33}O_{0.67}$, 2,873 K) (1 atomic fr. $U_{0.33}O_{0.67}$, 3,119 K)	$Zr_{0.7}O_{0.3}$-rich boundary of cubic $(U,Zr)O_{2-x}$ phase for $2,673 \geq T \geq 3,119$ K $Zr_{0.7}O_{0.3}O_{0.67}$ isopleth, Figure 11-4.
15.	See Table 11-3	Least squared deviation fit to the data of Latta and Fryxell
17.	a. For $3119 \geq T \geq 2,843$ K (0 atomic fr. $Zr_{0.33}O_{0.67}$, 3,119 K) (0.1 at. fr. $Zr_{0.33}O_{0.67}$, 2,843 K)	$U_{0.33}O_{0.67}$-rich cubic phase boundary, $U_{0.33}O_{0.67}$-$Zr_{0.33}O_{0.67}$ binary system, Figure 11-8. The equation for a was required to match the slope of the equation for $2,843 > T \geq 2,809$ K at 2,843 K and 0.1 atomic fraction. Equation 6 was required to have a min at 2,809 K. Datum at 2,843 K is from Hofmann
	b. For $2843 > T \geq 2,809$ K) (0.1 at. fr. Zr0.33^{O}0.67, 2,843 K) (0.5 at. fr. Zr0.33^{O}0.67, 2,809 K)	
18.	(0.6969 atomic fraction O, 1,926 K) (0.6947 atomic fraction O, 2,273 K) (0.6919 atomic fraction O, 2,873 K) $2,809 \geq T \geq 2,873$K	O-rich solid boundary for U-O binary, Figure 11-2

Table 11-5. Data used to produce solidus correlations. (Continued)

Number	Coordinations	Comments
19.	a. For 2,809 ≥ T ≥ 2,832 K (0.5 at. fr. Zr0.33O0.67, 2,809 K) (0.3 at. fr. Zr0.33O0.67, 2,832 K)	$Zr_{0.33}O_{0.67}$- rich cubic phase boundary,
	b. For 2,832 > T ≥ 2,973 K) (0.8 at. fr. Zr0.33O0.67, 2,832 K) (0.9 at. fr. Zr0.33O0.67, 2,874 K) (1.0 at. fr. Zr0.33O0.67, 2,973 K)	$U_{0.33}O_{0.67}$-$Zr_{0.33}O_{0.67}$ binary system, Figure 11-5. The equation for a was required to have a minimum at 2,809 K.
21.	(0.6916 atomic fraction O, 2,873 K) (0.6786 atomic fraction O, 2,994 K) (0.667 atomic fraction O, 3,119 K)	0-rich solid UO_{2+x} boundary for 2,873 ≤ T ≤ 3,119 K, U-0 binary system, Figure 11-2

The equations of Table 11-2 and Table 11-3 are expressions for the compositions at boundaries of the single liquid and solid phase regions as a function of temperature. In order to use these expressions with the lever rule and the mixing rule[11.1-9] to calculate fractions dissolved or precipitated, the distance between the boundaries of solid and liquid phases that are in equilibrium must be calculated. This is done by converting the composition to Cartesian coordinates centered on the lower left-hand side vertex of the Gibbs coordinate system with the transformation

$$X = f_0 \cos(60) + f_{Zr} \tag{11-10}$$

$$Y = f_0 \sin(60) \tag{11-11}$$

where

X,Y = Cartesian coordinates

f_o = atomic fraction oxygen

f_{Zr} = atomic fraction zircaloy.

In addition to the distances between compositions, calculations of the fractions dissolved or precipitated require knowledge of the tie lines connecting interacting solid and liquid phases. Since no data for tie lines are available, tie lines are assumed to progress between the limits of the two-phase regions they cross in fan shaped patterns. This is the simplest pattern that correctly joins to the binary systems at the edges and avoids the error of tie line crossing.

Calculation of the fractions dissolved or precipitated proceeds with a tedious but direct geometric approach to find the lengths and intersections required by metallurgical techniques once the tie lines are modeled The location of the point representing the solvent composition is compared to the liquidus and

solidus lines expressed in Cartesian coordinates to determine whether the solvent lies between the liquidus and solidus lines (supersaturated) or in the liquid-phase region (subsaturated). If the solvent is supersaturated, tie lines or tie triangles and the lever rule are used to calculate the fraction of the solvent that will freeze. If the solvent is subsaturated, the mixing rule is used to determine the amount of solute that must be dissolved to bring the solvent composition to the liquidus line where dissolution will stop (because additional mixing of the solute would move the gross composition into the multiple-phase region between the liquidus and solidus where formation of a solid phase would take place).

Figure 11-17 is an example showing how a calculation of the amount of UO_2 dissolved by two solvents at 2,500 K proceeds. Solvent A has 0.6 atomic fraction Zr and 0.4 atomic fraction O, while solvent B has 0.9 atomic fraction Zr and 0.1 atomic fraction O. The mixing rule shows that the solution formed when solvent A attacks UO_2 at 2,500 K contains only about 20% UO_2 (the distance from A to the liquidus along the A-UO_2 line divided by the distance from A to the point marked UO_2 on the plot). When solvent B attacks the UO_2, 55% of the solute will be contained in the solution at equilibrium. The tie lines shown as dashed lines in the figure would be used to calculate freezing from the solvent if the solvent composition had placed it in the two-phase region between the solid and liquid phase boundaries.

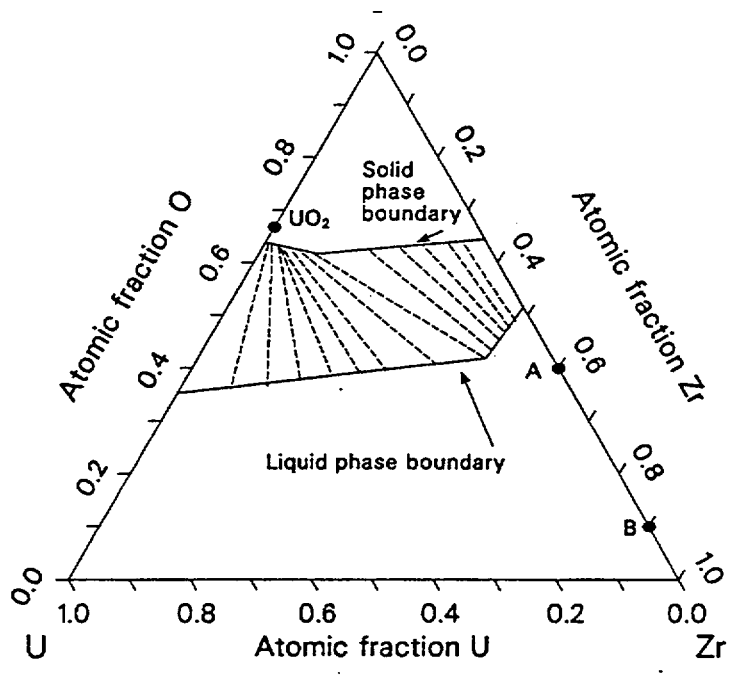

Figure 11-17. Solid and liquid phase boundaries with tie lines connecting compositions on the boundaries as they are represented for 2,500 K in the ZUSOLV code.

11.1.4 References

11.1-1. R. F. Domagala and D. J. McPherson, "System Zirconium Oxygen," *Journal of Metals, 6,* Transactions AIME 200, 1954, pp. 238-246.

11.1-2. R. Ruh and H. J. Garrett, "Nonstoichiometry of ZrO_2 and its Relation to Tetragonal-Cubic Inversion in ZrO_2," *Journal of the American Ceramic Society, 50,* 1966, pp. 257-161.

11.1-3. R. S. Roth, T. Negas, and L. P. Cook, *Phase Diagrams for Ceramists Volume IV*, The American Ceramic Society, 1981.

11.1-4. R. E. Latta and R. E. Fryxell, "Determination of Solidus-Liquidus Temperatures in the UO_{2+x} system (≤ 0.50 x < 0.2)," *Journal of Nuclear Materials, 35*, 1970, pp. 195-201.

11.1-5. A. Skokan, "High Temperature Phase Relations in the U-Zr-O System," *Fifth International Meeting on Thermal Nuclear Reactor Safety, Karlsruhe, German Federal Republic, September 9-13, 1984*, KfK 388011, December 1984, pp. 1035-1042.

11.1-6. K. A. Romberger, C. F. Bates, Jr., H. H. Stone, "Phase Equilibrium Studies in the UO_2-ZrO_2 System," *Journal of Inorganic and Nuclear Chemistry, 29*, 1966, pp. 1619-1630.

11.1-7. P. Hofmann, "SFD Singe Effects Laboratory Experiments," *Severe Fuel Damage and Source Term Research Program Review Meeting, Idaho Falls, ID, April 16-19, 1985.*

11.1-8. P. Hofmann and C. Politis, "The Kinetics of the Uranium Dioxide-Zircaloy Reactions at High Temperatures," *Journal of Nuclear Materials, 87*, 1975, pp. 375-397.

11.1-9. F. N. Rhines, *Phase Diagrams in Metallurgy, Their Development and Application*, New York: McGraw-Hill Book Company, Inc., 1956.

11.2 Specific Heat Capacity and Enthalpy (ZUCP, ZUNTHL, ZUCP1, ZUNTH1)

The function ZUCP provides the specific heat capacity of Zr-U-O compounds as a function of component concentrations and the compound temperature. ZUNTHL returns the Zr-U-O compound enthalpy as a function of component concentrations, the compound temperature, and a reference temperature for which the enthalpy will be zero. Functions ZUCP1 and ZUNTH1 provide the same information for considering all core components.

11.2.1 Zirconium-Uranium-Oxygen Compounds

The expression used to calculate the specific heat capacity is an atomic fraction weighted average of the molar heat capacities of UO_2, ZrO_2, and zircaloy

$$C_p(c) = \frac{C_p(UO_2)0.207f(UO_2) + C_p(ZrO_2)0.123f(ZrO_2) + C_p(Zr)0.091f(Zr)}{0.207f(UO_2) + 0.123f(ZrO_2) + 0.091f(Zr)} \quad (11\text{-}12)$$

where

$C_p(c)$ = specific heat capacity of the compound (J/kg K)

$C_p(UO_2)$ = specific heat capacity of UO_2 obtained from the FCP subcode (J/kg•K)

$C_p(ZrO_2)$ = specific heat capacity of ZrO_2 obtained from the ZOCP subcode (J/kg•K)

$C_p(Zr)$ = specific heat capacity of zircaloy obtained from the CCP subcode (J/kg•K)

$f(UO_2)$ = atomic fraction of UO_2

$f(ZrO_2)$ = atomic fraction of ZrO_2

f(Zr) = atomic fraction of zircaloy.

An analogous weighted average is used in ZUNTHL to calculate compound enthalpies. This technique has the advantage that the proper enthalpies are obtained for the limiting cases of UO_2, ZrO_2, or zircaloy, but the disadvantage that the heats of fusion are not constrained to appear between the solidus and liquidus temperatures of the compound.

Plots of the calculated specific heat capacity and enthalpy of a compound made up of 0.2 weight fraction UO_2 and 0.8 weight fraction ZrO_2 are shown in Figure 11-18 and Figure 11-19.

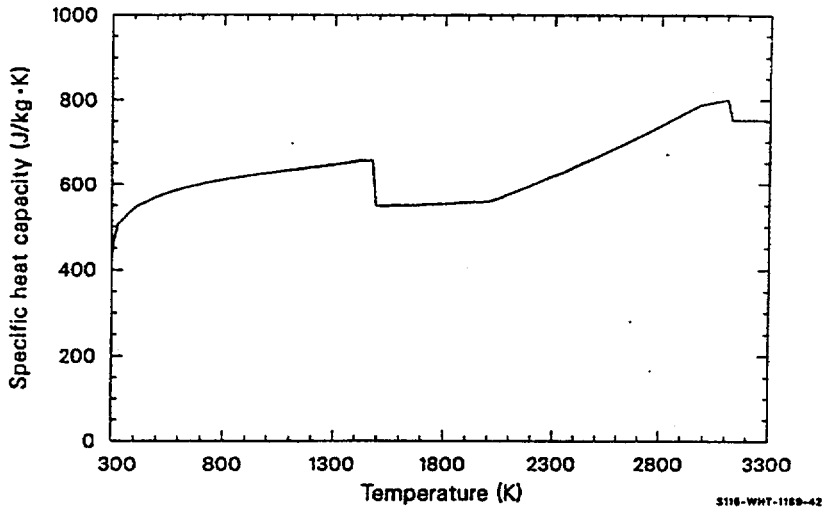

Figure 11-18. Specific heat capacity calculated for a 0.2 UO_2-0.8 ZrO_2 weight fraction compound.

Calculations with ZUNTHL are compared with enthalpies observed by Deem[11.2-1] for several UO_2 - ZrO_2 compounds in Table 11-6 through Table 11-9. (Deem's data are presented in Tables 14 through 17 of Reference 11.2-1.) The standard error of these predictions, 2×10^4 J/kg or about 0.1 of the predicted value, is the expected standard error of the ZUNTHL function.

A similar expected standard error, 0.1 of the predicted specific heat capacity, is adopted for ZUCP.

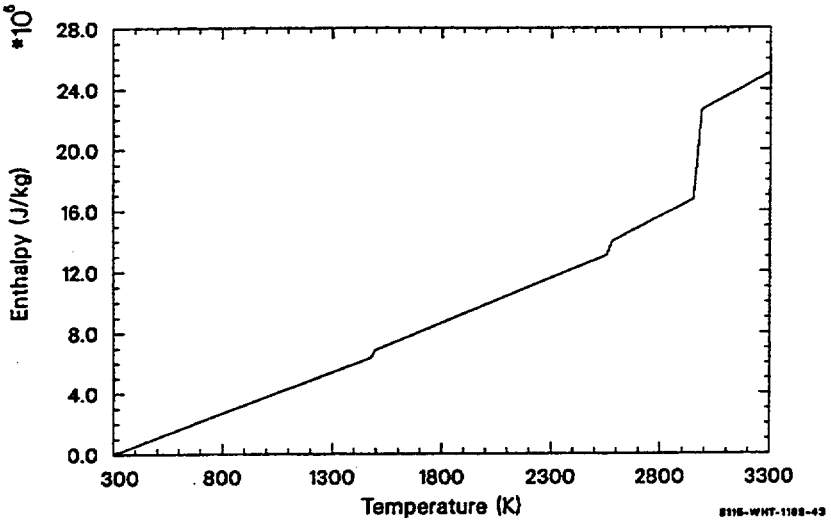

Figure 11-19. Enthalpy calculated for a 0.2 UO_2-0.8 ZrO_2 weight fraction compound.

11.2.2 Core Component Compounds

The expression used to calculate the specific heat capacity is an atomic fraction weighted average of the molar heat capacities of all components of the materials in the core.

$$C_p(c) = \frac{\sum_{i=1}^{n} C_p(i) af_i}{\sum_{i=1}^{n} \frac{MW_i}{100} af_i} \qquad (11\text{-}13)$$

where

$C_p(c)$ = specific heat capacity of the compound (J/kg•K)

$C_p(i)$ = specific heat capacity of the i-th core component material obtained from the specific heat subcode for that material (J/kg•K)

af_i = atomic fraction of the i-th core component material

MW_i = molecular weight of the i-th core component material

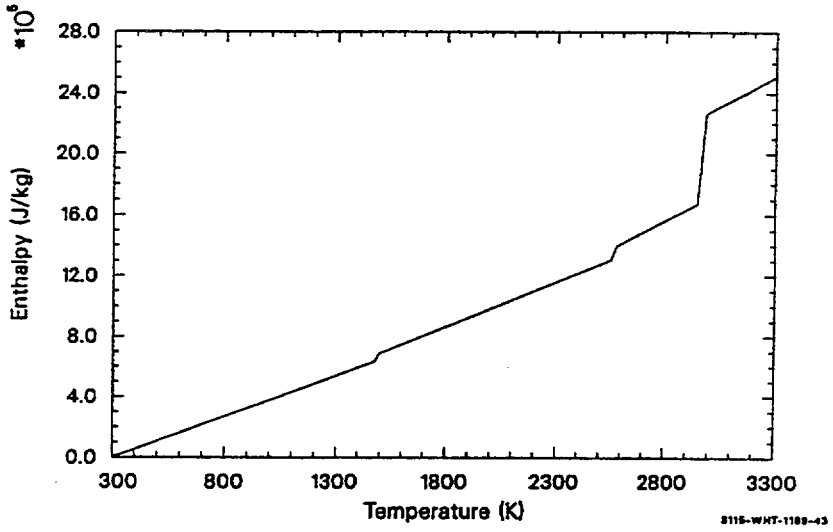

Table 11-6. ZUNTHL calculations and Deem's data[11.2-1] for a 0.2 UO_2-0.8 ZrO_2 weight fraction compound.

Temperature (K)	Observed enthalpy (10^4 J/kg)	Calculated enthalpy (10^4 J/kg)
273	0.00	0.00
370	4.23	4.16
370	4.31	4.16
378	4.64	4.53
469	9.16	8.85
596	15.69	15.24
596	15.56	15.24
727	23.05	22.08
868	30.92	29.66
870	31.00	29.77
1,095	42.59	42.22
1,257	52.05	51.40
1,479	63.97	68.11

Table 11-6. ZUNTHL calculations and Deem's data[11.2-1] for a 0.2 UO_2-0.8 ZrO_2 weight fraction compound. (Continued)

Temperature (K)	Observed enthalpy (10^4 J/kg)	Calculated enthalpy (10^4 J/kg)
1,750	79.50	83.05
2,108	101.0	103.10
2,256	112.0	111.92

Table 11-7. ZUNTHL calculations and Deem's data[11.2-1] for 0.32 UO_2-0.68 ZrO_2 weight fraction compound.

Temperature (K)	Observed enthalpy (10^4 J/kg)	Calculated enthalpy (10^4 J/kg)
273	0.00	0.00
348	2.93	2.97
349	2.96	3.01
371	3.95	3.93
372	3.96	3.98
390	4.74	4.75
390	4.77	4.75
408	5.57	5.54
408	5.61	5.54
541	11.97	11.63
543	11.95	11.72
690	19.20	18.82
691	19.36	18.87
829	26.21	25.76
829	26.22	25.76
947	32.30	31.78
951	32.56	31.99
1,069	37.24	38.11

Table 11-7. ZUNTHL calculations and Deem's data[11.2-1] for 0.32 UO_2-0.68 ZrO_2 weight fraction compound. (Continued)

Temperature (K)	Observed enthalpy (10^4 J/kg)	Calculated enthalpy (10^4 J/kg)
1,292	49.71	49.94
1,480	60.84	63.41
1,678	70.54	73.68
1,797	75.94	79.89
1,878	81.17	84.14
1,919	82.26	86.30
1,976	86.06	89.32
2,096	93.55	95.78
2,175	100.96	100.19
2,276	107.19	106.02
2,385	119.50	112.57
2,487	125.98	118.96

Table 11-8. ZUNTHL calculations and Deem's data[11.2-1] for a 0.5 UO_2-0.5 ZrO_2 weight fraction compound.

Temperature (K)	Observed enthalpy (10^4 J/kg)	Calculated enthalpy (10^4 J/kg)
273	0.00	0.00
339	2.33	2.32
339	2.37	2.32
367	3.41	3.37
367	3.44	3.37
383	4.02	3.99
385	3.97	4.06
401	4.76	4.69
543	10.63	10.50

Table 11-8. ZUNTHL calculations and Deem's data[11.2-1] for a 0.5 UO_2-0.5 ZrO_2 weight fraction compound. (Continued)

Temperature (K)	Observed enthalpy (10^4 J/kg)	Calculated enthalpy (10^4 J/kg)
547	10.83	10.67
702	17.60	17.40
702	17.62	17.40
877	25.81	25.27
878	25.66	25.31
978	30.44	29.91
979	29.96	29.96
1,102	34.98	35.70
1,243	42.05	42.38
1,273	43.43	43.82
1,484	53.39	56.46
1,521	63.64	58.19
1,796	67.66	71.20
1,889	72.17	75.66
1,995	77.74	80.82
2,086	84.60	85.34
2,188	89.66	90.60
2,297	99.33	96.47
2,430	105.94	104.01

Table 11-9. ZUNTHL calculations and Deem's data[11.2-1] for 0.94 UO_2-0.06 ZrO_2 weight fraction compound.

Temperature (K)	Observed enthalpy (10^4 /kg)	Calculated enthalpy (10^4 J/kg)
273	0	0
372	2.36	2.55
372	2.55	2.55
474	5.58	5.46
596	9.25	9.15
597	9.26	9.18
728	13.41	13.29
729	13.44	13.32
870	17.96	17.87
872	18.02	17.94
1,030	23.32	23.15
1,108	25.15	25.76
1,314	32.72	32.77
1,492	37.11	39.24
1,816	48.45	50.81
2,071	59.66	60.56
2,265	68.58	68.68

An analogous weighted average is used in ZUNTHL to calculate compound enthalpies. This technique has the advantage that the proper enthalpies are obtained for each core component material but the disadvantage that the heats of fusion are not constrained to appear between the solidus and liquidus temperatures of the compound.

The newer versions of the subcodes, ZUCP1 and ZUNTH1, were tested by inputting identical weight fractions to those used to test ZUCP and ZUNTHL, with all other components in the core input as zero, and comparing the results. The results were identical to those shown in Figure 11-18 and Figure 11-19. A comparison of the results obtained for several UO_2-ZrO_2 compounds using the later versions, ZUCP1 and ZUNTH1, and those obtained using ZUCP and ZUNTHL with enthalpies reported by Deem[11.2-1] showed that the results were identical. The standard error of these predictions, 2 x 10^4 J/kg, or about 0.1 of the

predicted value, is the standard error of the ZUNTH1 function. A similar standard error of 0.1 of the predicted specific heat capacity is used in ZUCP1.

11.2.3 Reference

11.2-1. H. W. Deem, *Fabrication, Characterization, and Thermal Property Measurements of ZrO_2-Base Fuels*, BMI-1775, June 1966.

11.3 Thermal Conductivity (ZUTCON, ZUTCO1)

11.3.1 Zirconium-Uranium-Oxygen Compounds

Required inputs to ZUTCON to calculate compound thermal conductivities are the component concentrations and compound temperature. The expression used for the compound conductivity is the smaller of k_{Zr} and

$$k(c) = f(UO_2)k(UO_2) + f(ZrO_2)k(ZrO_2) + f(Zr)k(Zr) - 0.4f(UO_2)k(ZrO_2) + 7.8f(UO_2)f(Zr) + 7.8f(ZrO_2)f(Zr) \quad (11\text{-}14)$$

where

k(c)	=	compound thermal conductivity (W/m• K)
$k(UO_2)$	=	UO_2 thermal conductivity obtained from the FTHCON subcode (W/m•K)
$k(ZrO_2)$	=	ZrO_2 thermal conductivity obtained from the ZOTCON subcode (W/m•K)
k(Zr)	=	zircaloy thermal conductivity obtained from the CTHCON subcode (W/m•K)
$f(UO_2)$	=	atomic fraction of UO_2
$f(ZrO_2)$	=	atomic fraction of ZrO_2
f(Zr)	=	atomic fraction of zircaloy.

Equation (11-14) is an atomic fraction weighted average of the thermal conductivities of UO_2, ZrO_2, and zircaloy modified to include cross-products. The modification was added to reproduce the parabolic shape typically seen in plots of conduction versus composition in binary mixtures.[11.3-1,11.3-2]

The coefficient of the UO_2-ZrO_2 cross-product was obtained by requiring Equation (11-14) to reproduce a thermal conductivity of 1.44 W/m• K at 2,073 K for a composition of 0.315 mole fraction UO_2 and 0.685 mole fraction ZrO_2 ($0.5UO_2$ - $0.5ZrO_2$ by weight). The thermal conductivity was obtained from a curve published as Figure 56 in Reference 11.3-3. A similar approach was used to determine the

coefficient of the Zr-UO_2 cross-product. A measurement from Rauch,[11.3-4] 11.09 W/m•K at 343 K for a composition of 0.80 weight fraction UO_2 and 0.20 weight fraction zircaloy, was employed. No data were found to evaluate the Zr-ZrO_2 cross-product coefficient, so the Zr-UO_2 cross-product coefficient was used as an estimate.

A plot of the calculated thermal conductivity of a compound made up of 0.2 weight fraction UO_2 and 0.8 weight fraction ZrO_2 is shown in Figure 11-20.

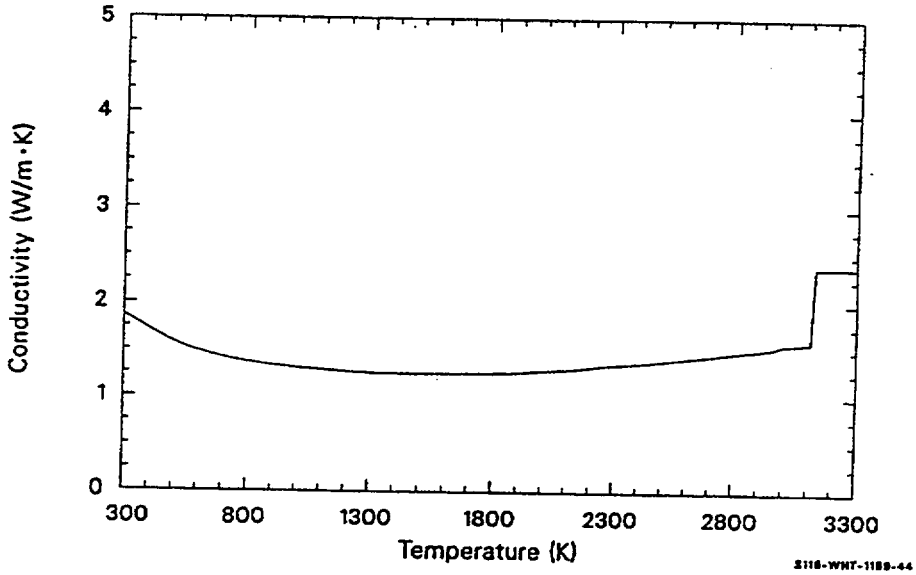

Figure 11-20. Thermal conductivity calculated for a 0.2 UO_2-0.8 ZrO_2 weight fraction compound.

Model predictions are compared to thermal conductivities calculated by Deem (Table 26 of Reference 11.3-3) from his data for several UO_2-ZrO_2 compounds in Table 11-10 through Table 11-14. The standard error of the ZUTCON calculations is ± 1 W/m, most of which is caused by serious overpredictions at low temperature and high UO_2 content.

Table 11-10. ZUTCON calculations and Deem's results[11.3-3] for 0.2 UO_2-0.8 ZrO_2 weight fraction compound.

Temperature (K)	Deem's conductivity (W/m• K)	Calculated conductivity (W/m•K)
423	2.8	1.7
473	2.6	1.6
573	2.30	1.51

Table 11-10. ZUTCON calculations and Deem's results[11.3-3] for 0.2 UO_2-0.8 ZrO_2 weight fraction compound. (Continued)

Temperature (K)	Deem's conductivity (W/m• K)	Calculated conductivity (W/m•K)
673	2.42	1.43
873	2.12	1.33
1,073	1.94	1.28
1,273	1.82	1.25
1,473	1.78	1.24
1,673	1.77	1.24
1,873	1.78	1.25
2,073	1.72	1.28
2,173	1.66	1.30
2,273	1.62	1.32

Table 11-11. ZUTCON calculations and Deem's results[11.3-3] for 0.32 UO_2-0.68 ZrO_2 weight fraction compound.

Temperature (K)	Deem's conductivity (W/m•K)	Calculated conductivity (W/m• K)
423	2.5	2.2
473	2.3	2.1
573	2.1	1.9
673	2.04	1.79
873	2.00	1.59
1,073	2.00	1.47
1,285	1.97	1.39
1,480	1.46	1.34
1,673	1.59	1.32
1,873	1.73	1.31

Table 11-11. ZUTCON calculations and Deem's results[11.3-3] for 0.32 UO_2-0.68 ZrO_2 weight fraction compound. (Continued)

Temperature (K)	Deem's conductivity (W/m•K)	Calculated conductivity (W/m• K)
1,943	1.58	1.32
2,073	1.76	1.33
2,273	1.87	1.38

Table 11-12. ZUTCON calculations and Deem's results[11.3-3] for 0.5 UO_2-0.5 ZrO_2 weight fraction compound.

Temperature (K)	Deem's conductivity (W/m• K)	Calculated conductivity (W/m•K)
423	2.2	3.3
473	2.0	3.1
573	1.8	2.7
673	1.75	2.44
873	1.71	2.06
1,073	1.69	1.82
1,273	1.67	1.66
1,473	1.64	1.55
1,673	1.60	1.48
1,873	1.54	1.44
2,073	1.44	1.45
2,183	1.41	1.47
2,293	1.79	1.51
2,373	1.77	1.54

Table 11-13. ZUTCON calculations and Deem's results[11.3-3] for a low-density 0.32 UO_2-0.68 ZrO_2 weight fraction compound.

Temperature (K)	Deem's conductivity (W/m• K)	Calculated conductivity (W/m• K)
423	2.2	2.2
473	2.1	2.1
573	1.8	1.9
673	1.55	1.79
873	1.53	1.59
1,073	1.53	1.47
1,273	1.53	1.39
1,473	1.17	1.34
1,673	1.28	1.32
1,873	1.36	1.31
2,073	1.40	1.33
2,173	1.30	1.35

Table 11-14. ZUTCON calculations and Deem's results[11.3-3] for 0.94 UO_2-0.06 ZrO_2 weight fraction compound.

Temperature (K)	Deem's conductivity (W/m.K)	Calculated conductivity (W/m. K)
423	3.8	7.8
473	3.6	7.2
573	2.8	6.1
673	2.41	5.32
873	2.32	4.19
1,073	2.19	3.45
1,273	2.05	2.93

Table 11-14. ZUTCON calculations and Deem's results[11.3-3] for 0.94 UO_2-0.06 ZrO_2 weight fraction compound. (Continued)

Temperature (K)	Deem's conductivity (W/m•K)	Calculated conductivity (W/m• K)
1,473	1.99	2.55
1,673	1.93	2.28
1,873	1.87	2.11
2,073	1.84	2.07
2,173	1.82	2.10

11.3.2 Core Component Compounds

Required inputs to ZUTCO1 to calculate compound thermal conductivities are the component concentrations and compound temperature. The expression used for the compound conductivity is the smaller of k(Zr) and

$$k_c = \sum_{i=1}^{n} f(ci)k(ci) \qquad (11\text{-}15)$$

where

k_c = compound thermal conductivity (W/m•K)

f(ci) = atomic fraction of the i-th core component

k(ci) = thermal conductivity of the i-th core component obtained from its thermal conductivity subcode

n = the number of individual core components.

Equation (11-15) is an atomic fraction weighted average of the thermal conductivities of all core components. Where all core materials were considered, cross-products were not used to obtain the total thermal conductivity of the core materials.

Model predictions using ZUTCO1 were compared to thermal conductivities calculated by Deem (Table 26 of Reference 11.3-3) from his data for several UO_2-ZrO_2 compounds in Table 11-10 through Table 11-14. The standard error of the ZUTCO1 calculations is ± 1 W/m, most of which is caused by serious overprediction at low temperature and high UO_2 content.

11.3.3 References

11.3-1. F. Rhines, *Phase Diagrams in Metallurgy and Their Development and Application*, New York: McGraw-Hill Book Company, 1956, pp. 110-113.

11.3-2. B. Abeles, "Lattice Thermal Conductivity of Disordered Semiconductor Alloys at High Temperatures," *Physical Review, 131*, 1963, pp. 1906-1911.

11.3-3. H. W. Deem, *Fabrication, Characterization, and Thermal Property Measurements of ZrO_2 Base Fuels*, BMI-1775, June 1966.

11.3-4. W. G. Rauch, *Uranium Zirconium Cermets*, ANL-5268, 1954.

11.4 Thermal Expansion and Density (ZUTEXP, ZUDEN, ZUTEX1, ZUDEN1)

11.4.1 Zirconium-Uranium-Oxygen Compounds

The function ZUTEXP calculates the thermal expansion strain of Zr-U-O compounds as a function of composition, temperature, and a reference temperature for which the thermal expansion strain will be zero. ZUDEN returns the compound density as a function of composition and density.

The expression used to calculate thermal expansion strains in ZUTEXP is

$$\varepsilon_c = \frac{2.46f(UO_2)\varepsilon(UO_2) + 2.12f(ZrO_2)\varepsilon(ZrO_2) + 1.39f(Zr)\varepsilon(Zr)}{2.46f(UO_2) + 2.12f(ZrO_2) + 1.39f(Zr)} \quad (11\text{-}16)$$

where

ε_c = compound thermal strain (m/m)

$\varepsilon(UO_2)$ = UO_2 thermal strain obtained from the FTHEXP subcode (m/m)

$\varepsilon(ZrO_2)$ = ZrO_2 thermal strain obtained from the ZOTEXP subcode (m/m)

$\varepsilon(Zr)$ = isotropic Zr thermal strain obtained from the CTHEXP subcode with COSTH2 = 1/3 and COSFI2 = 1/2(m/m)

$f(UO_2)$ = atomic fraction of UO_2

$f(ZrO_2)$ = atomic fraction of ZrO_2

$f(Zr)$ = atomic fraction of zircaloy.

This expression is a component volume fraction weighted average of the component strains. The volume fraction of each component is

$$f_V(i) = \frac{\frac{f(i)m(i)}{\rho(i)}}{\sum_{j=1}^{3} \frac{f(j)m(j)}{\rho(j)}} \qquad (11\text{-}17)$$

where

$f_V(i)$ = volume fraction of i-th component (m3/m3)

f(i) = mole fraction of i-th component

m(i) = mole weight of i-th component (kg/g mole) (0.270 for UO_2, 0.123 for ZrO_2, and 0.091 for Zr)

$\rho(i)$ = density of i-th component (kg/m^3) (10,980 for UO_2, 5,800 for ZrO_2, and 6,550 for Zr).

Equation (11-16) is derived by assuming that the compound is made up of components which produce independent thermal strains. The initial volume is thus

$$V_0 = V_0(UO_2) + V_0(ZrO_2) + V_0(Zr) \qquad (11\text{-}18)$$

$$= f(UO_2)\, V_0 + f(ZrO_2)\, V_0 + F(Zr)\, V_0 \qquad (11\text{-}19)$$

where

$V_0(UO_2)$, $V_0(ZrO_2)$, and $V_0(Zr)$ = initial component volumes (m^3) and f (UO_2), f (ZrO_2), and f (Zr) = component volume fractions (m^3/m^3).

The component volume after some thermal strain is

$$V = V_0(UO_2) \exp[3\varepsilon(UO_2)] + V_0(ZrO_2) \exp[3\varepsilon(ZrO_2)] + V_0(Zr) \exp[3\varepsilon(Zr)] \qquad (11\text{-}20)$$

or

$$V \approx V_0(UO_2)[1 + 3\varepsilon(UO_2)] + V_0(ZrO_2)[1 + 3\varepsilon(ZrO_2)] + V_0(Zr)[1+3\varepsilon(Zr)] \ . \qquad (11\text{-}21)$$

The compound volume strain, ε_{c_v} is

$$\varepsilon_{c_v} = \frac{V - V_0}{V_0} \quad . \tag{11-22}$$

$$\approx \frac{V_0(UO_2)3\varepsilon(UO_2) + V_0(ZrO_2)3\varepsilon(ZrO_2) + V_0(Zr)3\varepsilon(Zr)}{V_0(UO_2) + V_0(ZrO_2) + V_0(Zr)} \tag{11-23}$$

$$= f_V\,(UO_2)\,3\varepsilon\,(UO_2) + f_v\,(ZrO_2)\,3\varepsilon\,(ZrO_2) + f_V\,(Zr)\,3\varepsilon\,(Zr) \quad . \tag{11-24}$$

Replacement of the compound volume strain by three times the compound linear strain and substitution using Equation (11-17) completes the derivation of Equation (11-16).

The expression used in ZUDEN to calculate compound densities is

$$\rho_c = \frac{0.27f(UO_2) + 0.123f(ZrO_2) + 0.091f(Zr)}{\frac{0.270f(UO_2)}{\rho(UO_2)} + \frac{0.123f(ZrO_2)}{\rho(ZrO_2)} + \frac{0.091f(Zr)}{\rho(Zr)}} \tag{11-25}$$

where

ρ_c = compound density (kg/m^3)

$\rho\,(UO_2)$ = UO density obtained from the FDEN subcode (kg/m^3

$\rho\,(ZrO_2)$ = ZrO density obtained from the ZODEN subcode (kg/m^3)

$\rho\,(Zr)$ = zircaloy density obtained from the CDEN subcode (kg/m^3).

Equation (11-25) is derived by assuming that each compound component contributes a volume equal to the volume the component would have as a free substance. The compound density is thus the total mass divided by the total volume

$$\rho_c = \frac{\sum_{i=1}^{3} Nf_i m_i}{\sum_{i=1}^{3} \frac{Nf_i m_i}{\rho_i}} \tag{11-26}$$

where N is the number of moles present in the compound. Cancellation of the common factor N and substitution of the component mole weights in Equation (11-26) yields Equation (11-25).

Plots of the calculated thermal expansion strain and density of a compound made up of 0.2 weight fraction UO_2 and 0.8 weight fraction ZrO_2 are shown in Figure 11-21 and Figure 11-22.

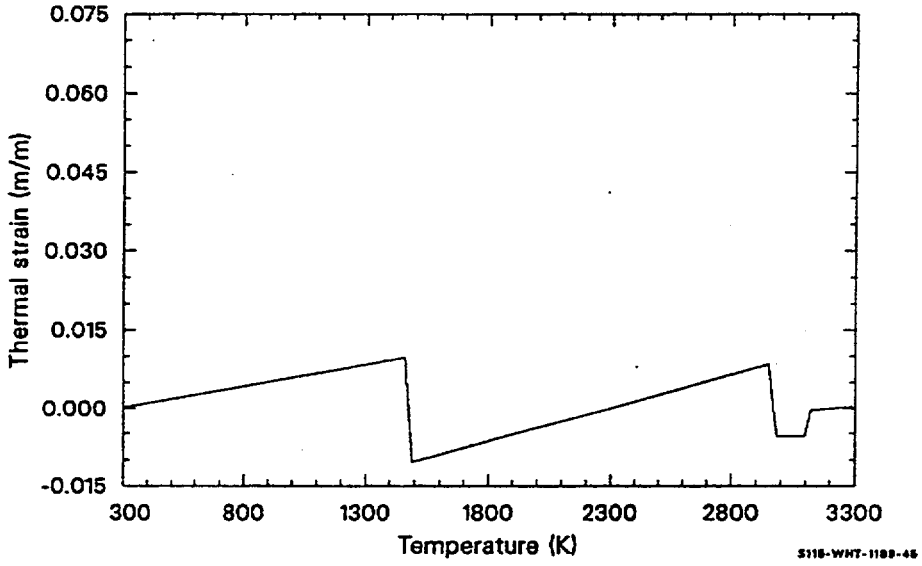

Figure 11-21. Thermal strain calculated for a 0.2 UO_2-0.8 ZrO_2 weight fraction compound.

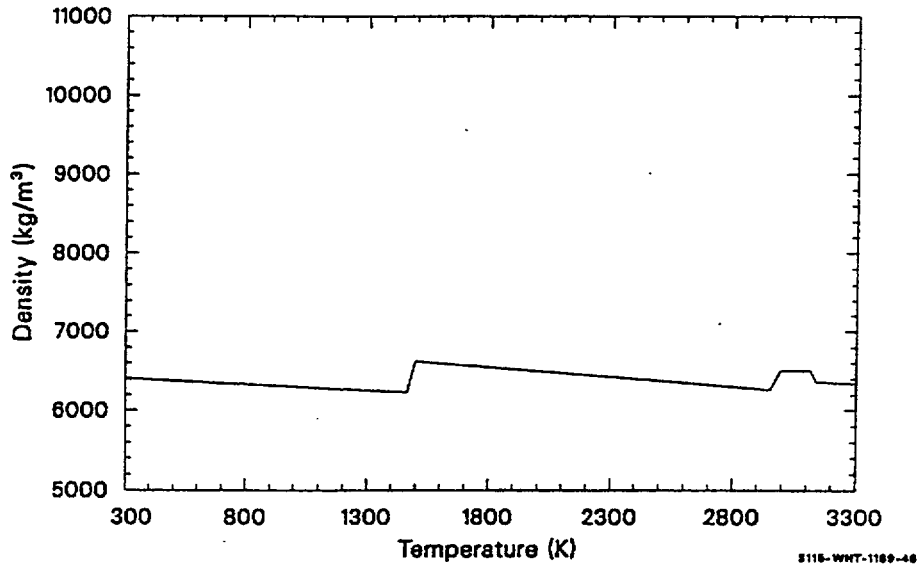

Figure 11-22. Density calculated for a 0.2 UO_2-0.8 ZrO_2 weight fraction compound

Model predictions are compared with thermal expansion strains measured from 293 to 2273 K and densities measured at 293 K by Deem (Table 12 of Reference 11.4-1 for several UO_2-ZrO_2 compounds in Table 11-15 through Table 11-19. The standard error of the ZUTEXP function calculations is $\pm$ 1.0 x 10^{-2}, and the standard error of the ZUDEN function calculations is $\pm$ 3 x 10^{2}. These standard errors are recommended as the expected standard errors of the ZUTEXP and ZUDEN function calculations.

Table 11-15. ZUTEXP calculations and Deem's data[11.4-1] for a 0.2 UO_2-0.8 ZrO_2 weight fraction compound.

Temperature (K)	Observed strain (10^{-2} m/m)	Calculated strain (10^{-2} m/m)
293	0	0
373	0.03	0.06
473	0.09	0.15
573	0.18	0.23
598	0.20	0.24
636	0.00	0.27
673	-0.33	0.31
873	-0.08	0.47
1,073	0.15	0.63
1,273	0.38	0.80
1,473	0.59	0.97
1,673	0.81	-0.84
1,873	1.04	-0.57
2,073	1.28	-0.31
2,273	1.58	-0.05

Table 11-16. ZUTEXP calculations and Deem's data[11.4-1] for 0.32 UO_2-0.68 ZrO_2 weight fraction compound.

Temperature (K)	Observed strain (10^{-2} m/m)	Calculated strain (10^{-2} m/m)
293	0	0
473	0.17	0.07
673	0.40	0.31

Table 11-16. ZUTEXP calculations and Deem's data[11.4-1] for 0.32 UO_2-0.68 ZrO_2 weight fraction compound. (Continued)

Temperature (K)	Observed strain (10^{-2} m/m)	Calculated strain (10^{-2} m/m)
873	0.65	0.48
1,073	0.88	0.65
1,273	1.11	0.82
1,473	1.35	1.00
1,673	1.57	-0.61
1,873	1.81	-0.35
2,073	2.05	-0.08
2,273	2.33	0.18

Table 11-17. ZUTEXP calculations and Deem's data[11.4-1] for a 0.5 UO_2-0.5 ZrO_2 weight fraction compound.

Temperature (K)	Observed strain (10^{-2} m/m)	Calculated strain (10^{-2} m/m)
293	0	0
473	0.16	0.15
673	0.37	0.32
873	0.61	0.50
1,073	0.84	0.68
1,273	1.08	0.87
1,473	1.32	1.06
1,673	1.56	-0.21
1,873	1.80	0.05
2,073	2.08	0.33
2,273	2.46	0.59

Table 11-18. ZUTEXP calculations and Deem's data[11.4-1] for 0.94 UO_2-0.06 ZrO_2 weight fraction compound.

Temperature (K)	Observed strain (10^{-2} m/m)	Calculated strain (10^{-2} m/m)
293	0	0
473	0.17	0.18
673	0.39	0.37
873	0.63	0.58
1,073	0.87	0.80
1,273	1.13	1.03
1,473	1.41	1.27
1,673	1.67	1.29
1,873	1.94	1.56
2,073	2.22	1.84
2,273	2.54	2.12

Table 11-19. ZUDEN calculations and Deem's compound density data.[11.4-1]

Composition (weight fractions)	Observed Density (10 kg/m)	Calculated Density (10 kg/m)
0.2 UO_2-0.06 ZrO_2	6.26	6.40
0.32 UO_2-0.8 ZrO_2	6.81	6.83
0.5 UO_2-0.5 ZrO_2	7.62	7.59
Low density 0.32 UO_2-0.68 ZrO_2	6.46	6.83
0.94 UO_2-0.06 ZrO_2	9.92	10.04

11.4.2 Core Component Compounds

The function ZUTEX1 calculates the thermal expansion strain of core component compounds as a function of composition, temperature, and a reference temperature for which the thermal expansion strain will be zero. ZUDEN1 returns the compound density as a function of composition and density.

The expression used to calculate thermal expansion strains in ZUTEX1 is

$$\varepsilon_c = \frac{\sum_{i=1}^{n} Aaf_i \varepsilon_i}{\sum_{i=1}^{n} Aaf_i} \qquad (11\text{-}27)$$

where

ε_c = compound thermal strain (m/m)

ε_i = i-th core component thermal strain obtained from its individual thermal strain subcode (m/m)

n = number of core components in the compound

af_i = atomic fraction of the i-th core component in compound

A = constant for each core component (Table 11-20).

Table 11-20. Constants for thermal expansion strain.

Component	A
Uranium	1.28
Zirconium	1.46
Stainless steel	0.771
Uranium dioxide	2.46
Zirconium dioxide	2.12
Silver-indium-cadmium	1.07
Boron carbide	2.554
Stainless steel oxide	2.97

This expression is a component volume fraction weighted average of the component strains. The volume fraction of each component is

$$f_{V_i} = \frac{\frac{f_i m_i}{\rho_i}}{\sum_{j=1}^{n} \frac{f_j m_j}{\rho_j}} \tag{11-28}$$

where

f_{V_i} = volume fraction of i-th core component (m^3/m^3)

f_i = mole fraction of i-th core component

m_i = mole weight of i-th core component (kg/g•mole)

n = number of core components in compound

ρ_i = density of i-th component (kg/m^3).

Expression (11-27) is derived by assuming that the compound is made up of components which produce independent thermal strains. The initial volume is thus

$$V_0 = \sum_{i=1}^{n} V_{0_i} \tag{11-29}$$

$$V_0 = \sum_{i=1}^{n} f_{V_i} V_o \tag{11-30}$$

where

V_{0_i} = initial volume of i-th core component

V_o = initial volume of the core components

f_{V_i} = volume fraction of the i-th core component

n = number of core components in the compound.

The component volume after some thermal strain is

$$V_0 = \sum^{n} V_{0_i} \exp(3\varepsilon_i) \tag{11-31}$$

or

$$V_0 \approx \sum^{n} V_{0_i} \exp(1 + 3\varepsilon_i) \tag{11-32}$$

where

V = component volume strain

ε_i = thermal expansion strain of the i-th core component.

The compound volume strain, ε_{c_v}, is

$$\varepsilon_{C_v} = \frac{V - V_0}{V_0} \tag{11-33}$$

or

$$V_0 \approx \sum_{i=1}^{n} \frac{3\varepsilon_i V_{0_i}}{V_{0_i}} \tag{11-34}$$

$$V_0 \approx \sum_{i=1}^{n} 3\varepsilon_i f_{V_i} \ . \tag{11-35}$$

Replacement of the compound volume strain by three times the compound linear strain and substitution using Equation (11-28) completes the derivation of Equation (11-27).

The expression used in ZUDEN to calculate compound densities is

$$\rho_c = \frac{\sum_{i=1}^{n} MW_i a f_i}{\sum_{i=1}^{n} \frac{MW_i a f_i}{\rho_i}} \tag{11-36}$$

where

ρ_c = compound density (kg/m^3)

ρ_i = density of the i-th core component obtained from its individual density subcode (kg/m^3)

MW_i = molecular weights for the i-th core component (kg)

af_i = atomic fraction of the i-th core component in the compound.

Equation (11-36) is derived by assuming that each compound component contributes a volume equal to the volume the component would have as a free substance. The compound density is thus the total mass divided by the total volume

$$\rho_c = \frac{\sum_{i=1}^{n} Nf_i m_i}{\sum_{i=1}^{n} \frac{Nf_i m_i}{\rho_i}} \qquad (11\text{-}37)$$

where N is the number of moles present in the compound. Cancellation of the common factor N and substitution of the component mole weights in Equation (11-37) yields Equation (11-36).

Plots of the calculated thermal expansion strain and density of a compound made up of 0.2 weight fraction UO_2 and 0.8 weight fraction ZrO_2 with the other core components assumed to be zero are identical to those shown in Figure 11-21 and Figure 11-22.

Model predictions with ZUTEX1 and ZUDEN1 were compared to measured thermal expansion strains in the 293 to 2273 K temperature range and to the densities calculated by ZUTEXP and ZUDEN and measured at 293 K by Deem (Table 12 of Reference 11.4-1) for several UO_2-ZrO_2 compounds shown in Table 11-15 through Table 11-19. The standard error of the ZUTEX1 function calculations is $\pm$ 1.0 x 10^{-2}, and the standard error of the ZUDEN1 function calculations is $\pm$ 3 x 10^2. These standard errors are recommended as the expected standard errors of the ZUTEX1 and ZUDEN1 function calculations.

11.4.3 Reference

11.4-1. H. W. Deem, *Fabrication, Characterization, and Thermal Property Measurements of ZrO_2-Base Fuels*, BMI-1775, June 1966.

11.5 Zirconium-Uranium-Oxygen Compounds Coefficients of Friction (ZUFRIC)

The function ZUFRIC returns the coefficient of friction of flowing Zr-U-O compounds. The correlations used for this coefficient are

$$F = (0.0791Re)^{-0.25}, Re > 7539.42 \quad (11\text{-}38)$$

$$F = \frac{64}{Re}, 7539.42 \geq Re > 10^{-6} \quad (11\text{-}39)$$

$$F = 6.4 \times 10^{7}, Re < 10^{-6} \quad (11\text{-}40)$$

where

F = compound coefficient of friction (Pa/Pa)

Re = Reynold's number (unitless).

The correlations are an engineering estimate and have an expected standard error of 0.90 of their calculated value. Figure 11-23 illustrates the coefficient of friction calculated with the ZUFRIC function.

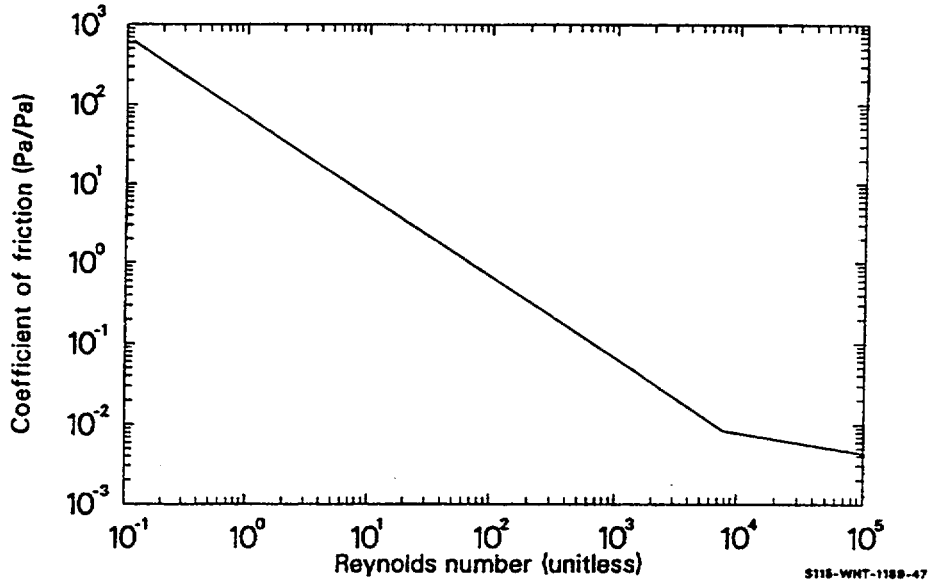

Figure 11-23. Coefficient of friction calculated with the ZUFRIC function.

11.6 Zirconium-Uranium-Oxygen Compounds Interfacial Surface Tension (ZUSTEN)

The function ZUSTEN returns the interfacial surface tension of molten Zr-U-O compounds on zircaloy cladding. The value used is

$$T = 0.45 \tag{11-41}$$

where T is the interfacial surface tension (N/m).

The value is an engineering estimate[a] and has an expected standard error of +1.0, -0.4.

11.7 Zirconium-Uranium-Oxygen Compounds Viscosity (ZUVISC)

11.7.1 Model Development

The function ZUVISC returns an estimate of the viscosity of both solid and liquid Zr-U-O compounds as a function of the composition and temperature of the compound. The expression used to calculate viscosity for temperatures below the solidus temperature (which is provided by the PSOL function) is

$$\eta_s = 1.38\exp\left(\frac{4.942\times10^4}{T}\right) \tag{11-42}$$

where η_s is the viscosity of solid Zr-U-O compounds (Pa• s).

This correlation is the expression used for solid UO_2 viscosity in the FVISCO subcode of MATPRO. For temperatures above the liquidus temperature, a mole fraction average of the component viscosities is used.

$$\eta_l = f(UO_2)\,\eta(UO_2) + f(ZrO_2)\,\eta(ZrO_2) + f(Zr)\,\eta(Zr) \tag{11-43}$$

where

η_l = viscosity of liquid Zr-U-O compounds (Pa• s)

$\eta(UO_2)$ = viscosity of liquid UO_2 (Pa• s)

a. L. J. Siefken, private communication, EG&G Idaho, Inc., October 14, 1982.

η (ZrO_2) = viscosity of liquid ZrO_2 (Pa• s)

η (Zr) = viscosity of liquid Zr (Pa• s).

η (UO_2) is calculated with the appropriate expression from the FVISCO subcode:

$$\eta\,(UO_2) = 1.23 \times 10^{-2} - 2.09 \times 10^{-6}\,T \quad . \tag{11-44}$$

η (ZrO_2) and η (Zr) are calculated with correlations recommended by Nazare, Ondracek, and Schultz[11.7-1]

$$\eta(ZrO_2) = 1.22\times10^{-4}\exp\left(\frac{10500}{T}\right) \tag{11-45}$$

$$\eta(Zr) = 1.90\times10^{-4}\exp\left(\frac{6500}{T}\right) \quad . \tag{11-46}$$

For temperatures between the solidus and liquidus temperatures of the compound, an interpolation scheme is used

$$\eta = \frac{\eta_l(T - T_{sol}) + \eta_s(T_{liq} - T)}{T_{liq} - T_{sol}} \tag{11-47}$$

where

T_{sol} = solidus temperature (K)

T_{liq} = liquidus temperature (K)

η = viscosity of Zr-U-O compounds (Pa• s).

Figure 11-24 illustrates the effect of temperature on the viscosity of a compound composed of two-thirds mole fraction zircaloy and one-third mole fraction UO_2. The expected standard error of viscosities is $\pm$ 0.8 of the predicted value because there are no data in support of the model.

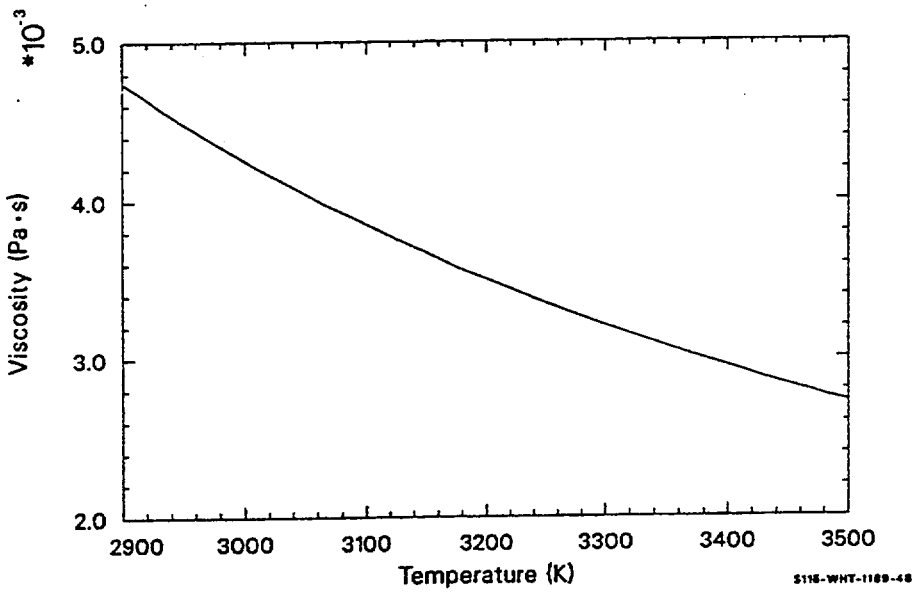

Figure 11-24. Viscosity of a compound composed of 0.33 mol% zirconium and 0.67 mol% uranium dioxide.

11.7.2 Reference

11.7-1. S. Nazare, G. Ondracek, and B. Schultz, "Properties of Light Water Reactor Core Melts," *Nuclear Technology, 32*, 1977, pp. 239-246.

11.8 Heat of Solution of Uranium Dioxide by Zirconium-Uranium-Oxygen Compounds (ZUSOLN)

11.8.1 Model Development

ZUSOLN returns an estimate of the heat required to liquefy UO_2 in a zircaloy-uranium-oxygen compound as a function of the compound composition. The expression used to calculate this heat is

$$Q = \frac{1.5Z + 1.5U - 0.5}{1.5Z + 2.5U - 0.5} 2.69\times10^5 + \left(\frac{U}{1.5Z + 2.5U - 0.5}\right) 2.74\times10^5 \qquad (11\text{-}48)$$

where

Q = heat required to dissolve a unit mass of UO_2 in a zircaloy-uranium-oxygen compound (J/kg)

U = atomic fraction uranium in solvent (atoms uranium/atoms solvent)

Z = atomic fraction zirconium in solvent (atoms zirconium/atoms solvent).

Equation (11-48) is an interpolation between the heat of fusion for UO_2, 2.74 x 10^5 J/kg,[a] and the heat of fusion for UO_2 minus the difference in the heats of formation of ZrO_2 and UO_2 given on page 208 of Reference 11.8-1. The coefficient of the UO_2 heat of fusion is the ratio of the molecular fraction of UO_2 to the sum of fractions of UO_2 and zircaloy in the solvent. (These fractions were derived at the beginning of Section 11). Thus, when this fraction is one, UO_2 is being melted in a mixture of UO_2 and ZrO_2, so the appropriate heat is the energy necessary to melt the UO_2.

The coefficient of the first term in Equation (11-48) is the ratio of the molecular fraction of zircaloy to the sum of the fractions of UO_2 and zircaloy in the solvent. When this fraction is one, UO_2 is being dissolved in zirconium. There are no data for the heat required to do this so it was estimated by approximating the dissolution as a fusion of UO_2, followed by removal of the O_2 from the uranium and addition of the O_2 to a zirconium atom. The resultant number is very similar to the heat of fusion of UO_2.

With the current numbers, 2.69 x 10^5 and 2.74 x 10^5, use of Equation (11-48) to interpolate is not necessary. However, the large uncertainty, $\pm$ 3 x 10^5, suggests that it is prudent to maintain the equation until measurements confirm that the actual number for the heat of solution of UO_2 by zirconium is near the heat of fusion of UO_2.

Figure 11-25 illustrates the small effect of solvent composition on the heat required to dissolve UO_2.

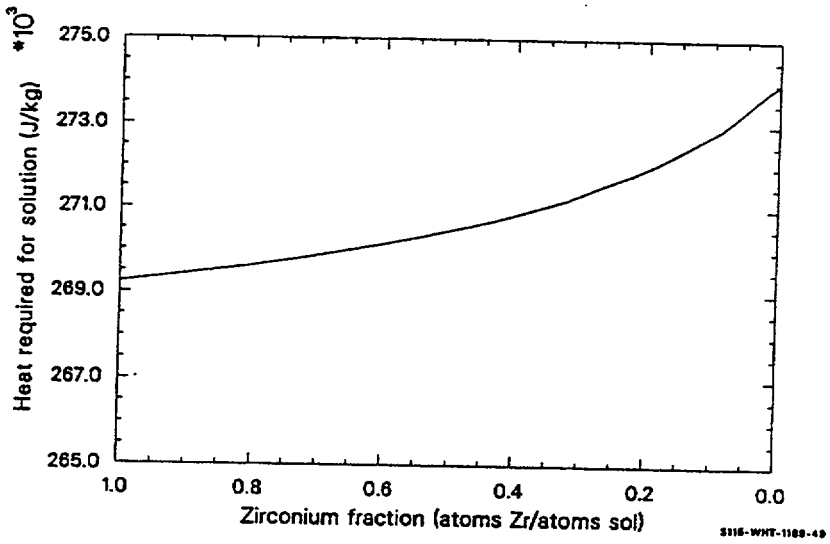

Figure 11-25. Effect of solvent composition of heat required to dissolve a kilogram of uranium dioxide.

a. This number is taken from the PHYPRP subroutine.

11.8.2 Reference

11.8-1. C. J. Smithells and E. A. Brandes (eds.), *Metals Reference Book*, London and Boston: Butterworths (TN671 S55 1956).

11.9 Heat of Fusion of Zirconium-Uranium-Oxygen Compounds (ZUFUSN)

The subcode ZUFUSN calculates the heat of fusion of a zirconium-uranium-oxygen compound as a function of component concentration. Atomic fractions of uranium and zirconium are input into the subcode. The expression used to calculate the heat of fusion of a Zr-U-O compound is a mole fraction weighted average of the molar heats of fusion of UO_2, ZrO_2, and zircaloy

$$L = \frac{2.74\times10^5(0.270)f(UO_2) + 7.06\times10^5(0.123)f(ZrO_2) + 2.25\times10^5(0.091)f(Zr)}{0.270f(UO_2) + 0.123f(ZrO_2) + 0.091f(Zr)} \quad (11\text{-}49)$$

where L is the heat of fusion of the Zr-U-O compound.

11.10 Coefficient of Thermal Expansion of Liquefied Mix (ZUBET1)

Subroutine ZUBET1 calculates coefficient of thermal expansion of liquefied mixture. Table 11-21 lists the required input calls.

Table 11-21. Input variable to the subroutine ZUBET1.

Input Variable	Description
afz	atomic fraction of zircaloy in mixture
afu	atomic fraction of metallic uranium
afs	atomic fraction of stainless steel
afa1	atomic fraction of silver-indium-cadmium
afa2	atomic fraction of boron carbide
afux2	atomic fraction of uranium dioxide
afzx2	atomic fraction of zirconium dioxide
afalup	atomic fraction of aluminum
aflith	atomic fraction of lithium

Table 11-21. Input variable to the subroutine ZUBET1. (Continued)

Input Variable	Description
afcadm	atomic fraction of cadmium
afsoil	atomic fraction of soil
temp	temperature of mixture (K)

The returned coefficient of thermal expansion of a liquefied mixture is calculated by:

$$\beta = \frac{\left(\frac{\rho(T)}{\rho(T+\Delta T)} - 1\right)}{\Delta T} \tag{11-50}$$

where

ρ = density as a function of temperature for the mixture

T = temperature of mixture (K)

ΔT = assumed differential change in temperature (10 K).

11.11 Position of Advancing Zr-UO_2 Interface (PSUZ)

11.11.1 Summary

Subroutine PSUZ calculates the position of the advancing liquid Zr-UO_2 interface.[11.11-1] The temperature dependent propagation constant is

$$\kappa = 8.67 \times 10^{-27} e^{[1.66 \times 10^{-2} T]} (m^2/s) \tag{11-51}$$

where

T = input temperature of liquid Zr-UO_2 region.

Once the propagation constant has been evaluated, the position of the liquid Zr-UO_2 interface may be found by

$$x_f = \sqrt{2\kappa\Delta t + x_o^2} \ . \tag{11-52}$$

11.11.2 Reference

11.11-1. W. Turk, *Design & Verification of Modular Computer Models for Interpreting Rod Melting Experiments*, INEL-TR-52, February 1980.

11.12 UO_2 Solubility in Oxygen Stabilized Zircaloy (PSLV)

11.12.1 Summary

Subroutine PSLV calculates the solubility of UO_2 in oxygen stabilized zircaloy. The temperature dependent solubility, S, is found by:

$$S = \begin{cases} 0 & \text{if } T \le 2103 \text{ K} \\ 1.9143754 + T(1.2127195 \times 10^{-3} + 3.1857023 \times 10^{-7} T) & \text{if } T < 2673 \text{ K} \\ 2.0859332 + T(-1.1311691 \times 10^{-3} + 2.5104264 \times 10^{-7} T) & \text{if } T > 2673 \text{ K and } T < 3119 \text{ K} \\ 1.0 & \text{if } T > 3119 \text{ K} \end{cases} \quad (11\text{-}53)$$

These expressions are interim correlations for the intersection of the line connecting UO_2 and Zr(O) and the solidus on the Gibbs plots discussed in Section 11.1. They should be used with caution because they assume a particular oxygen concentration in the initial oxygen stabilized zircaloy solvent.

11.13 Rate of Dissolution of UO_2 in Zr-U-O (UO2DIS, UO2SOL)

11.13.1 Introduction

Mechanistic modeling of severe core damage processes in LWRs requires models to describe the melting of core materials and the dissolution of UO_2 fuel by liquid zircaloy. The temperature of the zircaloy melt, initial oxygen content, and initial quantity of UO_2 is required to determine the amount of solid core material dissolved in molten zircaloy.

Three computer subcodes were developed to model the solution properties of Zr-U-O. The kinetics of UO_2 dissolution in melted zircaloy is modeled in DISUO2. The maximum atomic fraction of UO_2 that can be dissolved in a Zr-U-O solvent for a given temperature and solvent composition is modeled in UO2DIS, and the remaining solid phase composition is modeled in UO2SOL.

DISUO2 is based on experimental results by Hofmann et al.[11.13-1] on the dissolution kinetics of UO_2 in melted zircaloy. Expressions for the rate of dissolution of UO_2 in melted zircaloy as a function of temperature and prior dissolution were determined from the experiments. The rate equations are used to determine additional dissolution in a time step for each intact node with melted zircaloy.

UO2DIS and UO2SOL are based on analytical expressions for the solidus phase boundary compositions in the ternary Zr-U-O system. These expressions were produced by interpolating the solidus compositions determined as a function of temperature for the several available binary systems or isopleths for which solidus temperatures as a function of composition are known. The analytical expressions that

return the compositions are used with standard phase diagram techniques, the lever rule and the mixing rule, to calculate the maximum amount of UO_2 that can be dissolved by a given solvent.

11.13.2 Data for the Zr-U-O System

The equations for the solidus surfaces were obtained from numerous temperature composition phase diagrams available in the literature. In this section, all of these diagrams have been redrawn to a common scale and units of atomic fraction so that they might be easily compared and checked for consistency.

Solidus temperature curves for the zirconium oxygen mixture have been published by Domagala and McPherson[11.13-2] and modified by Ruh and Garrett.[11.13-3] The curves are made of several segments: one above the beta phase, one above the alpha phase, and one above the cubic ZrO_2 phase. Figure 11-26 shows a phase diagram drawn from these references with weight fraction converted to atomic fraction using the expression

$$f_0 = \frac{\frac{f_0^{mass}}{16}}{\frac{f_o^{mass}}{16} + \frac{(1 - f_o^{mass})}{91.22}} \qquad (11\text{-}54)$$

where

f_o = atomic fraction of oxygen in a Zr-O compound

f_o^{mass} = mass fraction of oxygen in a Zr-O compound.

Figure 11-27 is a temperature composition plot for the U-O binary system taken from Roth et al.[11.13-4] The diagram was converted to atomic fraction oxygen using the relation

$$f_0 = \frac{OM}{1 + OM} \qquad (11\text{-}55)$$

where OM is the oxygen-to-metal ratio (atoms oxygen/atoms uranium).

The figure shows four solidus segments enclosing the UO_2 region, two liquidus segments under the L_1 phase and another two liquidus segments under the L_2 phase. The development of the phase diagram is discussed by Hagrman in Section 11.1.

Figure 11-28 shows an isopleth (constant pressure section of the pressure temperature composition figure) extending from $Zr_{0.7}O_{0.3}$ (the approximate atomic fraction composition of alpha phase zirconium saturated with oxygen) to $U_{0.33}O_{0.67}$ (the uranium dioxide composition written in atomic fraction units). The isopleth was presented as a quasi-binary section by Skoken.[11.13-5]

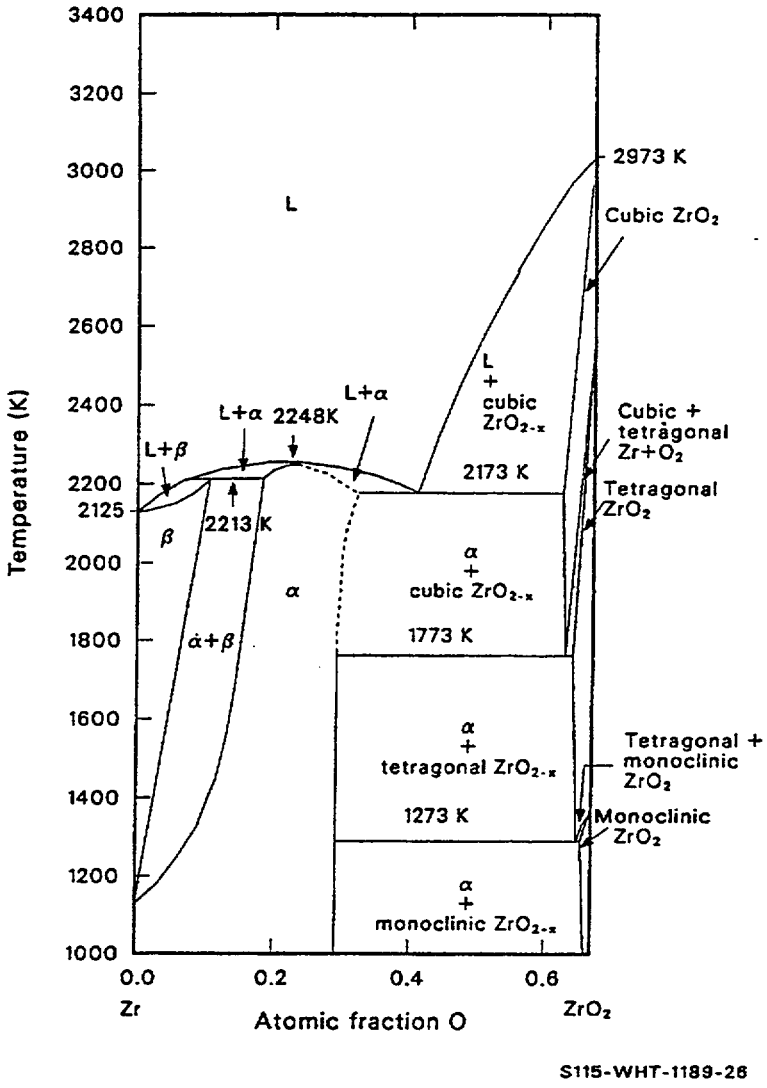

Figure 11-26. Zirconium-zirconium dioxide phase diagram.

Figure 11-29 shows the UO_2-ZrO_2 pseudo-binary system based on Romberger et al.,[11.13-6] and measurements by Hofmann,[11.13-7] which indicated a sharp drop in the solidus temperature as the composition moved away from pure UO_2 or ZrO_2. The minimum melting point occurs at a composition consisting of a 0.5-0.5 mix of the two components and at a temperature of 2,810 K.

Zr-U-O ternary diagrams have been constructed from the binary diagrams and other data.[11.13-5] The ternary phase diagram in Figure 11-30[11.13-8] is the Zr-U-O system at 2,273 K,[a] which is just above the complexities caused by the Zr-O phase transition that occurs from 2,125 to 2,248 K. This diagram is characteristic of the Zr-U-O system until 2,673 K, when a second liquid phase (L_2 in Figure 11-27 through Figure 11-30) appears and covers the temperature range of primary interest in fuel dissolution.

a. Private communication, P. Hofmann, 1985.

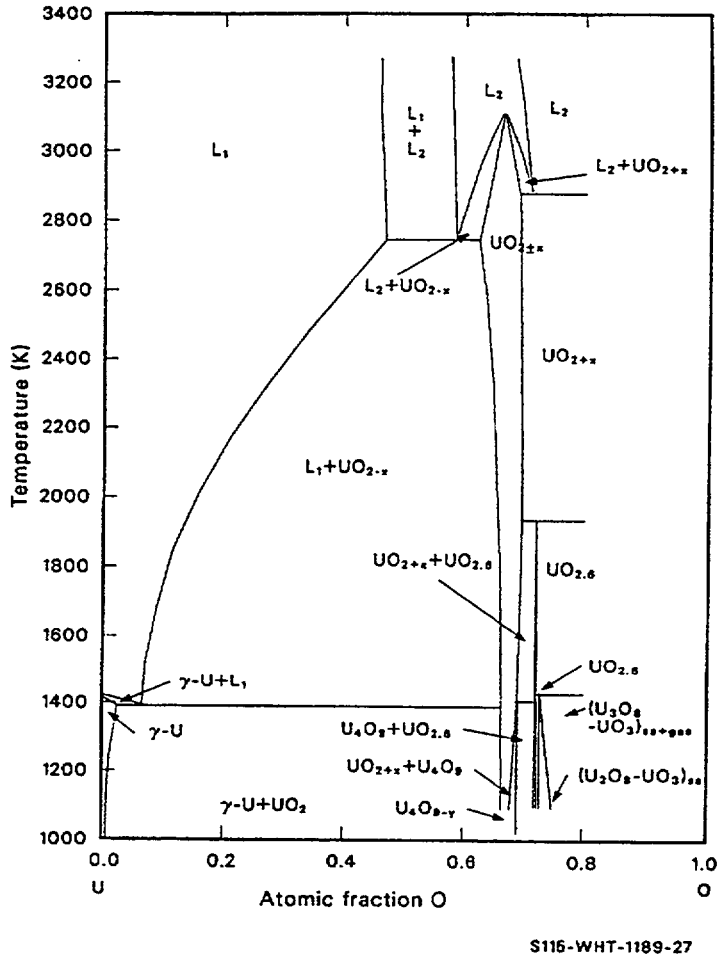

Figure 11-27. Uranium-oxygen phase diagram.

11.13.3 Model Development

The expressions used in the UO2DIS and UO2SOL subcodes were developed by constructing polynomial expressions for the solidus temperature as a function of composition for the various binary systems. Where additional correlations could be obtained from the ternary systems published, they were also employed. These expressions were then inverted to produce correlations for composition points as a function of temperature. These composition points on the ternary phase diagram are connected with straight lines to form the solidus boundary. Details of this development are presented in Section 11.1.

11.13.3.1 Ternary Zr-U-O Phase Diagram Models. Figure 11-31 shows the points connected to form the ternary Zr-U-O system solidus lines (detailed equations are presented in Section 11.1). Dashed lines in Figure 11-31 represent assumed tie lines across multiple phase regions and are therefore not a section through a solidus surface in the three-dimensional temperature composition phase diagram.

11.13.3.2 Calculation of Dissolution Limits. Figure 11-32 illustrates the method used to estimate the maximum fraction of UO_2 that can be dissolved in a Zr-U-O solvent and the solvent composition. Compositions that can be produced by mixing UO_2 (represented by point 4 in Figure 11-32)

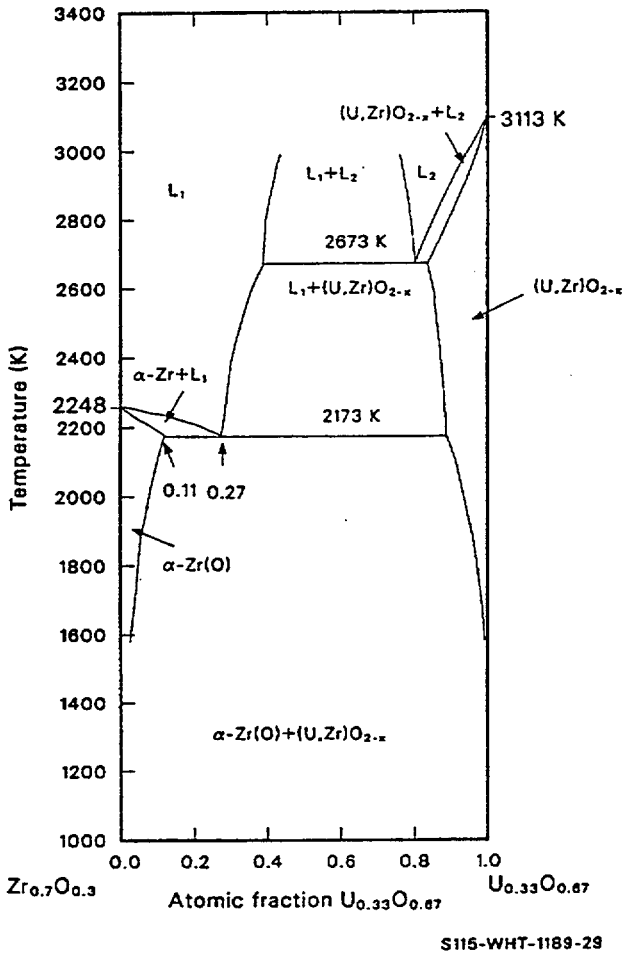

Figure 11-28. Oxygen saturated alpha phase zirconium - uranium dioxide isopleth.

and a partly oxidized zirconium melt (represented by point 1) lie along the line connecting the two points. The equilibrium composition of the liquid (solvent) is represented by point 2, the liquidus where the first solid precipitates appear. The equilibrium composition of the solid (solute or precipitate) is represented by point 3, the solidus where the first liquid phase appears.

The modification recommended by Hofmann et al.,[11.13-1] is to assume that the nonequilibrium slurry produced when zircaloy attacks UO_2 will continue to attack the UO_2 by dissolution along grain boundaries and removal of grains until the composition of the slurry is approximately equal to the liquidus point 3.

The lever and mixing rules state that the UO_2 fraction at 3 is the length from 1 to 3 divided by the length from 1 to 4. Thus, the line segment lengths have to be calculated. This is done using the Pythagorean theorem after converting the compositions of each point to Cartesian coordinates centered on the lower left side vertex of the Gibbs coordinate system with the transformation

$$x = f_o \cos 60 + f_{zr} \tag{11-56}$$

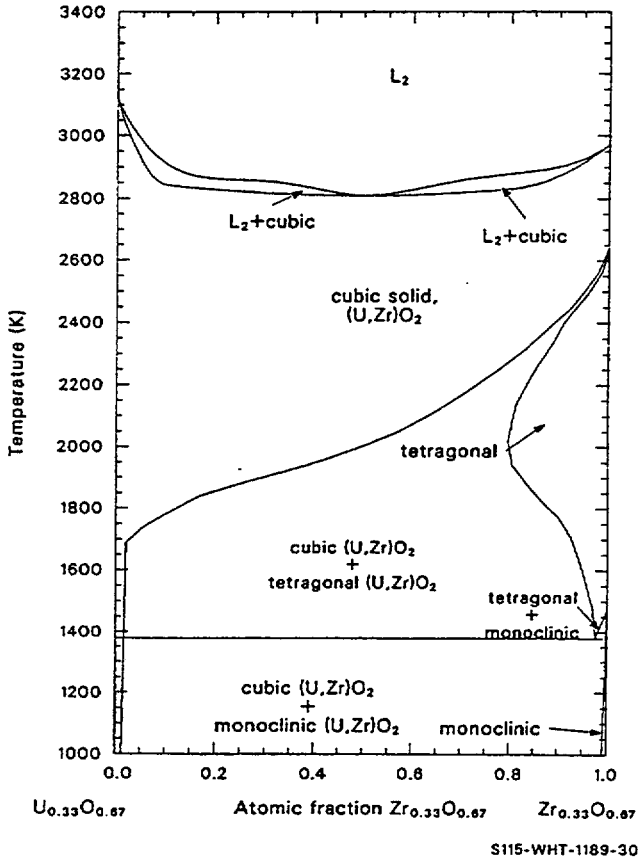

Figure 11-29. Quasi binary phase diagram for the ZrO_2-UO_2 system from Reference 11.13-6.

$$y = f_o \sin 60 \tag{11-57}$$

where

x,y	=	Cartesian coordinates
f_o	=	atomic fraction of oxygen
f_{zr}	=	atomic fraction of zirconium.

The subcode UO2SOL returns the solidus points in Cartesian coordinates as a function of temperature. The subcode UO2DIS connects the points with straight lines to form the solidus curve (the bottom of the upper shaded area of Figure 11-32) and finds the intersection (point 3 of Figure 11-32) between the solidus curve and the UO_2 solvent composition line (the line from 4 to1 in Figure 11-32). The atomic fraction of UO_2 in the solidus composition is then determined using the lever rule.

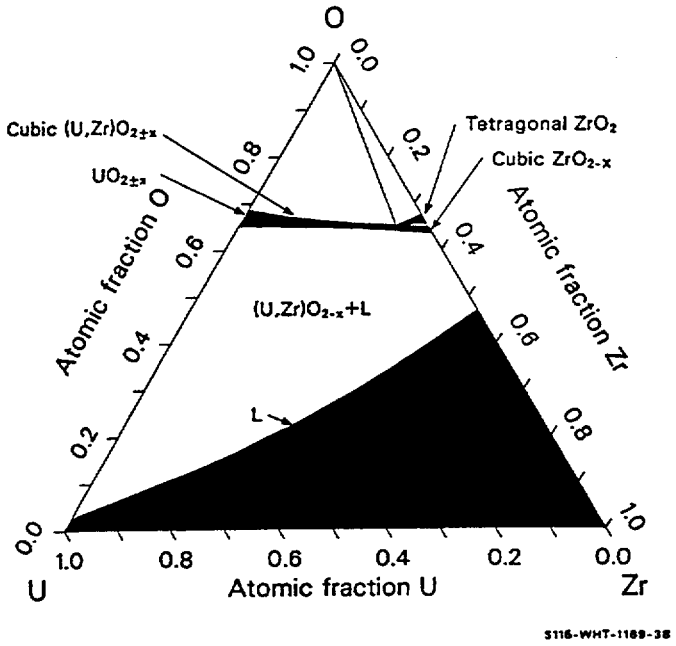

Figure 11-30. Zr-U-O isothermal section at 2,273 K according to Hofmann and Politis.

11.13.4 Uranium Dioxide Dissolution Kinetics

The reaction kinetics of molten zircaloy with solid UO_2 were investigated and reported by Hofmann et al.[11.13-1] A matrix of dissolution experiments was performed at various reaction temperatures and times with UO_2 crucibles and as received zircaloy in a nonoxidizing environment. The crucibles were then metallographically examined, and the area fraction of the (U, Zr)O_{2-x} ceramic phase in the once molten solvent was measured. A set of standards was established by dissolving known amounts of UO_2 in zircaloy and then measuring the ceramic area fraction so that the ceramic area fractions measured in the experiments could be correlated with the UO_2 content of the melt.

It was found that the fuel dissolution showed parabolic behavior after a short incubation period. (The first ceramic particles do not appear in the solidified melt until about 35.8 wt% UO_2 has been dissolved.) The parabolic equation for the wt% of UO_2 in the melt was given as

$$\text{wt\% } UO_2(T,t) = 35.8 + [K(T)\, t]^{0.5} \qquad (11\text{-}58)$$

where

K = parabolic rate constant [(wt% $UO_2)^2$/s]

T = temperature (K)

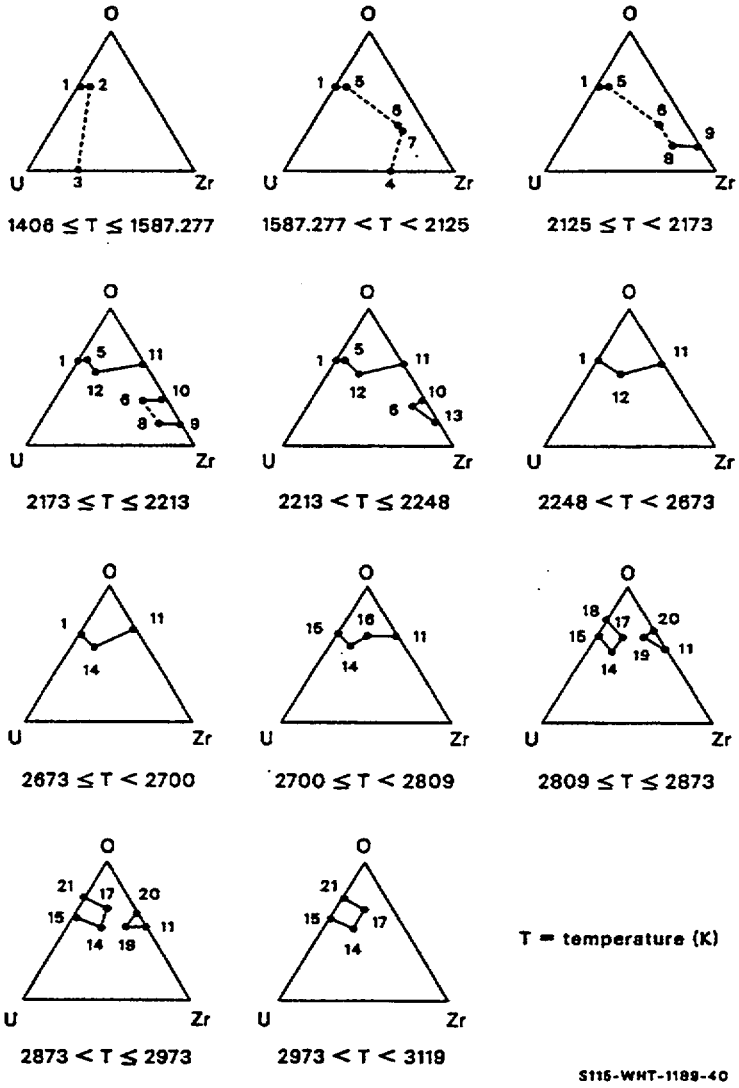

Figure 11-31. Points connected to form the ternary Zr-U-O system.

t = time (s).

The parabolic rate constant K was determined by fitting an Arrhenius function to the data, obtaining

$$K(T) = 1.0196 \times 10^{15} \exp(-677200/RT) \quad (11\text{-}59)$$

where R is the universal gas constant (8.314 J/mole•K).

The surface area present in the experiments is implicit in these equations, so the data were transformed by Hofmann into equivalent uniform receding interface positions and fit to a new Arrhenius function, yielding

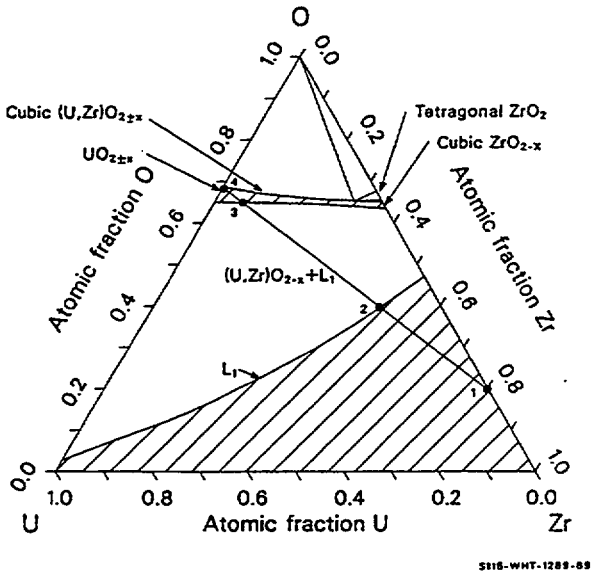

Figure 11-32. Zr-U-O isothermal section at 2,273 K according to Hofmann and Politis (revised).

$$\Delta \xi (T, t) = [K' (T) \cdot t]^{1/2} \tag{11-60}$$

where

$\Delta \xi$ = displacement of the dissolution interface (cm)

$K'(T)$ = $3.85 \times 10^{19} \exp(-1067000/RT)$ = parabolic rate constant for displacement (cm^2/s).

Information from U02DIS and U02SOL is passed into the SCDAP subcode DISUO2 which calculates the increment of fuel dissolved for a time step based on the dissolution interface model. The model is implemented for incremental calculations by:

$$X_{i+1} = [X_i^2 + K'(T) \cdot t]^{1/2} \tag{11-61}$$

where

X_i = dissolution from position at time step i (cm)

Δt = time step (s).

Dissolution of UO_2 is assumed to proceed according to Equation (11-61) until maximum dissolution occurs when the solvent reaches the solidus composition. The rate equations do not consider the effect of oxidation of the solvent, but the determination of dissolution limits does.

11.13.5 References

11.13-1. P. Hofmann, H. Uetsuka, A. N. Wilhelm, and E. A. Garcia, "Dissolution of Solid UO_2 by Molten Zircaloy and its Modeling," *International Symposium on Severe Accidents in Nuclear Power Plants, Sorrento, Italy, March 1988.*

11.13-2. R. F. Domagala and D. J. McPherson, "System Zirconium Oxygen," *Journal of Metals, 6,* Transactions AIME 200, 1954, pp. 238-246.

11.13-3. R. Ruh and H. J. Garrett, "Nonstoichiometry of ZrO_2 and its Relation to Tetragonal Cubic Inversion in ZrO_2," *Journal of the American Ceramic Society, 50,* 1966, pp. 257-261.

11.13-4. R. S. Roth, T. Negas, and L. P. Cook, *Phase Diagrams for Ceramist, Volume IV,* The American Ceramic Society, 1981.

11.13-5. A. Skokan, "High Temperature Phase Relations in the U-Zr-O System," *Fifth International Meeting on Thermal Nuclear Reactor Safety, Karlsruhe, German Federal Republic, September 9-13, 1984,* KfK 388011, December, 1984, pp. 1035-1042.

11.13-6. K. A. Romberger, C. F. Bates, Jr., and H. H. Stone, "Phase Equilibrium Studies in the UO_2-ZrO_2 System," *Journal of Inorganic and Nuclear Chemistry, 29,* 1966, pp. 1619-1630.

11.13-7. P. Hofmann, "SFD Singe Effects Laboratory Experiments," *Severe Fuel Damage and Source Term Research Program Review Meeting, Idaho Falls, ID, April 16-19, 1985.*

11.13-8. P. Hofmann and C. Politis, "The Kinetics of the Uranium Dioxide Zircaloy Reactions at High Temperatures," *Journal of Nuclear Materials, 87,* 1975, pp. 375-397.

12. NONCONDENSABLE GASES--HELIUM, ARGON, KRYPTON, XENON, HYDROGEN, NITROGEN, OXYGEN, CARBON MONOXIDE, CARBON DIOXIDE, WATER MIXTURES

Properties of the internal gas of LWR fuel rods have been included in MATPRO. The thermal conductivity (GASCON) of 10 gases (and their mixture in any combination) is modeled, as is gas viscosity (GVISCO). Gas viscosity and thermal conductivity are modeled as functions of temperature and composition. Also included are models of specific heat capacity (GCP), effective emissivity (GMISS), and mean free path (GMFP).

12.1 Thermal Conductivity, Gas Conductance, and Jump Distance (GASCON, GTHCON, GJUMP)

The heat conductance of gas-filled gaps or pores is dependent on the thermal conductivity of the gas mixture when the dimensions of the gas-filled regions are large compared to the mean distance between gas molecule collisions (mean free path of the gas molecules). When the mean free path is not smaller than the gap dimension, the conduction component of gas gap heat conductance becomes a function of the number of gas molecules present and the nature of the gas gap interfaces. This section presents data and correlations for the thermal conductivities of 10 gases of interest in fuel rod analysis. The effect of long mean free paths on gap conductance is also discussed.

12.1.1 Summary

Three functions are provided to meet various analytical needs for gas thermal conductivity. The GASCON function calculates gas thermal conductivity as a function of temperature and gas component fractions. To accomplish this, GASCON first calculates individual gas thermal conductivities through the use of Equations (12-1) through (12-4). Equation (12-5) is then used to calculate the mixture thermal conductivity. GASCON uses these equations in essentially the same form presented below. Though this is not the most simple format possible, it serves to reduce error caused by repeated manipulation of the data. GASCON also generates, but does not return, an uncertainty term for each thermal conductivity.

The GTHCON function calculates the conduction part of gas gap heat transfer as a function of the gas conductivity, the gas pressure, and gas gap width. The conductance includes a series of resistance terms that account for the cases in which the mean free path is not smaller than the gap dimensions. These terms have been previously introduced and are explained in Section 12.1.3. The final expression, Equation (12-8), combines Equation (12-5) with the resistance terms. The equation is again used in essentially unaltered form in the code.

The GJUMP function determines an effective jump distance derived from the models used in GTHCON and GASCON. The jump distance is the mixture thermal conductivity divided by the conductance part of the gap heat conductance, or GASCON divided by GTHCON. The GASCON function is called by GJUMP.

The correlations used for pure noble or diatomic gases are all of the form

$$K = AT^B \tag{12-1}$$

where

k = thermal conductivity (W/m•K)]

T = gas temperature (K).

The constants A and B for each noble or diatomic gas are given in Table 12-1.

Table 12-1. Constants used in gas thermal conductivity correlations.

Gas	A	B
He	2.639×10^{-3}	0.7085
Ar	2.986×10^{-4}	0.7224
Kr	8.247×10^{-5}	0.8363
Xe	4.351×10^{-5}	0.8616
H_2	1.097×10^{-3}	0.8785
N_2	5.314×10^{-4}	0.6898
O_2	1.853×10^{-4}	0.8729
CO	1.403×10^{-4}	0.9090

The following conductivity equations are used for carbon dioxide and steam:

$$k_{\text{carbon dioxide}} = 9.460 \times 10^{-6}\, T^{1.312} \ . \tag{12-2}$$

For $T \leq 973.15$,

$$k_{\text{steam}} = \left(-2.8516\times10^{-8} + 9.424\times10^{-10}T - 6.005\times10^{-14}T^2\right)\frac{p}{T} + \frac{1.009P^2}{T^2(T-273)^{4.2}} \\ 17.6 + 5.87\times10^{-5}(T-273) + 1.08\times10^{-7}(T-273)^2 - 4.51\times10^{-11}(T-273)^3 \tag{12-3}$$

$$k_{\text{steam}} = 4.44\times10^{-6}T^{1.45} + 9.5\times10^{-5}\left(\frac{2.1668\times10^{-9}}{T}P\right)^{1.3} \tag{12-4}$$

where

P = gas pressure (N/m^2).

The uncertainties of the values predicted by Equations (12-1) through (12-4) are summarized in Table 12-2.

Table 12-2. Uncertainty of the gas thermal conductivity correlations.

Gas	Uncertainty (W/m K)
He	$8.00 \times 10^{-7} T^{1.5}$
Ar	$4.96 \times 10^{-10} T^{2.25}$
Kr	$1.45 \times 10^{-9} T^{2}$
Xe	$2.77 \times 10^{-8} T^{1.5}$
H_2	$2.10 \times 10^{-6} T^{1.5}$
N_2	$2.64 \times 10^{-6} T$
0_2	$2.34 \times 10^{-9} T^{2}$
CO	for T between 300 and 400 K, 0.02 K;
	for T > 400 K, 0.002 + 4/3 (T - 400) x 10^{-4} K
CO_2	$8.78 \times 10^{-12} T^{3}$
H_2	O0.06 K

The thermal conductivity of gas mixtures is calculated with the expression

$$k_{mix} = \sum_{i}^{n} \left(\frac{k_i x_i}{x_i + \sum_{j=1}^{n} (1 - \delta_{ij}) \psi_{ij} x_j} \right) \tag{12-5}$$

where

$$\psi_{ij} = \phi_{ij} \left(1 + 2.41 \frac{(M_i - M_j)(M_i - 0.142 M_j)}{(M_i + M_j)^2} \right) \tag{12-6}$$

and

$$\phi_{ij} = \frac{\left[1 + \left(\frac{k_i}{k_j}\right)^{1/2}\left(\frac{M_i}{M_j}\right)^{1/4}\right]^2}{2^{3/2}\left(1 + \frac{M_i}{M_j}\right)^{1/2}} \tag{12-7}$$

and

δ_{ij} = Kronecker Delta = 1 for i = j, 0 otherwise (unitless)

n = number of components in mixture (unitless)

M_i = molecular weight of component i (kg)

x_i = mole fraction of the component i (unitless)

k_i = thermal conductivity of the component i (W/m•K).

The conduction part of the gas gap heat conductance is calculated with the equation

$$h = \sum_{i=1}^{n}\left(\frac{k_i x_i}{x_i + \sum_{j=i\neq 1}^{n} \psi_{ij} x_j}\right)\left(\frac{1}{t + \frac{\sqrt{M_i T}}{18}\left(\frac{\gamma_i - 1}{\gamma_i + 1}\right)\left(\frac{1}{a_i p}\right)\left(\frac{k_i}{x + \sum_{j=i}^{n} \delta_{ij}\psi_{ij} x_j}\right)}\right) \tag{12-8}$$

where

h = conduction part of the gas gap heat conductance ($W/m^2 \cdot K$)

γ_i = ratio of the specific heats at constant volume and constant pressure for component i (unitless)

a_i = a constant (provided in Table 12-3) that describes the nature of the gas gap interfaces (unitless)

t = gap width (m).

Table 12-3. Surface accommodation coefficients.

Gas	Factor a_i of Equation (12-8)	$a_{gas\text{-}zircaloy}$	$a_{gas\text{-}fuel}$
He	0.06	0.07	10.34
Ar	0.15	0.16	0.8
Kr	0.74	0.85	0.85
Xe	0.74	0.85	0.85
H_2	0.06	0.071	0.34
N_2	0.19	0.2	0.85
O_2	0.19	0.2	0.85
CO	0.19	0.2	0.85
CO_2	0.74	0.85	0.85
H_2O	0.19	0.2	0.85

Details of the development of the models used in the GTHCON subcode are presented in the following sections. Section 12.1.2 is a review of the data, and Section 12.1.3 is a discussion of the model development.

12.1.2 Gas Thermal Conductivity and Accommodation Coefficient Data

Most gas thermal conductivity data are for temperatures < 500 K. At higher temperatures of interest in reactor fuel behavior analysis, interpretation of experiment measurements (power transferred across a gas-filled gap at known temperatures) is difficult. Significant energy can be transferred by convection or radiation as well as by conduction. Also, the mean free path of the gas molecules can become nonnegligible compared to gap width for some combinations of pressure, temperature, and gap width. When this happens, experiment data measure not only the bulk gas thermal conductivity but also gap surface effects and numbers of molecules available to transfer energy across the gap.

Researchers usually correct their data for the effects of long mean free paths and convection by measuring power at several differing gas pressures. Since the mean free path is inversely proportional to pressure and the effect of convection is proportional to the square of the gas density (pressure),[12.1-1] it is usually possible to find combinations of experiment dimensions and pressures where the reciprocal conductance is independent of pressure or increasing linearly with reciprocal pressure. When the data show no pressure dependence, both mean free path and convection effects can be neglected. When the linear dependence is present, gas conductivity is found by extrapolation to infinite pressure. Groups of data with equal temperature and varying pressure are fit to an equation of the form

$$\frac{1}{h} = \frac{t}{k} + \frac{\text{constant}}{P} \quad . \tag{12-9}$$

Corrections for radiation heat transfer are applied when necessary by using the Stefan-Boltzmann law. In most experiments, the radiation correction is smaller than measurement uncertainty and the correction is neglected.

Data used in the development of the correlations for pure gas thermal conductivities were taken from the references listed in Table 12-4.[12.1-1 to 12.1-12] The method of correcting for long mean free paths and temperature range investigated are listed in the comment column. With the exception of the two publications by Timrot and Umanskii,[12.1-6,12.1-11] the references reported conductivities and temperatures that could be used without further analysis. The analysis of the high temperature data of Timrot and Umanskii is discussed below.

Table 12-4. Pure gas conductivity references.

Gas	Reference	Comments
He	Kannuluik and Carman[12.1-1]	Extrapolated to infinite pressure temperatures to 580 K
	Gambhir, Gandhi, and Saxena[12.1-2]	Pressure independent conductivity temperatures to 370 K
	von Ubisch[12.1-3]	Extrapolated to infinite pressure at 300 and 790 K
	Saxena and Saxena[12.1-4]	Pressure independent conductivity temperatures to 1,300 K
	Timrot and Totskii[12.1-5]	Radiation effects correction, but long mean free path correction not discussed
	Timrot and Umanskii[12.1-6]	Analysis discussed in the text of this report (Section 12.1.2), temperatures from 800 to 2,600 K
	Zaitseva[12.1-7]	Extrapolated to infinite pressure temperatures from 350 to 800 K
	Cheung, Bromley, and Wilke[12.1-8]	Extrapolated to infinite pressure at 370 and 590 K
	Johnston and Grilley[12.1-9]	Extrapolated to infinite pressure temperatures to 383 K
Ar	Kannuluik and Carman[12.1-1]	Extrapolated to infinite pressure temperatures from 370 to 380 K
	Gambhir, Gandi, and Saxena[12.1-2]	Pressure independent conductivity temperatures from 310 to 370 K
	von Ubisch[12.1-3]	Extrapolated to infinite pressure at 300 and 790 K
	Zaitseva[12.1-7]	Extrapolated to infinite pressure temperatures from 320 to 790 K

Table 12-4. Pure gas conductivity references. (Continued)

Gas	Reference	Comments
	Cheung, Bromley, and Wilke[12.1-8]	Extrapolated to infinite pressure at 370 and 590 K
	Schafer, as quoted by Brokaw[12.1-10]	At 1,370 K
Kr	Kannuluik and Carman[12.1-1]	Extrapolated to infinite pressure temperatures from 370 to 580 K
	Gambhir, Gandhi and Saxena[12.1-2]	Pressure independent conductivity temperatures from 310 to 370 K
	von Ubisch[12.1-3]	Extrapolated to infinite pressure at 300 and 790 K
	Zaitseva[12.1-7]	Extrapolated to infinite pressure temperatures from 310 to 800 K
Xe	Kannuluik and Carman[12.1-1]	Extrapolated to infinite pressure temperatures from 370 to 80 K
	Gambhir, Gandi, and Saxena[12.1-2]	Pressure independent conductivity temperatures from 310 to 370 K
	von Ubisch[12.1-3]	Extrapolated to infinite pressure at 300 and 790 K
	Zaitseva[12.1-7]	Extrapolated to infinite pressure temperatures from 310 to 790 K
H_2	Johnston and Grilley[12.1-9]	Extrapolated to infinite pressure temperatures to 370 K
	Geier and Schafer as quoted at 1,373 K by Brokaw[12.1-10]	
	Timrot and Umanskii[12.1-11]	Analysis discussed in the text of this report (Section 12.1.2)
N_2	Cheung, Bromley, and Wilke[12.1-8]	Extrapolated to infinite pressure at 380 and 590 K
	Figure 4, Keyes[12.1-12]	Temperatures from 320 to 620 K
O_2	Cheung, Bromley, and Wilke[12.1-8]	Extrapolated to infinite pressure at 370 and 590 K
O_2	Johnson and Grilley[12.1-9]	Extrapolated to infinite pressure temperatures to 380 K
CO	Johnston and Grilley[12.1-9]	Extrapolated to infinite pressure temperatures to 380 K

Table 12-4. Pure gas conductivity references. (Continued)

Gas	Reference	Comments
CO_2	Cheung, Bromley, and Wilke[12.1-8]	Extrapolated to infinite pressure at 380 and 590 K
	Johnston and Grilley[12.1-9]	Extrapolated to infinite pressure temperatures to 380 K
	Figure 4, Keyes[12.1-12]	Temperatures from 320 to 620 K

Data reported by Timrot and Umanskii are reduced power per unit length and temperatures for a coaxial cylindrical cell. The reduced power was defined to be the power per unit length that would be obtained with a small mean free path, and it was obtained from measurements of power at several pressures. The technique was similar to the approach of extrapolation to infinite pressure.

In contrast to most authors, Timrot and Umanskii correlated values of reduced power with temperature and determined their expression for gas thermal conductivity by taking the derivation of the correlation. The appropriate expression is

$$k = \frac{\ln\left(\frac{R}{r}\right) dW(T)}{2\pi dT} \tag{12-10}$$

where

$W(T)$ = equation for power per unit measured in the experiment (W/m)

R = outer wall radius of the cell (m)

r = inside wall radius of the cell (m).

The analysis by Timrot and Umanskii[12.1-6] is an excellent approach to modeling thermal conductivity with data from a single experiment, but it is inconvenient for use in conjunction with the other literature data. To use Timrot and Umanskii's data with data from other references, the reported values of reduced power and temperature have been used to find approximate point-by-point conductivities. The derivative of W with respect to temperature at temperature T_i was approximated with the expression

$$\frac{dW(T_i)}{dT} \approx \frac{1}{2}\left(\frac{W_{i+1} - W_i}{T_{i+1} - T_i} + \frac{W_i - W_{i+1}}{T_i - T_{i-1}}\right) \tag{12-11}$$

where the subscript i refers to the i-th measured value in a series of measurements listed in order of increasing temperature. Equations (12-11) and (12-12) convert the data reported by Timrot and Umanskii

to thermal conductivities.

When the mean free path of the gas molecules in a gap is long compared to the gap dimensions, the transfer of energy from the hot gap surface to the gas and then to the cold gap surface during individual molecular collisions becomes more important to the heat conductance than the bulk gas thermal conductivity. The experiment data of interest in this case are surface accommodation coefficients, defined by the relation

$$a_{sg} = \frac{T_2 - T_1}{T_s - T_1} \tag{12-12}$$

where

a_{sg} = surface accommodation coefficient for a particular gas-surface interface (unitless)

T_s = surface temperature of the hot gap surface (K)

T_1 = average temperature of the gas molecules impinging on the surface (K)

T_2 = average temperature of the gas molecules after striking and again leaving the surface (K).

Surface accommodation coefficients tend to be large for massive gas molecules, and they are increased when an intermediate gas layer is absorbed on the surface. For example, White[12.1-13] reports accommodation coefficients of 0.09, 0.041, 0.16, and 0.20 for H_2, helium, argon, and 0_2 on clean tungsten surfaces at 90 K. For heavy polyatomic molecules, accommodation coefficients are reported to be generally in the range 0.8 to 0.9. For helium on nickel with and without absorbed gas, White reported accommodation coefficients of 0.360 and 0.071 at 273 K. For helium on glass (a ceramic), the accommodation coefficient is 0.34, a value larger than the helium metal accommodation coefficients mentioned above.

Numerous sources of low temperature data were reviewed but not used in the development of the thermal conductivity model to avoid giving undue emphasis to data that have been replaced by more relevant information. These sources of data and some theoretical discussions are included in a bibliography at the end of this report.

12.1.3 Model Development and Uncertainty Estimates

Development of analytical models for gas gap conductance will be described in several steps. Initially, the data discussed in Section 12.1.2 are used to develop models for the thermal conductivity of pure gases. Uncertainties are discussed, and analytical expressions for these uncertainties are presented. The conductivity of mixed gases is discussed next, and the conduction contribution to the conductance of narrow gaps (or gas-filled fuel regions) is modeled.

An elementary treatment of gas conductivity that considers the gas to be a collection of hard spheres leads to the conclusion that the conductivity of a single-component gas is proportional to the square root of temperature, the square root of the molecular mass, and inversely proportional to the square of the molecule's diameter. The expression that results from the elementary treatment (given in most college statistical mechanics texts and therefore not repeated here) is

$$k_{ideal} = \frac{3m^{1/2}}{2\sigma} K_B^{3/2} T^{1/2} \qquad (12\text{-}13)$$

where

k_{ideal} = thermal conductivity of an idealized gas (W/m•K)

m = mass of the molecules (kg)

K_B = Boltzmann's constant (J/K)

σ = area of the sphere's cross-section (m^2).

For real gases where the molecules have structure and distant dependent interactions, Equation (12-13) must be replaced by an equation of the form

$$K = AT^B \qquad (12\text{-}14)$$

where A and B are constants for a given gas. Data referenced in Section 12.1.2 and the least-squares method were used to find the values of A and B given in the summary.

Figure 12-1 through Figure 12-4 illustrate the correlation predictions and the data base for the monatomic gases helium, argon, krypton, and xenon. The values of B for these four gases (0.7085, 0.7224, 0.8363, and 0.8616) increase with increasing boiling temperatures (4, 87, 120, and 166 K), an indication that the increasing departure from the idealized gas temperature dependence is due to increasing intermolecular forces. This regular trend and the fact that a single exponent serves to model the extensive helium data lends confidence to the extrapolations beyond the low temperature data available for krypton and xenon.

Dashed lines in Figure 12-1 through Figure 12-4 are the expected standard error of the correlations. Since the data show increasing scatter with increasing temperature, the expected standard error of the thermal conductivity was determined from the standard error of a new variable defined to be the thermal conductivity divided by a power of temperature. Trial values of the power were varied until the residuals of the new variable were temperature independent. Once the appropriate power was determined, the standard error of the new variable was calculated and the expected standard error of the conductivity was obtained by multiplying the standard error of the new variable by the power of the temperature.

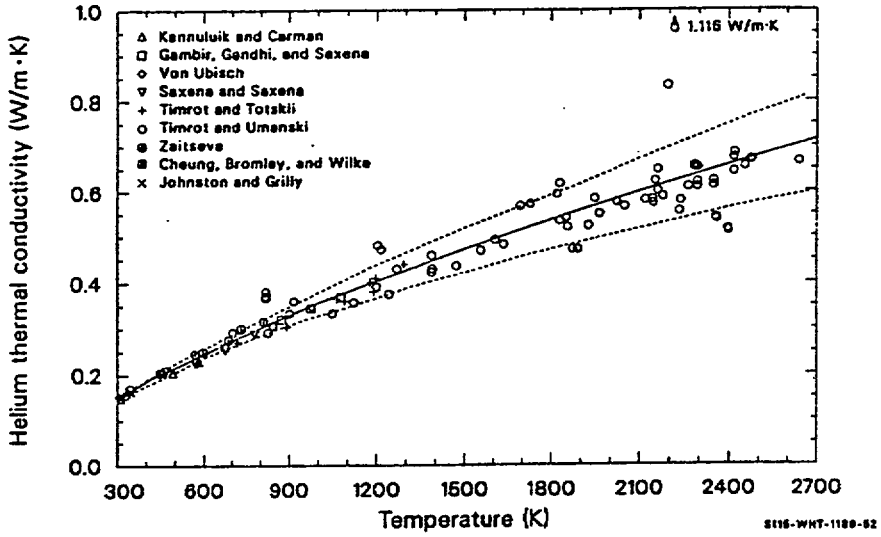

Figure 12-1. Thermal conductivity of helium as a function of temperature.

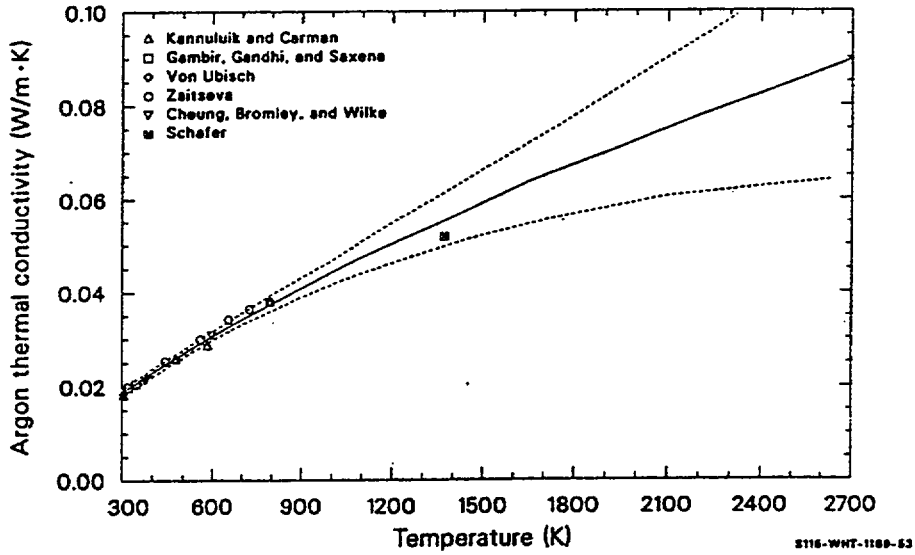

Figure 12-2. Thermal conductivity of argon as a function of temperature.

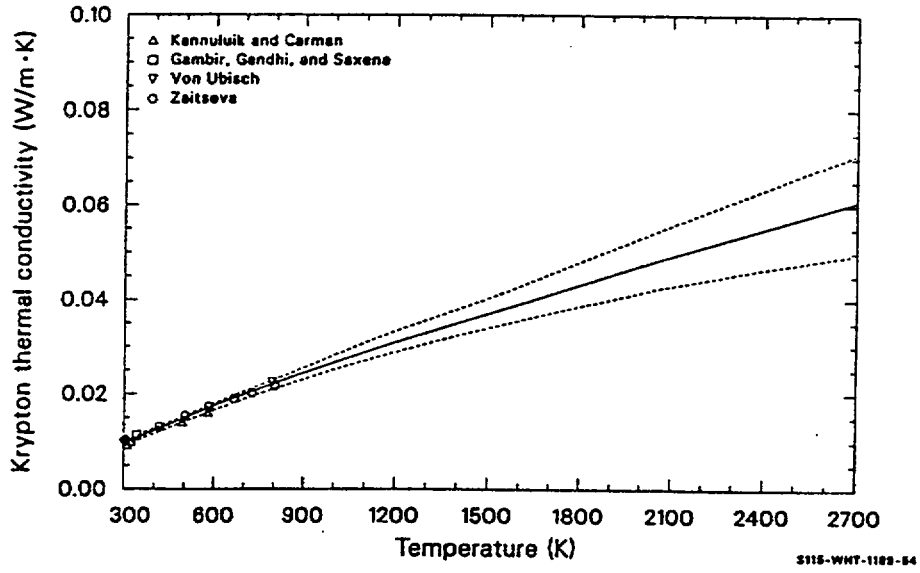

Figure 12-3. Thermal conductivity of krypton as a function of temperature.

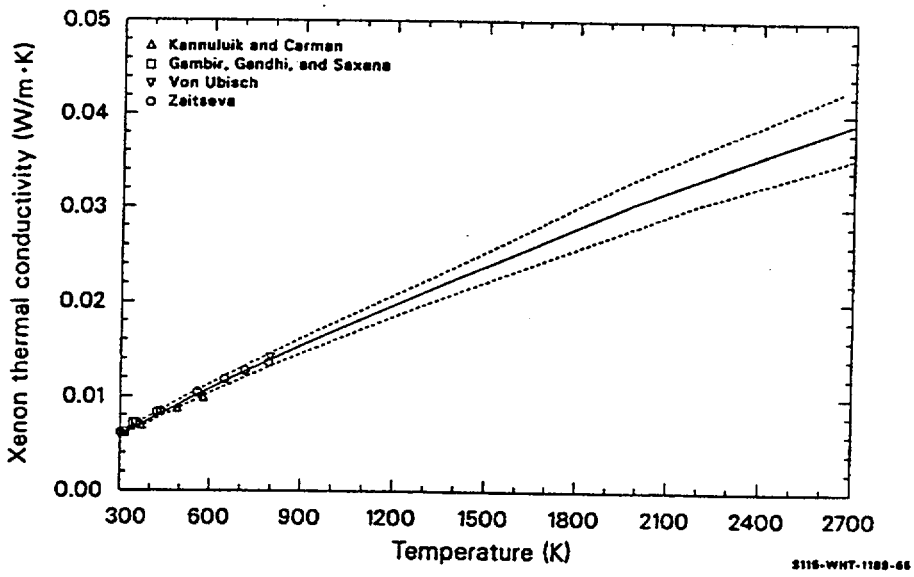

Figure 12-4. Thermal conductivity of xenon as a function of temperature

For the diatomic molecules, H_2, N_2, O_2, and CO, the relation between the exponent B in Equation (12-2) and boiling temperatures is no longer apparent. The conductivities of these gases cannot be expected to be related in any simple fashion because they transfer energy in complex molecular rotational and vibrational modes, in addition to translational modes. The data base, correlation predictions, and expected standard errors for these gases are shown in Figure 12-5 through Figure 12-8.

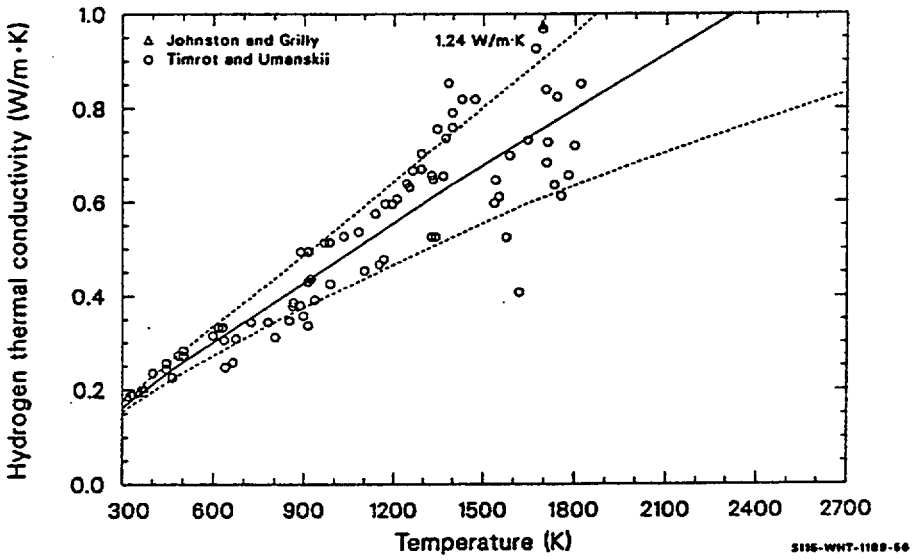

Figure 12-5. Thermal conductivity of hydrogen as a function of temperature.

The analysis of the diatomic gas data followed the procedure of the monatomic gases, with the exception of the determination of the expected standard error of the CO conductivity correlation. For carbon monoxide, only four data were available; and an arbitrary uncertainty of 0.02 times the thermal conductivity (typical of low temperature measurement scatter) was assigned over the temperature range of the data. The 0.02 was replaced with a linear function of temperature for temperatures > 400 K, and the coefficients in this function were determined to predict an expected standard error of 0.10 times the predicted thermal conductivity at 1,000 K.

Figure 12-9 is a comparison of the data base and correlation predictions for the thermal conductivity of CO_2. It is possible that the large exponent of temperature in the carbon dioxide correlation is due to an extreme departure from the idealized gas approximation at the low temperatures for which data are available. The vapor pressure of solid carbon dioxide is one atmosphere at 195 K,[a] and the data extend only over a range of two to three times this temperature. If the large exponent of temperature obtained from data in the range from 300 to 600 K is due to the fact that all the data are at temperatures where significant intermolecular forces are present, the exponent can be expected to decrease at temperatures >

a. There is no liquid phase of CO_2 at atmospheric pressure, so the closest measure of boiling point is the one given here.

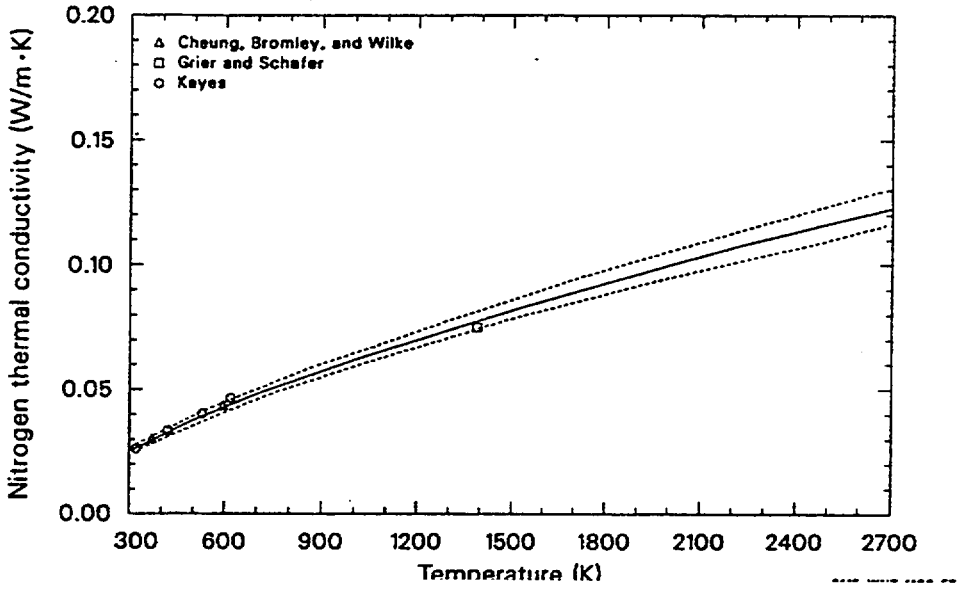

Figure 12-6. Thermal conductivity of nitrogen as a function of temperature.

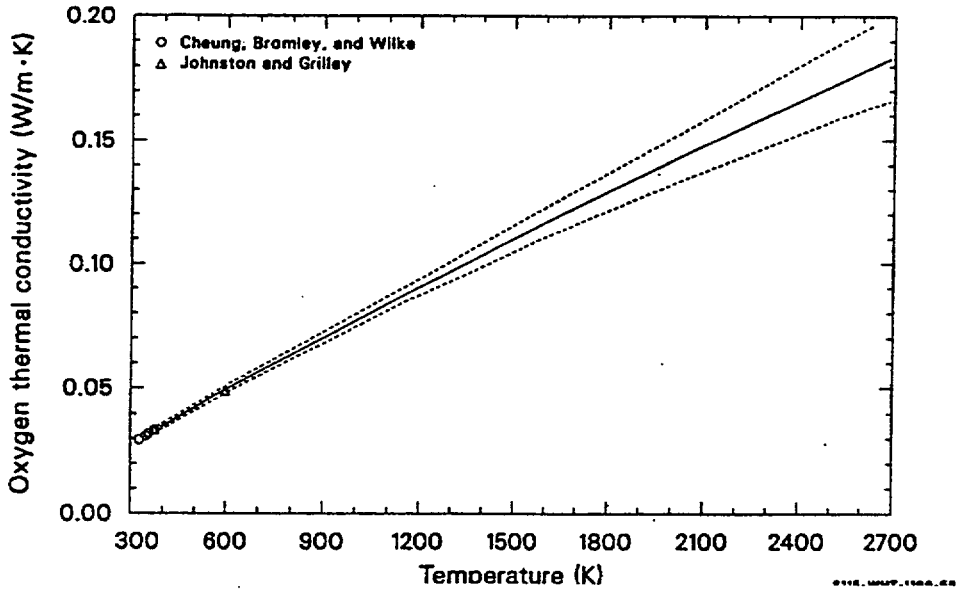

Figure 12-7. Thermal conductivity of oxygen as a function of temperature.

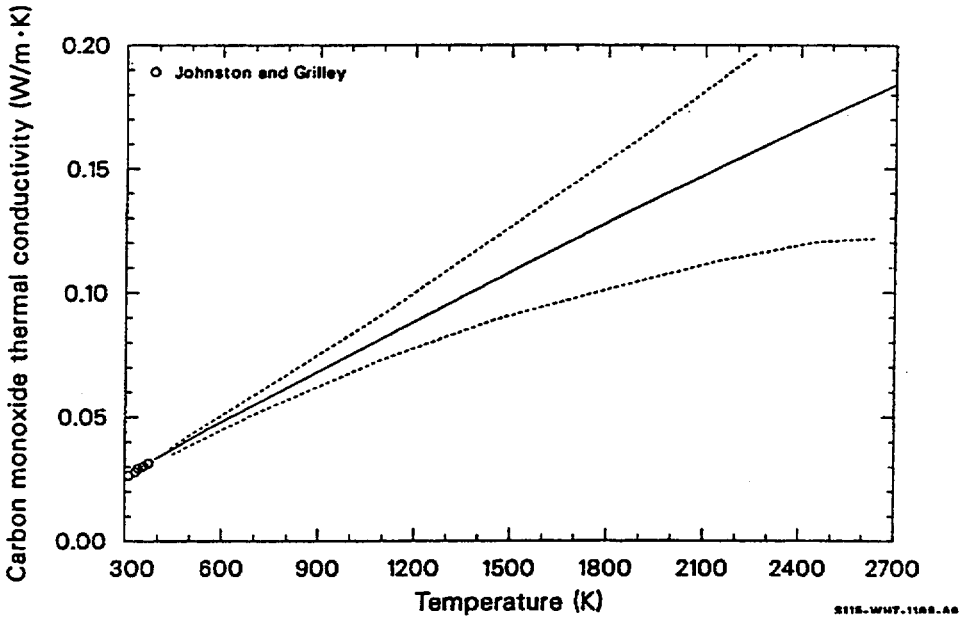

Figure 12-8. Thermal conductivity of carbon monoxide as a function of temperature.

600 K. The temperature dependence of the uncertainty has been forced higher than the dependence indicated by the limited CO_2 data to reflect this concern. A temperature cubed dependence for the expected standard error was selected because the cube is the largest exponent of temperature that gives physically reasonable conductivities over the range of solid fuel temperatures.

The low temperature part of the correlation for the thermal conductivity of steam was taken from the ASME steam tables;[12.1-14] and the tolerance given in this reference, 0.06, times the conductivity, has been adopted as the expected standard deviation.

The high temperature part of the MATPRO correlation was taken from Tsederberg.[12.1-15] Tsederberg's expression was used for high temperatures because the power law he used does not become negative at high temperatures. No data were found above the 973 K limit of the ASME steam tables.

When gases are mixed, the thermal conductivity of the mixture is not simply related to the conductivities of the mixture components because the ability of each component to diffuse through the mixture is affected by the presence of all the other components. The relation between pure gas conductivities and gas mixture conductivities, Equation (12-5), is taken from the work of Brokaw.[12.1-10] Figure 12-10 is a comparison of the conductivities predicted by Equation (12-5) to data reported by Von Ubisch[12.1-3] for helium- xenon mixtures at 793 K. The measurements show excellent agreement with the conductivities predicted by Equation (12-5).

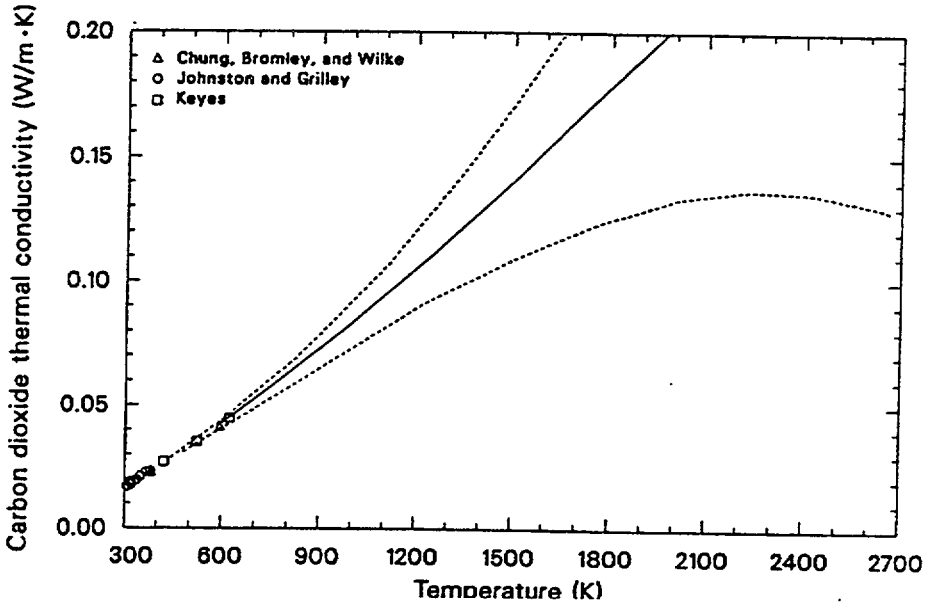

Figure 12-9. Thermal conductivity of carbon dioxide as a function of temperature.

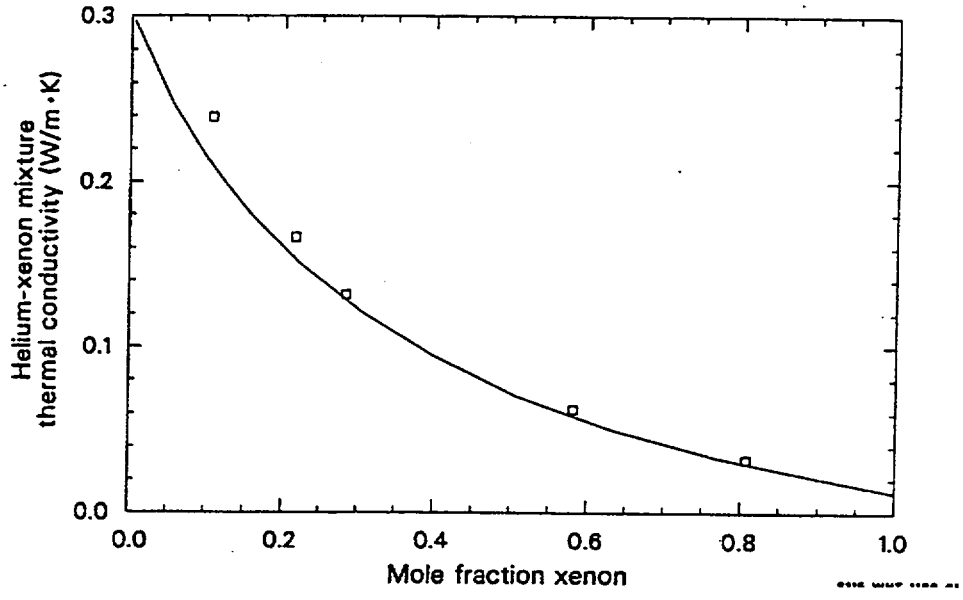

Figure 12-10. Thermal conductivity of helium xenon mixtures at 793 K.

Although less satisfactory agreement can be expected for mixtures containing diatomic molecules that transport energy in rotational and vibrational modes, Equation (12-5) is adequate for fuel rod analysis because the principal gas mixture components are monatomic.

Equation (12-8), the expression for the conduction contribution to the conductance of a gas-filled gap, is based on kinetic theory developed by Knudsen,[12.1-16] as well as the thermal conductivity correlations which have been developed. Knudsen studied low pressure gases and pointed out that molecules striking a surface do not attain thermal equilibrium with the surface in a single collision. The average speed and temperature of molecules that have just collided with a wall are somewhat less than the values implied by the wall temperature. Knudsen derived an expression for the power per unit area transferred from a hot surface to a cold gas

$$W_S = \left(\frac{2R}{\pi M T_g}\right)^{1/2} \frac{1}{4}\left(\frac{\gamma+1}{\gamma-1}\right) P(T_s - T_g) a_{sg} \tag{12-15}$$

where

W_s = power per unit area transferred across the surface (W/m^2)

R = the gas constant (J/(K-mole)

M = molecular weight of the gas (kg/mole)

γ = ratio of the constant volume to the constant pressure specific heats of the gas (unitless)

T_g = temperature of the gas (K)

a_{sg} = surface accommodation coefficient for a particular gas surface interface.

The corresponding expression for the energy transferred from a hot gas to a cold surface is

$$W_S = \left(\frac{2R}{\pi M T_g}\right)^{1/2} \frac{1}{4}\left(\frac{\gamma+1}{\gamma-1}\right) P(T_s - T_g)\left(\frac{a_{sg}}{1-a_{sg}}\right) . \tag{12-16}$$

If the mean free path of the gas molecules is long compared to the gap width, the power per unit area transferred across the gap in steady-state can be found by equating the expressions for the power per unit area across the two surfaces. The resultant expression[12.1-13] is

$$W_{SS} = \left(\frac{2R}{\pi M T_g}\right)^{1/2} \frac{1}{4}\left(\frac{\gamma+1}{\gamma-1}\right) P(T_h - T_c)\left(\frac{a_{hg} a_{cg}}{a_{hg} + a_{cg} - a_{hg} a_{cg}}\right) \tag{12-17}$$

where

W_{ss} = power per unit area transmitted across the gap in the steady-state (W/m^2)

T_h = temperature of the hot gap surface (K)

T_c = temperature of the cold gap surface (K)

a_{hg} = surface accommodation coefficient for the hot surface gas interface (unitless)

a_{cg} = surface accommodation coefficient for the cold surface gas interface (unitless).

Equation (12-17) could have been obtained less rigorously by defining a thermal impedance for each surface

$$r_S = \frac{\Delta T}{W_{ss}} \tag{12-18}$$

where

r_s = thermal impedance for surfaces S ($K\ m^2/W$)

ΔT = temperature difference between the surface and gas (K)

and adding the two series impedances that represent the surfaces to find an effective impedance for the entire gap in the limit of mean free paths that are much longer than gap width. This thermal impedance approach has been adopted to model the conductivity of a fuel rod gap when the gas mean free path is not long compared to gap width.

Single-component gases are considered first. The expression for the power per unit area transferred across the gas is

$$W_B = \frac{k\Delta T_B}{t} \tag{12-19}$$

where

W_B = power per unit area transferred across a region of gas (W/m^2)

ΔT_B = temperature change across the gas (K).

The thermal impedance of the gas is

$$r_B = 1/k \tag{12-20}$$

where r_B is the thermal impedance of gas. Summation of the series thermal impedances that represent the two surfaces and the gas bulk produces the following expression for gap impedance

$$r_{eff} = \frac{t}{k} + \left(\frac{\pi M T_g}{2R}\right)^{1/2} 4\left(\frac{\gamma - 1}{\gamma + 1}\right) + \frac{1}{aP} \tag{12-21}$$

where r_{eff} is the effective impedance of a gap containing a single-component gas (W/m^2K) and $a = a_{hg}a_{cg}/(a_{hg} + a_{cg} - a_{hg}a_{cg})$. The gap conductance is the reciprocal of the effective impedance

$$h = \frac{k}{t + 4\frac{k}{aP}\left(\frac{\gamma - 1}{\gamma + 1}\right)\left(\frac{\pi M T_g}{2R}\right)^{1/2}} \tag{12-22}$$

where h is the gap conductance for a gap containing a single-component gas (W/m^2 K).

Equation (12-22) illustrates several features of gap conductance. The surface impedance term in the denominator is not important for large gaps. For gaps of a given width, the surface impedance is large at low pressures and high temperatures. Finally, the impedance term is most important for gases with large thermal conductivities.

Equation (12-8) is derived with a slight generalization of the arguments just given for a single-component gas. Inspection of Equation (12-5), the expression for the thermal conductivity of gas mixtures, shows that the i-sum in the equation represents the combination of parallel impedances due to each component of the mixture. (The j-sum represents the modification of the scattering cross-section seen by each component due to the presence of all the other components.) The arguments just given for a single-component gas can be repeated for impedance due to each component of the gas mixture. The resultant expression for the gap conductance due to the i-th component of the gas mixture is

$$h_i = \frac{x_i}{t + 4\frac{x_i}{a_i P_i}\left(\frac{\gamma_i - 1}{\gamma_i + 1}\right)\left(\frac{\pi M_i T_g}{2R}\right)^{1/2}} \tag{12-23}$$

where

h_i = gap conductance due to the i-th component of the gas mixture (W/m^2 K)

x_i = i-th term in Equation (12-5)

P_i = partial pressure of i-th component of mixture

a_i = value of factor a of Equation (12-20) for each gas component and the two gap surfaces (unitless)

γ_i = ratio of constant volume to constant pressure specific heats for component i.

The partial pressure of the i-th gas component is given in terms of the mole fraction of the component and the total pressure by the idealized gas law. The relation is

$$P_i = PX_i \ . \qquad (12\text{-}24)$$

Equation (12-8) is obtained by substituting Equation (12-23) into Equation (12-22) and combining the parallel gap conductances due to each component of the mixture.

Values of V_i and M_i are contained in the GTHCON subroutine. The specific heat ratios were taken from Zemansky,[12.1-17] and the molecular weights were taken from the *Handbook of Chemistry and Physics.*[12.1-18]

The surface accommodation coefficients required to use Equation (12-8) were estimated from data and trends mentioned in Section 12.1.2. The coefficients and values of a_i that result are listed in Table 12-3. The accommodation coefficients for helium on zircaloy and fuel were approximated with helium nickel and helium glass data. Hydrogen accommodation coefficients were assumed to be approximately the same as those of helium because of the similar masses of these molecules. The accommodation coefficient for argon on zircaloy was assumed equal to the argon-tungsten coefficient. An estimate for the argon fuel coefficient was obtained by using the ratio of argon and helium coefficients on zircaloy to multiply the helium fuel coefficient. For heavy molecules (krypton, zenon, and carbon dioxide), White's estimate of 0.85 is used for the accommodation coefficients of both fuel and zircaloy. The nitrogen-zircaloy coefficient was adopted for nitrogen, oxygen, carbon monoxide, and steam because of the similar masses of these molecules. A heavy molecule estimate of 0.85 was used for the fuel surface accommodation coefficient of the nitrogen-like group because the estimate obtained from scaling up with the zircaloy surface coefficients was greater than one.

The effective jump distance calculated by GJUMP is determined with Equations (12-5) and (12-8). The mixed gas conductivity is divided by the heat conductance for a gap with zero width and with the two surface accommodation coefficient replaced by the single-surface accommodation coefficient.

12.1.4 References

12.1-1 W. G. Kannuluik and E. H. Carman, "The Thermal Conductivity of Rate Gases," *The Proceedings of the Physical Society, 65*, 1952, pp. 701-709.

12.1-2 R. S. Gambhir, J. M. Gandhi, and S. C. Saxena, "Thermal Conductivity of Rare Gases, Deuterium and Air," *Indian Journal of Pure and Applied Physics, 5*, 1967, pp. 457-463.

12.1-3 H. von Ubisch, "The Thermal Conductivities of Mixtures of Rare Gases at 29° C and at 520° C," *Arikiv foer Fysik, 16,* 7, 1959, pp. 93-100.

12.1-4 V. K. Saxena and S. C. Saxena, "Measurement of the Thermal Conductivity of Helium Using a Hot Wire Type of Thermal Diffusion Column," *British Journal of Applied Physics, 1*, 1968, pp. 1341-1351.

12.1-5 D. L. Timrot and E. E. Totskii, "Dilatometric Method for the Experimental Determination of the Thermal Conductivity of Corrosive Gases and Vapors at High Temperatures," *High Temperature, 3*, 1965, pp. 685-690.

12.1-6 D. L. Timrot and A. S. Umanskii, "Investigation of the Thermal Conductivity of Helium in the Range 400 to 2,400 K," *High Temperature, 3*, 1965, pp. 345-351.

12.1-7 L. S. Zaitseva, "An Experimental Investigation of the Heat Conductivity of Monatomic Gases Over Wide Temperature Intervals," *Soviet Physics Technical Physics, 4*, 1959, pp. 444-450.

12.1-8 H. Cheung, L. A. Bromley, and C. R. Wilke, "Thermal Conductivity of Gas Mixtures," *AIChE Journal, 8*, 1962, pp. 221-228.

12.1-9 H. L. Johnston and E. R. Grilley, "Thermal Conductivities of Eight Common Gases between 97 and 380 K," *Journal of Chemical Physics, 14*, 1946, pp. 223-238.

12.1-10 R. S. Brokaw, "Predicting Transport Properties of Dilute Gases," *IREC Process Design and Development, 8*, 1969, pp. 240-253.

12.1-11 D. L. Timrot and A. S. Umanskii, "Thermal Conductivity of Hydrogen and Argon," *High Temperature, 4*, 1966, pp. 289-292.

12.1-12 F. G. Keyes, *The Heat Conductivity, Viscosity, Specific Heat and Prandtl Numbers for Thirteen Gases*, NP-4621, 1952.

12.1-13 G. K. White, *Experimental Techniques in Low Temperature Physics*, London: Oxford Press, 1959, pp. 181-183.

12.1-14 *Thermodynamic and Transport Properties of Steam*, NewYork: American Society of Mechanical Engineers, 1968.

12.1-15 N. V. Tsederberg, *Thermal Conductivity of Gases and Liquids*, Cambridge: The M.I.T. Press, 1965.

12.1-16 M. Knudsen, *Kinetic Theory of Gases*, New York: John Wiley and Sons, Inc., 1950.

12.1-17 M. W. Zemansky, *Heat and Thermodynamics*, NewYork: McGraw-Hill Book Company, Inc., 1957.

12.1-18 C. D. Hodgman, ed., *Handbook of Chemistry and Physics*, Thirty Eighth Edition, Chemical Rubber Publishing Co., 1956.

12.2 Viscosity (GVISCO)

Viscosity is important in describing the dynamic behavior of fluids. According to kinetic theory, for a gas having a net mass motion, molecules tend to lose forward momentum due to the proximity of stationary surfaces. This loss is described in terms of a viscosity, and it is pertinent to the flow of gas in a fuel cladding gap as well as through a cladding rupture. In particular, the rate at which gas flows into the ballooning section of a fuel rod is inversely proportional to the fill gas viscosity for narrow gaps, becoming less dependent on the gas viscosity as the gap widens and flow becomes turbulent.

12.2.1 Model Development

Bretsznajder,[12.2-1] Bird et al.,[12.2-2] and Hirschfelder et al.,[12.2-3] have discussed in detail the functional relationships for viscosity, which in summary showed dependence on temperature, pressure, and gas composition. The formulation used in the routine GVISCO was taken from Bird et al., and is

$$\mu_{mix} = \sum_{i=1}^{n} \frac{X_i \mu_i}{\sum_{j=1}^{n} X_j \Phi_{ij}} \tag{12-25}$$

where

μ_{mix} = viscosity of gas mixture (kg/m s)

n = number of chemical species in the mixture

X_i, X_j = the mole fractions of species i and j

μ_i, μ_j = the viscosities of species i and j (kg/m s).

Φ_{ij} is a dimensionless parameter defined as

$$\Phi_{ij} = \frac{1}{\sqrt{8}}\left(1 + \frac{M_i}{M_j}\right)^{-1/2}\left[1 + \left(\frac{\mu_i}{\mu_j}\right)^{1/2}\left(\frac{M_j}{M_i}\right)^{1/4}\right]^2 \tag{12-26}$$

where M_i, M_j are the molecular weights of species i and j (kg/mole).

The viscosity of a pure monatomic species may be expressed as

$$\mu_i = 8.4411\times10^{-24}\left(\frac{\sqrt{MT}}{\sigma^2 k\frac{T}{\varepsilon}}\right) \quad (12\text{-}27)$$

where

μ_i = viscosity of specifies i (kg/m s)

M = molecular weight of species (kg/mole)

σ = the collision diameter (m)

T = absolute temperature (K)

ε = the maximum energy of attraction between a pair of molecules (J/molecule)

k = Boltzmann's constant = 1.38×10^{-23} (J/K).

Bird et al. state that Equations (12-25) through (12-27) are useful for computing viscosities of nonpolar gases and gas mixtures at low density from their tabulated values of the intermolecular force parameters σ and ε. Figure 12-11 shows the viscosities for three different cases calculated from Equation (12-25): (a) helium only, (b) an equal molar mixture of helium and zenon, and (c) an equal molar mixture of helium, argon, krypton, and zenon. The routine GVISCO currently allows 10 gases to be considered: helium, argon, krypton, zenon, hydrogen, nitrogen, oxygen, carbon monoxide, carbon dioxide, and steam. Additional nonpolar gases may be readily added to GVISCO if desired.

The viscosity of steam, μ_s, is taken from Meyer et al.[12.2-4]

$$\mu_s = (0.407T - 30.77) \times 10^{-7} \quad (12\text{-}28)$$

where

μ_s = viscosity of steam (kg/m• s)

T = temperature (K).

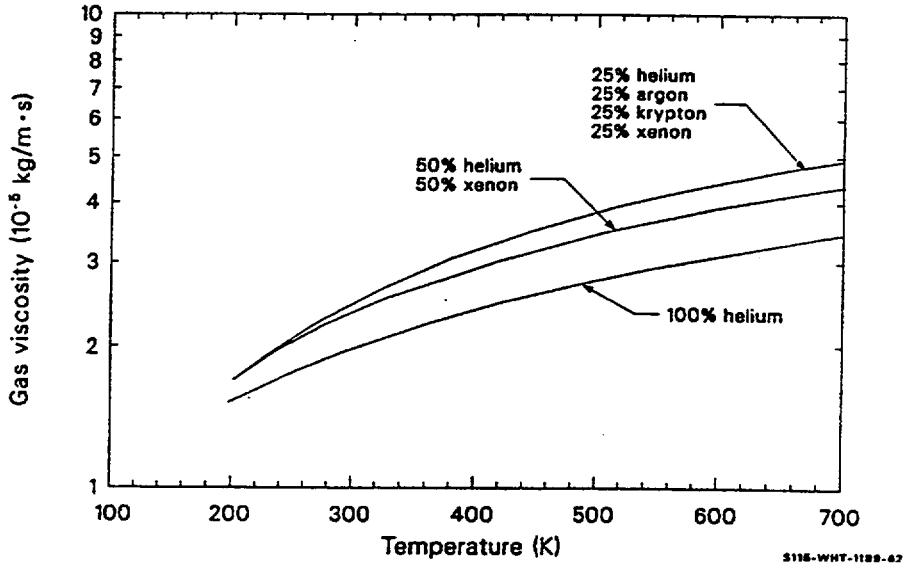

Figure 12-11. Gas viscosity as a function of temperature for pure helium, a binary mixture of helium and xenon, and for an equal molar mixture of helium, argon, krypton, and xenon.

A density correction could be applied, but examination of tabular data indicates the correction is small at typical fuel rod temperatures.

12.2.2 References

12.2-1 S. Bretsznajder, *Prediction of Transport and Other Physical Properties of Fluids*, New York: Pergamon Press, 1971.

12.2-2 R. B. Bird, W. E. Stewart, and E. N. Lightfoot, *Transport Phenomena*, New York: John Wiley and Sons, Inc., 1954.

12.2-3 J. O. Hirschfelder, C. F. Curtiss, and R. B. Bird, *Molecular Theory of Gases and Liquids*, New York: John Wiley and Sons, Inc., 1954.

12.2-4 C. A. Meyer et al., *Thermodynamic and Transport Properties of Steam*, New York: The American Society of Mechanical Engineers, 1967.

13. VESSEL AND COOLANT SYSTEM MATERIALS

Components of the primary coolant system and the reactor pressure vessel lower head, when subjected to high temperature and pressure during an accident, may fail by creep rupture. Leakage through a ruptured primary coolant system component or a steam generator tube will reduce the system pressure, and thus affect the high pressure melt scenario; the timing of vessel failure affects fission gas release and direct containment heating.

A model was developed to calculate the rupture time and creep damage term for A-508 Class 2 carbon steel, SA533 carbon steel, 316 stainless steel, and Inconel 600. This model uses the master creep rupture curves developed by Harris et al.,[13.1-1] and Chavez et al.[13.1-2] The subcode RUPTUR calculates the rupture time and creep damage terms, the subcode TRUPT supplies the parameters and arguments used in RUPTUR, and the subcode CALTAV calculates the average temperature during the time step.

13.1 Rupture Time and the Creep Damage Term Calculations (RUPTUR, TRUPT, CALTAV)

The subcode RUPTUR calculates creep damage and rupture time for A-508 Class 2 carbon steel, 316 stainless steel, and Inconel 600, and SA533B vessel carbon steel. The subcode TRUPT supplies the parameters and arguments used in RUPTUR, and the subcode CALTAV calculates the average temperature during the time step. The input values needed to calculate creep rupture information are the inner and outer wall stresses (Pa), the inner and outer radii of the component (m), the average through-wall temperature during the time step (K) (calculated in the subcode CALTAV), the component material to be considered, the shape of the component, the time since the last rupture calculation, and the previous creep rupture damage term (0.0 for the first creep rupture calculation).

RUPTUR uses the master creep rupture curves developed by Harris et al.[13.1-1] and Chavez et al.[13.1-2] The A-508 Class 2 carbon steel master creep rupture curves use data from creep rupture testing performed at the INEL; 316 stainless steel and Inconel 600 curves use data from available literature,[13.1-3,13.1-4] SA533B vessel carbon steel curves use combined data from creep rupture testing at the INEL and available literature.13.1-2

13.1.1 Model Description

The creep model in RUPTUR calculates creep damage and creep rupture time based on the applied stress and average through-wall temperature histories. Applied stress is calculated for cylindrical and spherical geometries; whereas, if the geometry of the system is rectangular, no stress calculations are performed and the stress is set equal to 0.0. RUPTUR calculates hoop stress and effective (Mises) stresses from the geometry and the pressure differential across the component wall and uses the larger stress. For cylindrical geometry, the largest stress is the hoop stress:

$$s = \frac{p_i r_i - p_o r_o}{r_o - r_i} \quad . \tag{13-1}$$

For a spherical geometry the effective stress is largest:

$$s = \frac{p_i r_i^2 - p_o r_o^2}{r_o^2 - r_i^2} + \frac{p_i - p_o}{2} \qquad (13\text{-}2)$$

where

s = stress (ksi)

p_i = inner pressure (ksi)

p_o = outer pressure (ksi)

r_i = inside wall radius (m)

r_o = outside wall radius (m).

Appropriate conversion factors are used to change input pressure from Pa to ksi, and in some cases stress in ksi to MPa, depending on the units used in the master creep curves. For A-508 Class 2 carbon steel, 316 stainless steel and Inconel 600, the master creep curves were developed using ksi units for stress and Rankine units for temperature. For SA533B vessel carbon steel, the master creep curves were developed using MPa units for stress and Kelvin units for temperature.

The code applies lower bounds to the temperatures and stresses used in creep damage calculations. Significant creep does not occur below approximately half the melt temperature of a given material. For A-508 Class 2 carbon steel, 316 stainless steel, Inconel 600, and SA533B carbon steel, if the average through-wall temperature is below 800 K (1260 R), creep rupture calculations are not performed. The master creep curves may not extrapolate properly for stresses lower than the experimental data. For all materials, if the stress is very close to zero (less than 0.001 ksi or 0.001 MPa), the creep rupture calculations are not performed. For A-508 Class 2 carbon steel, 316 stainless steel, and Inconel 600, if the stress is between 0.001 and 1.0 ksi, the stress is set to 1.0 ksi. Similarly, for SA533B, if the stress is between 0.001 and 3.4 MPa, the stress is set to 3.4 MPa.

The subcode RUPTUR uses the relationships in Table 13-1 and Table 13-2 and a time damage rule to calculate creep damage and rupture time. Larson-Miller[13.1-5] or Manson-Haferd[13.1-6,13.1-7] parameter is correlated to calculate stress using a best-fit analysis for each material (see Table 13-1). In Table 13-1, P_{lm} is the Larson-Miller parameter, P_{mh} is the Manson-Haferd parameter, s is stress and T is temperature. Time to rupture (t_r) is calculated from the parameter definition (Table 13-2) using the average through-wall temperature from CALTAV.

Table 13-1. Creep parameter-to-stress correlations.

Material	Parameter-to-stress correlation	Units
A-508 carbon steel s < 14 ksi	$P_{mh} = 157.233\ (\log)s - 255.346$	s (ksi)

Table 13-1. Creep parameter-to-stress correlations. (Continued)

Material	Parameter-to-stress correlation	Units
A-508 carbon steel $s \geq 14$ ksi	$P_{lm} = -9{,}603.0 (\log)s + 46{,}454.0$	s (ksi)
316 stainless steel $s < 52$ ksi	$P_{lm} = -13{,}320.0 (\log)s + 54{,}870.0$	s (ksi)
316 stainless steel $s \geq 51$ ksi	$P_{lm} = -64{,}000.0 (\log)s + 142{,}000.0$	s (ksi)
Inconel 600	$P_{lm} = -11{,}333.0 (\log)s + 43{,}333.0$	s (ksi)
SA533B carbon steel $s < 60$ MPa and $T \leq 1{,}000$ K	$P_{mh} = -0.014519 (\log)s + 9.8268E\text{-}05$[a]	s (MPa)
SA533B carbon steel $s \geq 60$ MPa and $T \leq 1{,}000$ K	$P_{mh} = -0.021086 [\log(s)]^2 + 0.070806 \log(s) - 0.084949$	s (MPa)
SA533B carbon steel $T > 1{,}000$ K	$P_{mh} = -0.005480 (\log)s - 0.003182$	s (MPa)

a. This correlation differs from Chavez et al.[13.1-2] It offers a better fit to data.

Table 13-2. Time to rupture from parameter definition.

Material	Time to rupture from parameter definition	Units
A-508 carbon steel $s < 14$ ksi	$\log(t_r) = T - 1{,}503.69)/P_{mh} + 3.499$	T (R), t_r (h)
A-508 carbon steel $s \geq 14$ ksi	$\log(t_r) = P_{lm}/T - 20.0$	T (R), t_r (h)
316 stainless steel	$\log(t_r) = P_{lm}/T - 20.0$	T (R), t_r (h)
Inconel 600	$\log(t_r) = P_{lm}/T - 15.0$	T (R), t_r (h)
SA533B carbon steel $T \leq 1{,}000$ K	$\log(t_r) = P_{mh}(T - 440.0) + 14.5$	T (K), t_r (h)
SA533B carbon steel $T > 1{,}000$ K	$\log(t_r) = P_{mh}(T - 520.0) + 7.57$	T (K), t_r (h)

If the vessel remained at a constant stress and temperature throughout its history, no further calculations would be needed. However, since stress and temperature often fluctuate, a time damage rule is used to predict failure. Temperature and stress are assumed constant over individual time steps. Incremental damage for a given time step is defined as the time step divided by the calculated rupture time (with appropriate conversion factors between hours and seconds). Total damage is the sum of incremental damages over all time steps. Creep rupture is predicted when total damage reaches 200% (1.0).

For each location where a creep rupture calculation is to be performed, the total creep rupture damage term is initialized to 0.0 for the first calculation (this is done in the subcode TRUPT) and the calculated damage term from RUPTUR is stored in TRUPT for use in the creep rupture calculation at the next time step. For each time step, the incremental creep damage term is calculated and added to the previous total damage term using the following equation:

$$DCREEP = DCREEP + dt/3600\ t_r \qquad (13\text{-}3)$$

where

DCREEP = the total creep damage term

dt = the time step (seconds)

t_r = rupture time (h) at the current average wall temperature and pressure

$dt/(3600\ t_f)$ = incremental creep damage over current time stress.

Creep rupture calculations are not performed if the following conditions exist in the system: the inner stress minus the outer stress is less than or equal to zero; the stress value is less than 0.01 ksi; or the value for the total creep damage term is 1.0. If the incremental damage term is 1.0, then the wall has already ruptured and additional creep rupture information is not needed.

13.1.2 Model Development

The creep rupture data by Harris et al.[13.1-1] and Chavez et al.,[13.1-2] were used to develop the master creep rupture curves. Table 13-2 and Table 13-3 list data obtained from creep rupture tests performed at the INEEL using A-508 Class 2 carbon steel obtained from Oak Ridge National Laboratory. The creep rupture data used to develop the master curves for 316 stainless steel and Inconel 600 were obtained from the literature and are shown in Table 13-4 and Table 13-5, respectively. Lower temperature ($T \leq 1000$ K) master curves for SA533B carbon steel were developed from literature and INEEL testing.[13.1-2] These data (137 data points) are too numerous to list here. High temperature ($T > 1000$ K) master curves for SA533B carbon steel were developed from INEEL testing, as listed in Table 13-6.

Table 13-3. Creep rupture data of A-508 pressure vessel carbon steel.

Number	Temperature (K)	Stress (ksi)	Rupture time (h)	Minimum creep rate percent (h)	Time to tertiary creep (h)
18	900	20.41	13.7	.62	5.70
14	900	16.23	43.7	.15	12.32
5	925	16.26	9.4	1.02	3.94
15	925	14.24	23.7	.44	9.06

Table 13-3. Creep rupture data of A-508 pressure vessel carbon steel. (Continued)

Number	Temperature (K)	Stress (ksi)	Rupture time (h)	Minimum creep rate percent (h)	Time to tertiary creep (h)
13	925	12.24	42.5	.25	15.03
7	950	16.21	2.449	4.56	0.92
12	950	14.26	4.6	2.66	2.09
10	950	12.17	10.1	1.10	3.77
6	975	16.23	0.440	24.15	0.19
16	975	14.23	1.117	8.99	0.51
11	975	12.22	2.664	4.87	1.23
8	1,000	16.23	0.124	103.44	0.04
9	1,000	12.15	1.006	14.98	0.34
17	1,000	8.16	6.9	2.93	2.58
19	1,025	12.17	0.409	52.38	0.12
20	1,025	8.11	2.603	8.88	0.78

Table 13-4. Stainless steel creep rupture data.

	Stress (ksi) to produce rupture in			
Temperature (F)	1 h	10 h	30 h	100 h
800	64.5	64.5	64.5	64.5
850	63.3	63.3	63.5	63.3
900	62.2	62.2	62.2	62.2
950	60.0	60.0	60.0	60.0
1,000	58.5	58.5	55.0	51.7
1,050	56.0	52.9	47.5	43.4
1,100	53.5	45.1	40.0	36.4
1,150	46.5	38.4	34.0	30.5
1,200	40.0	32.7	29.0	25.6
1,250	35.0	27.8	24.3	24.1

Table 13-4. Stainless steel creep rupture data. (Continued)

Stress (ksi) to produce rupture in				
Temperature (F)	**1 h**	**10 h**	**30 h**	**100 h**
1,300	30.0	23.7	20.8	18.0
1,350	26.0	20.0	17.5	15.0
1,400	22.5	17.1	14.8	12.4
1,450	19.5	14.6	12.6	10.5
1,500	17.0	12.5	10.6	8.8

Table 13-5. Inconel 600 creep rupture data.

Stress (psi) to produce rupture in					
Temperature (F)	**10 h**	**100 h**	**1000 h**	**10,000 h**	**100,000 h**
1,000	74,000	50,000	34,000	23,000	16,000
1,200	34,000	23,000	14,500	9,400	6,000
1,400	13,000	8,400	5,600	3,600	2,400
1,600	7,500	4,800	3,000	1,900	1,200
1,800	4,400	2,800	1,800	1,150	730
2,000	2,100	1,400	920	620	420

Table 13-6. High temperature SA533B creep rupture data.

Temperature (K)	Stress (MPa)	Fail time (h)
1,073.0	70.0	0.95
1,073.0	50.0	5.40
1,073.0	40.0	15.50
1,073.0	30.0	27.00
1,173.0	35.0	1.09
1,173.0	26.0	4.55
1,173.0	19.0	18.10
1,173.0	14.8	42.30

Table 13-6. High temperature SA533B creep rupture data. (Continued)

Temperature (K)	Stress (MPa)	Fail time (h)
1,273.0	16.9	1.90
1,273.0	11.5	7.54
1,273.0	8.7	29.64
1,473.0	9.0	0.98
1,473.0	6.0	7.26
1,473.0	4.0	48.20
1,473.0	3.4	55.10
1,050.0	26.3	18.90
1,150.0	26.5	4.10
1,150.0	12.5	54.70
1,250.0	26.5	0.05
1,250.0	12.6	2.20
1,250.0	8.0	61.20
1,373.0	7.0	0.70
1,373.0	3.5	46.90

Master creep curves were developed from experimental data using the following procedure. Empirically defined parameters (either Larson-Miller[13.1-5] or Manson-Haferd[13.1-6,13.1-7]) were calculated from experimental temperature, experimental rupture time, and material-dependent constants (see Table 13-2). The parameters were plotted against their corresponding experimental stresses. The one or more material constants included in parameter definitions were optimized to provide the best fit for the parameter-to-stress correlation. (These are the numerical constants listed in Table 13-2.) For the carbon steels, a comparison of the best fit for Larson-Miller-to-stress and Manson-Haferd-to-stress plots determined the parameter choice. Evaluations of the remaining materials used only the Larson-Miller parameter. Table 13-1 lists the parameter-to-stress correlations from least-squares fits performed for each of the materials. Figure 13-1 through Figure 13-5 show the parameter versus stress plots.

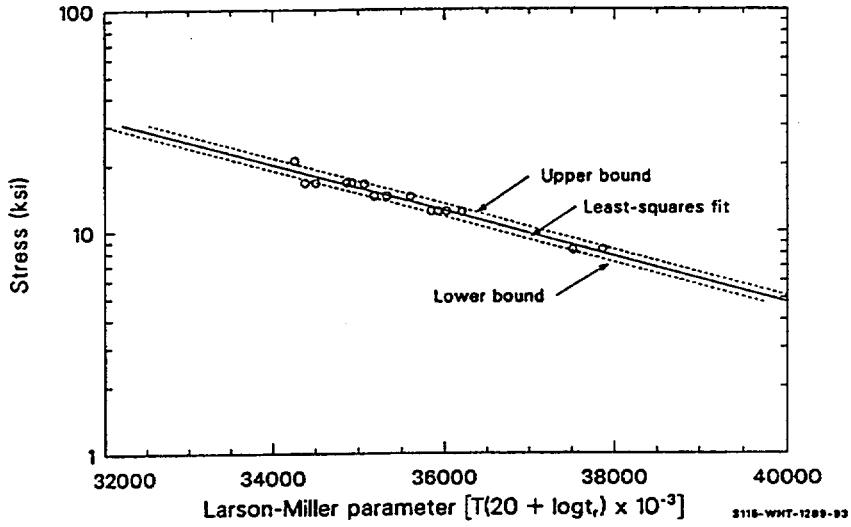

Figure 13-1. Master creep rupture curve for A-508, Class 2 carbon steel.

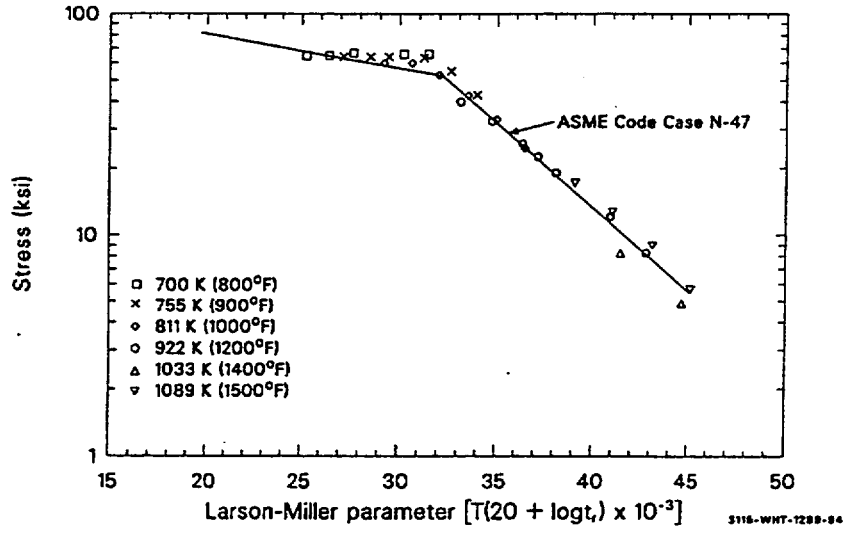

Figure 13-2. Master creep rupture curve for 316 stainless steel.

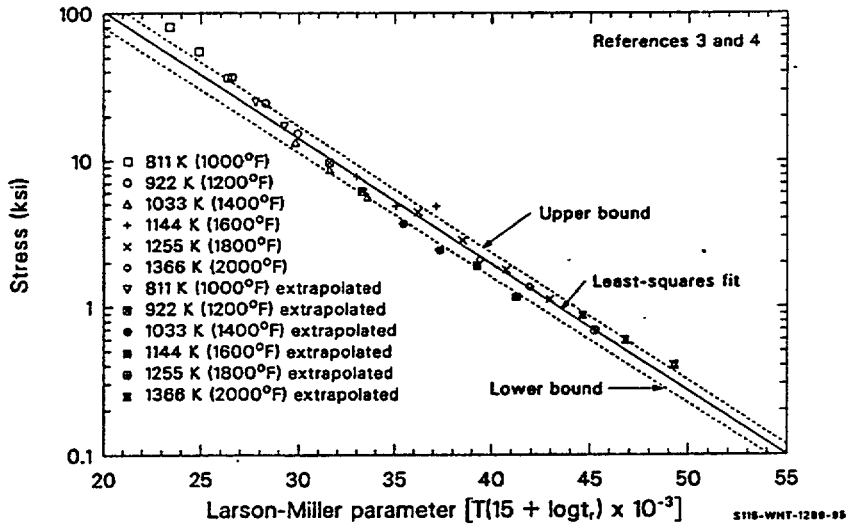

Figure 13-3. Master creep rupture curve for Inconel 600.

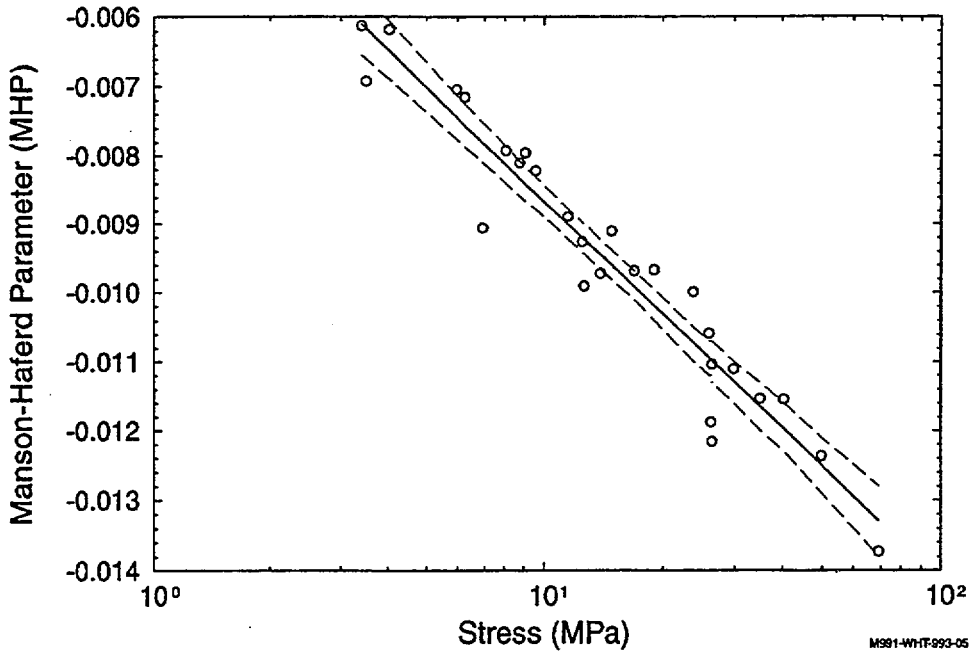

Figure 13-4. Master creep rupture curves for SA533B carbon steel with 95% certainty bounds, T > 1000 K.

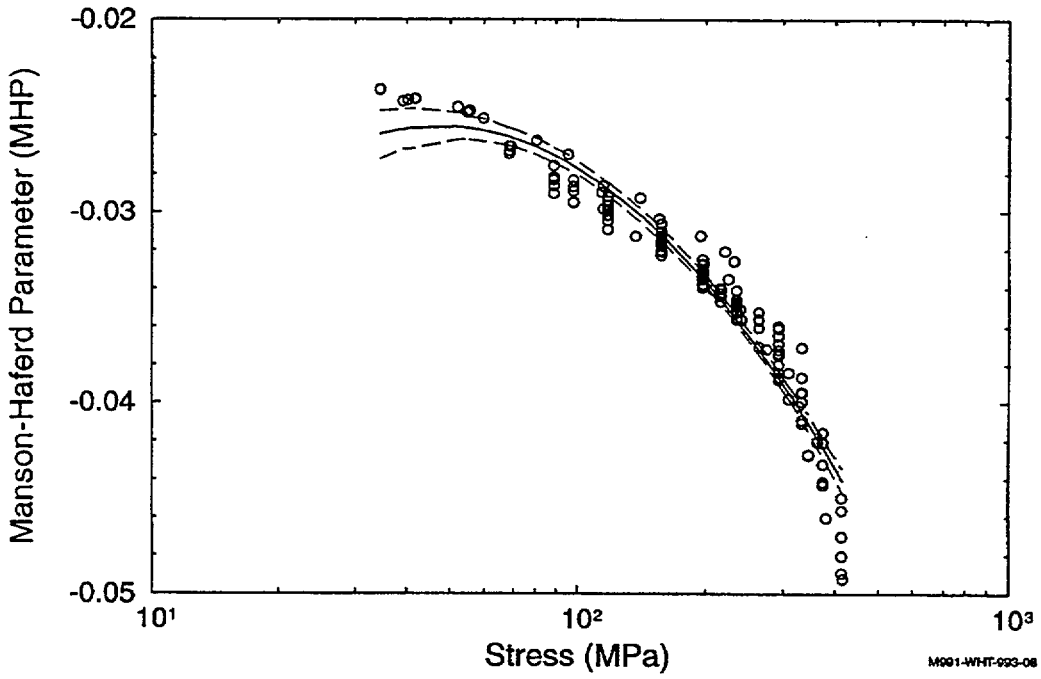

Figure 13-5. Master creep rupture curve for SA533B carbon steel with 95% certainty bounds, T < 1000 K.

13.1.3 References

13.1-1 B. L. Harris, V. N. Shah, and G. E. Korth, *Creep Rupture Failure of Three Components of the Reactor Primary Coolant System During the "TMBL" Accident*, EGG-EA-7431, November 1986.

13.1-2 S. A. Chavez et al., "Comparison of Stress-Based and Strain-Based Creep Failure Criteria for Severe Accident Analysis," *Nuclear Engineering and Design, 155,* 1995, pp. 603-622.

13.1-3 American Society of Mechanical Engineers, *ASME Boiler and Pressure Vessel Code Case*, N-47-22, April 5, 1984.

13.1-4 *Inconel 600 Technical Bulletin*, International Nickel Co., Inc., 5th Edition, 1978.

13.1-5 F. R. Larson and J. Miller, "A Time Temperature Relationship for Rupture and Creep Stress" *Transactions of the ASME*, July 1952, pp. 765-775.

13.1-6 S. S. Manson and A. M. Haferd, *A Linear Time Temperature Relation for Extrapolation of Creep and Stress Rupture Data*, NACA TN 2890, March 1953.

13.1-7 S. S. Manson, "Design Considerations for Long Life at Elevated Temperatures," *ASME/ASTM/IME Joint International Conference on Creep, New York/London, James Clayton Lecture, 1963.*

14. TUNGSTEN

14.1 Specific Heat (TUNGCP)

Specific heat is calculated by subroutine TUNGCP as a function of temperature. The temperature dependent specific heat[14.3-1] values are shown in Table 14-1. Linear interpolation is provided for temperature calls which fall between tabular values. Calls to TUNGCP that are outside of the table range will be returned with either the first or last table value.

Table 14-1. Specific heat of tungsten as a function of temperature.

Temperature (K)	Specific heat (J/kg.K)
295	138.2
373	141.2
573	148.6
773	155.6
1,023	163.9
1,273	171.6
1,523	178.8
1,773	185.3
2,023	191.3
2,273	196.7
2,523	201.6
2,723	205.1
3,073	210.2

14.2 Thermal Conductivity (TUNGK)

Thermal conductivity is calculated by subroutine TUNGK as a function of temperature. The temperature dependent thermal conductivity[14.3-1] values are shown in Table 14-2. Linear interpolation is provided for temperature calls which fall between tabular values. Calls to TUNGK that are outside the table range will be returned with either the first or last table value.

Table 14-2. Thermal conductivity of tungsten as a function of temperature.

Temperature (K)	Thermal Conductivity (W/m-K)
573	124.7
673	122.9
773	121.2
873	119.4
1,073	161.1
1,773	114.5
1,373	111.5
1,573	108.6
2,573	96.73
2,973	93.16
3,173	91.63

14.3 Density Correlations (TUNGRO)

A constant value density[14.3-1] is returned by subroutine TUNGRO. The density value returned is 19,600 (kg/m^3).

14.3.1 Reference

14.3-1 M. Firnhaber, K. Trambauer, S. Hagen, and P. Hofmann, *Specification of the International Standard Problem ISP-31: CORA 13 Experiment on Severe Fuel Damage*, Gesellschaft für Reaktorsicherheit (GRS) mbH, August 1991.

15. DIFFUSIVITIES

15.1 Diffusion of Oxygen in Oxidic Layer

A correlation for the coefficient of diffusion of oxygen in the oxide layer[15-1] for oxide layer temperatures less than 1773 K is

$$D_{ox} = 75.0\times10^{-4}\exp(-22600/T) \quad (15\text{-}1)$$

where

D_{ox} = diffusion coefficient of oxygen in oxide layer (m^2/s),

T = temperature of oxide layer (K).

Equation (15-1) is based upon constants for modeling of oxidation by parabolic kinetics, which in turn are based upon data obtained from experiments on the oxidation of Zircaloy cladding.

For an oxide layer temperature greater than 1773 K, a correlation for the coefficient of diffusion of oxygen in the oxide layer[15-1] is

$$D_{ox} = 20\times10^{-4}\exp(-24000/T). \quad (15\text{-}2)$$

15.2 Diffusion of Oxygen in Metallic Layer

A correlation[15-1] for the coefficient of diffusion of oxygen in the metallic layer of the cladding is:

$$D_M = 4.1\times10^{-4}\exp(-25700/T). \quad (15\text{-}3)$$

15.3 Alternative Correlations for Diffusion of Oxygen in Oxidic and Metallic Layers

An alternative set of correlations for oxygen diffusion coefficients is provided in Reference 15-2. According to this reference, for the temperature range of 1273 K to 1798 K, the correlations for oxygen diffusion coefficients are:

$$D_{ox} = 8.67\times10^{-4}\exp(-40495/RT) \quad (15\text{-}4)$$

Diffusivities

$$D_{\alpha M} = 1.54\times10^{-4}\exp(-48020/RT) \tag{15-5}$$

$$D_{\beta M} = 0.263\times10^{-5}\exp(-28200/RT) \tag{15-6}$$

where

$D_{\alpha M}$ = oxygen diffusion coefficient in alpha phase of cladding (m^2/s),

$D_{\beta M}$ = oxygen diffusion coefficient in beta phase of cladding (m^2/s),

R = $1.987 cal/mole \cdot K$.

For temperature in the range of $1798 \le T \le 2098 K$, D_{ox} is given the correlation

$$D_{ox} = 0.47\times10^{-5}\exp(-25803/RT). \tag{15-7}$$

15.4 Correlation for binary diffusivity in $H_2O + H_2$ mixture

A correlation[15-1] for the binary diffusivity in a $H_2O + H_2$ mixture is

$$D_g = \frac{1.03\times10^{-4}}{p_{tot}}\left(\frac{T}{1273}\right)^{1.68} \tag{15-5}$$

where

D_g = binary diffusivity in a $H_2O + H_2$ mixture (m^2/s),

T = temperature of bulk gas (K),

p = bulk pressure (MPa).

15.5 References

15-1. D. R. Olander, "Materials chemistry and transport modeling for severe accident analyses in light-water reactors, I: External cladding oxidation," Nuclear Engineering and Design 148,1994, pages 253-271.

15-2. A. V. Berdyshev, L. V. Matveev, and M. S. Veshchunov, "Development of the Data Base for the Kinetic Model of the Zircaloy 4/Steam Oxidation at High Temperature ($1000°C \leq T \leq 1825°C$)." IBRAE-97-05, Russian Academy of Sciences, Nuclear Safety Institute, March 1997.

16. UTILITIES

This section describes subcodes that are not logically part of the MATPRO library but are called often by the subcodes in the package. Subcodes described in this section are POLATE, linear interpolation; CTXTUR, texture factor calculations; QFUSON, heats of fusion; PMOLE and PMASS, mass fraction mole fraction conversions; ZUINT, the reciprocal of thermal conductivity; and ATOMFR, which calculates mass fractions of compound materials.

16.1 Linear Interpolation (POLATE, POL8)

A number of the MATPRO subcodes contain tables for a property rather than analytical expressions. POLATE and POL8 are similar subcodes used to interpolate values from tables. POLATE returns an interpolated number x(yy), using an input table consisting of up to 20 x, y pairs, whereas POL8 can handle no more than 13 x, y pairs. These interpolation subcodes are used when analytical expressions based on theory are not available or are too complex, as in the case of cladding specific heat capacity.

The POLATE or POL8 function returns the interpolated value of y(xx), using an input value of xx (the independent variable for which an interpolated dependent variable is desired), the values for the independent variable (up to 20 values for POLATE, only 13 for POL8), and the values for the dependent variable (up to 20 for POLATE, only 13 for POL8). To increase the efficiency of the POLATE or POL8 function, an estimate of the expected location of the value of the input xx in the table of numbers is also accepted. The number of the pair used in a previous interpolation is often used for this estimate.

Beginning with its initial estimated value, the index K is raised or lowered until a pair of xx_k and xx_{k+1} are found which bound xx. $Y(xx_k)$ and $Y(xx_{k+1})$ are then used to interpolate for Y(xx).

If xx is outside the range of the set of xx_k given as input, the y_k of the member of the set of xx_k closest to xx is returned by the POLATE or POL8 functions.

16.2 Cladding Texture Factors (CTXTUR)

Texture factors are required to model all structure sensitive material properties. The subroutine CTXTUR calculates the numbers needed to describe material texture for those material properties subcodes that specifically consider texture variations.[a]

16.2.1 Model Description

The input information for the subcode CTXTUR is obtained from a basal pole figure. The pole figure is a stereographic plot of the relative number of basal poles found at specified orientations. Figure 16-1 is a schematic illustration showing the relation between the basal pole intensity (concentration found from X-ray diffraction) at one orientation and the intensity on a typical pole figure. The intensity, I, at an angle h to the radial direction and u to the circumferential direction of a cladding sample, is projected from its orientation on a sphere of arbitrary diameter to the radius r and angle u in the circumferential axial plane and recorded on the plot as a number, I.

a. In the MATPRO 11 package, only CELAST (Section 4.6) and CAGROW (Section 4.7) require this information.

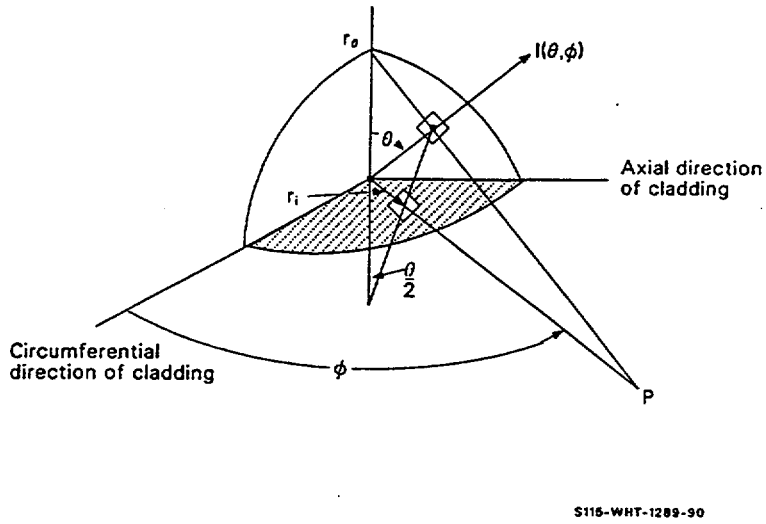

Figure 16-1. Schematic illustration showing the relation between basal pole intensity at one orientation (h,u) and the plotted value of the intensity at (r,u) on a pole figure.

The radius r on the pole figure is related to the angle h by

$$\frac{r}{r_0} = \tan\left(\frac{\theta}{2}\right) \tag{16-1}$$

where r_0 is the radius of the sphere shown in Figure 16-1 and of the pole figure plot.

The input information required by CTXTUR is a 9 X 9 array of basal pole intensities from a pole figure. If h and u are the angles defined in Figure 16-1, element (1,1) of the input array is the average intensity for h from 0 to 10 degrees and u from 0 to 10 degrees. Element (1,2) is the average intensity for h from 0 to 10 degrees and u from 10 to 20 degrees, and so on.

A typical input grid is presented in Figure 16-2. Input element (1,1) would be the average basal pole intensity in the area labeled (1,1) and so on. For the present version of this routine, the pole figure is assumed to represent material with mirror plane symmetry about the planes containing two of the three axes so only one quadrant of the pole figure is used.

Eight volume fraction weighted averages of various cosines are returned by the CTXTUR subcode. In each case, the volume weighted average is defined by the integral

$$\langle g \rangle = \int_0^{2\pi} \int_0^{\pi} g(\theta,\phi)\rho(\theta,\phi)\sin(\theta)d\theta d\phi \tag{16-2}$$

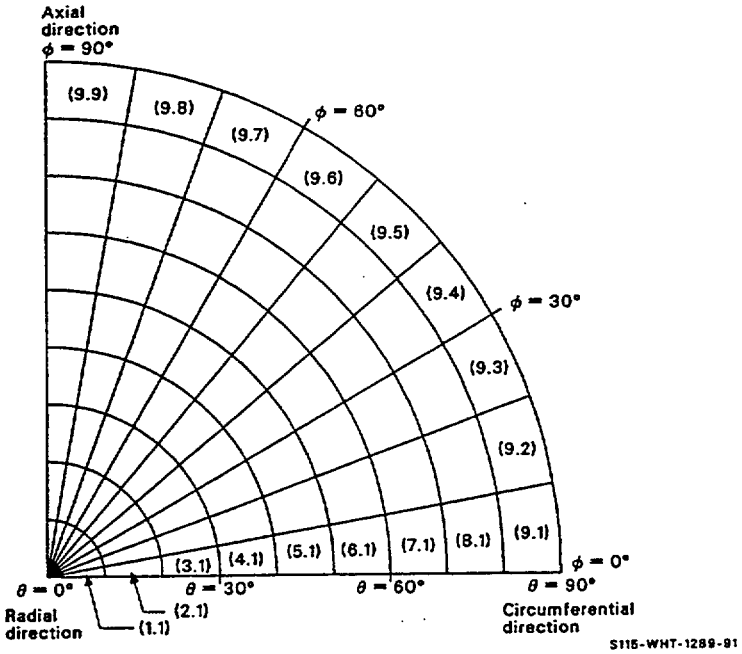

Figure 16-2. Input grid for CTXTUR subcode.

where

g	=	any function of the angles θ and ϕ that have been previously defined
<g>	=	volume fraction weighted average of g
ρ (θ, ϕ)	=	volume fraction of grains with their c-axis oriented in the region sinθdθdϕ about θ and ϕ.

The function ρ is determined by normalizing the input average intensity values to 1/4p for randomly distributed basal poles. The exact normalization equation is

$$\rho(\theta, \phi) = \frac{I(\theta, \phi)}{\frac{2\pi\pi}{\int\int I(\theta, \phi)\sin(\theta)d\theta d\phi}} \qquad (16\text{-}3)$$

$$0\ 0$$

where I (θ, ϕ) is the diffracted X-ray intensity of the basal planes at (h,u), as plotted in basal pole figures.

Equation (16-3) is approximated with a sum of the average X-ray intensities, which is required input information.

$$\rho_{r,s} = \frac{\text{Inputelement}(r, s)}{\sum_{i=1}^{9}\sum_{j=1}^{9} \text{Inputelement}(i, j)\sin\theta_i\left(\frac{\pi}{18}\text{radians}\right)^2} \quad (16\text{-}4)$$

where

$\rho_{r,s}$ = average fraction of grains with their c axis oriented in the (i,j)-th grid element

$\sin\theta_i$ = sine of the angle θ at the center of the (i,j)-th grid element.

Once the weighting factors, $\rho_{r,s}$ have been obtained from the pole figure, the averages defined in Equation (16-2) are approximated with the sum

$$\langle g\rangle = \sum_{r=1}^{9}\sum_{s=1}^{9} \rho_{r,s} g_{r,s} \sin\theta_{r,s}\left(\frac{\pi}{18}\text{radians}\right)^2 \quad (16\text{-}5)$$

where $g_{r,s}$ is the value of g at the center of the (r,s) element.

The eight volume fraction weighted averages returned by the CTXTUR subcode are $\langle\cos^2\theta\rangle$, $\langle\cos^4\theta\rangle$, $\langle\cos^2\alpha\rangle$, $\langle\cos^4\alpha\rangle$, $\langle\cos^2\theta\cos^2\alpha\rangle$, $\langle\cos^2\theta\cos^4\alpha\rangle$, $\langle\cos^4\theta\cos^2\alpha\rangle$, and $\langle\cos^4\theta\cos^4\alpha\rangle$[a], where α is the complement of ϕ.

Several other frequently used texture factors can be obtained from the eight averages returned. For example, the cosine of the angle between the direction defined by θ and ϕ in Figure 16-3 and the circumferential direction of the cladding is

$$\cos\Psi = \sin\theta\sin\alpha \ . \quad (16\text{-}6)$$

The circumferential texture factor defined by Kearns[16.2-1] is thus

$$f_\theta = \langle\cos^2\Psi\rangle = \langle 1\rangle - \langle\cos^2\theta\rangle - \langle\cos^2\alpha\rangle + \langle\cos^2\theta\cos^2\alpha\rangle \quad (16\text{-}7)$$

where f_θ is the circumferential texture factor. Similarly, the axial texture factor of Kearns is

a. For the mirror plane symmetry assumed in this routine, some of these outputs are redundant. For instance, $\langle\cos^2\theta\cos^2\alpha\rangle = \langle\cos^2\alpha\rangle \langle\cos^2\theta\rangle$. The extra outputs are included in case the routine needs to be generalized to consider material without mirror plane symmetry.

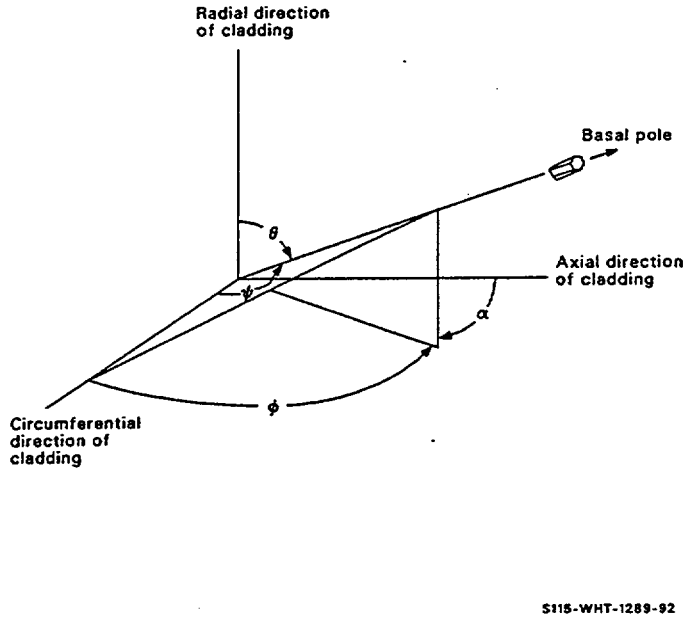

Figure 16-3. Relation between angles used in the definition of Kearn's texture factor (f_u) and angles averaged by CTXTUR subcode.

$$f_z = \langle \cos^2\alpha \rangle - \langle \cos^2\theta \cos^2\alpha \rangle \quad (16\text{-}8)$$

where f_z is the axial texture factor.

16.2.2 Reference

16.2-1 J. J. Kearns, *Thermal Expansion and Preferred Orientation in Zircaloy*, WAPD-TM-472, November 1965.

16.3 Collected Heats of Fusion (QFUSON)

QFUSON calculates the heat of fusion of uranium dioxide, zircaloy, silver-indium-cadmium or boron carbide absorber material, 304 stainless steel, Inconel 718, and zirconium-uranium-oxygen compounds. The required input data are an indicator specifying which kind of neutron absorber is to be considered and the composition of the zirconium-uranium-oxygen compound.

16.3.1 Model Development

The values of the heat of fusion used in QFUSON are given in Table 16-1. All but the last two entries of the table have been discussed in conjunction with enthalpy subcodes. For Inconel 718, the heat of fusion

was estimated by multiplying the molar heats of fusion of nickel and chromium, the main components of Inconel 718, by the atomic fraction of these elements in the alloy[a] and dividing the sum by 0.111, the weight of a gram mole of the alloy in kilograms. The elemental heats of fusion were obtained from pages 186-188 of Reference 16.3-1. For Zr-U-0 compounds, a similar mole fraction weighted average of the molar heats of fusion of $U0_2$, $Zr0_2$, and zircaloy is employed.

Table 16-1. Heats of fusion calculated in QFUSON.

Material	Heat of Fusion (J/kg)
Uranium dioxide	2.74×10^5
Zircaloy	2.25×10^5
Zircaloy oxide	7.06×10^5
Silver-indium-cadmium	9.56×10^4
Boron carbide	2.74×10^5
304 stainless steel	2.5×10^5
Inconel 718	3.2×10^5
Zr-U-O compound	$\frac{(2.74\times10^5)0.27f_{UO_2} + (7.06\times10^5)0.123f_{ZrO_2} + (2.25\times10^5)0.091f_{Zr}}{0.27f_{UO_2} + 0.123f_{ZrO_2} + 0.091f_{Zr}}$

16.3.2 Reference

16.3-1 C. J. Smithells and E. A. Brandes (eds.), *Metals Reference Book,* London and Boston: Butterworths, 1956.

16.4 Mass Fraction Mole Fraction Conversions (PMOLE, PMASS)

PMOLE is a subroutine that calculates the atomic fraction of uranium, zirconium, and oxygen in a uranium-zirconium-oxygen compound given the mass fractions of uranium and zirconium. The inverse conversion is performed by PMASS.

The expressions used to find atomic fractions from mass fractions are:

$$U = \frac{\frac{WU}{0.238}}{\frac{WU}{0.238} + \frac{WZ}{0.091} + \frac{WX}{0.016}} \qquad (16\text{-}9)$$

a. A composition of 0.769 atomic fraction nickel and 0.231 atomic fraction chromium was assumed.

$$Z = \frac{\frac{WZ}{0.091}}{\frac{WU}{0.238} + \frac{WZ}{0.091} + \frac{WX}{0.016}} \quad (16\text{-}10)$$

$$X = 1 - U - Z \quad (16\text{-}11)$$

where

U = atomic fraction of uranium in compound (atoms uranium/atoms compound)

Z = atomic fraction of zirconium in compound (atoms zirconium/atoms compound)

X = atomic fraction of oxygen in compound (atoms oxygen/atoms compound)

WU = mass fraction of uranium in compound (kg uranium/kg compound)

WZ = mass fraction of zirconium in compound (kg zirconium/kg compound)

WX = mass fraction of oxygen in compound (kg oxygen/kg compound).

To find mass fractions from atomic fractions, the following expressions are used:

$$WU = \frac{0.238U}{0.238U + 0.091Z + 0.016X} \quad (16\text{-}12)$$

$$WZ = \frac{0.091Z}{0.238U + 0.091Z + 0.016X} \quad (16\text{-}13)$$

$$WX = 1 - WU - WZ \ . \quad (16\text{-}14)$$

All of these equations can be deduced by regarding the atomic weights of uranium, zirconium and oxygen (0.238 kg/g-mole, 0.091 kg/g-mole, and 0.016 kg/g-mole, respectively) as factors which convert fractions of a kilogram of compound to moles or fractions of a mole of compound to kilograms. Equations (16-11) and (16-14) are simplified forms that use the constraint that all fractions of a compound must sum to one.

16.5 Integral of the Reciprocal of Thermal Conductivity (ZUINT)

The subroutine ZUINT calculates the integral of the reciprocal of thermal conductivity (+ 1/K dt). Required inputs to ZUINT are the percent composition, compound temperature, and a reference temperature. ZUINT returns the integral of the reciprocal of thermal conductivity for each thermal

conductivity computed in the subcode ZUTCON over a temperature range from a reference temperature $\geq$ 200 K to a compound temperature $\leq$ 3,300 K.

Calculation of

$$\int_{RFTEMP}^{ZUTEMP} \frac{1}{K} dt \tag{16-15}$$

is complicated by the fact that the thermal conductivity for each compound shows a discontinuity at phase changes. At the present time, ZUTCON simplistically assumes these phase changes occur at the phase changes of the components. To incorporate variable temperatures and the phase change discontinuities into the subroutine, the integral is divided at temperatures corresponding to these phase changes.

$$\int_{RFTEMP}^{ZUTEMP} \frac{1}{K} dt = \int_{RFTEMP}^{T} \frac{1}{K} dt + \int_{T_1}^{T_2} \frac{1}{K} dt + \ldots + \int_{T_n}^{ZUTEMP} \frac{1}{K} dt \ . \tag{16-16}$$

Integrals from T_i to T_{i+1} on the right-hand side are contained in one data statement, DTEMP, and the temperatures $T_1 \cdots T_n$ are contained in another, TEMP. The two data statements are used to evaluate all except the right and left terms on the right-hand side of Equation (16-16). The end terms, which contain no discontinuities, are evaluated with standard numerical integration techniques. This format allows any reference temperature > 200 K and any component temperature larger than the reference temperature and $\leq$3,300 K to be used. The final value for + 1/K dt is obtained by summing the contribution from each section of the curve.

16.6 Atomic Fraction (ATOMFR)

A number of MATPRO subcodes used the atomic fractions of uranium, zirconium, and oxygen to calculate the materials properties of a Zr-U-O mixture. The masses of uranium dioxide, zirconium, and oxygen due to oxidation in the mixture are input into the subcode ATOMFR; and the mass fractions of uranium and zirconium in the mixture are calculated. These mass fractions are then input into the MATPRO subcode PMOLE to calculate the atomic fractions of uranium, zirconium, and oxygen in the Zr-U-O mixture. The mass fractions of uranium and zirconium are calculated using the following relationships:

$$WTOT = WUO2 + WZR + WOX \tag{16-17}$$

where

WTOT = the total mass of the input materials

WUO2 = mass of uranium dioxide

WZR = mass of zirconium

WOX = mass of oxygen due to oxidation

and

$$FU = (a \ WUO2)/WTOT \quad (16\text{-}18)$$

where

FU = mass fraction of uranium

a = weight fraction of uranium in UO_2 = .8814814

and

$$FZR = WZR/WTOT \quad (16\text{-}19)$$

where FZR is the mass fraction of zirconium.

APPENDIX A

IMPROVEMENTS TO THE MATPRO LIBRARY OF MATERIALS PROPERTIES (PROPERTIES RELATED TO HIGH BURNUP FUEL)

CONTENTS

FIGURES

A1. INTRODUCTION

The MATPRO Library of Material Properties, supplied as part of the SCDAP/RELAP5 severe accident analysis computer code was originally developed in the early 1970s for use with the fuel behavior codes, FRAPCON and FRAP-T. The original release of MATPRO was intended to provide a common ground for materials properties correlations used in fuel behavior analysis. Later, as the need to analyze core behavior during a severe accident arose, extensions, deletions, and improvements were implemented into MATPRO for use with SCDAP/RELAP5 and other severe accident codes. The changes described in this appendix include extensions and improvements related to the availability of new data and new SCDAP/RELAP5 or FRAPCON code capabilities. These new capabilities required broader temperature ranges, or the consideration of additional materials and mixtures of materials. The SCDAP/RELAP5 computer code package, of which MATPRO is a significant part, is being developed under the primary sponsorship of the Office of Nuclear Regulatory Research of the U. S. Nuclear Regulatory Commission, USNRC. The last released version of MATPRO documentation occurred in June of 1995 as part of the general release of SCDAP/RELAP5/MOD3.1. The document released at that time consisted of editorial changes.

The extensions and changes to the MATPRO Library of Materials Properties described in this appendix resulted from continued research at universities and laboratories worldwide and the development of models to consider the behavior of extended burnup fuel in response to requests by utilities and vendors to increase the allowable fuel burnup. In addition, vendors of advanced reactor designs in the U. S. are proposing the use of fuel with higher burnup limits than allowed in current reactor designs. To study the feasibility of extending the time between refueling shutdowns, the fuel behavior code, FRAPCON, was extended to predict the behavior of fuel rods using fuel with higher burnup limits. MATPRO-11 Revision 2 was used for this task. This version of MATPRO contained several cladding behavior routines, CCRPR, CESOID, CHITOX, CSRUPT, and CSIGMA, along with a series of fuel and cladding evaluation subprograms used for licensing assessment calculations and licensing purposes. As part of the high burnup FRAPCON development, changes were made to the MATPRO-11 library of materials properties. Several changes such as those to FSWELL, FTHCON, FUDENS, and CHUTHK could be considered general to MATPRO, others, such as those to CMLIMIT and CKMN, are high burnup fuel rod specific. The development of new correlations by PNNL for use in MATPRO-11, Revision 2, with FRAPCON3 included modeling changes that reflected the known differences in the failure mode between high burnup and fresh fuel. The changed properties include the swelling and cracking of cladding related to the increase in fuel rod internal pressure associated with higher burnup fuel as well as some differences in thermal properties. Modified fuel and cladding behavior subprograms, designated as high burnup, were implemented in MATPRO. The cladding behavior models not presently in the official version of MATPRO and the LBLOCA evaluation and licensing models have also been implemented into MATPRO to extend the applicability of the materials property library over a wider range of fuel burnup and operating conditions.

The sections in this appendix describe the extensions to MATPRO being released with SCDAP/RELAP5/MOD3.3. The described modifications are the materials properties models associated with development of FRAPCON3 for high burnup fuel. The changes to the MATPRO Library described in this appendix will expand the applicability of the MATPRO Library to situations outside the realm of severe accident analysis and standardize the materials properties correlations used in computer codes worldwide. Presently MATPRO correlations are used in MAAP, MELCOR, ATHLET/SA, FRAPCON, FRAP-T6 and numerous single usage codes.

A2. MATERIALS PROPERTY CHANGES FROM HIGH BURNUP FRAPCON DEVELOPMENT

The MATPRO library of material properties subprograms, supplied with SCDAP/RELAP5, has become the standard used for material properties worldwide. As new experimental data become available there is a need to extend the capabilities and applicability of the MATPRO library of material properties subprograms. This appendix describes the modeling changes and modifications to the fuel behavior subprograms for thermal conductivity (FTHCON), specific heat capacity (FCP), enthalpy (FENTHL), swelling (FSWELL), and densification (FUDENS); and the cladding behavior subprograms for hydrogen uptake (CHUPTK), axial growth (CAGROW), low temperature oxidation (CORROS), the equation of state parameters, (CKMN) and mechanical limits (CMLIMT) developed by Pacific Northwest National Laboratory (PNNL). The PNNL models were developed from recently obtained experimental data and the analytical studies performed during the development of the high burnup (greater than 40,000 MWd/MTU) fuel behavior code FRAPCON-3. The models described in this appendix have been implemented in the Idaho National Engineering and Environmental Laboratory (INEEL) version of the MATPRO Library of Material Properties as special high burnup routines supplied with the SCDAP/RELAP5 severe accident computer code.

The new models are the result of recent studies that indicate cladding failure of fuels with higher burnup levels occur by a different mechanism than what was observed for fresh or low burnup fuel rods were used. The cladding on extended burnup fuel rods tends to become oxygen embrittled, with the cladding failure enthalpy being considerably less than that observed for fresh or low burnup fuel rods. An investigation focusing on the changes in materials properties and cladding failure mechanisms for high burnup fuels was undertaken during the development of FRAPCON-3. (FRAPCON-3 contains extensions and modifications to FRAPCON-2, a fuels behavior computer code, for use in predicting the behavior of fuel rods with extended burnup.) MATPRO-11 Revision 2,[A2-1] an older version of MATPRO than the version maintained at the INEEL supplied with SCDAP/RELAP5, was used for the FRAPCON-3 development effort. This version of MATPRO contained several cladding subprograms and a series of steady state evaluation subprograms for large break loss of coolant accidents, LBLOCA, that are not in the present version of the code. Changes made to several subprograms in MATPRO-11, Revision 2, included the incorporation of improved materials property data for cladding and fuel, changes in the temperature ranges covered by the correlations, and in some cases, materials properties correlations developed specifically for high burnup fuel. To make MATPRO applicable to fuel behavior analysis with high burnup, changes were implemented as high burnup specific subprograms in the version of MATPRO being released with SCDAP/RELAP5/MOD3.3 that must be explicitly called.

A2.1 Reinstatement into MATPRO of fuel specific subprograms

MATPRO, the standard for materials properties, is used by many severe accident and fuel behavior computer codes. The following subroutines, CCRPR, CESOID, CHITOX, CSIGMA, and CSRUPT, related to fuel rod cladding behavior currently in MATPRO II Revision 2, were reinstated in the version of MATPRO released with SCDAP/RELAP5/MOD3.2 and maintained under NRC sponsorship at the INEEL. Also, the steady state fuel and cladding behavior evaluation and licensing subprograms contained in MATPRO-II Revision 2, were re-implemented in MATPRO. The implementation of these subprograms makes MATPRO a more versatile and robust code. The models described in this section were transferred from the modified version of MATPRO-11 Revision 2, to the INEEL maintained version of MATPRO, since they were validated and assessed as part of the FRAPCON-3 development effort discussed earlier. A more detailed discussion of the reimplemented subprograms is contained in the MATPRO-11 Revision 2 reference manual.

A2.1.1 Description of Subprograms Re-implemented in MATPRO

CCRPR - The subprogram CCRPR calculates the primary and irradiation caused circumferential components of cladding creep strain at the end of a time step as a function of cladding temperature, the circumferential component of cladding stress, fast neutron flux, time step size, and the primary circumferential component of cladding strain at the beginning of the time step.

CESOID - The subprogram CESOID calculates the quantity of cesium and iodide isotopes available to the fuel rod gap and the maximum temperature attained at a mesh point during operation of the reactor to the end of the time step.

CHITOX - The subprogram CHITOX calculates the zircaloy oxide thickness at the beginning and at the end of a time step, the power generated in the cladding due to a metal-water interaction, and the diameter of the remaining unoxidized portion of the fuel rod cladding.

CSIGMA - The subprogram CSIGMA calculates the power law true stress as a function of true cladding strain, the true cladding strain rate, cladding temperature, average oxygen concentration in the cladding, fast neutron fluence, and cold work.

CSRUPT - The subprogram CSRUPT calculates the fractional increase in the circumference of the cladding at failure in a steam environment as a function of temperature, fast neutron fluence, and cold work.

The evaluation subprograms and their MATPRO equivalents are listed below. These subprograms were incorporated in the MATPRO version being released with the SCDAP/RELAP5 severe accident computer code.

EMCCP (CCP) - cladding specific heat capacity

EMCLEM (CELMOD) - cladding elastic moduli

EMCPIR (CPOIR) - cladding Poissons' ratio

EMCTON (CTHCON) - cladding thermal conductivity

EMCTHXP (CTHEXP) - cladding thermal expansion

EMFCP (FCP) - fuel specific heat capacity

EMFEOD (FELMOD) - fuel elastic moduli

EMFESS (FEMISS) - fuel emissivity

EMFPIR (FPOIR) - fuel Poissons' ratio

EMFTON (FTHCON) - fuel thermal conductivity

EMFTXP (FTHEXP) - fuel thermal expansion

EMGTON (GTHCON) - gas thermal conductivity

EMSTRN - A routine developed specifically for evaluation and licensing purposes. The model which calculates zircaloy strain as a function of temperature and stress, was derived from an evaluation model developed by F. Coffman of the Atomic Energy Commission in 1974 and is described in detail in the MATPRO-11 Revision 2 manual.

A2.1.2 Reference

A2-1. D. L. Hagrman, G. A. Reymann, and R. E. Mason (eds.), *MATPRO Version II (Revision 2) A Handbook of Materials Properties for use in the Analysis of Light Water Reactor Fuel Rod Behavior,* NUREG/CR-0497, TREE-1280, Rev. 2, August 1981.

A2.2 MATPRO - High Burnup Fuel Subprograms

The material properties literature research performed during the development of FRAPCON-3 revealed some newer and better material property data for use in MATPRO. The changes developed from this data and implemented in nine fuel property, cladding property, and constitutive model subprograms, are described in the following sections.

A2.2.1 FTHCONH (FTHCON) - Fuel Thermal Conductivity

The subroutine, FTHCON, which calculates the thermal conductivity of fuel pellets, was modified during the development of FRAPCON-3 to account for fission-induced fuel degradation and the effects of the burnable poison gadolinia (UO_2-GdO_2) content on fuel behavior. The use of fuel containing burnable poisons has become more extensive as fuels are taken to higher burnup levels. The modifications to the fuel pellet thermal conductivity subprogram included a model developed by Lucuta[A2-2] at Chalk River National Laboratory for burnup dependent thermal conductivity, a model developed by Massih[A2-3] to predict the thermal conductivity of fuel rods containing the burnable poison, gadolinia, and porosity effects. The development of the new model is described in the following sub-sections.

A2.2.1.1 Development of the New FTHCONH Model - The Lucuta Correlation. Lucuta and co-workers at Chalk River National Laboratory created unirradiated, sintered urania fuel samples with burnup levels simulated by the addition of a mixture of rare earths. The laser flash method was used to measure the thermal diffusivity of the test samples and calorimetry was used to determine their specific heat capacity. The thermal conductivity of the simulated extended burnup fuel was then deduced from the diffusivity data. The simulated fuel samples used for this study were prepared with burnup levels of 0, 3, and 6 atom percent. Diffusivity measurements were taken for each sample as the sample temperature was increased from 300 to 1,800 K. The thermal conductivity of the simulated fuel was then determined over the entire experimental temperature range. The inverse of the conductivity (resistivity) plotted against temperature for each simulated fuel sample produced parallel straight lines with the offset from the predicted 0% burnup data proportional to the percent of simulated burnup in the fuel sample. The resistivity data suggested fuel degradation due to the accumulation of fission products could be accounted for by adding a term to the denominator of the phonon portion of the thermal conductivity expression. The

thermal conductivity expression, developed by Lucuta from his experimental data to account for the effect of increased burnup levels is described by the following expression.

$$K = 1/[0.053 + (2.2 - 0.005 * b) * 10^{-4} * T + 0.016 * b] \quad \text{(A2-1)}$$

where

K = thermal conductivity (W/m-K)

T = temperature (K)

b = burnup in atom percent of initial uranium atoms.

Burnup in atom percent of initial uranium atoms was determined using the following conversion:

1 MWd = 8.64 e^{+10} joules

1 fission = 200 MeV/fission = 3.204 e^{-11} joules

1 MWd = 2.697 e^{+21} fissions

1 MTU = 2.53 e^{+27} atoms

1 MWd/MTU = 1.066 e^{-6} fissions/U atom, or

= 1.066 e^{-4} atom percent

9383 MWd/MTU = 1 atom percent burnup.

If the expression developed by Lucuta directly replaced the phonon term in the MATPRO correlation for thermal conductivity, the entire thermal conductivity expression, including the porosity correlation for the high temperature electronic contribution, would have to be re-derived by fitting the reference data. Therefore, to simplify the incorporation of the burnup effects, developed by Lucuta, into FTHCONH, a term 0.016 * C_v * b, was added to the central term in the denominator of the phonon term of the MATPRO-11 equation for thermal conductivity where C_v is the specific heat in joules per kilogram and b the local burnup in atom percent.

Thermal conductivity values predicted by the fuel thermal conductivity subprogram, FTHCONH, where the term 0.016 * C_v * b was used to represent the Lucuta correlation, were compared to values obtained using the Lucuta correlation, as derived, for 0, 3, and 6 atom percent burnup. The predicted thermal conductivities, shown in Figure A2-1 through Figure A2-3, from the two correlations agreed to within 5% in the temperature range of interest. Both expressions replicated the measured thermal behavior of the high burnup, thermally stable fuel rods from an experiment performed in the Halden reactor, indicating that the use of the derived adjustment to the correlation used in previous versions of MATPRO was justified. Burnup dependent thermal conductivity was well predicted with the simplified Lucuta term in the denominator of the original MATPRO thermal conductivity correlation.

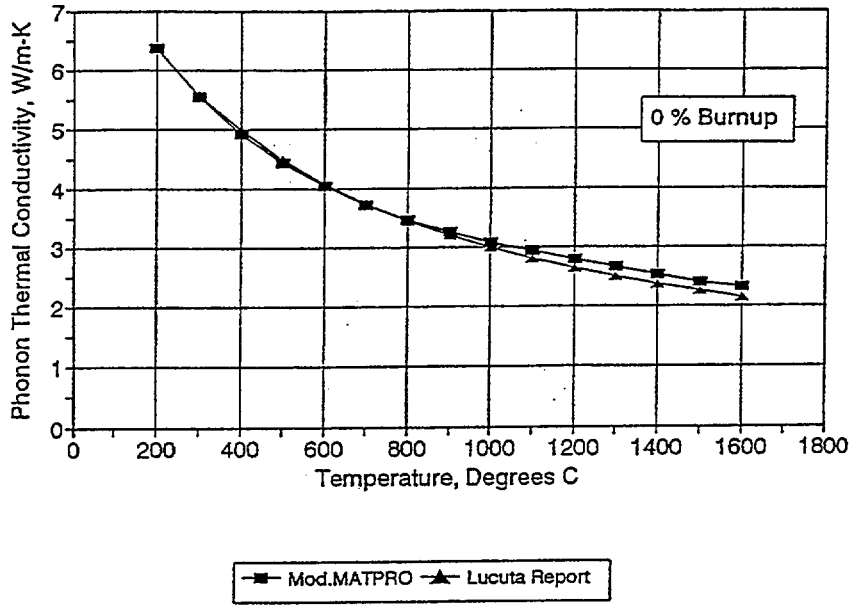

Figure A2-1. Modified MATPRO predicted thermal conductivity from the FTHCONH subprogram, compared to the Lucuta correlation for 0% burnup fuel.

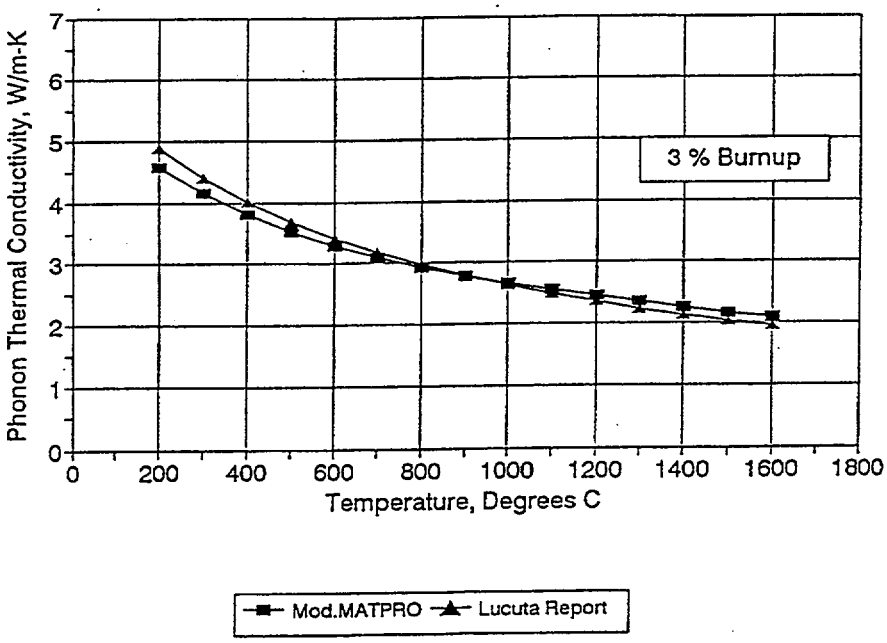

Figure A2-2. Modified MATPRO predicted thermal conductivity from the FTHCONH subprogram, compared to the Lucuta correlation for 3% burnup.

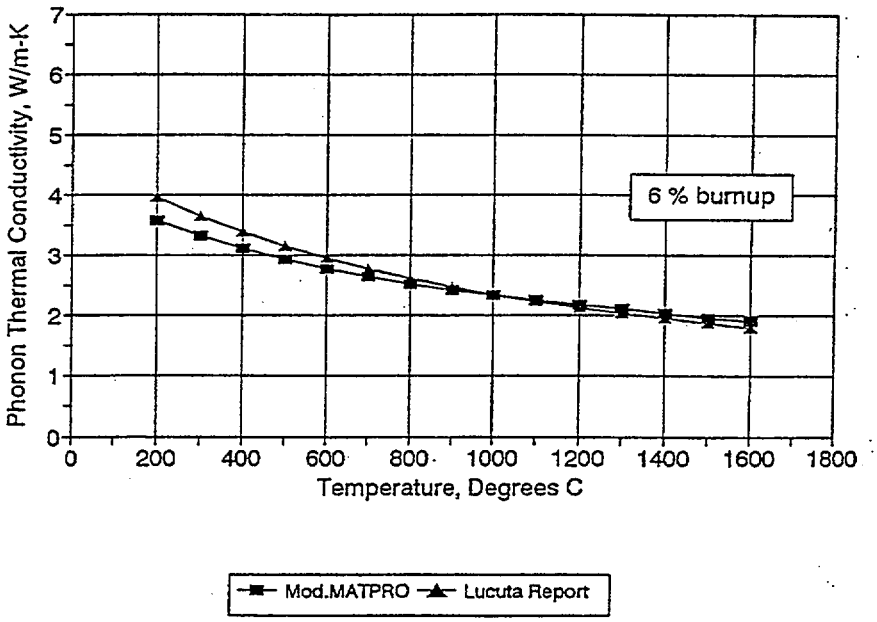

Figure A2-3. Modified MATPRO predicted fuel thermal conductivity from the FTHCONH subprogram, compared to Lucuta correlation for 6% burnup fuel.

A2.2.1.2 Development of the New FTHCONH MODEL - Effects of Gadolinia on Fuel Thermal Conductivity. In reactor cores where high burnup levels are expected, the use of fuels containing a burnable poison (UO_2-GdO_2) has become quite extensive. The effects of the addition of gadolinia, as a burnable absorber for power peaking control early in the life of a fuel assembly, was not considered in previous versions FTHCON, the fuel thermal conductivity subprogram. The addition of gadolinia to the fuel, which effects the fuel grain lattice and phonon-type heat transfer, significantly impacts the thermal conductivity of the fuel. A model, based on ex-reactor experimental measurements for fuel containing gadolinia, developed by Massih, was also added to FTHCONH in the version of MATPRO modified for fuels with high burnup levels. The development of this model is described in the following paragraphs.

The Massih correlation was developed from Babcox and Wilcox laser-flash diffusivity data for urania-gadolinia conductivity.[A2-4,A2-5] Massih used two specific gadolinia concentrations, 2.98 and 5.66 wt%, to develop the following correlation which is similar to the one in the version of MATPRO released as the materials properties package with SCDAP/RELAP5/MOD3.1.

$$K = P * [1.0/(A + a * x + B * T) + C * \exp(d * T)] \qquad \text{(A2-2)}$$

where

K = thermal conductivity (W/m-K)

A = constant 0.1149

P = standard porosity correction factor

a = constant 1.1599

x = weight fraction gadolinia

B = constant 2.48 e^{-4}

T = temperature (K)

C = constant 0.01216

d = constant 0.001867.

The reduction of fuel thermal conductivity due to the effects of the addition of 2, 4, 6, and 8 wt% gadolinia predicted by the Massih model is shown in Figure A2-4. Since the model developed by Massih is very similar in form to the current MATPRO model, the inclusion of the gadolinia term, a * x, (1.1599 * gadoln) in the denominator of the correlation was also implemented in FTHCONH.

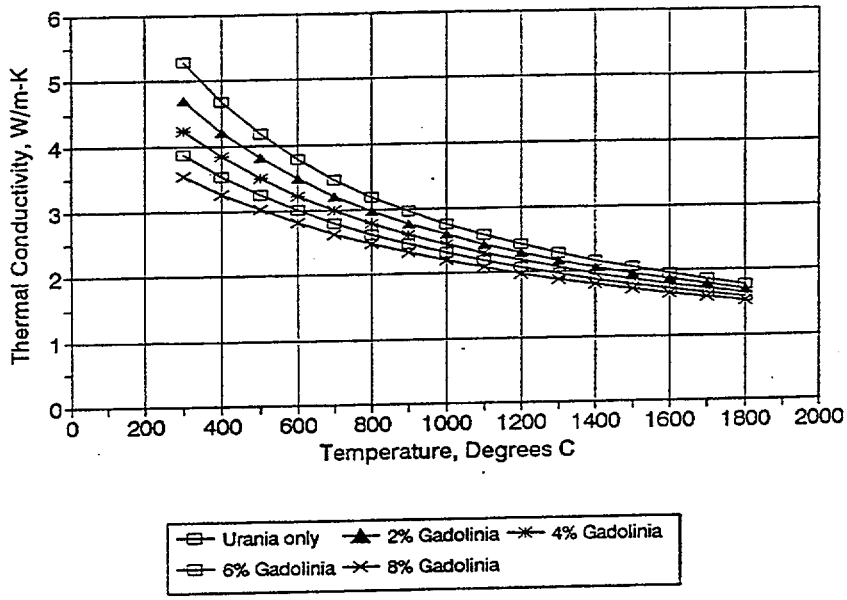

Figure A2-4. Predicted thermal conductivity of fuel samples containing 0 to 8% gadolinia using the Massih model.

To verify the validity of a model, developed using data with a gadolinia content under 5.66 wt%, for fuels with higher gadolinia concentrations, predictions with the proposed model were compared to data from experimental programs that used fuels with higher gadolinia concentrations. The two experimental

programs used for model verification were; (1) the Hirai experiments,[A2-6] and (2) the Fukushima experiments.[A2-7] The Hirai experiments measured thermal conductivities using the laser-flash diffusion method on sintered samples containing 0, 3, 5, 7, and 10 wt% gadolinia over the temperature range of 20 to 1,750 °C; the Fukushima experiments measured the thermal diffusivity of each sample over a temperature range of 400 to 1,350 °C and deduced from this data the thermal conductivity of fuel with gadolinia concentrations from 0 to 10.3 wt%. The comparison of predicted thermal conductivities from the Massih model for 4, 8, and 10 wt% to measured results from these two experiments is shown in Figure A2-5 through Figure A2-7. Predictions from the model were found to be in relatively good agreement with data correlations developed from the above described experiments. As an additional validity check, B&W diffusivity data for fuel samples containing 0, 2.98, 5.66, and 8.5 wt% gadolinia were reduced to obtain thermal conductivity values. The thermal conductivity values determined from the B&W data[A2-4,A2-5] were then compared to both the original stand-alone Massih model and the modified MATPRO FTHCON model, which modeled the high burnup and gadolinia effects. Results from these comparisons are shown in Figure A2-8 and Figure A2-9, and were found to be in relatively good agreement. Figure A2-8 shows the predicted thermal conductivity using the original stand-alone Massih model for fuel with 5.66 wt% gadolinia content compared to experimental data. Figure A2-9 shows the predicted thermal conductivity using the modified Massih model for fuel with the same gadolinia content compared to the experimental data. The Massih model was implemented in the FTHCONH subcode for high burnup fuel because it; (a) is slightly conservative when compared to available experimental data, and (b) was relatively straight forward to implement within the existing MATPRO fuel thermal conductivity framework.

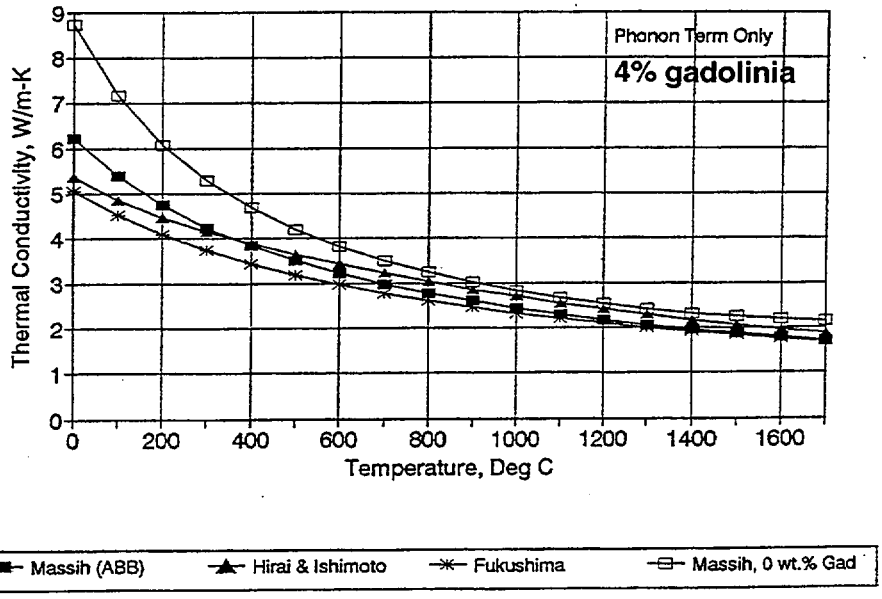

Figure A2-5. Predicted fuel thermal conductivity using the Massih model compared to experimental results for fuel containing no gadolinia.

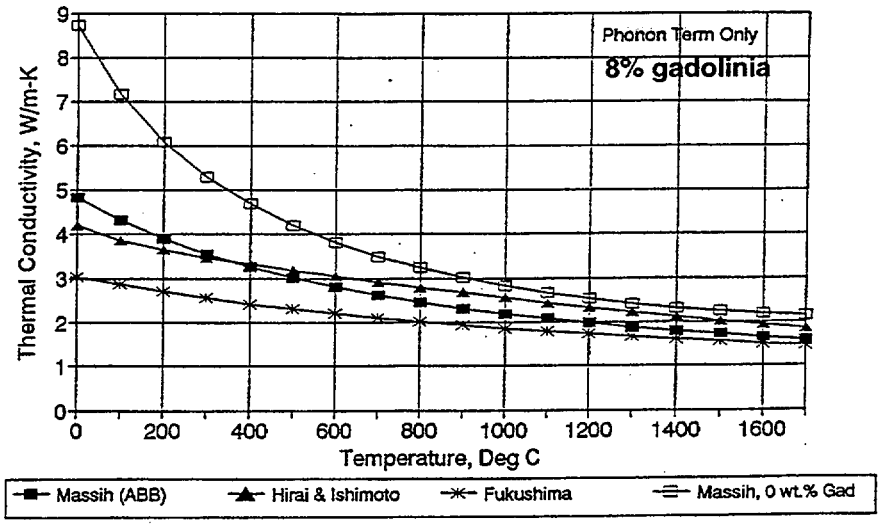

Figure A2-6. Predicted fuel thermal conductivity using the Massih model compared to experimental results and to results from fuel containing no gadolinia.

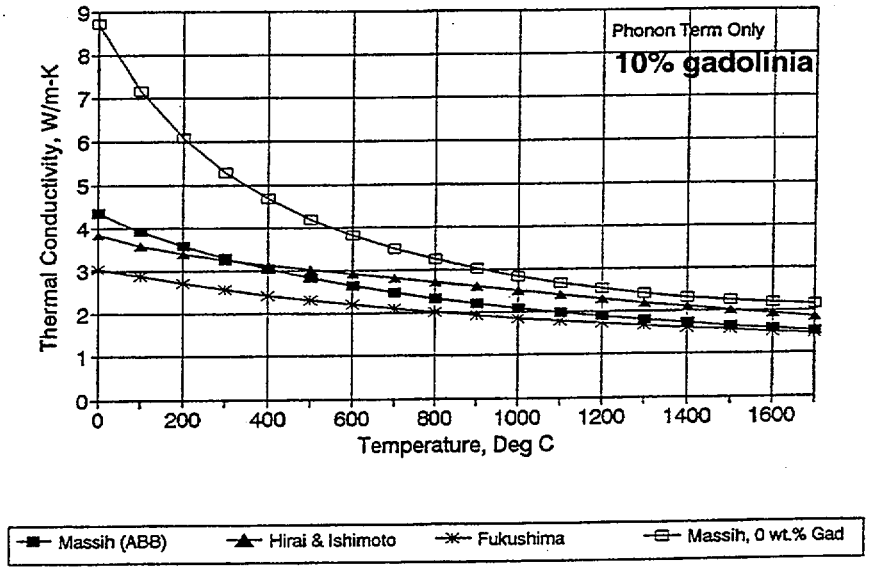

Figure A2-7. Predicted fuel thermal conductivity using the Massih model compared to experimental results and to results from fuel containing no gadolinia.

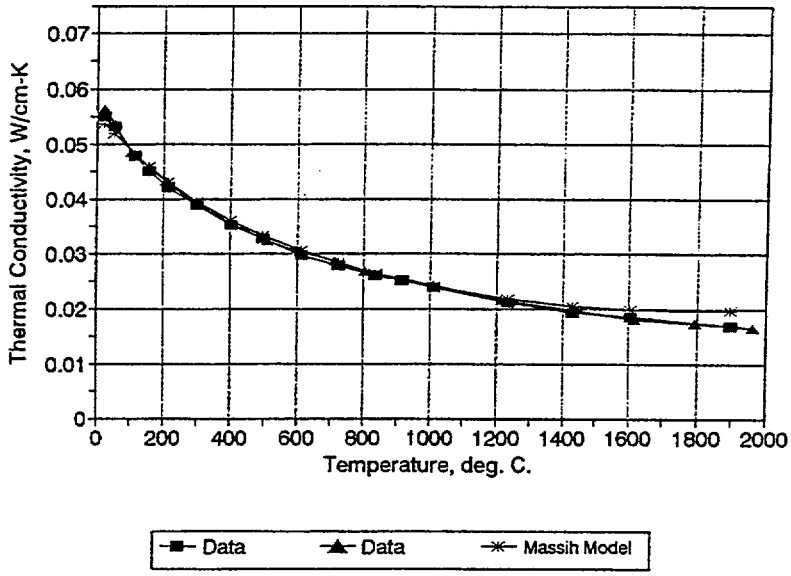

Figure A2-8. Predicted fuel thermal conductivity using the stand-alone Massih model compared to experimental results for fuel with a 5.66 wt% gadolinia content.

A2.2.1.3 Development of the New FTHCONH Model - Effects of Porosity. Additional investigations indicated that fuel porosity can cause a significant temperature dependence at fuel temperatures below 1,000 °C (1273 K). Therefore, a porosity factor was also included in the high burnup FTHCONH correlation used to predict thermal conductivity of fuel. The porosity factor P proposed for the correlation has the form:

$$P = frden/[1.0 + beta * (1.0 - frden)] \quad \text{(A2-3)}$$

where

frden = fuel fractional density (fraction of theoretical density)

beta = a complex function of temperature.

$6.50\text{-}4.69\ e^{-3} * t$ for temperatures < 1,364.647 K

$15.811308\text{-}t * (0.01833647\text{-}t * 5.\ e^{-6})$ for $1{,}364.647 < T \leq 1{,}833.647$

-1.0 for T > 1,833.647

Predicted values for fuel porosity, for a 0.95 fuel fractional density, range from 0.78 at a temperature

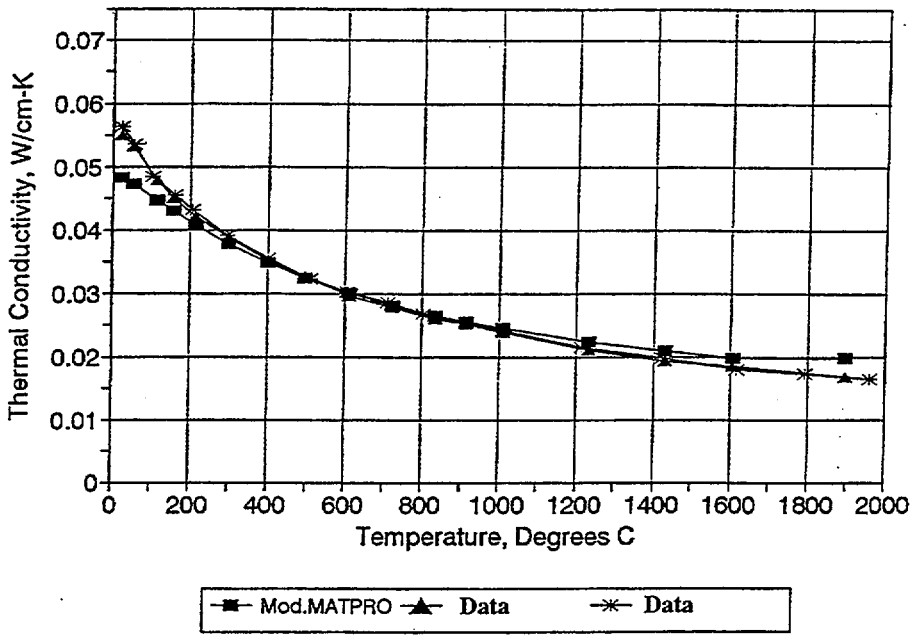

Figure A2-9. Predicted fuel thermal conductivity using a modified MATPRO routine for fuel with the same gadolinia content compared to the experimental data.

of 200 °C (473 K) to 1.0 for temperatures above 1,400 °C (1,673 K). The inclusion of the porosity term in the adjustment factor developed for high burnup fuel from the Lucuta experimental data improved the predicted thermal conductivity considerably. The improvement is shown in Figure A2-10 and Figure A2-10. Figure A2-10 compares the predicted thermal conductivity using the modified FTHCONH subprogram without the porosity correction to the Lucuta experimental data. Figure A2-10 compares FTHCONH predicted thermal conductivity using the porosity correction to the same data. The predicted thermal conductivity for fuel using the modified Lucuta correlation with the porosity term is slightly lower than that predicted by the correlation in earlier versions of MATPRO. The porosity adjustment to the phonon term of the denominator was accomplished by including the value for P, calculated with Equation (A2-3) to the denominator. The phonon term in the denominator of the new correlation which includes the Lucuta term, and a porosity factor becomes

$$0.016 * C_v * P * b \qquad \text{(A2-4)}$$

where

C_v = specific heat capacity

P = porosity

b = burnup in atom percent.

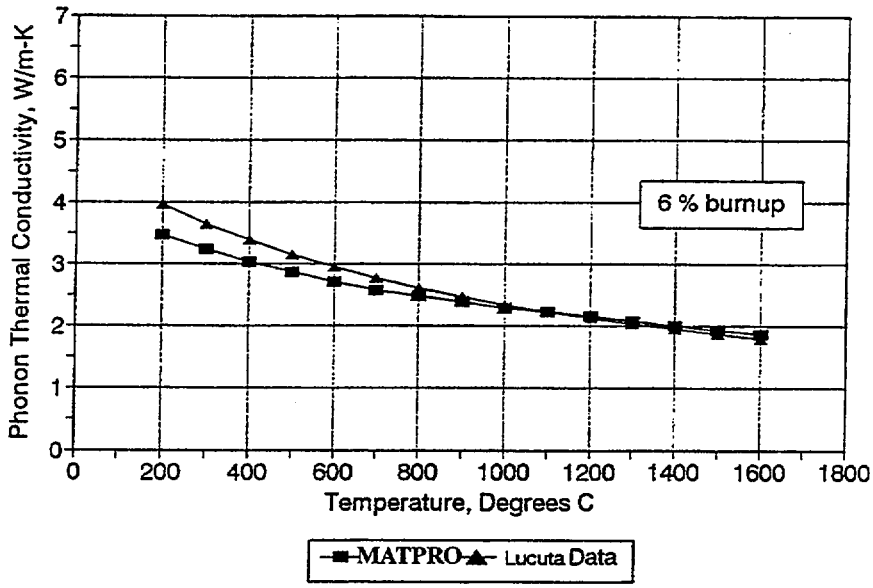

Figure A2-10. Modified MATPRO correlation without porosity correction compared to Lucuta data.

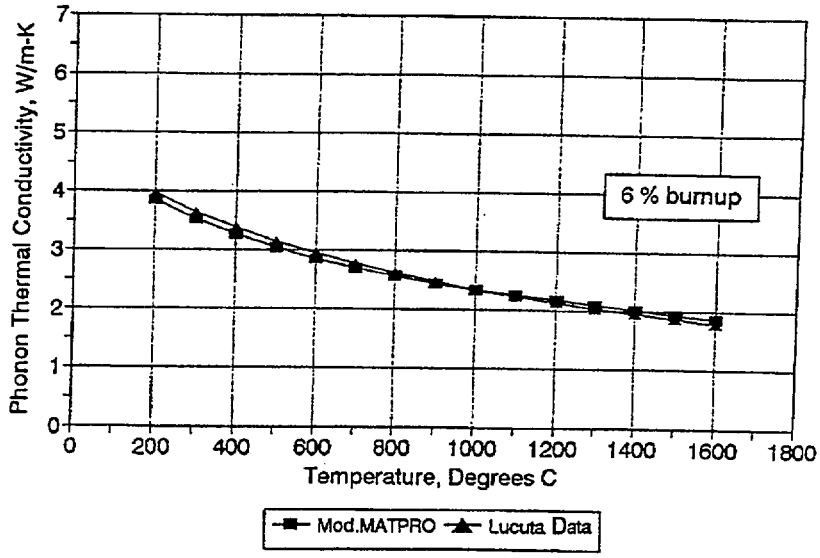

Figure A2-11. Modified MATPRO correlation with porosity correction compared to Lucuta data.

A2.2.1.4 Implementation of FTHCONH into the MOD3.2 MATPRO Source. The above described modeling changes to FTHCONH were implemented in MATPRO-11, Rev 2.[A2-8] The MATPRO FTHCONH subprogram containing the Lucuta correlation, porosity modifications and the effects of gadolinia in fuel with higher burnup levels were implemented in the version of MATPRO maintained under USNRC sponsorship with a high burnup identifier as part of the SCDAP/RELAP5 development effort at the INEEL. The FORTRAN changes to the original FTHCON model in MATPRO-11, Revision 2, and the high burnup identified MATPRO subprogram are summarized below.

1. The local burnup variable BURNUP was added to the FTHCONH variable list. This variable is the current local, ring-average, burnup in MWd/MTU.

2. The local burnup value was divided by 9,383 to convert the burnup term to atom percent.

3. The recommended adjustment term of $0.016 * C_v * b$, developed from the Lucuta data, was included in the denominator of the phonon term in the FTHCONH expression for thermal conductivity.

4. A porosity correction factor, P, was included in the denominator of the phonon term of the thermal conduction correlation.

5. The effects of gadolinia developed by Massih were included in the correlation.

The subprogram developed at PNNL for FRAPCON-3 was implemented into MATPRO, as FTHCONH with the H at the end of the subprogram name indicating that it is a subroutine associated with high burnup fuel. This subprogram, FTHCONH, contains the variables GADOLIN and BURNUP in the argument list and the phonon term correction based on the Lucuta correlations augmented by the term 1.1599 * GADOLIN (Massih) in the denominator of the thermal conductivity expression. Both FTHCON and FTHCONH are in the version of MATPRO being released with SCDAP/RELAP5.

A2.2.2 Thermal Conductivity References

A2-2. P. G. Lucuta et al., "Thermal Conductivity of SIMFUEL," *Journal of Nuclear Materials, 188,* 1992, pp. 198-204.

A2-3. A. R. Massih et al., "Modeling of $(U,Gd)O_2$ Fuel Behavior in Boiling Water Reactors," *Proceeding of Symposium E on Nuclear Materials for Fission Reactors of the 1991 E-MRS Fall Conference, Journal of Nuclear Materials 188,* 1992, pp. 319-330.

A2-4. L. W. Newman, *Development and Demonstration of an Advanced Extended Burnup Fuel Assembly Design incorporating Urania and Gadolinia,* DOE/ET/34212-36, B&W-11681-2, 1982.

A2-5. L. W. Newman, *Thermal and Physical Properties of Urania and Gadolinia Fuel,* DOE/ET/34212-43, B&W-1759.

A2-6. Hirai and S. Ishimoto, "Thermal Diffusivities and Thermal Conductivities of UO_2-Gd_2O_3." *Journal of Nuclear Science and Technology, 28,* 1991, pp. 995-1000.

A2-7. S. Fukushima et al,, "The Effect of Gadolinia Content on the Thermal Conductivity of Near-Stoichiometric (U,Gd)O_2 Solid Solutions," *Journal of Nuclear Material, 105,* 1982, pp. 201-210,

A2-8. D. L. Hagrman, G. A. Reymann, and G. E. Mason, *MATPRO-Version 11 (Revision 2),* NUREG/CR-0479, TREE-1280, Revision 2, 1981.

A2.2.3 FCPH (FCP) Fuel Specific Heat Capacity

The subprogram FCP returns the specific heat capacity for fuel. The function FCP in the MATPRO-11 and INEEL SCDAP/RELAP/MOD3.1 MATPRO source code did not include the effect of the burnable poison gadolinia in the subprogram which predicts the specific heat capacity for fuel. Typical gadolinia burnable poison additions to fuel are less than 8 wt%. It was determined[A2-6,A2-7] that for gadolinia concentrations of less that 8 wt% in the fuel, the magnitude and temperature dependence of the urania and gadolinia specific heats are similar, therefore the impact of limited gadolinia additions to the urania fuel on predicted specific heat capacity is small, less than 5%, and the use of the standard mixing rule is adequate to predict specific heat capacity.

Since the specific heat of the fuel is used to calculate thermal conductivity, for consistency with the high burnup thermal conductivity subprogram, FTHCONH, the effects of gadolinia content on the predicted specific heat capacity were included in the heat capacity subprogram developed by PNNL for use with FRAPCON-3. The variable GADOLN (gadolinia content) was included in the argument list for the high burnup specific heat capacity subprogram, FCPH. The burnup level needed to predict heat capacity is taken from a value stored in the common block PHYPRO as input by the user. The version of the subprogram developed for high burnup fuel by PNNL was implemented in the version of MATPRO source supplied as part of the SCDAP/RELAP5 code package as FCPH with the tailing H indicating that the subprogram is high burnup fuel specific. The parameters used in the high burnup subprogram to calculated the heat capacity function were re-defined to include the influence of burnup from the common block PHYPRO, and the effects of the burnable poison, gadolinia. The parameters used for the gadolinia properties, developed from data obtained from a paper written by Eberle and Stackman[A2-9] and a curve fit of the data for temperatures below 1,500 K were implemented in FCPH as a data set. The specific heat of the urania-gadolinia mix was then determined using the gadolinia property parameters and weighting the urania-gadolinia specific heats by their respective mass fractions.

The changes to the FCPH subprogram included the addition of a gadolinia data set and the addition of an additional equation to predict specific heat capacity changes as a function of gadolinia content in the fuel. The equation used to consider the effects of the gadolinia content in the fuel is as follows:

$$fcp = fcp * (1\text{-}gadoln) + gadolin * cp(c1gd,c2gd,c3gd,thgd,edgd,t,fotmtl) \quad \text{(A2-5)}$$

where

fcp	=	specific heat capacity
gadolin	=	weight fraction gadolinia
fotmtl	=	oxygen to metal ratio

cp = preliminary specific heat for gadolinia calculated by a function defined internally in the subprogram.

The above equation is applied to the initial specific heat capacity term predicted by the correlation in the MOD3.1 MATPRO and MATPRO-11 source. The addition of the equation which corrects the specific heat capacity as a function of gadolinia will also allow the subprogram FCPH to be used with FRAPCON-3, for fuels with 0% to 15 wt% gadolinia. If the wt% gadolinia in the fuel is zero, the predicted specific heat capacity will be identical to that calculated using the original MATPRO correlation.

A2.2.4 Specific Heat Reference

A2-9. R. Eberle and J. Stackman, *Recommended Material Correlation for Thermal Conductivity, Heat Capacity, and Solidus Temperature of UO_2/Gd_2O_3 Fuel,* Erlangen Report B111/84/eZ48a, 1984.

A2.2.5 FENTHLH (FENTHL) - Enthalpy of the Fuel

The subprogram FENTHL, which calculates the enthalpy of the fuel, modified to include the influence of burnable poison, gadolinia, during the development of a version of FRAPCON for high burnup fuels is not a part of the MATPRO-11 Revision 2 source but is a part of the FRAPCON-3 source code. During the early 1990's, materials properties subprograms in the SCDAP/RELAP5 source program were removed from the source and implemented in MATPRO, making the MATPRO materials properties library more robust. The modifications made to the FENTHL subprogram in FRAPCON are similar to those made in FCP. The high burnup version of FENTHL was implemented in the INEEL maintained MATPRO source code as FENTHLH.

The subprogram FENTHL currently in the version of MATPRO supplied with SCDAP/RELAP5 does not return a fuel enthalpy term for fuel assemblies containing the burnable poison, gadolinia. Typical gadolinia additions to the fuel are less than 8 wt%. For gadolinia additions of less that 8 wt%, the magnitude and temperature dependence for urania and gadolinia enthalpies are similar, therefore the impact of limited gadolinia additions on the predicted enthalpy is small and the use of the standard mixing rule is adequate to predict the enthalpy.

To be consistent with the changes to the thermal conductivity, FTHCONH, and specific heat capacity, FCPH, subprograms, which include the effects of the burnable poison, gadolinia, the following changes were implemented in the function, FENTHL for high burnup fuel. The variable GADOLN, weight percent gadolinia, was included in the argument list passed into the subprogram and a set of parameters defining gadolinia properties were implemented in the function as a data statement. The enthalpy of the urania-gadolinia mix is then determined by weighting the predicted urania and gadolinia enthalpies by their respective mass fractions. The equation implemented to predict enthalpy changes as a function of gadolinia content in the fuel is given below:

$$\text{fenthl} = \text{fenthl} * (1-\text{gadoln}) + \text{gadoln} * \text{enthl}(\text{c1gd},\text{c2gd},\text{c3gd},\text{thgd}, \text{edgd},\text{t},\text{fotmtl}) \quad \text{(A2-6)}$$

where

gadoln = weight fraction gadolinia

t	=	temperature
fotmtl	=	oxygen to metal ratio
enthl	=	enthalpy of gadolinia calculated using a enthalpy function defined internally in the subprogram.

The implementation of the above equation in the INEEL maintained MATPRO would require the inclusion of the variable gadoln in the function argument list, the addition of the equation to predict enthalpy based on the quantity of gadolinia in the fuel, and the definition of the gadolinia term in each calling subprogram (through input stored in common). The inclusion of the equation to predict enthalpy based on gadolinia content does not effect the predicted results for fuel containing no gadolinia. The high burnup function, FENTHL was implemented in the INEEL maintained MATPRO source as FENTHLH, the ending H identifying the routine as high burnup.

A2.2.6 FSWELLH (FSWELL) - Fuel Swelling

The function FSWELL in MATPRO-11 and the SCDAP/RELAP5/MOD3.1 version of MATPRO calculates the fuel swelling caused by the buildup of solid and gaseous fission products during irradiation, returns a swelling term based on the (1) predicted fission product-induced, and (2) gas-induced swelling as a function of the burnup increment in the current time step. The subprogram modified during the development FRAPCON-3 predicts the swelling of fuels with higher burnup levels. The high burnup model eliminated gas-induced swelling as a factor in the predicted fuel swelling and enhanced the fission product-induced swelling term. These modifications were implemented by PNNL in the MATPRO-11, Revision 2, subprogram, FSWELL, after a review of fuel pellet swelling data from commercial PWRs, BWRs, and test reactors indicated that the fuel swelling model in both the INEEL maintained MATPRO and MATPRO-11 under-predicted solid swelling and over-predicted gaseous swelling.

The fission product induced solid swelling rate in MATPRO-11, $\Delta V/V$, is 7.74e-9 MV-s/kgU for 95% theoretical density fuel, corresponds to a rate of 0.669% per 10 GWd/MTU. Estimates of the solid swelling rate for fuels with higher burnup levels, obtained from data derived from fuel pellets irradiated in commercial PWRs, ranged from 0.7 to 1.0% per 10 GWd/MTU.[A2-10-A2-14] A least squares fit of high burnup swelling data yielded a line with a slope corresponding to a rate of 0.77% per GWd/MTU with an uncertainty of 10% of the predicted value shown in Figure A2-12. Simulations and sensitivity studies using the swelling correlations in MATPRO-11 subprogram FSWELL, showed a negligible contribution from the gaseous fuel swelling term to total fuel swelling. Information obtained from comparing results from this series of sensitivity studies using a model modified to reflect the new rate to experimental data indicated that a correction factor of 1.15 (0.77/0.699) should be applied to the predicted solid fission product induced swelling rate. The solid swelling term in the subprogram was thus changed from

$$soldsw = 2.5\ e^{-23} * Bu \qquad \text{(A2-7)}$$

to

$$soldsw = 2.875\ e^{-23} * Bu \qquad \text{(A2-8)}$$

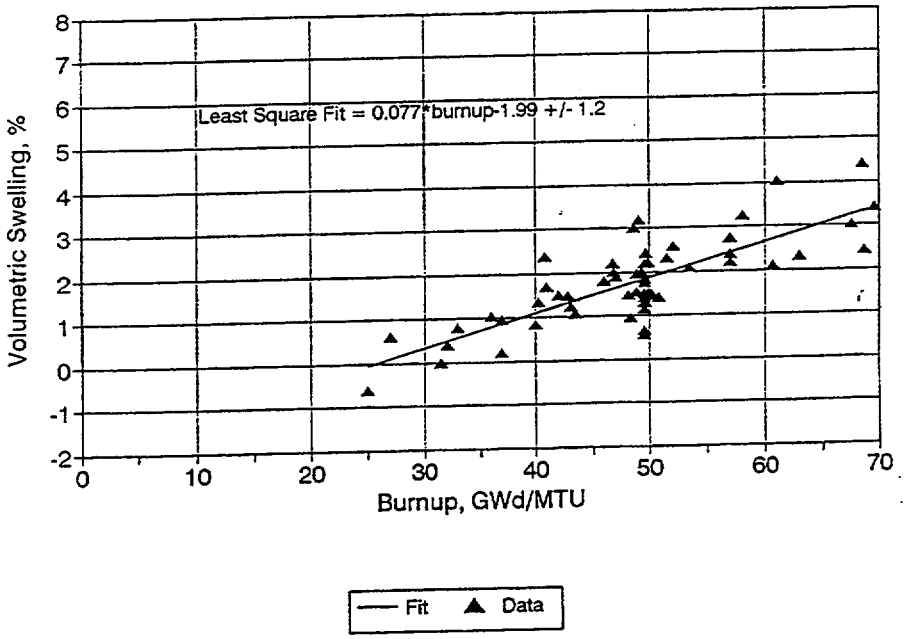

Figure A2-12. Least squares fit of recent volumetric swelling data.

where

Bu = burnup.

The gas-induced swelling term in MATPRO-11 is a complex function of temperature multiplied by an exponentially decreasing function of the burnup level. Gas induced swelling predicted by the MATPRO-11 model results from an increase in the number of bubbles of fission gases within the fuel pellets. As a first step in the development of the high burnup model, the unmodified version of FSWELL in MATPRO-11 was used to predict gas-induced swelling for fuels with higher burnup levels and the predicted results compared to swelling results from the high burnup model and measured data. Figure A2-13 shows predicted percent fuel swelling from the unmodified version of FSWELL predicted percent swelling from the modified FSWELL, and fuel swelling data taken from a rod, IFA-432, irradiated in the Halden reactor.[A2-15] The figure shows the unmodified FSWELL model significantly over-predicting fuel swelling, whereas the high burnup FSWELL model, which does not consider the gas-induced swelling term is in good agreement with experimental Halden fuel swelling data. The gas-induced swelling model in the unmodified FSWELL predicts gas-induced swelling to increase significantly when a small fraction of the fuel pellet exceeds 1,500 K. This increased swelling when combined with the swelling predicted by the solid fission-induced swelling model resulted in the observed over-prediction. Results from the comparison of predicted swelling from the high burnup model and the MATPRO-11 model with experimental data as shown in Figure A2-13 indicated that the gas-induced swelling model did not apply well to fuel pellets constricted by their own thermal stresses and constrained by cladding. Some experiments[A2-16] indicated that gas induced swelling may be burnup dependent when the fuel burnup is greater than 25 GWd/MTU. The FSWELL model in MATPRO-11 does not contain a dependence on burnup level.

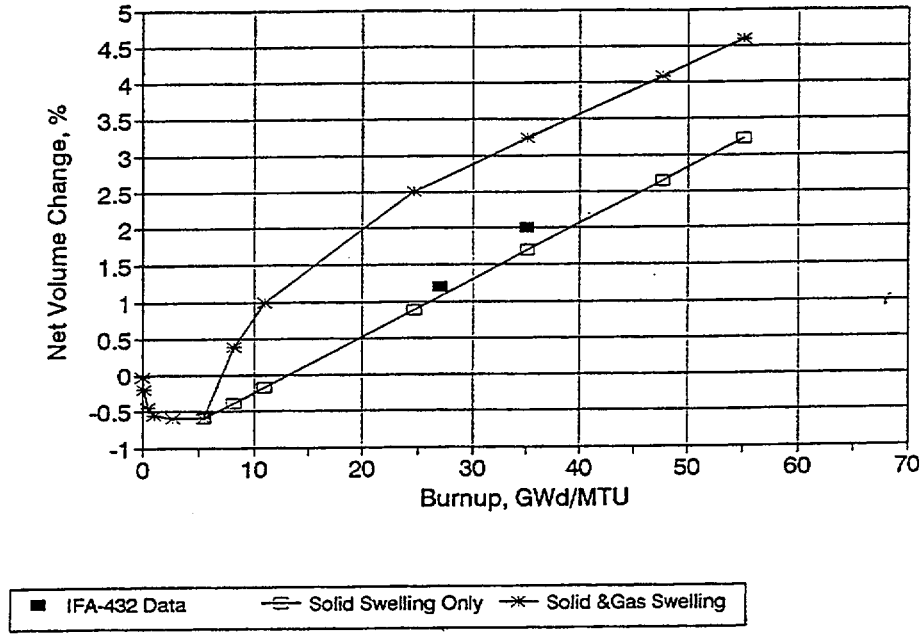

Figure A2-13. Predicted MATPRO fuel swelling compared to data from the Halden IFA-432 rod data.

Comparing swelling data from experiments using BWR fuel rods, which may experience higher fuel temperatures due to thermal feedback, with PWR fuel rod data shown in Figure A2-14, shows the BWR data lying within the normal scatter band. The figure shows that the uncertainty bands derived from the solid swelling rate bound the swelling data for both PWRs and BWRs. Therefore, the gas induced swelling term can be removed from the correlations used to predict fuel swelling.

Presently there is a lack of fuel performance and swelling data at high temperatures and burnup levels greater than 45 GWd/MTU for model verification. A concern exists that at high burnups, greater than 55 GWd/MTU, gas induced swelling may be the dominant factor for fuel swelling, due to the presence of additional fission gases within the grains and or on the grain boundaries. The additional gas induced swelling could lead to significant cladding stresses and strains during power transients and possibly lower thresholds for cladding failure. As data becomes available, the inclusion of burnup dependency for gas induced swelling at high burnup levels will be investigated.

The modifications to FSWELL described above have been implemented in the INEEL maintained MATPRO source code as FSWELLH, indicating that the subprogram was developed for high burnup fuel.

A2.2.7 References for FSWELLH

A2-10. A. M. Garde, *Hot Cell Examination of Extended Burnup Fuel from Fort Calhoun,* DOE/ET/34030-11, 1980.

A2-11. C. G. Dideon, *Fuel Performance under Extended Burnup for the B&W 15 x 15 Design,* DOE/ET/34212, 1983.

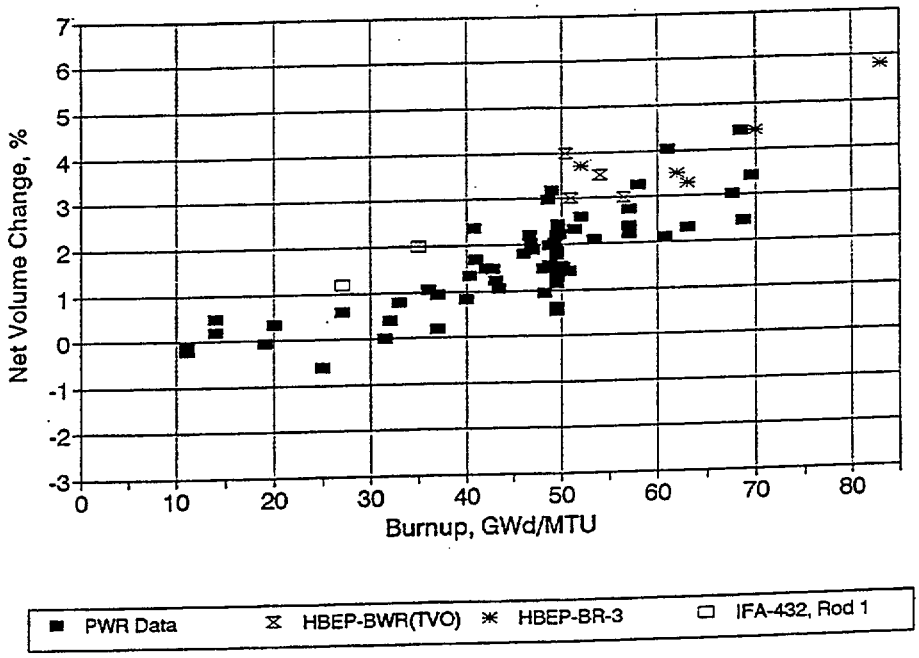

Figure A2-14. Comparison of fuel swelling experimental data from PWR and BWR fuel rods.

A2-12. L. W. Newman, *Hot Cell Examination of Oconee 1 Fuel Rods after Five Cycles of Irradiation,* DOE/ET/34212-50, 1986.

A2-13. G. P. Smith, *The Evaluation and Demonstration Method for Improved Nuclear Fuel Utilization,* DOE/ET/34013-13, 1994. (For CE 16 x 16 ANO-2 Fuel rods.)

A2-14. G. P. Smith, *Hot Cell Examination of Extended Burnup Fuel from Calvert Cliffs-1,* TR-103302-V2, 1993 (For CE 14 x 14 Calvert Cliffs fuel rods.)

A2-15. D. D. Lanning and E. R. Bradley, *Irradiation History and Interim Postirradiation Data for IFA-432,* NUREG/CR-3071, 1984.

A2-16. J. O. Barner et al., *High Burnup Effects Program Summary Report,* DOE/NE/3406-1, 1990.

A2.2.8 FUDENSH (FUDENS) - Fuel Densification

The fuel densification model in both the INEEL maintained MATPRO and MATPRO-11, FUDENS did not predict the correct radial strain across the fuel pellet for high burnup fuel. The densification model calculates fuel dimensional changes due to irradiation induced densification of UO_2 and $(U,Pu)O_2$ during the first few thousand hours of LWR operation, as a function of burnup, temperature, and initial density. The original MATPRO subprogram was developed from fuel stack UO_2 length change measurements in experiments performed by Rolstad in the Halden HBWR reactor,[A2-17] and from pellet density resintering and in-reactor densification data determined from pre- and post-irradiation measurements of samples from

an EPRI fuel densification experiment.[A2-18] The INEEL maintained MATPRO and previous MATPRO-11 model uses one of two methods to predict the maximum density change during irradiation. If a non-zero value for the density change for resintered fuel pellets is input the following equations are used to predict the dimensional change due to irradiation.

For temperatures less than 1,000 K

$$(\Delta L/L)_m = - (0.0015)RSNTR \quad \text{(A2-9)}$$

and for temperatures greater than 1,000 K,

$$(\Delta L/L)_m = - (0.00285)RSNTR \quad \text{(A2-10)}$$

where

$(\Delta L/L)_m$ = maximum dimensional change due to irradiation

RSNTR = resintered fuel density change.

If no resintering density change is input into the subprogram, the following equations are used to predict the dimensional change due to irradiation.

For temperatures less than 1,000 K

$$(\Delta L/L)_m = - (22.2)(100 - DENS)/(TSINT - 1180) \; . \quad \text{(A2-11)}$$

For temperatures greater than 1,000 K

$$(\Delta L/L)_m = - (66.6)(100 - DENS)/(TSINT - 1180) \quad \text{(A2-12)}$$

where

DENS = theoretical density (%)

TSINT = sintering temperature (K).

The fuels used in the mid-1970's to obtain data for the correlations in the INEEL maintained MATPRO and MATPRO-11 came from very low density, unstable fuel for which the maximum densification was very large. Modern power reactor fuel assemblies contain highly stable fuel pellets,[A2-19] controlled by standardized re-sintering tests. The maximum in-reactor density increase, under normal operating conditions, for the newer fuel pellets is less than or equal to 1% of the as fabricated value. There is no clear evidence that the newer fuels show a temperature dependence on maximum densification. Also

recent investigations of reactor fuels indicate that the originally determined reduction in fuel density for temperatures less than 1,000 K may have been flawed by PCMI effects, which can occur at low linear heating rates.

The MATPRO function FUDENS was changed during the development of FAPCON3 by PNNL to incorporate experimental data obtained from experiments performed using the newer, stabler fuels. The following changes were made to FUDENS by PNNL; (1) the low temperature option used to predict the maximum dimensional change due to irradiation was removed from the function to reflect the incorporation of newer data in the correlation, and (2) the default variable for the resintered density change, rstnr, was changed from 0.0 to 100 kg/m^3. The change in the value for the resintered density will yield a maximum densification of approximately 1%, the upper bound for modern fuel. In the high burnup version of FUDENS, the following relationship

```
if[(ftemp.ge.1000.).and.(rsntr.gt.0.)] dlen1=0.00285 * rsntr
```

was changed to read

```
if(rsntr.gt.0) dlen1=100. * rsntr/(3 * fdens)
```

where

fdens = input fuel density.

The PNNL densification changes to FUDENS have been implemented in the INEEL maintained MATPRO source code as the function FUDENSH. The H flags the subprogram as one developed as part of the PNNL developed high burnup computer program FRAPCON-3. The inclusion in MATPRO of the high burnup modified subprogram, FUDENSH will extend the applicability of the function to new fuels, such as those modeled in FRAPCON-3.

A2.2.9 References for FUDENSH

A2-17. E. Rolstad, "In-Reactor Measurements of Fuel Stack Shortening," *Enlarged Halden Program Group Meeting on Computer Control and Fuel Research, June 4-7, 1974.*

A2-18. E. W. Brite et al, *EEI/EPRI Fuel Densification Project, Research Project 131, Final Report,* revised June, 1975.

A2-19. D. D. Lanning, Pacific Northwest Laboratories, letter dated May 20, 1996.

A2.2.10 CHUPTKH (CHUPTK) - Cladding Hydrogen Uptake

The subroutine CHUPTK calculates the average weight fraction of hydrogen in zircaloy at typical reactor operation temperatures of 523 to 650 K. After a review of high burnup fuel rod data which focused on fuel oxidation and the hydrogen content[A2-20-A2-24] in the cladding, subprogram CHUPTK was modified by PNNL in MATPRO-11 during the development of FRAPCON-3 for use with fuels with higher burnup levels. The weight fraction of hydrogen picked up by the cladding, pickup fraction, predicted by CHUPTK is defined as the ratio of the average quantity of hydrogen per unit length of the cladding less the initial hydrogen concentration to the total hydrogen produced by waterside oxidation of

the cladding assuming the following stoichiometric relation:

$$Zr + 2H_2O \rightarrow ZrO_2 + 2H_2 \ . \qquad \text{(A2-13)}$$

The INEEL maintained MATPRO and MATPRO-11 subprogram CHUPTK assume a post transition fraction of 0.12. Postirradiation examinations of PWR fuel rod cladding typically report pickup fractions to be between 10 and 20%. The examination of cladding oxidation and cladding hydrogen concentration post irradiation examination data from a number of fuel rods with rod-average burnups ranging from 38 to 62 GWd/MTU indicated an average hydrogen pickup fraction for PWR fuel rod cladding of 15%. These examinations also revealed no consistent trend related to oxide thickness or temperature for observed variances in the predicted pick up fraction.

The CHUPTK model in MATPRO-11 for post-transition hydrogen uptake for PWR cladding uses a post-transition average hydrogen pickup factor of 12%, but actually predicts hydrogen concentrations in the 5 to 6% range. This underprediction occurs since the calculated hydrogen concentration is divided by a temperature-dependent corrosion irradiation enhancement factor with a value near 2.0. Experimental studies performed for the N-reactor at PNNL showed that hydrogen pickup was enhanced to the same degree as fuel oxidation in the reactor,[A2-25] therefore it was determined that the division by the irradiation enhancement factor should not be performed. To correct this model and extend it to correspond to recent high burnup data, the following changes to the model were made; (1) The division by the radiation enhancement factor A was eliminated, and (2) the post-transition pickup fraction was increased from 0.12 to 0.15 for PWRs. The modified correlations are as follows:

$$H_{cf} = [Zd_0/(d_0)^2 - (d_i)^2] * [b/8 * (x_f - x_i)] \qquad \text{(A2-14)}$$

for oxide films thinner than the transition thickness

$$H_{cf} = \{Zd_0/(d_0 - d_i)^2] * [b/8(x_{tran} - x_i) + [c * (b/8)] * (x_f - x_{tran})\} \qquad \text{(A2-15)}$$

for oxide films equal to the transition thickness and

$$H_{cf} = [Zd_0/(d_0^2 - d_i)^2] * [c * (b/8) * (x_f - x_i)] \qquad \text{(A2-16)}$$

for oxide films greater than the transition thickness

where

H_{cf} = weight fraction of hydrogen added to the cladding

d_0 = cladding outside diameter

d_i = cladding inside diameter

Z	=	constant 9.0 e^5
b	=	fraction of hydrogen liberated by the reaction with the coolant that is absorbed by the cladding during pre-transition oxidation
c	=	fraction of hydrogen liberated by the reaction with the coolant that is absorbed by the cladding during post-transition oxidation
x_i	=	oxide layer thickness at start of the current time step (m)
x_f	=	oxide layer thickness at end of the current time step (m)
x_{tran}	=	oxide layer thickness at transition point (typically 2.0 e^{-6} m).

Hydrogen concentrations predicted by the revised model were compared to measured concentrations and were in good agreement with the measured data. The comparison of the modified CHUPTK predicted results to the measure data is not presented in this appendix since the hydrogen uptake data is proprietary. Very little measured data exists for hydrogen uptake in the fuel rod cladding associated with the uniform oxidation of BWR fuel. Uniform oxidation associated with BWR fuel rod cladding is considerably less than the oxidation associated with PWR fuel rod cladding, thus the uptake of hydrogen by the cladding is considerably less. After comparing results using the CHUPTK model, with the enhancement factor A removed, to available BWR data,[A2-26] it was determined that the post-transition hydrogen pickup factor used in the subprogram CHUPTK in MATPRO-11 should remain at 0.12 for BWRs. With the enhancement factor removed, the MATPRO-11 correlation in CHUPTK will produce an upper bound prediction for hydrogen concentration in BWR cladding. The cladding hydrogen pickup rate is larger and more strongly dependent on the oxide thickness for BWR zircaloy-2 cladding as opposed to BWR zircaloy-4 cladding. Measured BWR pick-up rates are in qualitative agreement with predictions from the BWR CHUPTK model presently in MATPRO-11, with the enhancement factor A removed.

The changes described above were implemented in the subprogram CHUPTK by PNNL. This version of CHUPTK was implemented in the INEEL maintained version of MATPRO as CHUPTKH (the tailing H flagging the subprogram as high burnup). The changes, based on new data, are of a general nature and will give good results over a wide range of burnup levels, 0 to 62 GWd/MTU.

A2.2.10.1 References for CHUPTKH.

A2-20. A. M. Garde, *Hot Cell Examination of Extended Burnup Fuel from Fort Calhoun,* DOE/ET/34030-11, 1980.

A2-21. C. G. Dideon, *Fuel Performance under Extended Burnup for the B&W 15 x 15 Design,* DOE/ET/34212, 1983.

A2-22. L. W. Newman, *Hot Cell Examination of Oconee 1 Fuel Rods after Five Cycles of Irradiation,* DOE/ET/34212-50, 1986.

A2-23. G. P. Smith, *The Evaluation and Demonstration Method for Improved Nuclear Fuel Utilization,* DOE/ET/34013-13, 1994. (For CE 16 x 16 ANO-2 fuel rods.)

A2-24. G. P. Smith, *Hot Cell Examination of Extended Burnup Fuel from Calvert Cliffs-1,* TR-103302-V2, 1993 (For CE 14 x 14 Calvert Cliffs fuel rods.)

A2-25. D. D. Lanning et al, "Corrosion and Hydriding in N-Reactor Pressure Tubes," *Zirconium in the Nuclear Industry, Eight International Symposium,* ASTM-STP-1023, 1989, pp. 3-19.

A2-26. A. Seibold and K. N. Woods, "BWR Advanced Material," *Proceedings of the International Topical Meeting on Light Water Reactor Fuel Performance, West Palm Beach, FL, April 17-21, 1994.*

A2.2.11 CAGROWH (CAGROW) - Fraction Change in Length of Cladding Due to Irradiation

The model in the INEEL maintained MATPRO and MATPRO-11 function CAGROW predicts axial cladding growth strains as a function of temperature, fast neutron flux, time, texture and cold work. This model underpredicts cumulative growth strains as a function of fast neutron fluences when fluences are greater than 1.0 e^{+21} n/cm^2. This under-prediction, shown in Figure A2-15, is due to the fact that the MATPRO-11 model was developed using fast neutron fluences under 1.0 e^{+21} n/cm.^{2} D. G. Franklin[A2-27] developed a model based on high neutron fluence PWR data, and on the proportionality between axial growth and fluence raised to the 0.845 power. Figure A2-15 compares the previous MATPRO model and the new Franklin model to axial growth experimental data.[A2-28-A2-35]

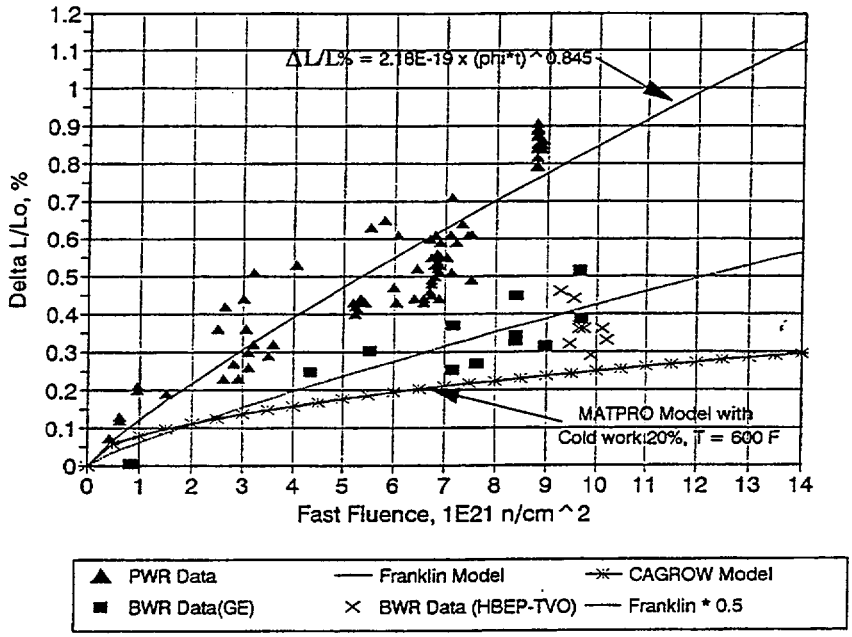

Figure A2-15. Comparison of the recommended Franklin model and the current model to measured cladding growth strain.

As shown in the figure, the Franklin model gives a good best estimate fit to the measured data except for fully-annealed Zr-2 clad BWR fuel rods. To check the accuracy of the new Franklin model, a zero-intercept linear regression analysis of measured versus predicted data was performed. The results of this accuracy check are shown in Figure A2-16. The slope of the measured versus predicted line was 0.97, very close to 1.0, with a 0.095% standard deviation. The two figures also show the Franklin model overpredicting the cladding growth strains for fully annealed Zr-2 BWR fuel rods by a factor of 2. To account for this overprediction, the cladding growth strains predicted by the Franklin model for fully annealed Zr-2 cladding BWR fuel rods were reduced by a factor 0.5. The Franklin model described below, can be used for either high burnup or low burnup fuels,

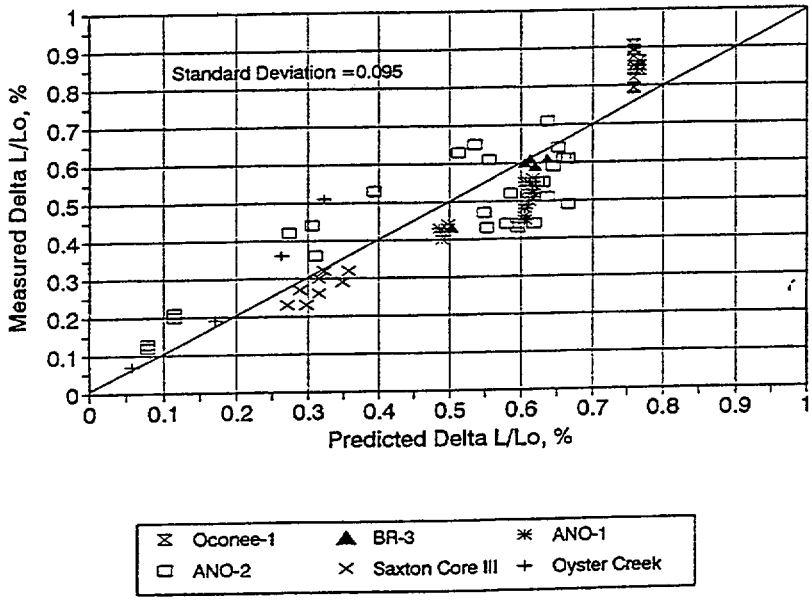

Figure A2-16. Calculated versus measured cladding axial growth.

ax1 = 2.18e-21 * (fluence/10000)**2

ax2 = 2.18e-21 * [(fluence - flux * time)/10000]**2

cagrow = ax2 - ax1

where

ax1 = axial growth strain at start of time step

ax2 = axial growth strain at end of time step

cagrow = cumulative cladding growth strains.

The Franklin model was implemented in CAGROW during the development of the FRAPCON-3

high burnup fuel behavior code. The new CAGROW model calculates the fluence increment based on the end of time step fluence and the current time step. The FRAPCON-3 developed axial growth subprogram CAGROW was implemented in the INEEL maintained version of MATPRO as CAGROWH. The tailing H flags the subprogram as being developed for high burnup fuels. The new model calculates the axial growth term once for each time step, improving the efficiency of the subprogram and the changes which expand the accuracy of the model to fluences greater than 1.0 e^{+21} n/cm^2 improve the predicted axial growth.

A2.2.12 References for the Subprogram CAGROWH

A2-27. D. G. Franklin, "Zircaloy Cladding Deformation during Power Reactor Irradiation," *Proceedings of the Fifth International Symposium on Zirconium in the Nuclear Industry,* ASTM-STP-754, 1982, pp. 235-67.

A2-28. M. G. Balfour, *BR-3 Burnup Fuel Rod Hot Cell Program, Final Report, Volume 1,* DOE/ET/34073-1, 1982.

A2-29. C. G. Dideon, *Fuel Performance under Extended Burnup for the B&W 15 x 15 Design,* DOE/ET/34212, 1983.

A2-30. L. W. Exarhos, *Extended Burnup Demonstration Reactor Fuel Program: Final Project Report,* DOE/ET/34006-50, 1986.

A2-31. L. W. Newman, *The Hot Cell Examination of Oconee 1 Fuel Rods After Five Cycles of Irradiation,* DOE/ET/34212-50, 1986.

A2-32. W. R. Smalley, *Evaluation of Saxton Core III Fuel Material Performance,* WCAP-3385-57, 1974.

A2-33. G. P. Smith, *The Nondestructive Examination of Fuel Assemblies with Standard and Advanced Design after Three Cycles of Irradiation,* DOE/ET/34013-12, 1986.

A2-34. J. S. West et al., *EOC9-Final Fuel Bundle Examination at Monticello Nuclear Generating Station,* DOE/ET/34031-16, 1983.

A2-35. J. O. Barner et al., *High Burnup Effects Program Summary Report,* DOE/NE/3406-1, 1990.

A2.2.13 CORROSH (CORROS) - Low Temperature Oxidation

The subroutine CORROS returns an expression for the thickness of the oxide layer on zircaloy fuel rod cladding during typical reactor operation for temperatures between 523 and 673 K. An extensive literature review[A2-36-A2-41] and a comparison of predicted oxide thicknesses using the INEEL maintained and MATPRO-11 model with recent experimental data covering a wide range of burnup levels was performed by PNNL, along with an independent model review by T. J. Haste, AEA Technology, Winfrith UK.[A2-42] These reviews showed the need to revise the present low temperature oxidation model. A model-to-data comparison showed the MATPRO-11 model predicting an oxide thickness four to five times lower than measured. In addition, the reviews revealed a post-transition correlation being used to predict pre-transition oxide growth. The corrosion model, CORROS, was revised by PNNL for use with high burnup

fuel. The required input values for the revised subcode CORROS are temperature at the cladding water interface, initial oxide film thickness, length of time the fuel remained at a given temperature, type of reactor (BWR or PWR), heat flux across the oxide layer, zircaloy oxide thermal conductivity, and fast neutron flux. Neither the INEEL nor MATPRO-11 version of CORROS consider the effects of fast neutron flux.

Cladding oxidation under normal LWR operating conditions for high burnup fuel occurs in two stages, as does the oxidation of low burnup or fresh fuel rods, depending on the oxide thickness and to some extent on the temperature of the oxide. The revised CORROS subcode for high burnup fuel employs the uniform oxidation models developed by the Electric Power Research Institute (EPRI) for the ESCORE (EPRI Steady-State Core Reload Evaluation) computer code.[A2-43] The pre-transition oxidation stage, where the oxide layer is very thin, uses a standard cubic law oxidation expression, whereas, for the post-transition oxidation stage, where oxide layers are thicker, a fast neutron flux enhanced linear expression is used to predict oxide thickness. The revised version of CORROS uses centimeters as the length and thickness terms to calculate oxide growth as a function of the cladding oxide interface temperature. Therefore, the length or thickness terms passed into CORROS from the calling program are internally converted to the correct units for use with new correlations and then converted back to the units needed in the calling routine before being passed back. Initially a cladding oxide interface temperature is calculated using the following expression;

$$T_{cok} = T_{coi} + q_i * X_i/k \qquad \text{(A2-17)}$$

where

T_{cok} = cladding oxide interface temperature (K)

T_{coi} = cladding oxide-water interface temperature (K)

q_i = cladding surface heat flux (W/m^2)

X_i = oxide layer thickness at start of time-step

k = thermal conductivity of the cladding before oxide growth is calculated.

Pre-transition oxide growth follows the cubic rate law until the transition oxide thickness of 2.0 microns on the cladding surface is attained. The rate equation used to predict pre-transition oxide growth is

$$\frac{ds}{dt} = \left(\frac{A}{S^2}\right)\exp\left(\frac{-Q_1}{RT_1}\right) \qquad \text{(A2-18)}$$

where

$\frac{ds}{dt}$ = oxidation rate

A = 6.3×10^9 μm^3/day

S = thickness

Q_i = 32.289 cal/mol

R = 1.98 cal/mol-K°

T_1 = metal oxide interface temperature.

After transition occurs, oxidation proceeds according to a linear law rate. The oxide growth rate expression developed by EPRI for ESCORE is

$$\frac{ds}{dt} = [K_0 + u(M\phi)^p]\exp\left(\frac{-Q_2}{RT_1}\right) \quad \text{(A2-19)}$$

where

$\frac{ds}{dt}$ = oxidation rate

K = 8.04×10^7 μm/day

u = 2.38×10^8 μm/day

M = 1.91×10^{-15} cm-sec/m

p = 0.24

Q_2 = 27354 cals/mol.

During the assessment of the pre-transition cubic rate model and the EPRI linear post-transition model using the differential form of the growth equations, it was discovered that these equations were extremely dependent on time step size. The time step dependency for post-transition oxide growth was directly related to the use of a heat flux term in a highly temperature sensitive expression. In the revised version of CORROS, the integrated forms of the above expressions, where the limits of integration are zero and current time step size, were used to remove the temperature dependency. The integrated form of the cubic rate equation is

$$X_f = \left[1.89e^{10} * \exp\left(\frac{-32889}{T_i R}\right) * dt + (X_i * 1.0e^6)^3\right]^{1/3} \quad \text{(A2-20)}$$

where

X_f = cladding oxide thickness at end of time step

X_i = cladding oxide thickness at beginning of time step

dt = time (days).

The above integration is done without regard to the feedback between oxide layer thickness and oxide-metal interface temperature, due to the fact that the transition layer thickness is small and no significant feedback occurs.

The integrated linear equation, developed by Garzarolli[A2-36] for post-transition oxide growth is

$$w = \frac{RT_i^2\lambda}{0.6789Qq''}\ln\left[1 - \frac{0.6789Qq''}{RT_i^2\lambda}k_o\exp\left(\frac{-Q}{RT_i}\right)\exp\left(\frac{0.6789Qq''\Delta W_i}{RT_i^2\lambda}\right)\right]dt \quad \text{(A2-21)}$$

where

w = oxide weight gain

K_0 = rate constant

Q = activation energy

q" = heat flux

λ = oxide thermal conductivity.

This equation considers the feedback between the oxide layer thickness and the oxide-metal interface temperature. Since the model was developed in terms of weight gain instead of oxide thickness, the incremental weight gain is first calculated and then transformed to a thickness using a standard proportionality constant.

The corrosion model developed for the high burnup version of CORROS uses the linear rate equation in both the pre- and post-transition phases for BWR fuel. The equation has the form

$$\frac{ds}{dt} = K\left[\exp\frac{-Q}{RT_i}\right]\left[1 + Cq''\exp\frac{Q}{RT_i}\right] \quad \text{(A2-22)}$$

where

Q = 27,350 cal/mole

K = 8.04×10^{-7} μm/day

q" = surface heat flux.

As with the PWR model, this equation is integrated over the current time step using the Garzarolli approximation on the first term, and simply integrating the temperature-independent constant rate second term. The calculated thickness growth increment is added to the previous cumulative thickness.

Results from these oxide growth equations were compared to available cladding thickness and oxide growth data from fuel rods with high burnup levels from the Calvert Cliffs, ANO-2, Oconee, and Fort Calhoun nuclear power plants. Comparisons of the predicted oxide growth with the measured data indicated that the oxide growth predicted by the new models was satisfactory, though some additional adjustments to correct the temperature dependence may be needed. (The comparison data is proprietary, and therefore, comparison plots are not shown.)

The oxide growth models developed for the high burnup version of FRAPCON were implemented into INEEL maintained MATPRO source code as CORROSH so that a complete oxidation and oxide growth package is available to all users for any fuel rod design. The changes described in this section are applicable for fuel rods with varying levels of burnup. The implementation of the new model developed for high burnup fuels in MATPRO should considerably improve predicted oxidation rates and oxide thickness, currently underpredicted in the code.

A2.2.14 References for CORROSH

A2-36. F. Garzarolli et al., *Review of PWR Fuel Rod Waterside Corrosion Behavior,* EPRI-NP-1472, Electric Power Research Institute, Palo Alto, CA, 1980.

A2-37. A. B. Johnson, Jr., *Zirconium Alloy Oxidation and Hydriding Under Irradiation,* Review of Pacific Northwest Laboratory Test Program Results, EPRI-NP-5132, Electric Power Research Institute, Palo Alto, CA, 1987.

A2-38. IAEA Staff, *Corrosion of Zirconium Alloys in Nuclear Power Plants (a review of 297 references),* IAEA-TECDOC-684, Vienna, Austria, 1993.

A2-39. F. Garzarolli "Progress in Understanding PWR Fuel Rod Waterside Corrosion," *ANS/ENS International Topical Meeting on Light Water Fuel Performance, Orlando, FL, 1985, pp. 3-55.*

A2-40. F. Garzarolli et al., *Review of PWR Fuel Rod Waterside Corrosion Behavior,* EPRI-NP-2789, Project 1250 Final Report, Electric Power Research Institute, Palo Alto, CA., 1982.

A2-41. M. Limback, "Corrosion and Hydriding Performance of Zircaloy-2 and Zircaloy-4 Cladding Materials in PWRs," *ANS/ENS International Topical Meeting on Light Water Fuel Performance, West Palm Beach, FL, 1994, p. 286.*

A2-42. T. J. Haste, AEA Technology, Winfrith U. K., private communication.

A2-43. I. B. Fiero et al., *ESCORE - the EPRI Steady-State Core Reload Evaluator Code,* EPRI-NP-5100, Electric Power Research Institute, Palo Alto, CA., 1987.

A2.2.15 Cladding Constitutive Models, CKMNH (CKMN) and CMLIMTH (CMLIMT)

A2.2.15.1 CKMNH - Parameters for the Cladding Equation of State. Recent mechanical property data associated with the zircaloy-4 cladding on fuels with high burnup levels for yield strength, tensile strength, and uniform strain spanning fast neutron fluence levels between 0 and 12 x 10^{25} n/m^2, oxide thicknesses between 4 and 100 micrometers, and total hydrogen content in the cladding between 10 and 720 ppm[A2-44-A2-46] were compared to predictions from the mechanical property model in MATPRO-11. Figure A2-17 to Figure A2-19 show the MATPRO-11 model under-predicting the uniform cladding strain and overpredicting both yield strength and tensile strength for irradiated fuel.

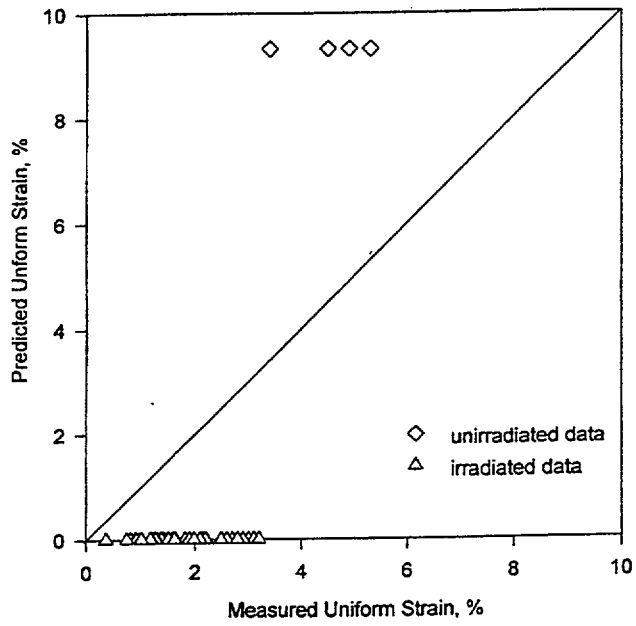

Figure A2-17. Predicted versus measured uniform strains from the current MATPRO model.

An analysis of new zircaloy-4 cladding data obtained for fuels with high burnup levels showed that the formation of cladding hydrides degraded the strength and ductility of the cladding. The accumulation of hydrogen in the zircaloy cladding resulting from oxidation occurring on the cladding surface increases as fuel burnup levels increase. A fraction of the hydrogen produced during cladding oxidation is absorbed in the metallic zircaloy cladding. The absorbed hydrogen then begins migrating to cooler regions in the cladding, reacting with that zircaloy and finally precipitating as a zircaloy hydride when its concentration exceeds the solubility limit for hydrogen in zircaloy for a given temperature.[A2-47] The axial distribution of hydrogen and hydrides in the cladding is proportional to the oxide thickness along the length of a fuel rod and the radial distribution of hydrides across a section of cladding shows a higher density of hydrides near the outer surface of the cladding and a much lower hydride density at the inner surface.

Hydrides form in a circumferential direction as a result of stress exhibited by the cladding. At low hydride concentrations, it is believed that hydride pin dislocations during the deformation processes tend to strengthen the cladding. Once the hydride concentration in the cladding exceeds 300 ppm, a significant

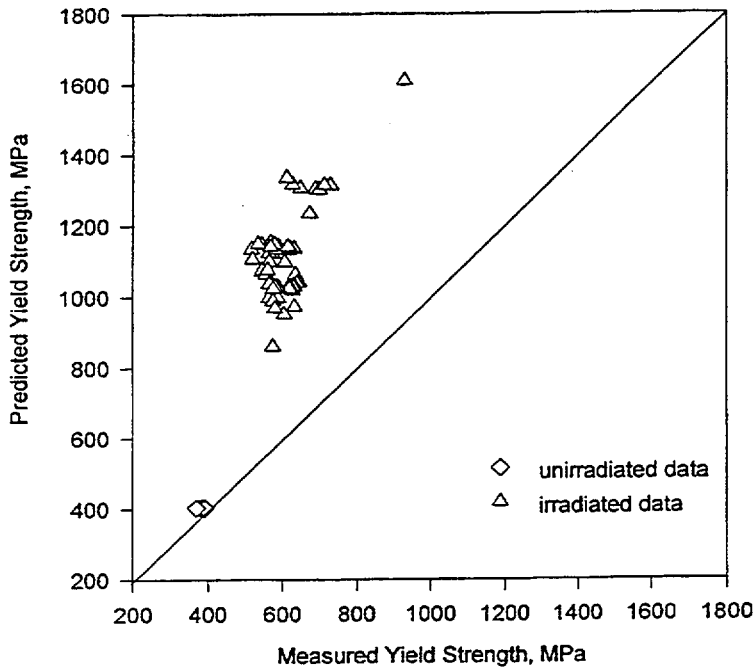

Figure A2-18. Predicted versus measured yield strengths from the current MATPRO model.

increase in the formation of crack initiation sites in the metallic zircaloy occur. Continued increase in cladding hydride concentrations results in the formation of additional crack initiation sites and a continued degradation of the cladding tensile strength until the maximum cladding yield strength at 550 to 600 ppm hydrogen dissolved in the cladding is attained. The formation of hydrides in the cladding also has an adverse effect on the uniform strain which provides a measure for cladding ductility. As long as the hydrogen concentration remains below the solubility limit there is no noticeable effect on the strain. Once the hydrogen solubility limit is exceeded, a noticeable reduction in uniform strain and ductility is observed.

The experimental data focusing on the mechanical properties of high burnup fuel rod cladding and the effects of the formation of hydrides in the cladding indicated that modifications to the models used to calculated the strength coefficient and the strain hardening exponent in the MATPRO function CKMN were needed for fuel with high burnup levels. Comparisons to measured data indicated that the strain hardening dependence on fast neutron fluence in the current MATPRO mechanical models was inadequate for high fast neutron fluences, therefore, a revised strain hardening term as a function of fast neutron fluence was developed for use with high burnup fuels.

The new model for true stress was developed by curve fitting all available mechanical properties data for both high burnup fuels and low burnup fuels. The true stress equation determined from the curve fitting procedure and implemented in the high burnup version of CKMN is

$$a = K * e^{n} \qquad \text{(A2-23)}$$

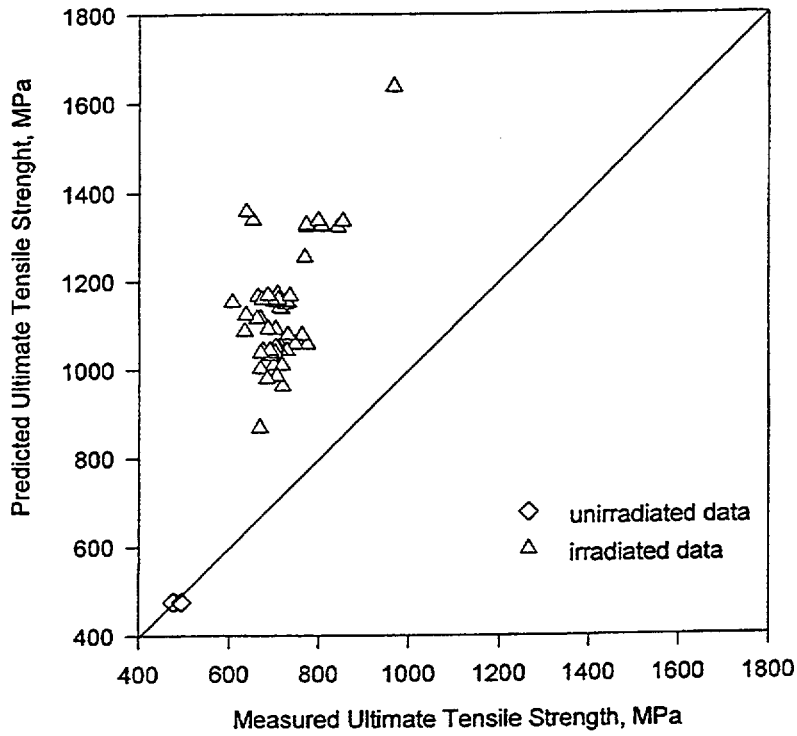

Figure A2-19. Predicted versus measured ultimate tensile strength from the current MATPRO model.

where

a	=	true stress (MPa)
e	=	true strain (unitless)
K	=	strength coefficient (MPa)
n	=	strain hardening exponent (unitless).

The determination of the values to be used for the strength coefficient, K, and the strain hardening exponent, n are discussed in the following sections. In the modified mechanical model the parameters K and n describe the metallurgical state of the cladding and vary as a function temperature, cold work, fast fluence, and hydrogen content. These new parameters were verified by comparing the stress predicted by the new MATPRO CKMN model to data from both irradiated and unirradiated fuel. Predicted results were well within the expected error for the model.

2.2.15.1.1 Strength Coefficient K. A hydrogen dependent term was developed for inclusion in the high burnup CKMN MATPRO strength coefficient model assuming that the current temperature, cold work, and fast fluence terms were correct. The new model assumed a cold work term of 0.5, based on an initial cold work of 75% after the last reduction in tubing wall thickness followed by a stress relief process

at 766.5 K for 8 hours. The assumed cold work term was verified by discussion with various individuals at ABB, CE, B&W, Westinghouse, and Sanvik Special Metals Corporation.[A2-48]

Test specimens having hydrogen concentrations less than the solubility limit were used to verify the modified model. After subtracting the temperature, cold work, and fast fluence dependent terms from the measured strength coefficient terms for all data (hydrogen less than or greater than the solubility limit), the result was analyzed for a dependency related to the quantity of hydrogen above the solubility limit. The change in the strength coefficient, ΔK, showed a strong dependency on the hydrogen concentration at hydrogen concentrations above the solubility limit. A linear regression was performed using all data to develop a third order polynomial fit. The model developed for the strength coefficient of high burnup fuels is described by the following equations.

$$K = K(T) + K(CW,\text{fluence}) + K(h) \quad \text{(A2-24)}$$

$$K(T) = 1.17628\,E^{9} + T * [4.54859\,E^{5} + T * (-3.28185\,E^{3} + T * 1.72752)] \quad \text{(A2-25)}$$

$$K(CW,\text{fluence}) = 0.546 * CW * K(T) + 5.54E^{-18} * \text{fluence} \quad \text{(A2-26)}$$

$$K(h) = h * [1.288\,E^{6} + h * (7.546\,E^{3} - h * 17.84)] \quad \text{(A2-27)}$$

where

T	=	temperature (K)
CW	=	cold work (unitless)
fluence	=	in n/m^2
h	=	hydrogen concentration in excess of solubility limit (ppm).

Figure A2-20 showing a zero-intercept linear regression plot of measured versus predicted strength coefficients provides and indication of the accuracy of the model. As shown in the figure the model does a good job of predicting the strength coefficient for both irradiated and unirradiated fuel. The figure shows the predicted results to be within the uncertainty bounds.

2.2.15.1.2 Strain Hardening Exponent, n. The procedure used to develop the strain hardening exponent, n, was similar to that used for the strength coefficient. The fast fluence term used in the current MATPRO did not perform well for high burnup fuel, therefore a linear fluence term was developed for use with high burnup fuels. The temperature dependence was removed from measured data for samples with low hydrogen concentrations using the MATPRO strain hardening exponent temperature dependent term. The data was then analyzed as a function of fast fluence and the revised strain hardening exponent term, Figure A2-21. The analysis showed a slight linear dependence on fast fluence with the cold work term being absorbed into the new strain hardening coefficient. A strain hardening exponent with a hydrogen excess dependency was then developed by removing the temperature and fluence dependencies from the

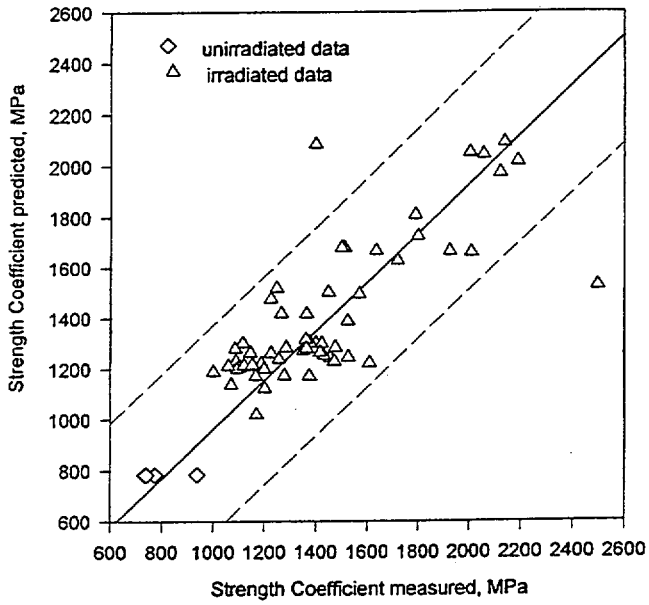

Figure A2-20. Calculated strength coefficient using the modified MATPRO versus the measured value.

data using the temperature dependence term in the MATPRO model and a linearly increasing fluence term. The modified model is described by the following equation

$$n = n(T) * n(\text{fluence}) * n(h_{ex}) \quad \text{(A2-28)}$$

$$n(T) = -9.49\,E^{-2} + T * [1.165\,E^{-3} + T * (-1.992\,E^{-6} + T * 9.588\,E^{-10})] \quad \text{(A2-29)}$$

$$n(\text{fluence}) = 1.369 + 0.032\,E^{-25} * \text{fluence} \quad \text{(A2-30)}$$

$$n(h_{ex}) = 1. + 2.298\,E^{-3} * h_{ex} + 4.138\,E^{-6} * (h_{ex})^2 - 1.5\,E^{-8} * (h_{ex})^3 \quad \text{(A2-31)}$$

where

T = temperature (K)

fluence = n/m^2

h_{ex} = hydrogen concentration in excess of solubility limit (ppm).

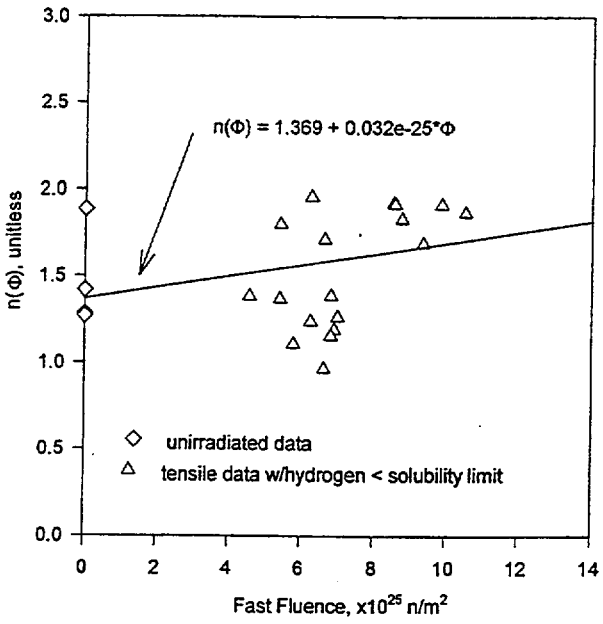

Figure A2-21. Predicted values using the modified model for the strain hardening exponent.

Figure A2-22 shows a comparison of the predicted versus measured values for n. As shown in the figure, the majority of predicted values for unirradiated and irradiated data are well within the error bounds for the model.

2.2.15.1.3 Uniform Strain, ε. Uniform strain data was analyzed as a function of temperature and found to decrease linearly with increasing temperature in the 580 to 680 K temperature range. The temperature dependence was removed from the hydrogen data for specimens with hydrogen concentrations under the solubility limit to determine a dependence on fast fluence. The data, Figure A2-23, shows uniform strain to exponentially decrease with increasing values for the fast fluence, reaching an asymtopic value at approximately 4.0 x 10^{25} n/m2. Once the temperature and fluence dependencies were determined they were removed from the data set to reduce the data to a term reflecting a change in the uniform strain as a function of cladding hydrogen content. The expression used to determine the true uniform strain is

$$\text{true uniform strain} = 0.096 - 1.142 * 10^{-4} * T + 0.01856 * \exp(\text{fluence}/10^{-25}) - (h/804976.)^{0.5} \qquad \text{(A2-32)}$$

where

T = temperature (K)

fluence = n/m^2

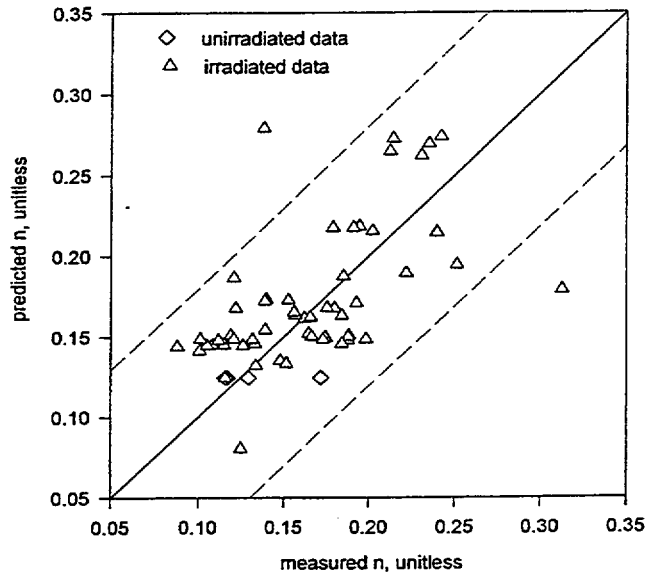

Figure A2-22. Predicted strain hardening exponent values using to modified MATPRO model versus the measured value.

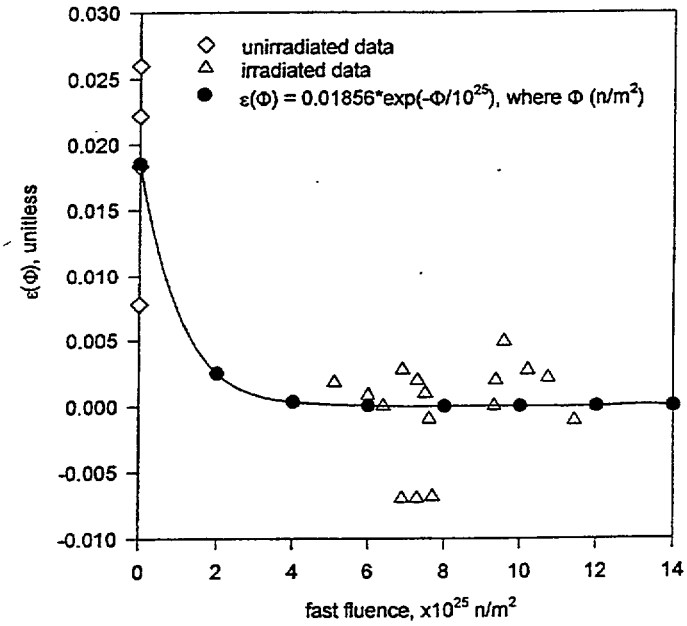

Figure A2-23. Predicted uniform strain using the modified MAPTRO model compared to experimental data.

h = hydrogen concentration in excess of solubility limit (ppm).

Figure A2-24 shows that the expression used to calculate true uniform strains for unirradiated and irradiated fuel samples predicts uniform strains well within the uncertainty bounds of the new model.

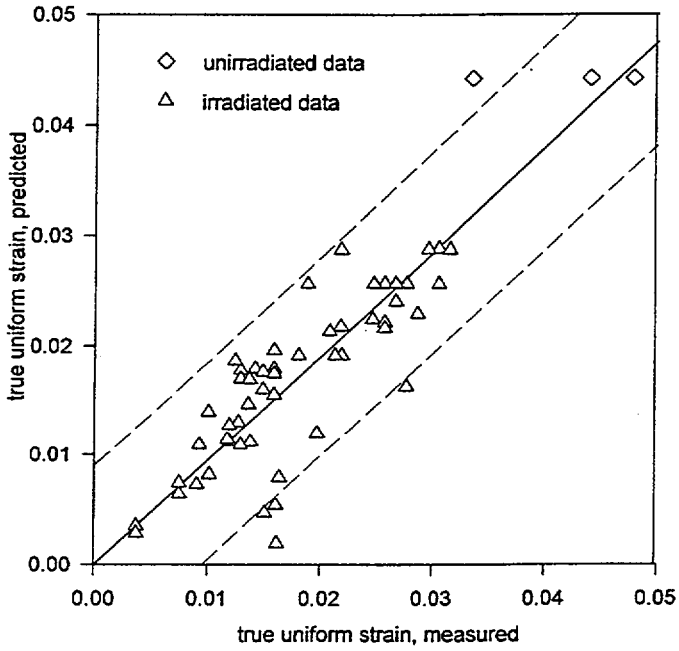

Figure A2-24. Predicted true uniform strain using the modified MATPRO model versus the measured strain.

A2.2.16 References for Cladding Constitutive Models

A2-44. L. W. Newman, *Development of an Extended Burnup Mark B Design,* 1990.

A2-45. G. P. Smith, *Hot Cell Examination of Extended Burnup Fuel from Calvert Cliffs-1,* TR-103302-V2, 1993.

A2-46. G. P. Smith, *The Evaluation and Demonstration of Methods for Improved Nuclear Fuel Utilization,* DOE/ET/34013-15, 1994.

A2-47. A. Sawatzy and B. J. Wilkins, "Hydrogen Solubility in Zirconium Alloys Determined by Thermal Diffusion," *Journal of Nuclear Material, 22,* 1967, pp. 304-310.

A2-48. G. A. Berna, private communication, 1996.

A2.2.16.1 CMLIMTH (CMLIMT) - Elastic Plastic Transition Yield and Cladding Failure Under Tensile Stress. The subprogram CMLIMT defines the elastic-plastic transition (yield) and cladding failure under tensile stress, as well as the ultimate engineering strength and uniform elongation under uniaxial stress. The modeling changes developed for fuel with higher burnup limits include slight modifications to the equations in the INEEL maintained version of MATPRO and MATPRO-11. The new model CMLIMTH includes a term for the quantity of hydrogen above the solubility limit in zircaloy cladding in the argument list. This term was included since the correlations used in the high burnup model CKMNH predict parameters for the cladding equation of state as a function of hydrogen concentration above the solubility limit. The changes implemented in CMLIMT for a high burnup version of MATPRO are described below.

Changes implemented for high burnup fuel include the prediction of a true ultimate strength rather than true stress as calculated by CMLIMT in the INEEL maintained version of MATPRO and MATPRO-11. The modified true ultimate strength equation in the new model is described below.

$$\sigma = K * (\epsilon'/10^{-3})^m * (\epsilon_{p+e})^n \qquad \text{(A2-33)}$$

where

σ	=	true ultimate strength (MPa)
K	=	strength coefficient (MPa)
ϵ'	=	strain rate (unitless)
m	=	strain rate sensitivity constant (unitless)
ϵ_{p+e}	=	true strain at maximum load (unitless)
n	=	strain hardening exponent (unitless).

The current MATPRO model uses a true strain rate ($\dot{\epsilon}$) to predict a true stress term. The equations in the subprogram CMLIMT used to predict true yield strength and true strain at yield remained unchanged from those in MATPRO-11 and the INEEL version of MATPRO released with SCDAP/RELAP5 for the high burnup version of CMLIMT.

The modified version of CMLIMT, designated CMLIMTH, for use with MATPRO uses a correlation developed by Chad Painter of PNNL in 1995[A2-49] to predict uniform strain. This correlation described below predicted uniform strain as a function of the fast fluence term for strength and the quantity of hydrogen in the cladding above the zircaloy solubility limit.

$$\varepsilon = 0.096 - 1.142*10^{-4}\,T + 0.01856 * \exp(-fnck/10^{25}) - \sqrt{\frac{h}{804967}} \qquad \text{(A2-34)}$$

where

e	=	uniform strain
T	=	temperature
fnck	=	fast fluence for strength
h	=	quantity hydrogen above the solubility limit in zircaloy.

Figure A2-25 to Figure A2-27 show a zero-intercept linear regression analyses of measured versus predicted values for the uniform strain, yield strength, and tensile strength, respectively. Ninety-five percent prediction intervals are included in the figures to provide a measure of accuracy for the models. The figures show that 95% of the measured data will fall within the calculated interval. For tensile strength the error is approximately 17% which is consistent with the standard error in the previous CMLIMT subprogram.

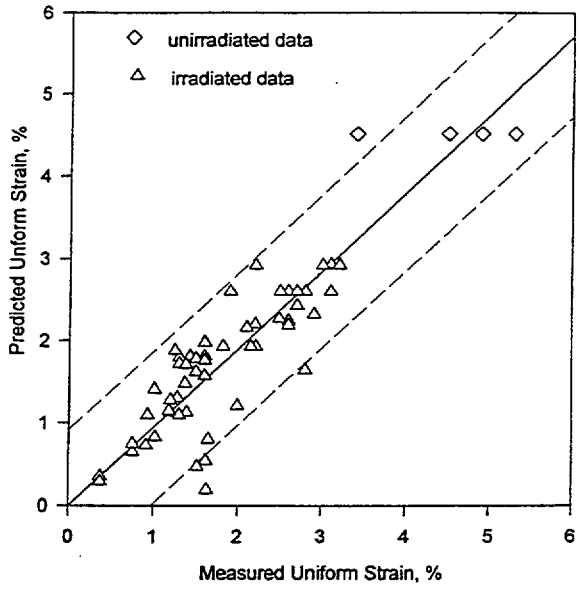

Figure A2-25. Predicted uniform strain from the modified MATPRO model versus measured uniform strain (%).

A2.2.16.2 Limitations of the Proposed Cladding Constitutive Models. Two limitations have been identified for the above described new constitutive models, CKMNH and CMLIMTH. The first limitation is that both models can only be considered valid over the temperature range of the supporting data, 580 - 680 K. This temperature range covers the normal operating temperatures for a reactor at power but is more limited than the temperature range covered by the models in the current version of MATPRO-11 and the version of MATPRO maintained at the INEEL and released with the SCDAP/RELAP5 computer code. Although the strength coefficient model should provide acceptable results over a larger

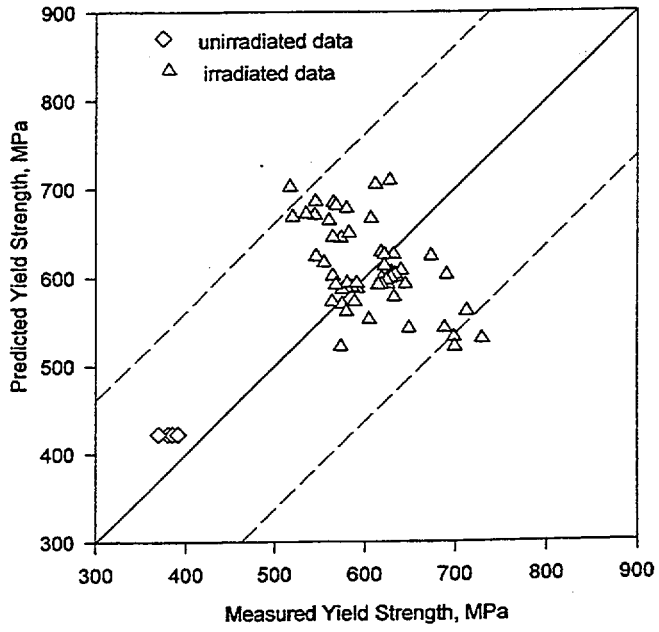

Figure A2-26. Predicted yield strength from the modified MATPRO model versus measured yield strength.

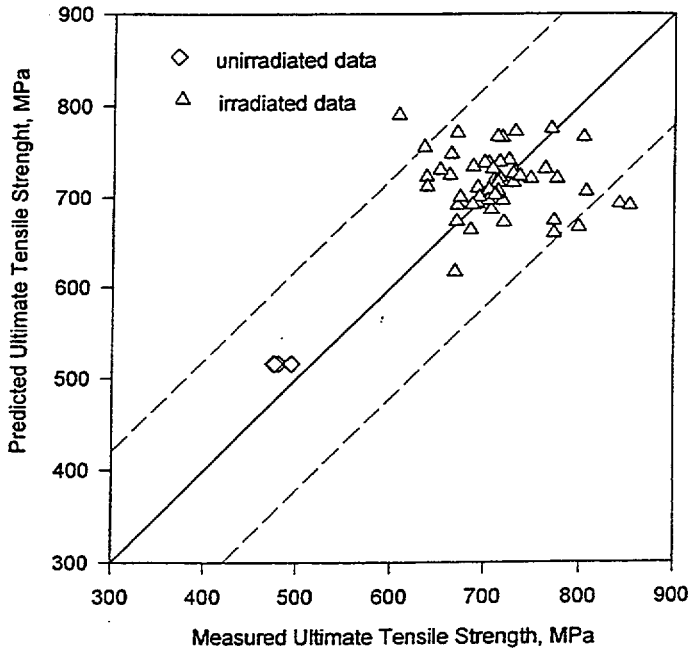

Figure A2-27. Predicted ultimate tensile strength using the modified MATPRO model versus measured data.

range of temperatures and fast neutron fluence, it is unknown how well the model will predict fuel cladding mechanical limits for temperatures outside this range and for cladding with hydrogen concentrations in excess of 650 ppm. The strain hardening exponent model most likely will not accurately predict the effects of fast fluence and cladding hydrogen concentrations in excess of 650 ppm for temperatures outside the 580 - 680 K range. Therefore, the predicted uniform strain would be in error at higher hydrogen concentrations and temperatures. The second limitation of the models is related to the removal of the cold work term from the strain hardening exponent. Therefore, no cold work, other than the assumed 0.5 cold work term inherent in the model, can be incorporated into the prediction of uniform strain. The removal of the cold work in predicting the strain hardening exponent limits the adaptability of the model to different types of cladding.

A2.2.16.3 Implementation of the CKMNH and CMLIMTH in MATPRO. The high burnup subprograms CKMNH and CMLIMTH, developed during the extension of FRAPCON for the fuels with high burnup levels, were incorporated into the INEEL maintained version of MATPRO as routines specifically identified as high burnup. These subprograms should be used only in the correct temperature range and for high burnup fuels for the following reasons; (1) the modified routines are limited to a considerably narrower temperature range than the ones currently in the INEEL maintained version of MATPRO, and (2) the use of a hardwired cold work term limits the applicability of the new model to zircaloy cladding.

A2.2.17 Reference for the Cladding Equations of State

A2-49. Letter from Chad Painter to Larry Siefken, August 3, 1995.

A2.3 Extensions to Include Different Fuels and Cladding Materials

Earlier versions of MATPRO, including MATPRO-11, Revision 2, used a common block PHYPRO to pass variables, such as melting temperatures, heats of fusion, burnup, etc. for fuel into a fuel materials property subprograms. In 1982 this common block was removed from MATPRO and the materials properties previously input to a subprogram through the PHYPRO common block were hardwired into the subprogram. The hardwired properties were specifically for UO_2 fuels. The major driving force for the removal of the PHYPRO common block in the early 1980's was that variables used in the common block were not adequately defined in the manual or subcode. Many codes released in the late 1970's and early 1980's tended to use inadequately defined variables in common blocks which resulted in confusion over the true meaning of each variable and the units used for the variable being passed into the subroutine.

MATPRO, to become a robust materials properties library should have the capability to predict fuel and cladding behavior for fuels other than UO_2 with zircaloy-4 or zircaloy-2 cladding. The common block PHYPRO has been re-implemented in the INEEL version of MATPRO for use with the fuel behavior routines, such as FTHCONH, FCPH, and FSWELLH. The implementation of this materials properties common block will make the MATPRO package more robust and expand its usage to alternate fuels and fuel rod claddings.

NRC FORM 335 (2-89)
NRCM 1102, 3201, 3202

U.S. NUCLEAR REGULATORY COMMISSION

BIBLIOGRAPHIC DATA SHEET

(See Instructions on the reverse)

1. REPORT NUMBER (Assigned by NRC, Add Vol., Supp., Rev., and Addendum Numbers, if any.)
NUREG/CR-6150, Rev. 2
Volume 4
INEL-96/0422

2. TITLE AND SUBTITLE
SCDAP/RELAP5/MOD3.3 Code Manual, Volume 4: MATPRO -- A Library of Materials Properties for Light-Water-Reactor Accident Analysis

3. DATE REPORT PUBLISHED
MONTH: January
YEAR: 2001

4. FIN OR GRANT NUMBER
W6095

5. AUTHOR(S)
L. J. Siefken, E. W. Coryell, E. A. Harvego, J. K. Hohorst

6. TYPE OF REPORT
Technical

7. PERIOD COVERED (Inclusive Dates)

8. PERFORMING ORGANIZAITON - NAME AND ADDRESS (If NRC, provide Division, Office or Region, U.S. Nuclear Regulatory Commission, and mailing address; if contractor, provide name and mailing address.)

Idaho National Engineering and Environmental Laboratory
P.O. Box 1625
Idaho Falls, ID 83415-3129

9. SPONSORING ORGANIZATION - NAME AND ADDRESS (If NRC, type "Same as above"; If contractor, provide NRC Division, Office or Region, U.S. Nuclear Regulatory Commission, and mailing address.)
Division of Systems Technology
Office of Nuclear Regulatory Research
U.S. Nuclear Regulatory Commission
Washington, DC 20555-0001

10. SUPPLEMENTARY NOTES
S. A. Arndt, NRC Project Manager

11. ABSTRACT (200 words or less)

The SCDAP/RELAP5 code has been developed for best-estimate transient simulation of light water reactor coolant systems during a severe accident. The code models the coupled behavior of the reactor coolant system and reactor core during severe accidents as well as large and small break loss-of-coolant accidents, operational transients such as anticipated transient without SCRAM, loss of offsite power, loss of feedwater, and loss of flow.

Volume 4 describes the material properties correlations and computer subroutines (MATPRO) used by SCDAP/RELAP5. Formulation of the materials properties are generally semi-empirical in nature. The materials property subroutines contained in this document are for uranium, uranium dioxide, mixed uranium-plutonium dioxide fuel, zircaloy cladding, zirconium dioxide, stainless steel, stainless steel oxide, silver-indium-cadmium alloy, cadmium, boron carbide, Inconel 718, zirconium-uranium-oxygen melts, fill gas mixtures, carbon steel, and tungsten. This document also contains descriptions of the reaction and solution rate models needed to analyze a reactor accident, including changes incorporated since the manuals were released in July 1998.

12. KEY WORDS/DESCRIPTORS (List words or phrases that will assist researchers in locating the report.)
SCDAP/RELAP5; material properties; transient simulation; LWR; coolant system; reactor core

13. AVAILABILITY STATEMENT
Unlimited

14. SECURITY CLASSIFICATION
(This page)
Unclassified
(This report)
Unclassified

15. NUMBER OF PAGES

16. PRICE

NRC FORM 335 (2-89)

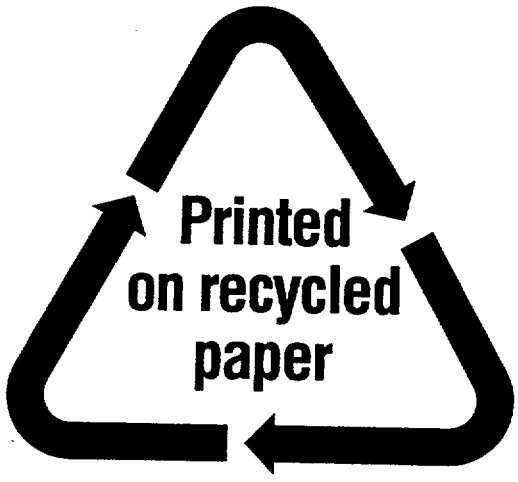

Federal Recycling Program

UNITED STATES
NUCLEAR REGULATORY COMMISSION
WASHINGTON, DC 20555-0001